

Universidade Federal de Minas Gerais
Instituto de Ciências Exatas
Departamento de Química

Egon Campos dos Santos

**Computational simulation of the pyrite/arsenopyrite
interface- galvanic effects in chemical reactivity of minerals**

Belo Horizonte,
2019

UFMG/ICEx/ DQ. 1349

T. 616^a

Egon Campos dos Santos

**Simulação computacional da interface
pirita/arsenopirita- efeitos galvânicos na reatividade
química de minerais**

Tese de doutorado apresentada
ao Departamento de Química do
Instituto de Ciências Exatas da
Universidade Federal de Minas
Gerais sob orientação do Prof.
Dr. Hélio Anderson Duarte,
como requisito parcial para a
obtenção do grau de Doutor em
Química, Química Inorgânica,
Físico-química inorgânica.

Belo Horizonte,

2019

Ficha Catalográfica

S237s Santos, Egon Campos dos
2019 Simulação computacional da interface
D pirita/arsenopirita - efeitos galvânicos na
reatividade química de minerais [manuscrito] / Egon
Campos dos Santos. 2019.
[xvi], 129 + [31] f. : il.

Orientador: Hélio Anderson Duarte.

Tese (doutorado) - Universidade Federal de Minas
Gerais - Departamento de Química.

Inclui bibliografia.

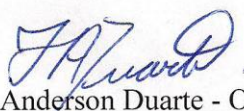
1. Química inorgânica - Teses 2. Sulfetos -
Metalurgia - Teses 3. Piritas - Teses 4. Química de
superfície - Teses 5. Funcionais de densidade - Teses
6. Minas - Drenagem - Teses I. Duarte, Hélio Anderson,
Orientador II. Título.

CDU 043

"Computational Simulation of the Pyrite/ Arsenopyrite Interface - Galvanic Effects in Chemical Reactivity of Minerals"

Egon Campos dos Santos

Tese aprovada pela banca examinadora constituída pelos Professores:



Prof. Hélio Anderson Duarte - Orientador
UFMG



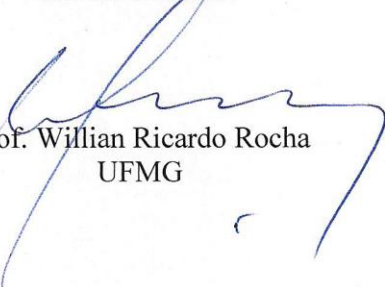
Prof. Alfredo Mayall Simas
UFPE



Prof. Alexandre Braga da Rocha
UFRJ



Profa. Virginia Sampaio Teixeira Ciminelli
DEMET/UFMG



Prof. Willian Ricardo Rocha
UFMG

Belo Horizonte, 26 de junho de 2019.

Acknowledgements

The Brazilian people.

My parents: Regina M. Campos, Welington F. Santos.

My friend Juliana Y. Kadooca.

Professor Hélio Anderson Duarte.

Professor Lars Pettersson.

Dr. Joakim Halldin Stenlid.

My co-workers: Alexandre, Aline, Antônio, Catarina, Claudio, Fernando, Gustavo, Guilherme, Jessyca, Juliana, Maicon, Matheus, Maurício, Mirelle, Pâmella, Paulo, Sabrina, Selma, Thales, Walber.

My friends: Djalma B. Reis, Gabriel Libânio, Giancarlo G. Almeida, Henrique Neiva e Lucas Moreira.

My family.

Contents

<i>List of Abbreviations</i>	<i>iv</i>
<i>List of Figures</i>	<i>vii</i>
<i>List of Tables</i>	<i>xiii</i>
<i>Resumo</i>	<i>xvii</i>
<i>Abstract</i>	<i>xix</i>
<i>Chapter 1 – Sulfide minerals and galvanic interactions</i>	<i>1</i>
<i>Sulfide minerals and acid rock drainage</i>	<i>1</i>
Galvanic effects on sulfide minerals oxidation	<i>5</i>
Pyrite/arsenopyrite galvanic pair	<i>7</i>
<i>Objective</i>	<i>9</i>
<i>Chapter 2 - Simulation techniques</i>	<i>11</i>
Density functional theory	<i>11</i>
Plane waves	<i>15</i>
Pseudopotentials	<i>16</i>
The DFT+U method	<i>18</i>
Topological analysis of the electron density	<i>20</i>
Density-functional tight-binding theory	<i>20</i>
CI-NEB calculations	<i>23</i>
Final considerations	<i>25</i>
<i>Chapter 3 – Pyrite/arsenopyrite interface formation</i>	<i>26</i>
<i>Introduction</i>	<i>26</i>
<i>Computational details</i>	<i>27</i>
<i>Pyrite/arsenopyrite coherent interface construction</i>	<i>30</i>
<i>Structure and electronic properties</i>	<i>33</i>
<i>Interface adhesion and stability</i>	<i>43</i>
<i>Conclusion</i>	<i>46</i>
<i>Chapter 4 – Pyrite/arsenopyrite interface local reactivity</i>	<i>48</i>
<i>Introduction</i>	<i>48</i>
<i>Methodology details and nomenclature of the systems</i>	<i>49</i>
<i>I-SLABs construction starting from the I-BULKs</i>	<i>51</i>
<i>Pyrite/arsenopyrite I-Bulks electronic reconstruction</i>	<i>53</i>

<i>Pyrite/arsenopyrite I-SLABs cleavage plane energies.....</i>	<i>55</i>
<i>Pyrite/arsenopyrite I-SLABS chemical reactivity in the presence of water</i>	<i>56</i>
<i>Final observations</i>	<i>58</i>
<i>Chapter 5 – Pyrite/Arsenopyrite interface band offset</i>	<i>60</i>
<i>FeS₂/FeAsS interface construction</i>	<i>60</i>
<i>The commensurability of the phases</i>	<i>61</i>
<i>Interface model</i>	<i>62</i>
<i>Computational details</i>	<i>63</i>
<i>The band offset calculation approach.....</i>	<i>64</i>
<i>Pyrite and arsenopyrite calculation</i>	<i>65</i>
<i>Pyrite/arsenopyrite interface band offset.....</i>	<i>67</i>
<i>Environmental implications and conclusion</i>	<i>68</i>
<i>Chapter 6 – DFTB2 parametrization for Pyrite/Water interface.....</i>	<i>71</i>
<i>Liquid water: a contemporary challenge for simulations.....</i>	<i>71</i>
<i>Water parametrization.....</i>	<i>72</i>
<i>Pyrite “Fe-X” pair parametrization</i>	<i>74</i>
<i>Results: Bulk water properties</i>	<i>74</i>
<i>Results: Pyrite bulk and surface properties.....</i>	<i>80</i>
<i>Results: Water adsorption on pyrite (100) surface.....</i>	<i>82</i>
<i>Conclusion</i>	<i>83</i>
<i>Chapter 7 – SO₃ and SO₄ formation on pyrite (100) surface</i>	<i>85</i>
<i>Introduction.....</i>	<i>85</i>
<i>Theoretical framework.....</i>	<i>87</i>
<i>Results and discussion</i>	<i>89</i>
<i>Final remarks</i>	<i>94</i>
<i>Chapter 8 – Final considerations and perspectives</i>	<i>98</i>
<i>Bibliography</i>	<i>104</i>
<i>Appendix</i>	<i>A1</i>

List of Abbreviations

ARD (Acid Rock Drainage)

B (Bond)

BG (Band Gap)

BM (Bulk Modulus)

BO (Band Offset)

CS (Core Shell)

CBM (Conduction Band Minimum)

CI-NEB (Climbing Image- Nudged Elastic Band)

DFT (Density functional theory)

DFTB (Density-Functional Tight-Binding)

DOS (Density of States)

ELF (Electron Localization Function)

FASP (Framework for Automatization of SLAKO Parametrization)

FS (Final State)

GGA (Generalized Gradient Approximation)

HF (Hartree-Fock)

HATR-IR (Horizontal Attenuated Total Reflectance Infrared)

HK (Hohenberg and Khon)

HRTEM (High Resolution Transmission Electron Microscopy)

I-BULK (Interface Bulk)

I-SLAB (Interface Slab)

IS (Initial State)

KS (Khom and Sham)

LDA (Local Density Approximation)

LP (Lone Pair)

MEP (Minimum Energy Pathway)

NEB (Nudged Elastic Band)

PBE (Perdew-Burke-Ernzerhof)

PDOS (Projected Density of States)

PES (Potential Energy Surface)

PP (Pseudopotential)

RLCAO (Relativistic Linear Combination of Atomic Orbitals)

RMC (Reverse Monte Carlo)

RP (Rest Potential)

SCC (Self-consistent charge)

SCF (Self-Consistent Field)

SLAKO (Slater-Koster)

TS (Transition State)

UFF (Universal Force Field)

VBM (Valence Band Maximum)

VSEPR (Valence Shell Electron Pair Repulsion)

XAS (X-ray Absorption Spectroscopy)

XC (Exchange-Correlation)

XPS (X-ray Photoelectron Spectroscopy)

List of Figures

<i>Figure 1- Sulfide minerals and crystallographic structures.....</i>	<i>2</i>
<i>Figure 2- Self-catalytic oxidation of pyrite. The initial process of pyrite dissolutive oxidation is shown.</i>	<i>4</i>
<i>Figure 3- Dissolution rate (mol.m⁻².s⁻¹) for single and two phases system. Obtained from Ref. [40].</i>	<i>6</i>
<i>Figure 4- Scheme showing the oxidation of arsenopyrite in the presence of pyrite.</i>	<i>8</i>
<i>Figure 5- Illustration showing the SCF procedure for DFT methods.....</i>	<i>14</i>
<i>Figure 6- Construction of the pseudo wave function $\phi(r)$ by the pseudopotential method. Figure quoted from Reference [95].....</i>	<i>18</i>
<i>Figure 7- Minimum energy path illustration and force decomposition in NEB calculations. Figure adapted from Ref. [107].</i>	<i>23</i>
<i>Figure 8- Pyrite and arsenopyrite calculated band gaps as function of the Hubbard (U-J) parameter. Black and red dashed lines represent the experimental band gap for pyrite[166, 167] (0.90 eV) and arsenopyrite[119, 168] (0.82 eV), respectively.....</i>	<i>28</i>
<i>Figure 9- Scheme showing how to construct a coherent interface model that increases the overlapping area, SA/B, between phase A and B.....</i>	<i>31</i>
<i>Figure 10- Interface structure. In (a) is shown the interface layered structure along the c-axis. In (b) are shown the pyrite and arsenopyrite bulk, where is highlighted the two Fe-Fe bond distances (short and long) in the structure of arsenopyrite. In (c) are shown the interfacial Fe-Fe bonds and the interface types. From left to right the interfaces in (c) are: FeS₂(100)/FeAsS(001), FeS₂(100)/FeAsS(100)-As, and FeS₂(100)/FeAsS(100)-S. The red, yellow, and green spheres represent, respectively, the Fe, S, and As atoms. The red dotted lines represent the normal interfacial plane formed by the contact of the two phases.</i>	<i>36</i>

Figure 11- Strain influence in the electronic structure of pyrite (a) and arsenopyrite (b) minerals..... 37

Figure 12- Electron localization function (ELF) for (a) FeS₂(100)/FeAsS(001), (b) FeS₂(100)/FeAsS(100)-As, and (c) FeS₂(100)/FeAsS(100)-S interface planes located in the pyrite region (left side) and arsenopyrite region (right side). The axial Fe-X bonds are shown in Figure A6. 38

Figure 13- (Left) Illustration of the structure of arsenopyrite and (Right) isosurface and section of the 4c-2e electron state at -2.5 eV below Fermi level, calculated at the Γ point. The Isosurface factor of 0.01 e/Å³ was set. Color code: yellow - Sulfur, green - Arsenic, brown -Iron. 40

Figure 14- Density of states (DOS) projected for the interface atoms in the range of -8 to 4 eV: (a) is the FeS₂(100)/FeAsS(001) system, (b) the FeS₂(100)/FeAsS(100)-S, and (c) the FeS₂(100)/FeAsS(100)-As system. The band gap (BG) was calculated from the band structures shown in Figure A7. 41

Figure 15- Projected density of states. “Bulk” and “Int” meanings the density of states from the bulk region and interface region, respectively. 42

Figure 16- Nomenclature used in the present Chapter for (a) pyrite and arsenopyrite crystal bulk, (b) pyrite and arsenopyrite surface, (c) interface bulk (I-BULKs)..... 50

Figure 17- I-SLABs obtained from the I-BULKs. The blue dot lines represent the cleavage plane perpendicular [(1)_⊥] to the interface, and the red dot lines the four parallel cleavage planes close to the interface region [(1)_∥ ,(2)_∥ ,(3)_∥ , and (4)_∥]. The red, yellow and green spheres represent the iron, sulfur and arsenic atoms in the structures above. The dotted circles show the iron sites that were used to adsorb water molecules..... 52

Figure 18- Structure and Charge density difference, $\Delta\rho$, for the interfaces. (a) is the FeS₂(100)/FeAsS(001) interface, (b) the FeS₂(100)/FeAsS(100)-As interface, and (c) the FeS₂(100)/FeAsS(100)-S interface. Isosurfaces are shown for 0.01 e/Å³. Red, yellow, and green spheres represent, respectively, the Fe, S, and As atoms. 54

Figure 19- Water adsorption on the “FeS₂(100)/FeAsS(100)-As” I-SLABs. (a) adsorption on the parallel I-SLAB model, (b) adsorption on the perpendicular I-SLAB with the water located in the pyrite side, and (c) water adsorption on the perpendicular I-SLAB with the water located in the pyrite side. 57

Figure 20- Interface model construction. (a) is the FeS₂(100) pyrite bulk, (b) the FeAsS(100)-As arsenopyrite bulk, and (c) the FeS₂(100)/FeAsS(100)-As interface. The FeS₂(100)/FeAsS(001) and FeS₂(100)/FeAsS(100)-As constructions are shown in Figure A12 and Figure 16, respectively. 61

Figure 21- Displacement calculation for the FeS₂(100)/FeAsS(100)-As interface model. The results found for the FeS₂(100)/FeAsS(001) and FeS₂(100)/FeAsS(100)-S interfaces are shown, respectively, in Figure A10 and Figure A11. 65

Figure 22- Valence band maximum (VBM) and Conduction band minimum (CBM) vs (U-J) Hubbard parameter for (a) pyrite and (b) arsenopyrite bulk minerals. Vertical lines represents the band gaps obtained for (U-J)= 1.5 eV. Grey shaded regions mean the occupied states level. 66

Figure 23- Interface frontier’s orbitals for the FeS₂(100)/FeAsS(100)-As interface. The results found for the FeS₂(100)/FeAsS(001) and FeS₂(100)/FeAsS(100)-S interfaces are shown, one-to-one, in Figure A13 and Figure A15. 67

Figure 24- Interface band offset for (a) FeS₂(100)/FeAsS(001), (b) FeS₂(100)/FeAsS(100)-As, and (c) FeS₂(100)/FeAsS(100)-As interfaces. Grey shaded areas mean the occupied states level. The upper panel shows qualitatively the band alignment obtained for the three FeS₂/FeAsS interfaces. 68

Figure 25- O-O and O-H radial distribution function obtained at different temperatures for neutral water. Experimental values quoted from Refs. [235-237]. 75

Figure 26- Water-matsci, water-matsci-UFF, matsci and the experimental (FREE, Ref. [236]) distribution of the angles O₁-O_c-O₁. All calculations were done for liquid water at 298 K. 76

<i>Figure 27- Pyrite projected density of states in the vicinity of Fermi level. Inset figure represents pyrite unit cell.</i>	81
<i>Figure 28- Water adsorption on pyrite (100) surface. Color code: yellow, sulfur; brown, iron; red, oxygen; and white, hydrogen.</i>	83
<i>Figure 29- Pyrite oxidation mechanism in aqueous medium explained by Type I and Type II reactions. Figure quoted from Ref. [185].</i>	86
<i>Figure 30- Side (a) and top (b) view of pyrite slab used in all calculations. Fragment of pyrite (c) used to show the reactions. Colour code: yellow - Sulfur, brown - Iron.</i> ..	88
<i>Figure 31- Fragment of pyrite (100) surface depicting the initial steps of pyrite oxidation. Energies in electronvolt and bond distances in Angstrom. Colour code: yellow - Sulfur, red - oxygen, white - hydrogen, brown - Iron.</i>	90
<i>Figure 32- SO₂ dissociation on pyrite surface to form (SO₂)_d.</i>	91
<i>Figure 33- (SO₃)_d, (HSO₃)_d, (HSO₄)_d and (SO₄)_d formation on pyrite surface by Type II reactions.</i>	92
<i>Figure 34- (SO₄)_d and (HSO₄)_d and formation on pyrite surface by Type III reactions.</i>	93
<i>Figure 35- (SO₃)_d and (HSO₃)_d and formation on pyrite surface by Type III reactions.</i>	93
<i>Figure 36- Scheme showing the oxidation mechanism of pyrite (100) surface in three different stages [(1), (2) and (3)]. Activation energies (E_a) for stage (1) quoted from literature.[185] All “E_a” calculations are in the same theoretical level. Values in electronvolt [eV].</i>	96
<i>Figure 37- Scheme showing how complex is the oxidation of pyrite/arsenopyrite interface in ambient conditions.</i>	102
<i>Figure A1- Convergence test for the total energy as a function of the K-points meshes. In the graph E_{1x1x1} represents the total energy for the calculation at the Γ point and</i>	

n_{atom} is the total number of atoms in the pyrite unit cell. In all calculations, the cutoff of 80 Ry was used. A1

Figure A2- Convergence test for the total energy as a function of the cutoff. In the graph E_{30} represents the total energy for the calculation with 30 Ry cutoff and *n_{atom}* is the total number of atoms in the pyrite unit cell. In all calculations, the 6x6x6 K-points meshes was used..... A1

Figure A3- Convergence test for the total energy as a function of the K-points meshes. In the graph $E_{1 \times 1 \times 1}$ represents the total energy for the calculation at the Γ point and *n_{atom}* is the total number of atoms in the pyrite unit cell. In all calculations, the cutoff of 80 Ry was used. A2

Figure A4- Convergence test for the total energy as a function of the cutoff. In the graph E_{30} represents the total energy for the calculation with 30 Ry cutoff and *n_{atom}* is the total number of atoms in the pyrite unit cell. In all calculations, the 6x6x6 K-points meshes was used..... A2

Figure A5- Crystallographic transformation of the arsenopyrite (010) surface from triclinic to an orthorhombic structure..... A5

Figure A6- Electron localization function for (a) $FeS_2(100)/FeAsS(001)$, (b) $FeS_2(100)/FeAsS(100)-As$, and (c) $FeS_2(100)/FeAsS(100)-S$ Fe- X_{ax} bonds.A11

Figure A7- Band structure. BG meanings the band gap of the interfaces. K-Path G-Y-H-C-E-M1-A-Z-D-G-A-X-H1-G from the monoclinic lattice.A12

Figure A8- Structures used to calculate the formation energy of the interfaces and the pyrite and arsenopyrite bulk.....A13

Figure A9- Interface cleavage planes along the (010) direction. (a), (b) and (c) represents, one-to-one, the interfaces: $FeS_2(100)/FeAsS(001)$, $FeS_2(100)/FeAsS(100)-As$, and $FeS_2(100)/FeAsS(100)-S$. The blue line is the plane direction, and dashed ellipses indicate the cleaved As-S and S-S bonds.....A14

<i>Figure A10- Displacement calculation for the FeS₂(100)/FeAsS(001) interface model.</i>	A16
<i>Figure A11- Displacement calculation for the FeS₂(100)/FeAsS(100)-S interface model.</i>	A16
<i>Figure A12- Illustration showing the FeS₂(100)/FeAsS(001) interface model construction from pyrite and arsenopyrite isolated phases.</i>	A17
<i>Figure A13- (left) VBM and (right) CBM states for the FeS₂(100)/FeAsS(001) interface model.</i>	A17
<i>Figure A14- Illustration showing the FeS₂(100)/FeAsS(100)-S interface model construction from pyrite and arsenopyrite isolated phases.</i>	A18
<i>Figure A15- (left) VBM and (right) CBM states for the FeS₂(100)/FeAsS(100)-S interface model.</i>	A18
<i>Figure A16- Radial distribution function for O-O obtained by RMC NVT molecular dynamics. It includes the original matsci RDF.</i>	A19
<i>Figure A17- Radial distribution function for O-O obtained by RMC NVT molecular dynamics. It includes the original matsci RDF.</i>	A19
<i>Figure A18- Radial distribution function for O-O obtained by RMC. NVT and NVE molecular dynamics.</i>	A20
<i>Figure A19- Radial distribution function for O-H obtained by RMC. NVT and NVE molecular dynamics.</i>	A20
<i>Figure A20- DFT and DFTB2 band structure of iron-FCC (a) and pyrite (b) bulk structures.</i>	A21
<i>Figure A21- SO dissociation on pyrite surface. Color code: yellow - Sulfur, green - Arsenic, brown -Iron.</i>	A23

List of Tables

<i>Table 1- Rest potential for different sulphide minerals at pH 4. Values quoted from Ref. [25].</i>	5
<i>Table 2: Formation energy, E_f, for pyrite and arsenopyrite phases. Δ represents the percentage error between the calculated value and the experimental value.</i>	29
<i>Table 3: Pyrite and arsenopyrite mismatch parameter, ξ, calculation. All the ξ values were calculated considering the (100) surface of pyrite. In brackets are the surface energy values for the surfaces related to the most stable interfaces estimated by our theoretical level.</i>	32
<i>Table 4: Work of adhesion, W_{ad}, and formation energy for the most stable interfaces. W_{pyrite} and $W_{arsenopyrite}$ meanings the work of self-adhesion for pyrite and arsenopyrite, respectively.</i>	45
<i>Table 5- Surface energy calculated for the different cleavage planes shown in Figure 17.</i>	56
<i>Table 6- Values of q parameter in the distribution of θ angles for different DFTB2 parameter sets compared to values from RMC fits to scattering data of Ref. [236].</i>	78
<i>Table 7- Neutral water self-diffusion coefficient ($\text{\AA}^2/\text{ps}$) of the oxygen atom at different temperatures. Quoted references in parenthesis.</i>	79
<i>Table 8- Water adsorption energy (calculated by Eq. (4.3)) and Fe-OH₂ distance. DFT values quoted from Ref. [185].</i>	82
<i>Table A1: Pyrite Hubbard (GGA+U) parameter test. The cutoff of 50 Ry and the K-point of 4x4x4 were used in all the calculation. BG meanings the band gap of the system for the tested GGA+U parameters.</i>	A3
<i>Table A2: Arsenopyrite Hubbard (GGA+U) parameter test for arsenopyrite structure. The cutoff of 50 Ry and the K-point of 4x4x4 were used in all the calculation.</i>	A4

Table A3: Arsenopyrite Hubbard (GGA+U) parameter test for arsenopyrite structure and band gap (BG). The cutoff of 50 Ry and the K-point of 4x4x4 were used in all the calculations..... A4

Table A4: Fe- X_{eq} and X-S bond distances of the three interfaces..... A6

Table A5- Fe- X_{ax} and interfacial contact distances, δ_p of the three interface systems. In the red parenthesis are the percentage difference between the interfaces structure parameters and the arsenopyrite bulk structure. In the green brackets are the percentage difference** between the interfaces and the arsenopyrite bulk. A6**

Table A6: Spin test for the arsenopyrite (001) surface. “TM” meanings the total magnetization of the system and “AM” the absolute magnetization of the system. The cutoff of 50 Ry and the K-point of 4x4x4 were used in all the calculations..... A7

Table A7: Spin test for the arsenopyrite (100)-As surface. “TM” meanings the total magnetization of the system and “AM” the absolute magnetization of the system. The cutoff of 50 Ry and the K-point of 4x4x4 were used in all the calculations..... A7

Table A8: Spin test for the arsenopyrite (100)-S surface. “TM” meanings the total magnetization of the system and “AM” the absolute magnetization of the system. The cutoff of 50 Ry and the K-point of 4x4x4 were used in all the calculations..... A7

Table A9: Py(100)/AsPy(001) total energy. The cutoff of 50 Ry and the K-point of 4x4x4 were used. In all the calculations the lattice parameters were fixed, and only the atom positions were allowed to move freely in the optimization process. Highlighted in red the structure with the lowest energy..... A8

Table A10: FeS₂(100)/FeAsS(100)-As total energy. The cutoff of 50 Ry and the K-point of 4x4x4 were used. In all calculations the lattice parameters were fixed, and only the atom positions were allowed to move freely in the optimization process. Highlighted in red the structure with the lowest energy..... A8

Table A11: FeS₂(100)/FeAsS(100)-S total energy. The cutoff of 50 Ry and the K-point of 4x4x4 were used. In all calculations the lattice parameters were fixed, and only the

atom positions were allowed to move freely in the optimization process. Highlighted in red the structure with the lowest energy..... A8

Table A12: Spin teste for the FeS₂(100)/FeAsS(001) interface. "ALT" meanings that alternated initial spin states were used, following the sequencie Up-Down-Up-Down for the iron, sulfur and arsenic sites in the interface region. "Up" meanings all spin states up and "0" that no spin polarization was used for the atoms in the DFT SCF calculations. "TM" is the total magnetization, and "AM" the absolute magnetization. The cutoff of 50 Ry and the K-point of 4x4x4 were used. A9

Table A13: Spin teste for the FeS₂(100)/FeAsS(100)-As interface. "ALT" meanings that alternated initial spin states were used, following the sequencie Up-Down-Up-Down for the iron, sulfur and arsenic sites in the interface region. "Up" meanings all spin states up and "0" that no spin polarization was used for the atoms in the DFT SCF calculations. "TM" is the total magnetization, and "AM" the absolute magnetization. The cutoff of 50 Ry and the K-point of 4x4x4 were used.A10

Table A14: Spin teste for the FeS₂(100)/FeAsS(100)-S interface. "ALT" meanings that alternated initial spin states were used, following the sequencie Up-Down-Up-Down for the iron, sulfur and arsenic sites in the interface region. "Up" meanings all spin states up and "0" that no spin polarization was used for the atoms in the DFT SCF calculations. "TM" is the total magnetization, and "AM" the absolute magnetization. The cutoff of 50 Ry and the K-point of 4x4x4 were used.A10

Table A15: Structural parameters obtained for the structures shown in Figure A8.A13

Table A16: Hubbard parameter (U-J) test for pyrite isolated mineral. A cutoff of 40 Ry and 6x6x4 k-point mesh were used in all the calculations. BG means the band gap of the system for the tested (U-J) parameters.A15

*Table A17- Hubbard parameter (U-J) test for arsenopyrite structure. A cutoff of 40 Ry and 6x6x4 k-point mesh were used in all the calculations. BG means the band gap of the system for the tested (U-J) parameters. (%erro **)A15*

Table A18- (U-J) influence in band offset calculation. All the calculation were done following the Eq. (1). For the total energy calculation it was used the 4x4x2 k-points grid and the cutoff of 40 Ry.A15

Table A19- Repulsion energy parametrization. Atomic pairs, reference systems, dependencies for a-b pairs, E_{bnd} and E_{ref} interception point (IP), the cut radius (R_{cut}), and bond distances. Only singlet spin configuration was considered for all reference systems.A22

Resumo

Efeitos galvânicos desempenham um papel importante no mecanismo de oxidação de sulfetos minerais. A pirita (FeS_2) é o sulfeto mineral mais abundante na Terra e, na presença de arsenopirita (FeAsS), sua oxidação diminui. Consequentemente, a taxa de oxidação de arsenopirita é aumentada, liberando as espécies As(III) e As(V) no meio. Estas espécies são um perigo para o meio ambiente e podem se tornar um problema de saúde nas regiões de mineração. Nesta tese reportamos a investigação do par galvânico gerado pela interface pirita/arsenopirita a partir de cálculos DFT/ondas planas (Capítulo 3). Para construir os modelos de interface, inicialmente testou-se a comensurabilidade entre a superfície (100) de pirita (superfície de pirita com maior ocorrência na natureza) com as doze superfícies de arsenopirita relatadas na literatura. Dentre todas as superfícies avaliadas, foram construídas as interfaces mais estáveis e avaliadas a sua estabilidade junto com suas propriedades eletrônicas. Como a pirita e arsenopirita apresentam diferentes (i) distâncias de ligação e (ii) parâmetros das redes cristalinas, não é possível combinar perfeitamente as fases. Como consequência, sítios octaédricos distorcidos e tensões estruturais são formados na região interfacial. Esta observação está de acordo com a análise do trabalho de adesão estimado e com os cálculos de energia de formação. Ambos os parâmetros sugerem que a formação da interface pirita/arsenopirita não é termodinamicamente favorável. Isto está de acordo com o que é observado em amostras naturais.

A reatividade local das interfaces foi avaliada a partir da adsorção de água (Capítulo 4). Foram encontrados valores de adsorção comparáveis entre as três interfaces $\text{FeS}_2/\text{FeAsS}$ e as fases isoladas (FeS_2 e FeAsS). Isto sugere que a possível formação da interface ocorre sem modificar as propriedades ácido-base de Lewis dos sítios ativos na ruptura do material. Cálculos de *Band Offset* (Capítulo 5) mostraram que seus valores de *band gap* das interfaces são pelo menos três vezes menores que os valores encontrados para a pirita ou a arsenopirita isoladas. Uma vez que os sulfetos minerais são materiais semicondutores que podem participar de reações eletroquímicas, a diminuição do *band gap* facilita a transferência de elétrons ao longo de sua estrutura. Este fato contribui para explicar por que as interações galvânicas aumentam a oxidação de arsenopirita na presença de pirita. O presente estudo ressalta a importância de efeitos galvânicos para entender o mecanismo de oxidação da arsenopirita na presença de pirita.

Foi desenvolvida uma metodologia capaz de simular a interface água/pirita (capítulo 6). É sabido na literatura que o método DFTB2 não descreve bem propriedades estáticas e dinâmicas da água líquida. Por isso foi feita a reparametrização dos parâmetros DFTB2 a partir de uma correção empírica da energia de repulsão DFTB2 construindo os parâmetros nomeados nesta tese como water-matsci. Funções radiais do tipo O-O e O-H foram descritas com ótimo acordo com dados experimentais. Além disso, os novos parâmetros são capazes de descrever a tetraedralidade das moléculas de água nas temperaturas de 298 e 254 K. Finalmente, foi observado que a modificação dos parâmetros não modifica a energia de adsorção de água na superfície (100) da pirita.

Os cálculos de uma nova rota para a oxidação da espécie adsorvida SO_2 amplia a compreensão do mecanismo de oxidação da pirita (Capítulo 7). Até o momento apenas as etapas iniciais do processo de oxidação da pirita foram feitas a partir de cálculos teóricos. De acordo com os nossos cálculos, observa-se que a dissociação da espécie SO_2 pode ocorrer sobre a superfície (100) da pirita. A energia de ativação (0.44 eV) foi estimada em aproximadamente metade do valor da energia de ativação da etapa limitante da reação global (0.80 eV), o que sugere que esta espécie pode ser formada na superfície da pirita. Além do mais, a espécie SO_2 leva a formação dos intermediários SO_3 e SO_4 com energias de ativação menores que 0.16 eV (valor 5 vezes menor que a etapa limitante). Outro aspecto importante do mecanismo proposto por nossos cálculos é o fato que a molécula de oxigênio é capaz de reagir com a espécie SO_2 na superfície. Esse tipo de reação sobre a superfície da pirita ainda não tinha sido explorado por cálculos teóricos, porém já tinha sido sugerido com análises experimentais. A rota investigada de oxidação do SO_2 adsorvido pelo oxigênio molecular foi denominada reações do Tipo III que ocorrem na superfície da pirita.

Palavras-chave: Sulfetos minerais, pirita, arsenopirita, pares galvânicos, interfaces, DFT, DFTB.

Abstract

Galvanic effects play an important role in the oxidation mechanism of sulfide minerals. Pyrite (FeS_2) is the most common sulfide mineral in the Earth, and in the presence of arsenopyrite (FeAsS) its oxidation is delayed and the oxidation rate of arsenopyrite is increased, releasing As(III) and As(V) species in the medium. These arsenic ions are an environment hazards and become health problem in the vicinities of the mining regions. We report a DFT/plane waves study of the pyrite/arsenopyrite galvanic cell (Chapter 3). To build the interface models we tested the commensurability of the pyrite (100) surface (the pyrite surface with highest occurrence in the nature) with the twelve arsenopyrite surfaces reported in the literature. Among all evaluated surfaces the most stable interfaces were built, and their structure, stability, and electronic properties were evaluated. As pyrite and arsenopyrite have different (i) bond distances and (ii) crystal lattice parameters, it is not possible to perfectly match the phases, and distorted octahedral sites are formed in the interfacial region. Consequently, strained structures are observed. This structural observation agrees with the word of adhesion and the formation energy analysis. Both parameters suggest that the formation of $\text{FeS}_2/\text{FeAsS}$ interface is not favourable. This is in agreement with what is observed in natural samples.

The local reactivity of the interfaces was evaluated by water adsorption energies (Chapter 4). Comparable adsorption values were found among the interfaces ($\text{FeS}_2/\text{FeAsS}$) and isolated phases (FeS_2 and FeAsS). This suggests that the possible interface formation would occur without modifying the Lewis acid-base properties of the active sites in the event of material rupture. Band offset (Chapter 5) calculations for the most stable interfaces showed that their band gap values are at least three times lower than the values found for the pure pyrite or arsenopyrite. Since sulfide minerals are semiconductor materials that can participate in electrochemical reactions, the decrease in the band gap thus facilitates electron transfer at the pyrite/arsenopyrite interface. This fact contributes to explain why the galvanic interactions increase the oxidation of arsenopyrite in the presence of pyrite. The present study underlines the importance of galvanic effects to understand the oxidation mechanism of arsenopyrite in the presence of pyrite.

It was developed a methodology capable of simulating the water/pyrite interface (chapter 6). It is known in the literature that the DFTB2 method does not describe well static and

dynamic properties of liquid water. Therefore, the DFTB2 parameters were reparametrized from an empirical correction of the DFTB2 repulsion energy by constructing the parameters labelled in this thesis as water-matsci. Radial functions of type gO-O and gO-H were described in agreement with experimental data. In addition, the new parameters are capable of describing the tetrahedrality of the water molecules at temperatures 298 and 254 K. Finally, it was observed that the modification of the parameters does not modify the water adsorption energy at the pyrite surface (100).

All calculations of a new route for the adsorbed SO₂ oxidation extend the knowlegment about the pyrite oxidation mechanism (Chapter 7) As far as we know, only the initial stages of the pyrite oxidation process have been made from theoretical calculations. According to our calculations, it is observed that the dissociation of SO₂ species can occurs on the surface. The activation energy (0.44 eV) was estimated to be approximately two times the activation energy of the limiting step of the global reaction (0.80 eV), suggesting that this species can be formed on the pyrite surface. Moreover, the SO₂ species leads to the formation of adsorbed SO₃ and SO₄ species on the surface with activation energies lower than 0.16 eV (this value is 5 times less than the rate limiting step). Another important aspect of the mechanics proposed by our calculations is the fact that oxygen molecule is capable to react with the SO₂ species on the surface as it was suggested by experimental analyses, but up to date, it was not theoretically calculated. The investigated route for the adsorbed SO₂ oxidation by the molecular oxygen was labelled as Type III reactions that occur on the pyrite surface.

Key-words: Sulfide Minerals, pyrite, arsenopyrite, galvanic couples, interfaces, DFT, DFTB.

Chapter 1 – Sulfide minerals and galvanic interactions

Preamble: Noble and base metals of economic importance are normally associated to metal sulfides (pyrites) and their extraction may imply in important environmental impact, mostly due to the acid rock drainage (ARD). When exposed to atmosphere and humidity, sulfide minerals are oxidized to form sulfuric acid in the medium. In addition, the oxidation of mineral sulfides directly affects soil quality, since toxic metals and metalloids (such as Hg, As and Cd) are released in the environment. Several factors act accelerating oxidation processes of these minerals, and the association of two or more minerals in galvanic pairs greatly aggravates the rate of dissolution of these minerals. This work aims to study the galvanic interaction between pyrite and arsenopyrite. Pyrite is the most abundant sulfide mineral and it is mostly responsible for the formation of ARD products. Arsenopyrite is also associated with gold, copper ores, among others, and in nature and its dissolution process releases arsenic into the environment.

Sulfide minerals and acid rock drainage

Sulfide minerals are considered the most diverse minerals in terms of its physical, chemical, and structural properties (Figure 1). Such diversity originates from their more complex crystal and electronic structures when compared to other class of materials.[1, 2] The main reasons are found in the variety of oxidation states, coordination numbers, symmetry, density and stoichiometry. Furthermore, sulfide minerals can participate in both acid–base and redox reactions, thus their exposed surfaces can be the place where different reaction mechanisms can occur. Accordingly to Vaughan *et al.*,[3] the electrical and magnetic properties of metal sulfides are arguably the most diverse found in any group of materials. They are diamagnetic insulators (e.g. ZnS), diamagnetic semiconductors (e.g. FeS₂, PbS, and FeAsS), antiferromagnetic semiconductors (e.g. CuFeS₂), and even magnetic and non-magnetic metallic conductors (e.g. Fe₇S₈ and Fe₉S₁₀). Recently, new developments have been achieved in superconductor synthesis, such as CuS.[4, 5] On this sense, several new technological materials are synthesized exploring the properties of these minerals. Their applications are broad: production of solar and photochemical cells, solid batteries, superconductors and in heterogeneous catalysis.[6]

Another important point is the fact that it has been argued that sulfide minerals can catalyze reactions responsible for the origin of life on Earth.[7, 8]

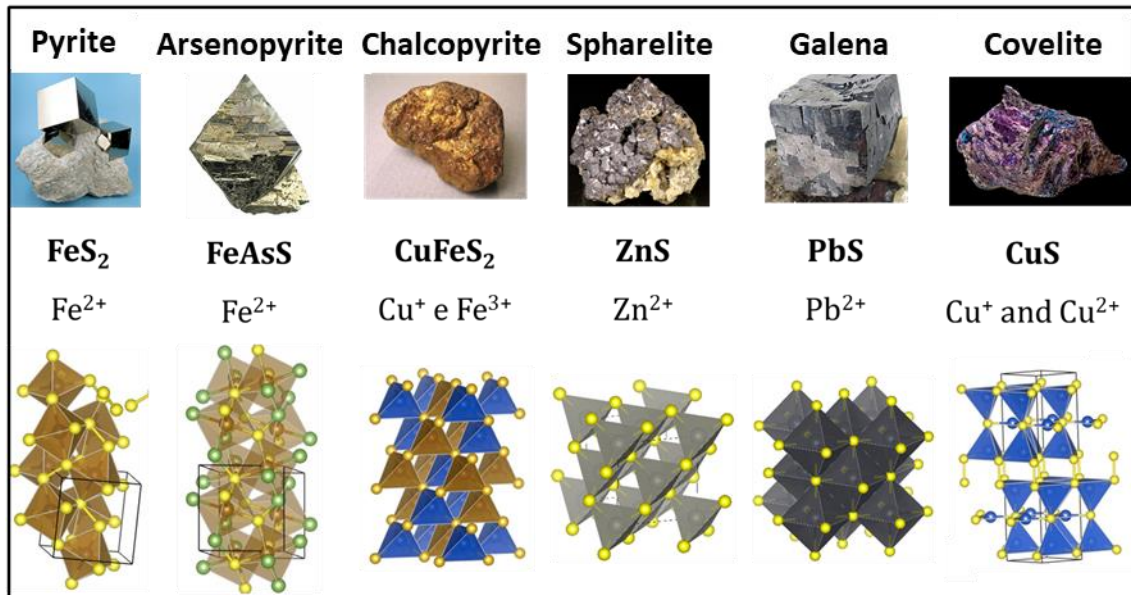


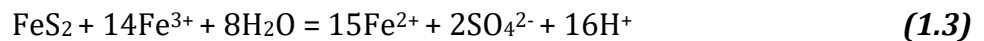
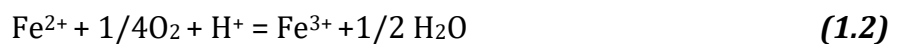
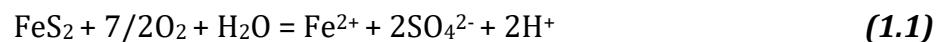
Figure 1- Sulfide minerals and crystallographic structures.

Sulfide minerals form one of the most important classes of minerals and are source of non-ferrous metals on Earth, hence different processes of metal extraction are used in the mining industry.[9] There are two possible routes for obtaining the metals from the sulfide minerals. Traditionally, the preferred route is the pyrometallurgical. Although widely used, the pyrometallurgical process is currently less attractive due to the lower copper content in the available ore in nature, increasing the extracting cost of the desired metals. An alternative to the pyrometallurgical extraction procedure, is the hydrometallurgical process. The latter process is based on ore leaching, which consist in extracting an element component through their dissolution in a solution. The advantage of the hydrometallurgical route is that it is able to treat ores with low metal content, making it more economically viable than the pyrometallurgical route.

Besides the industrial/economic importance of the sulfide minerals, they have been studied due to the consequences of their spontaneous oxidative dissolution when they are exposed to the environment.[10, 11] The technological and environmental importance of this phenomenon makes it an important subject of research from both fundamental and industrial perspectives. Particularly, sulfide minerals when exposed to atmospheric air and humidity are oxidized to form sulfuric acid in the medium. This

phenomenon is called Acid Rock Drainageⁱ (ARD) and has several consequences for the balance of biological and chemical systems found in the environment.[9] The ARD solutions carry significant environmental problems because ARD waters can be harmful to humans and other life forms.[10, 12] A major problem related to ARD is the acidification of aquifers near mining areas. This directly disturbs all the biodiversity around the affected areas. In addition, the oxidation of mineral sulfides directly affects soil quality, since toxic metals (such as Hg, As and Cd) are released to the environment.

The ARD chemical reactions can be explained considering the pyrite oxidative process. It is the most abundant sulfide mineral and a reference for studying other important mineral sulfides.[13] The pyrite oxidation reactions are given in Eqs. (1.1)–(1.5). The initial step is described in Eq. (1.1), where the dissolution of the mineral occurs, forming the SO_4^{2-} , Fe^{2+} , and H^+ ions in the medium. After the oxygen molecule reacts with pyrite releasing $\text{Fe}^{2+}(\text{aq})$, acid and sulfates, the $\text{Fe}^{2+}(\text{aq})$ ions are subsequently oxidized to Fe^{3+} (Eq. (1.2)). As the concentration of Fe^{3+} increases, the oxidation proceeds following the reaction described by Eq. (1.3) increasing the pH of the medium. As the concentration of dissolved Fe^{3+} decreases with increasing pH, parallel Fe^{3+} precipitation reactions occur forming hydroxides ($\text{Fe}(\text{OH})_3$) and oxy-hydroxides (FeOOH), following the Eq. (1.4) and Eq. (1.5), respectively.



Comparing the oxidation reactions of the different mineral sulfides, it is possible to comprehend the general reactions of the process as a self-catalytic cycle. Taking again pyrite as a reference, Figure 2 shows a simple scheme that summarizes the oxidative process of sulfide minerals. Initially, the oxidation occurs by the O_2 and H_2O agents. In aqueous media or even in direct contact with the air, both molecules are present, and can oxidize any sulfide mineral. The former reaction release ions in the medium (in the case

ⁱ When associated to mining industry, it is also called as Acid Mine Drainage (AMD).

of pyrite, it releases ferric ion in the medium). The ferric ions (Fe(III)) act as oxidant agents of the pyrite surface forming ferrous (Fe(II)) ions. The ferrous ions react with the oxygen molecule and the hydronium to form again the ferric ion. A $\text{Fe}^{2+}/\text{Fe}^{3+}$ cycle between the iron species occurs until the oxidation reaction finishes.

Numerous factors can affect the oxidation kinetics of the mineral sulfides. Generally, sulfides dissolution oxidation are accelerated (or retarded) by several factors including pH,[14] oxidant type (eg. O_2 and Fe^{3+}),[15-17] oxidant concentration,[15-17] grain size,[18, 19] and non-sulfide minerals (the most common is the SiO_2). Oxidation is further complex since the electrochemical nature of sulfides are affected by trace element contents such as Cu, Zn, Ni, Co, Ag, As, Ti, Mg, Mn, Al and Si. Then, the exact chemical composition of the sample will dictate the specific oxidation pathway.[20-24] ARD is a spontaneous process, nevertheless its production is also catalyzed in the presence of the bacterial species: *Acidithiobacillus ferrooxidans*, *Acidithiobacillus thiooxidans* and *Leptospirillum ferrooxidans*. Different reaction pathways are also observed in the presence of these microorganisms.

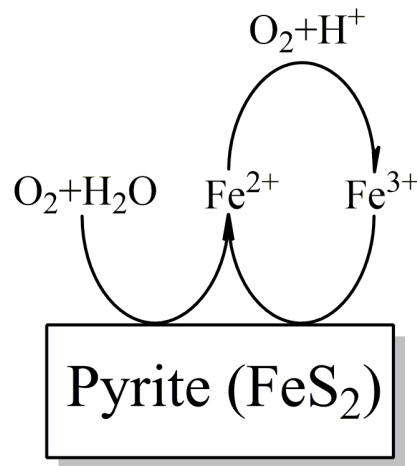


Figure 2- Self-catalytic oxidation of pyrite. The initial process of pyrite dissolutive oxidation is shown.

Chemical, biological and physical factors added to intrinsic characteristics of each mine make ARD highly variable site-to-site. Furthermore, there are no standardized methods for measure or reducing the risk of ARD in the environment.[10] Likewise, the separation of sulfide minerals (generally pyrite from the other minerals) by flotation and leaching methods increases the costs for mining industry.[10, 18] It has been reported

[18] that the cost to treat and remediate ARD mining concentrates in the world are more than 100 billion dollars. New approaches for predicting and mitigating the ARD can only be envisaged if its mechanism is understood in detail at a molecular level.

Galvanic effects on sulfide minerals oxidation

In addition to the factors mentioned above, it is extremely important to consider that sulfide minerals are associated forming galvanic pairs. In nature, sulfuriferous ores are complex solid mixtures and, consequently, their structural, mechanical and especially their electrochemical properties are difficult to be assessed. Nowadays, hydrometallurgical routes are also considered for treating low-grade ores instead of pyrometallurgical processes. However, the secondary reactions provoked by the galvanic interactions between associated minerals within the concentrates can prevent the recovery of noble metals. In aqueous leaching or bioleaching systems the galvanic interaction substantially increases the oxidative dissolution of one or both of the minerals that constitute the galvanic cell.[25-39] This will depend on the electrochemical characteristics of the minerals and on the occurrence of the distinct sulfides contained in the soils, sediments, substrates and ore concentrates. Since pyrite is ubiquitous mineral in Earth's, it is commonly found associated with other important minerals, such as: sphalerite,[40] galena,[25, 26, 37] marcasite,[25] covellite,[25, 40] bornite,[25, 40] chalcopyrite[40-47] and arsenopyrite.[48-55]

Table 1- Rest potential for different sulphide minerals at pH 4. Values quoted from Ref. [25].

Mineral	Formula unit	RP, V vs. SHE
Pyrite	FeS ₂	0.66
Marcasite	FeS ₂	0.63
Chalcopyrite	CuFeS ₂	0.56
Sphalerite	ZnS	0.46
Covellite	CuS	0.45
Bornite	Cu ₅ FeS ₄	0.42
Galena	PbS	0.40
Argenite	Ag ₂ S	0.28
Stibnite	Sb ₂ S ₃	0.12
Molybdenite	MoS ₂	0.11

The contact of distinct sulfide minerals initiates the galvanic effect in the presence of an electrolyte. One mineral will act as anode promoting the oxidation reaction and the other as cathode, in which the reduction reaction occurs.[29, 56] The reactivity of minerals forming mixtures or solid solutions can be measured from its rest potential (RP), see Table 1.[25, 29, 30, 36, 38] As previously defined,[25] the RP of a mineral electrode is the potential difference across the mineral–solution interface when the mineral surface is at electrical equilibrium with respect to electrochemical processes. Pyrite has the highest RP among the sulfides, thus, pyrite is the least reactive sulfide minerals, and, consequently, it will rule the oxidation process of the other associated minerals.[25, 33] Consequently, pyrite acts as a cathode in the oxidative process and more reactive sulfides as an anode (see Table 1).

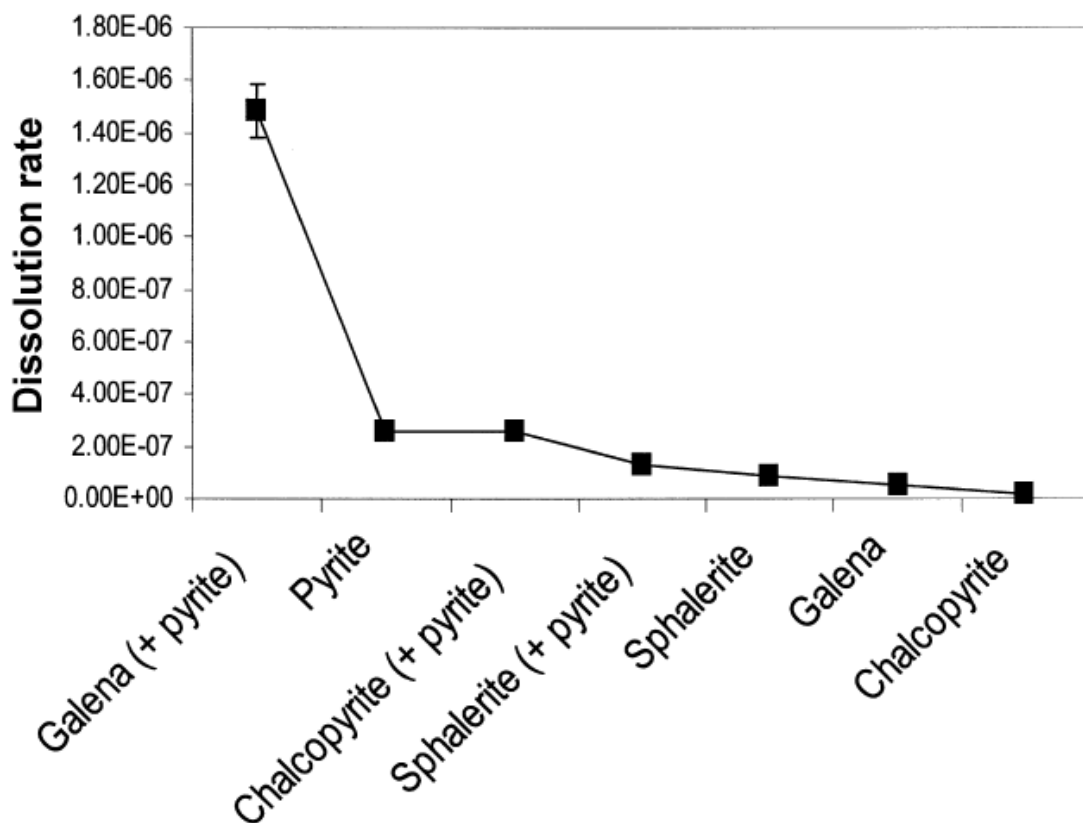


Figure 3- Dissolution rate (mol.m⁻².s⁻¹) for single and two phases system. Obtained from Ref. [40].

One might argue that the ideal formula is not found naturally for any mineral, and trace element contents are responsible to vary the absolute value of pyrite RP. Notwithstanding, electrochemical measurements for a large number of samples from a

variety of geological environments showed a slight variation in the rest potentials measurements.[30, 38, 57] The data suggest that the rest potentials are more affected by the galvanic processes due to the associated minerals than by its elemental composition. Therefore the galvanic processes are the most important effect governing the dissolution rate of sulfide minerals in hydrometallurgical and natural systems.[57]

Abraitis et al.[40] studied the kinetics of metal sulfides oxidation in acidic medium (pH 2.5 and 25 °C) monitoring the cation products (Zn^{2+} , Fe^{2+} , Cu^+ and Pb^{2+}) by ICP-AES (Inductively Coupled Plasma- Atomic Emission Spectroscopy). In order to compare the oxidative behaviour of the target minerals and measure the influence of the galvanic effects in the reaction, the author studied at the same conditions the oxidation of the isolated phases and their oxidation in the presence of pyrite. The studied systems were galena/pyrite, chalcopyrite/pyrite, sphalerite/pyrite, pyrite, galena, and chalcopyrite. The oxidation rates obtained after 200 min of reaction are shown in Figure 3. The results showed that in the presence of pyrite the dissolution of sulfides mixed-mineral systems can be dramatically affected by galvanic effects, and the rates can increase by factor as greater than 3 or 5 times if compared with the isolated phases in the same experimental conditions. By analysing in detail the results shown in Figure 3, it is possible to observe that the galena/pyrite galvanic pair presented an anomalous result, being the dissolution rate of the interface around 30 times greater than the oxidation of the isolated phases.

Pyrite/arsenopyrite galvanic pair

In the study of the galvanic interactions between sulfide minerals, a better understanding of the pyrite/arsenopyrite galvanic interaction is important by many reasons. Arsenopyrite ($FeAsS$) is an important mineral because it is primarily associated with other sulfide minerals and valuable metals (e.g., copper, silver, and gold). In certain ores, it has considerable economic significance since it carries the major portion of gold in the ore. Its exposition to the environment leads to acid rock drainage releasing arsenite [$As(III)$] and arsenate [$As(V)$] in addition to acid and heavy metals, which is hazardous for the environment. Also, arsenopyrite environmental problems have been a major concern in the mineral industry.

Natural arsenopyrite samples are always associated with pyrite, and in its composition generally it is found large randomly contact domains of pyrite distributed in its structure.[58-61] In several studies the galvanic pair formed by arsenopyrite and pyrite minerals increases the dissolution oxidation process.[48-55] Urbano *et al.*[55] carried out a voltammetric study of arsenopyrite containing 11.84% of pyrite mineralogical impurity and compared the results to the oxidation of a natural pyrite mineral containing 98.96% of purity. The authors concluded that the reactivity in the presence of galvanic effects are electrochemically modified, and the pyrite oxidation is delayed when it is associated to the arsenopyrite. Consequently, the oxidation process of arsenopyrite is enhanced with larger production of arsenic in the medium.

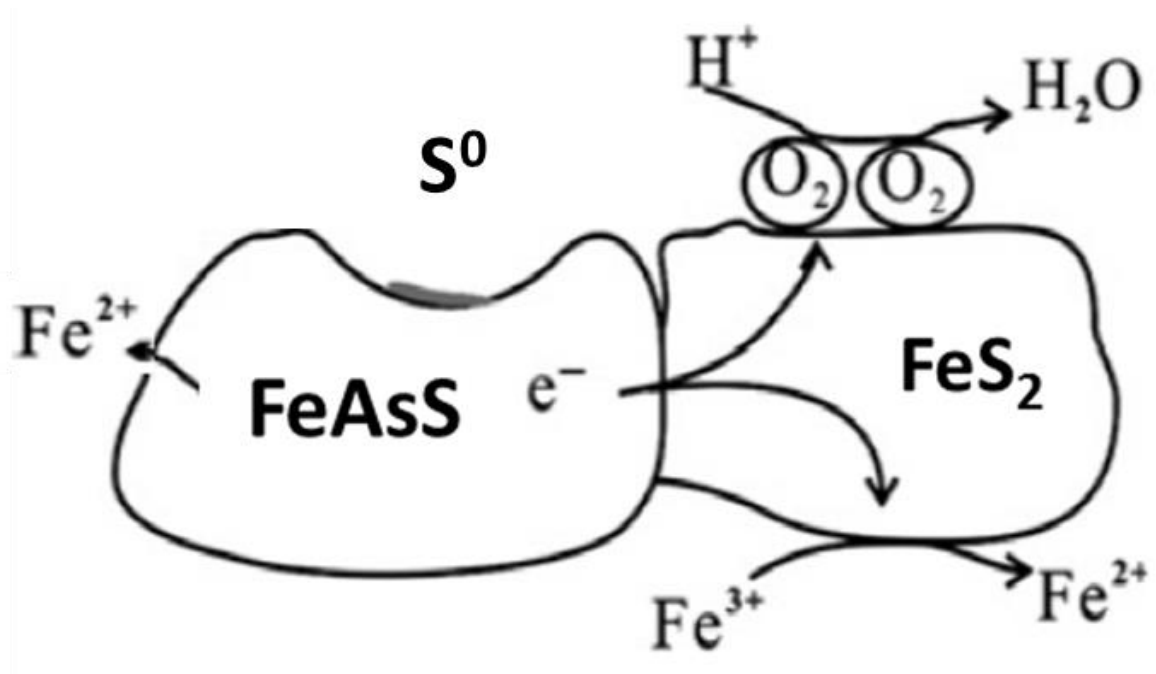


Figure 4- Scheme showing the oxidation of arsenopyrite in the presence of pyrite.

The electrochemical behaviour of pyrite and arsenopyrite minerals in contact to each other has been intensely investigated.[30, 54] It has been found that oxidation of the pyrite/arsenopyrite is similar to the isolated pyrite or arsenopyrite, and a large quantity of sulfate is produced. However, the reaction mechanism has not been identified. Other authors[25, 48, 53, 55] found that pyrite oxidation proceeds via a complex sequence of series and parallel reaction steps which can be proposed from the electrochemical data. Briefly, the oxidation of arsenopyrite in the presence of pyrite can be understood according to the scheme shown in Figure 4, where a sequence of cathodic and anodic reactions is shown.

Objective

The knowledge about the surface chemistry of these minerals and their chemical reactivity is the first step to understand and determine the oxidation mechanism of the mineral sulfides. Its relevance is related to the development of improved methods for controlling the ARD and for metal extraction with better environmental performance are present. Many studies on the reactivity of mineral sulfides are available in the literature.[45, 48, 55] The reactivity of the minerals is directly related to their atomic structure, composition, geometry and its electronic properties. Computer simulation of this intricate reactions can provide insights about the reaction mechanism at a molecular level and help to interpret the large experimental data reported in the literature. The development of efficient computational methods makes computational chemistry an important tool for investigating the microscopic behaviour of these mineral surfaces. Density Functional Theory (DFT) is widely used for investigating reactions and is particularly important in the study of solid phase materials. The DFT enables accurate estimates of the chemical properties in a reasonable calculation time. Recently, modelling the oxidation mechanism of pyrite[62, 63] and arsenopyrite[64] in the presence of oxygen and water has been subject of investigations. However, to the best of our knowledge, no tentative to model the pyrite inlay in arsenopyrite has been modelled.

The main objective of this thesis is to provide initial insights on structural and electronic properties of the pyrite/arsenopyrite interface and its comparison with the results for the isolated pyrite and arsenopyrite are provided. To achieve this goal, the following steps were pursued:

1. To study the crystalline phases of pure pyrite and arsenopyrite minerals, and then identify their most favoured surfaces exposed in nature (**chapter 3**).
2. To propose a model of the pyrite associated with arsenopyrite (**Chapter 3**).
3. To study the stability and the electronic structure of the pyrite/arsenopyrite interface and compare to the electronic structure of the isolated phases of pyrite and arsenopyrite (**Chapter 3**).
4. To evaluate the local reactivity of slabs based on the interface-bulk structures obtained in chapter 3 (**Chapter 4**).

5. To study the galvanic interaction of pyrite/arsenopyrite by means of the Band Offset **(Chapter 5)**.

In parallel, two other topics were studied in this thesis.ⁱⁱ

6. To develop DFTB (more details in Chapter 2) parameters in order to describe liquid water in contact with pyrite (100) surface **(Chapter 6)**.
7. To extend our understanding of the oxidation mechanism of pyrite to include the formation of S-containing species **(Chapter 7)**.

ⁱⁱ **Topic 6 and 7 will be better introduced in their respective chapters.**

Chapter 2 - Simulation techniques

Preamble: Density functional theory (and its approximation DFTB) has been used with remarkable success in many fields and it is the first-choice method for investigating the solid state. The simulation codes can calculate a vast range of structural, electronic, chemical, and thermodynamic properties. In this Chapter, we present an overview of the fundamentals of DFT and its applications. Not all the theoretical aspects will be approached in this work, additional discussions can be found in the quoted references.

Density functional theory

The development of quantum mechanics in the early twentieth century made feasible the estimation of structural, electronic, electrical, and mechanical properties of solids and molecules. Although the analytical solution of the Schrödinger equation is limited to systems containing only one electron, approximate numerical methodologies allow the solution of a multielectron problem with an acceptable level of accuracy. Among these methodologies, the Hartree-Fock (HF) method stands out, although the electronic correlation is neglected. The correlation energy is important to describe many chemical processes, and can be included in the calculations by the so-called post-Hartree-Fock[65-68] (such as: Møller–Plesset perturbation, coupled-cluster, and configuration interaction) methods, and alternatively, by the Density Functional Theory (DFT). When compared to post-Hartree-Fock methods, the DFT method has lower computational cost, and because of that in the last decades DFT has been widely used to describe the electronic structure of large systems containing hundreds of atoms. Particularly, the DFT approach has been broadly used in the study of solids, surfaces, and interfaces. Therefore, in this work the DFT was chosen as a base methodology to perform the computations.

The practice of using the electronic density, $\rho(\mathbf{r})$, as a basic variable was first performed by Drude[69, 70] in early twentieth century. According to Drude,[71] the electron behaviour in a metal can be described as an homogenous gas and apply the kinetic theory of gas. Such approximation permitted to describe the thermal and electric conduction properties providing numbers with the same order of magnitude as the

experimental values. Starting from Drude's ideas different models have been developed,[71, 72] however, the use of $\rho(\mathbf{r})$ as a basic variable was only validated as an exact theory with the publication of two theorems by Hohenberg and Kohn (HK) in 1964.[73] These two theorems provided the fundamentals of the modern DFT. The HK theorems proves that the ground state of an electron system is a functional of the electron density, and in principle with the knowledge of the electron density only it is possible to calculate all the properties of the system. The first theorem of HK states that the external potential, $v(\mathbf{r})$, is a unique functional of the electronic density. In other words, it shows that the electron density of a system determines the external potential, $v(\mathbf{r})$ and the number of electrons, N :

$$N = \int \rho(\mathbf{r})d\mathbf{r}. \quad (2.1)$$

The Hamiltonian, \hat{H} , of the system is given by:

$$\hat{H} = \hat{T} + \hat{V}_e + \hat{U}. \quad (2.2)$$

In Eq. (2.2) \hat{T} is the kinetic energy operator, \hat{V}_e is the repulsion operator related to the electron-electron classical and non-classical interactions. \hat{U} is the electron-core operator defined by the atomic nucleus charge, Z_A , atomic position, \mathbf{R}_α , and electron position, \mathbf{r}_i :

$$\hat{U} = \sum_i^N \sum_A^M -\frac{Z_\alpha}{|\mathbf{R}_\alpha - \mathbf{r}_i|} = \sum_i^N v(\mathbf{r}_i). \quad (2.3)$$

The second HK theorem establishes the DFT variational principle. Since the exact electronic density describing the system is not known, an approximate electron density $\tilde{\rho}(\mathbf{r})$ will provide an energy equal to or greater than the exact energy of the system, ($E[\tilde{\rho}] \geq E[\rho] = E_0$).

In 1965, Khom and Sham[74] developed a methodology that allows the DFT calculations as it is done currently. Accordingly to Levy,[75] the Kohn-Sham equations can be interpreted as the solution of a non-interacting electron system that lead to the electron density of the interacting system. The Hamiltonian has an effective local potential, $v_{eff}(\mathbf{r})$, which generates the electron density of the interacting electron system:

$$H^{KS} = -\frac{1}{2}\nabla_i^2 + v_{eff}(\mathbf{r}). \quad (2.4)$$

To obtain the fundamental state of this reference system, Ψ^{KS} , the wave function is approximated by an antisymmetric-product of N Kohn-Sham orbitals of an electron, $\psi_i^{KS}(\mathbf{r}_i)$, represented by Slater's determinant:

$$\Psi^{KS} = \frac{1}{\sqrt{N!}} \begin{vmatrix} \psi_1^{KS}(\mathbf{r}_1) & \psi_2^{KS}(\mathbf{r}_1) & \dots & \psi_N^{KS}(\mathbf{r}_1) \\ \psi_1^{KS}(\mathbf{r}_2) & \psi_2^{KS}(\mathbf{r}_2) & \dots & \psi_N^{KS}(\mathbf{r}_2) \\ \vdots & \vdots & \ddots & \vdots \\ \psi_1^{KS}(\mathbf{r}_N) & \psi_2^{KS}(\mathbf{r}_N) & \dots & \psi_N^{KS}(\mathbf{r}_N) \end{vmatrix}. \quad (2.5)$$

The one electron Kohn-Sham orbitals, ψ_i^{KS} , and their eigenvalues, ε_i , are obtained from the Schrödinger-like equation:

$$\left(-\frac{1}{2}\nabla^2 + v_{eff}\right)\psi_i^{KS}(\mathbf{r}_i) = \varepsilon_i\psi_i^{KS}(\mathbf{r}_i), \quad (2.6)$$

and the electron density of the reference system can be calculated as a function of $\psi_i^{KS}(\mathbf{r}_i)$ by the Eq. (2.7).

$$\rho(\mathbf{r}) = \sum_i^N n_i |\psi_i^{KS}(\mathbf{r}_i)|^2, \quad (2.7)$$

The effective potential is local potential that is defined according to the following equation:

$$v_{eff}(\mathbf{r}) = v(\mathbf{r}) + \int \frac{\rho(\mathbf{r}_1)}{|\mathbf{r} - \mathbf{r}_1|} d\mathbf{r}_1 + v_{xc}(\mathbf{r}), \quad (2.8)$$

where the second term on the right side represents the Coulomb potential, and $v_{xc}(\mathbf{r})$ is the potential due to the exchange-correlation energy, $E_{xc}[\rho]$. The former potential can be defined as the functional derivative of $E_{xc}[\rho]$ with respect to $\rho(\mathbf{r})$, as indicated in the Eq. (2.9).

$$v_{xc}(\mathbf{r}) = \frac{\delta E_{xc}[\rho]}{\delta \rho(\mathbf{r})} \quad (2.9)$$

Briefly, the KS method consists of using a reference system in which the electrons do not interact, but which has the same electron density of the real system. This reference system is solved through the Schrödinger equation, Eq. (2.6), which includes a local effective potential. The solution of this equation follows the protocol to solve the equation of the Hartree-Fock method, and the wave function must be expressed by a Slater determinant, Eq. (2.5). Since the effective potential, $v_{eff}(\mathbf{r})$, depends on the electronic density, $\rho(\mathbf{r})$, the KS equations are solved by means of the Self-Consistent Field (SCF) procedure, Figure 5.

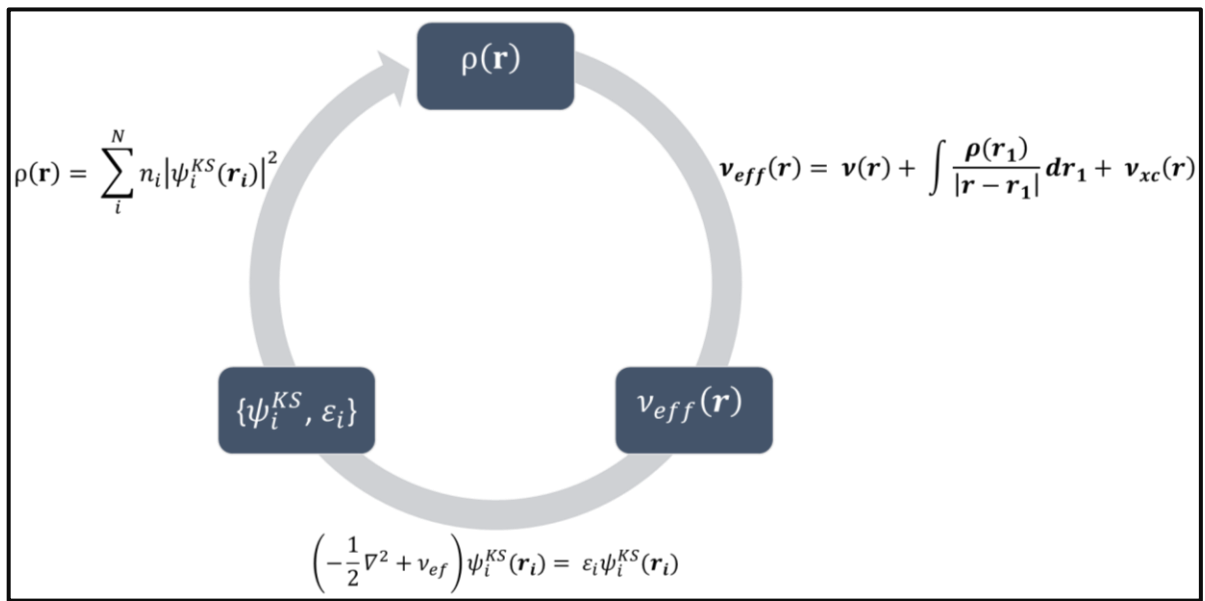


Figure 5- Illustration showing the SCF procedure for DFT methods.

Finally, the KS scheme allows to calculate the total electronic energy of the ground state:

$$E_0[\rho(\mathbf{r})] = \sum_i^N \varepsilon_i - \frac{1}{2} \int \frac{\rho(\mathbf{r})\rho(\mathbf{r}')}{|\mathbf{r} - \mathbf{r}'|} d\mathbf{r}d\mathbf{r}' + E_{xc} - \int \rho(\mathbf{r})v_{xc}(\mathbf{r})d\mathbf{r}. \quad (2.10)$$

Since the exact analytical form of the v_{xc} potential is not known, Eq. (2.9), these XC functionals are constructed from different approximations. Several works have been devoted to the development and test of the different approximations of the Exchange-correlation functional.[76-78] Basically, three approaches are mostly used for DFT quantum calculations: Local Density Approximation (LDA, references [79, 80]),

Generalized Gradient Approximation (GGA, references [81-86]) and hybrid functional[65, 87-92] are some of the most used XC functionals.

Plane waves

The inherent symmetry features of the solids is normally used to decrease the computer efforts and the number of atoms explicitly treated in the structure.[6] From a microscopic point of view, a crystalline solid can be represented as a minimum set of lattice points in a periodically-repeating environment, termed unit cell.[72] Since the macroscopic solid is defined by the translation of the unit cell, we can define a translation vector \mathbf{R} in real space. The Hamiltonian that describes the electrons in a crystalline solid is divided into the kinetic energy of the electrons, and the potential energy that obeys the following property: $V(\mathbf{r} + \mathbf{R}) = V(\mathbf{r})$. This is periodic boundary condition that is reinforced to assure the periodicity of the crystalline solid. Bloch's theorem[71, 72] states that the eigenvectors can be written in the form of a plane wave ($e^{i\mathbf{K}\cdot\mathbf{r}}$) multiplied by the periodic function $u_{n,\mathbf{k}}(\mathbf{r})$, as established in:

$$\psi_{n,\mathbf{k}}(\mathbf{r} + \mathbf{R}) = \psi_{n,\mathbf{k}}(\mathbf{r}) = e^{i\mathbf{K}\cdot\mathbf{r}} u_{n,\mathbf{k}}(\mathbf{r}), \quad (2.11)$$

here \mathbf{K} are vectors in reciprocal space and $u_{n,\mathbf{k}}(\mathbf{r})$ Bloch orbitals have the following property: $u_{n,\mathbf{k}}(\mathbf{r}) = u_{n,\mathbf{k}}(\mathbf{r} + \mathbf{R})$, consequently $\psi_{n,\mathbf{k}}(\mathbf{r} + \mathbf{R}) = \psi_{n,\mathbf{k}}(\mathbf{r})$. The term “n” in Eq. (2.11), is known as the band index,[71] and for each \mathbf{K} -point the Schrödinger equation is solved to obtain a set of eigenvectors and eigenvalues. The set of “n” eigenvalues for the different \mathbf{K} -points is known as the band structure.

To solve Schrödinger's equations, it is convenient to expand the wave function into a set of basis functions. For these systems, the $u_{n,\mathbf{k}}(\mathbf{r})$ is expanded into plane wave basis sets ($\sum_{\mathbf{G}} C_{i,\mathbf{G}} e^{i\mathbf{G}\cdot\mathbf{r}}$), where \mathbf{G} is a vector in the reciprocal space (i.e. a \mathbf{G} -vector is the representation of a \mathbf{R} -vector in the Brillouin zone). Hence, the Eq. (2.11) is written as:

$$\psi_{n,\mathbf{k}}(\mathbf{r}) = \sum_{\mathbf{G}} C_{i,\mathbf{k}+\mathbf{G}} e^{i(\mathbf{k}+\mathbf{G})\cdot\mathbf{r}}, \quad (2.12)$$

This expansion is normally truncated based on a kinetic energy cutoff (calculated by the expression: $(-1/2)|\mathbf{k} + \mathbf{G}|^2$).

Substituting the Eq. (2.12) in the Kohn-Sham expression, Eq. (2.6), we arrive at the following expression:

$$\left(-\frac{1}{2}\nabla^2 + v_{ef}\right) \sum_{\mathbf{G}} C_{i,\mathbf{k}+\mathbf{G}} e^{i(\mathbf{k}+\mathbf{G})\cdot\mathbf{r}} = \varepsilon_i \sum_{\mathbf{G}} C_{i,\mathbf{k}+\mathbf{G}} e^{i(\mathbf{k}+\mathbf{G})\cdot\mathbf{r}}. \quad (2.13)$$

By multiplying Eq. (2.13) by $e^{-i(\mathbf{k}+\mathbf{G}')\cdot\mathbf{r}}$ and integrating over the coordinate space, \mathbf{r} , we arrive at a particular form of the Kohn-Sham equation,[93] as shown in Eq. (2.14),

$$\sum_{\mathbf{G}} \left[\frac{1}{2} |\mathbf{k} + \mathbf{G}|^2 \delta_{\mathbf{G}\mathbf{G}'} + V_{ion}(\mathbf{G} - \mathbf{G}') + V_H(\mathbf{G} - \mathbf{G}') + V_{xc}(\mathbf{G} - \mathbf{G}') \right] = \varepsilon_i C_{i,\mathbf{k}+\mathbf{G}}, \quad (2.14)$$

where the first term on the left is the kinetic energy, being $\delta_{\mathbf{G}\mathbf{G}'}$, represented by the following integral:

$$\delta_{\mathbf{G}\mathbf{G}'} = \int e^{i(\mathbf{G}-\mathbf{G}')\cdot\mathbf{r}} d\mathbf{r}. \quad (2.15)$$

The electron-core attraction, $V_{ion}(\mathbf{G} - \mathbf{G}')$, coulombian electron-electron repulsion, $V_H(\mathbf{G} - \mathbf{G}')$, and the exchange/correlation, $V_{xc}(\mathbf{G} - \mathbf{G}')$, potentials are defined in terms of their Fourier transform, as indicated in Eq. (2.16).

$$V_{\mathbf{G}-\mathbf{G}'} = \int V(\mathbf{r}) e^{i(\mathbf{G}-\mathbf{G}')\cdot\mathbf{r}} d\mathbf{r} \quad (2.16)$$

The resolution of Eq. (2.14) is done by diagonalizing the $H_{K+G,K+G}$ Hamiltonian matrix, which elements are given on bracketed terms of Eq. (2.14).

Pseudopotentials

Expanding the wave function of a periodic system in a set of plane waves is a challenge by two main reasons. First, because heavy atoms have a very large number of electrons to be treated, which requires many plane waves to describe the electronic

structure of the systems. Second, the wave function oscillates very much in the core region, which also requires a very large number of plane waves for a correct description of this wave function in the valence. Thus, this problem can be overcome using pseudopotentials to describe the core electrons.[94, 95] In the pseudopotential technique, the core electrons are replaced by a potential that, when added in the Hamiltonian provides a pseudopotential that is felt by the valence electrons. Let's define $\psi_k^v(\mathbf{r})$ and $\psi_k^c(\mathbf{r})$ as the self-states that describe, respectively, the valence and core electrons and consider $\phi_k^v(\mathbf{r})$ as a new set of valence state functions that relates to $\psi_k^v(\mathbf{r})$ by the Eq. (2.21).

$$\psi_k^v(\mathbf{r}) = \phi_k^v(\mathbf{r}) - \sum_c \left(\int d\mathbf{r}' \psi_k^{c*}(\mathbf{r}') \phi_k^v(\mathbf{r}') \right) \psi_k^c(\mathbf{r}). \quad (2.17)$$

The core states are projected out by the second term on the right side of Eq. (2.17). Applying the Hamiltonian operator, \hat{H} , in the valence self-states, $\psi_k^v(\mathbf{r})$, and replacing the valence wave function with the expression of Eq. (2.17) we get the Eq. (2.18).

$$\hat{H} \phi_k^v - \sum_c \left(\int d\mathbf{r}' \psi_k^{c*} \phi_k^v \right) \hat{H} \psi_k^c = \varepsilon^v \left[\phi_k^v - \sum_c \left(\int d\mathbf{r}' \psi_k^{c*} \phi_k^v \right) \psi_k^c \right] \quad (2.18)$$

Using the $\hat{H} \psi_k^c = \varepsilon^c \psi_k^c$ relation and manipulating algebraically the Eq. (2.18), we arrive at the Eq. (2.19):

$$(\hat{H} + V^R) \phi_k^v = \varepsilon^v \phi_k^v, \quad (2.19)$$

where V^R is the operator defined as:

$$V^R \phi_k^v = \sum_c (\varepsilon^v - \varepsilon^c) \left(\int d\mathbf{r}' \psi_k^{c*} \phi_k^v \right) \psi_k^c. \quad (2.20)$$

Eq. (2.19) is an eigenvalue problem in which the valence electrons feel a potential given by: $\hat{V}^{PS} = \hat{V} + V^R$. Since the energy of the valence electrons, ε^v , is greater than the energy of the core electrons region, ε^c , the $V^R \phi_k^v$ term, Eq. (2.20), will be a positive contribution to the potential. The latter term acts as if it were "displacing" the valence electrons out of the core region. This new wave function describing the system, $\phi_k^v(r)$, is

smoother in the core region ($r < r_c$) and maintains the same characteristics of the original wave function in the valence region ($r > r_c$), see Figure 6.

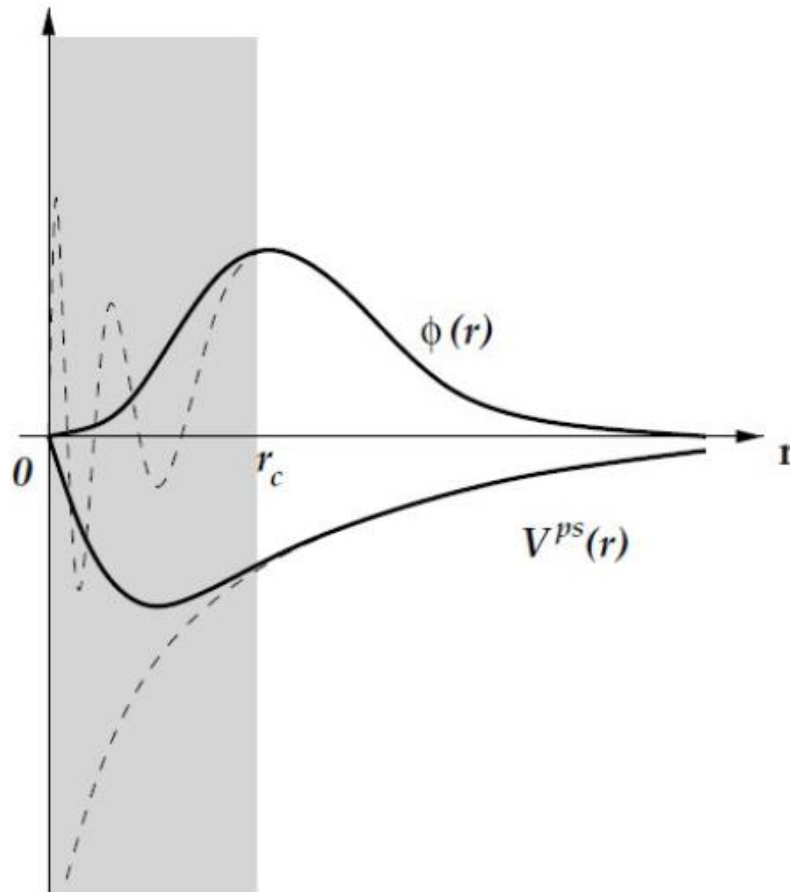


Figure 6- Construction of the pseudo wave function $\phi(r)$ by the pseudopotential method. Figure quoted from Reference [95].

The DFT+U method

Even with its limitations and well-known problems to describe the correct electronic interaction in complex systems,[96-98] the DFT still represents the main computational tool to perform electronic structure calculations. The efficiency of DFT is related to the possibility to express all the ground state properties of an electronic system as a functional of its electronic density. However, the exact expression of its total energy is unknown and approximations are needed in order to perform DFT calculations. As discussed before, in the DFT scheme the electron–electron interaction energy is written as shown in Eq. (2.8), where the effective potential, $v_{eff}(\mathbf{r})$, depends on the sum of the

classical Coulomb term ($\int \rho(\mathbf{r}_1)/|\mathbf{r} - \mathbf{r}_1| d\mathbf{r}_1$) and the XC term, $v_{xc}(\mathbf{r})$. By the DFT formalism, the $v_{xc}(\mathbf{r})$ term is supposed to contain all the electronic corrections not included in the Coulomb term. Due to the approximations in the $v_{xc}(\mathbf{r})$, the DFT functional commonly provide a poor representation of the N-electron many-body-interaction of the ground state. For these reasons, correlated systems (the systems that depend significantly on the $v_{xc}(\mathbf{r})$ term) are still a challenge on its electronic description.

An alternative to avoid this problem of the DFT is based on the Hubbard theory.[96, 97] Initially such theories were used to correct the LDA DFT XC functional. It was initially called LDA+U, but, with the XC functional developments and implementations, it started to be used also with GGA methods (the so-called GGA+U). In this work, it will be called as DFT+U, since this nomenclature contemplates both LDA+U and GGA+U methods.

The basic idea behind the DFT+U method is to treat the Coulomb interaction with an additional Hubbard model.[98] The Coulomb interactions are particularly strong for localized d and f electrons, but can be also important for p localized orbitals. In general, the DFT+U method modifies the frontiers orbitals (the orbital close to Fermi level), the core orbitals are treated by the standard DFT method (without the Hubbard correction). The strength of the interactions is usually described by parameters U (for the Coulomb term) and J (for the exchange term), including both terms the DFT+U total energy is given by:

$$E_{DFT+U} = E_{DFT} + \frac{U_{eff}}{2} \sum_a Tr(\rho^a - \rho^a \rho^a), \quad (2.22)$$

where E_{DFT} is the GGA (or LDA) DFT total energy and $U_{eff} = (U - J)$. ρ^a is the atomic orbital occupation matrix. The parameters U and J can be previously extracted from ab-initio calculations, but, as it will be shown in Chapter 3, these parameters can be obtained empirically. It is necessary to create a grid and evaluate the best $(U - J)$ parameter that will describe the target property.

In the present work, the $(U - J)$ parameter was optimized to describe the electronic properties of the interfaces (see Figure 8, at Chapter 3 and Figure 22, at Chapter 5).

Topological analysis of the electron density

In order to understand the nature of the bonds present in the interfaces it was evaluated the ELF analysis,[99-104] which is the topology analysis of the electron pair localization function. For a single-determinantal wave function built from Kohn-Sham orbitals, φ_i , ELF is calculated on a grid in three-dimensional space by the equation:

$$ELF(\mathbf{r}) = \left[1 + \left(\frac{D(\mathbf{r})}{D_h(\mathbf{r})} \right)^2 \right]^{-1}, \quad (2.23)$$

where $D(\mathbf{r})$ is the density of the excess kinetic energy for the corresponding system:

$$D(\mathbf{r}) = \sum_i |\nabla \varphi_i(\mathbf{r})|^2 - \frac{1}{4} \frac{|\nabla \rho(\mathbf{r})|^2}{\rho(\mathbf{r})}, \quad (2.24)$$

and $D_h(\mathbf{r})$ is the kinetic energy for the homogenous electron gas with spin-density equal to the local value of $\rho(\mathbf{r})$:

$$D_h(\mathbf{r}) = \frac{3}{5} (6\pi^2)^{2/3} \rho(\mathbf{r})^{5/3}. \quad (2.25)$$

The space defined by the electron density, $\rho(\mathbf{r})$, is partitioned in electronic basins corresponding to bonds (B), lone pair (LP) and atomic core shells (CS), which is consistent with Lewis' valence bond theory. The electron density integration over B, LP and CS basins volume are well known to follow the expected values and tendencies from the *aufbau* principle and the valence shell electron pair repulsion (VSEPR) theory. ELF is defined to restrict the possible values to the range of $0 < ELF(\mathbf{r}) < 1$, with the upper limit $ELF(\mathbf{r}) = 1$ corresponding to a complete localization of the electron, and $ELF(\mathbf{r}) = 1/2$ means an electron-gas-like pair probability, which is characteristic for metallic systems [$D(\mathbf{r}) = D_h(\mathbf{r})$].

Density-functional tight-binding theory

Even though DFT methods have been successfully applied for systems of increasing complexity and size, methods which can describe large atomic-system at

quantum level are still required. The Density-functional tight-binding (DFTB) is an approximated DFT method that describes the electronic properties of large systems with relatively low computational cost.[68] The main idea behind this method is to describe the Hamiltonian eigenstates with an atomic-like basis set and replace the Hamiltonian with a parameterized Hamiltonian matrix whose elements depend only on the internuclear distances and orbital symmetries. The DFTB2 total energy is described by the Eq. (2.26):

$$E = E_{bnd} + E_{SCC} + E_{rep}, \quad (2.26)$$

where E_{bnd} is the band (or electronic) energy and it is evaluated by the sum of the molecular orbital eigenvalues according to the Eq. (2.27).

$$E_{bnd} = \sum_{i=1}^M \varepsilon_i, \quad (2.27)$$

M is the number of electrons and ε_i is the i -th occupied molecular orbital energy. In order to calculate E_{bnd} , one has to build the tight-binding Kohn-Sham like Hamiltonian for the system. Then, for an electronic system, the Hamiltonian is described according to Eq. (2.28).

$$H_{\mu\nu}^0 = \begin{cases} \varepsilon_{\mu}^{\text{free atom}}, & \mu = \nu, \\ \langle \phi_{\mu} | T + v_{KS}[\rho_0^A, \rho_0^B] | \phi_{\nu} \rangle, & \mu \in \{A\}, \nu \in \{B\}, A \neq B, \\ 0, & \mu \neq \nu \in \{A\} \text{ or } \in \{B\}. \end{cases} \quad (2.28)$$

μ and ν are the indexes of the valence atomic basis function centred on the atoms A and B , respectively. Then, it is evaluated the generalized eigenvalue problem: $H^0 C = SC\varepsilon$ in order to obtain all ε_i states.[105]

The self-consistent charge (SCC) contribution[106] to the energy (E_{SCC}) is computed based on Eq. (2.29):

$$E_{SCC} = \frac{1}{2} \sum_{A,B}^N \gamma_{AB} \Delta_{q_A} \Delta_{q_B}, \quad (2.29)$$

where N is the number of atoms in the system and γ_{AB} is the gamma matrix obtained from functions that depend on the Hubbard parameter of the atoms U_A and U_B , for

instance. The Hubbard parameter is related to the hardness of the atoms and drives how the electron density is distributed between the atoms. The q_A is obtained from Mulliken population analysis.

The SCC contribution to the Hamiltonian is given by:

$$H_{\mu\nu}^1 = -\frac{1}{2}S_{\mu\nu}\sum_{\xi}^N(\gamma_{A\xi} + \gamma_{B\xi})\Delta q_{\xi}, \quad (2.30)$$

The overlap matrix of the confined atomic orbitals is $S_{\mu\nu}$. The final DFTB2 Hamiltonian is evaluated by:

$$H_{\mu\nu} = H_{\mu\nu}^0 + H_{\mu\nu}^1, \quad (2.31)$$

where the secular equation $HC = SC\varepsilon$ is solved by the general eigenvalue problem.[105, 106] One can observe that the Hamiltonian ($H_{\mu\nu}$) depends on the charges, which are calculated using the molecular orbital coefficients C . Therefore, a self-consistent procedure is necessary for solving the problem.

The repulsion energy (E_{rep}) contribution corresponds to the repulsion energy between the nuclear charges and corrects the tight-binding approximation of neglecting the three-centered integrals. Within the DFTB2 approximations, the Hamiltonian only depends on the superposition of electron densities of neutral atoms. Hence, E_{rep} is calculated using a set of adequate reference systems according to Eq. (2.32) and fitted to a polynomial.

$$E_{\text{rep}}(R_{AB}) = E_{\text{DFT}}(R_{AB}) - (E_{\text{bnd}}(R_{AB}) + E_{\text{SCC}}(R_{AB})). \quad (2.32)$$

In fact, by representing E_{rep} as a diatomic potential fitted to DFT values, errors arising from the approximations used in DFTB2 might be partially compensated. The quality of this parameterization is important to ensure the accuracy of the DFTB2 potential energy surface and gradients.

CI-NEB calculations

An important issue in theoretical chemistry and condensed matter physics is how to calculate transition states (TS) and estimate the rate law for chemical reactions and diffusion processes in solids and surfaces. By the chemical point of view, a precise determination of the activation energy and transition state structure is one of the major challenges of computational today. Mainly because to define the TS, not only the initial and final states of the processes should be taken into account, it is necessary to map the relevant points along the potential energy surface (PES). In other words, it is necessary to determine the most relevant transition state (i.e. with the lowest activation energy) that connect the two reference states.

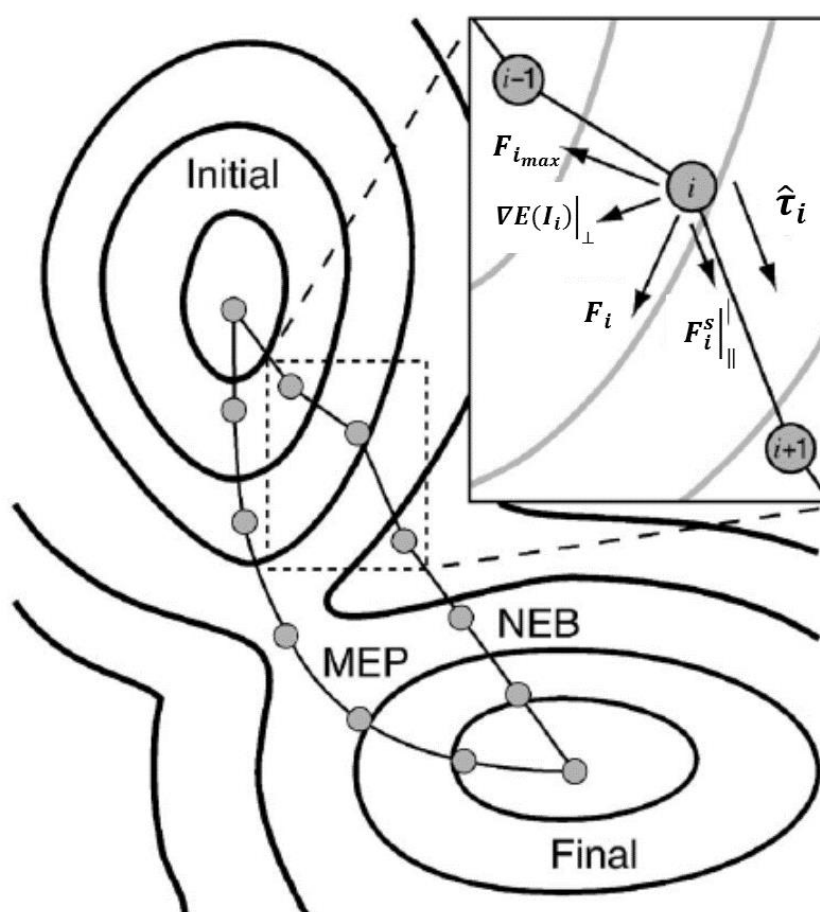


Figure 7- Minimum energy path illustration and force decomposition in NEB calculations. Figure adapted from Ref. [107].

The NEB (Nudged Elastic Band) is an efficient method to find the minimum energy pathway (MEP) between the initial and final states of a given chemical reaction.[107-111] In NEB, the MEP is found by constructing a set of images that define the reaction path.

Among two adjacent images, a spring interaction is added artificially to ensure continuity of the path, representing what would be an elastic band. NEB optimization involves minimizing forces acting on all images, bringing all images to the MEP. Figure 7 shows the decomposition of the forces acting on a NEB calculation. To decompose the forces, it is required to estimate the tangent ($\hat{\boldsymbol{\tau}}_i$) with respect to the reaction path in each image. In this procedure, the elastic approximation is used to define the position of the atoms along the interaction, but the energy calculation must be done for every image. The energy derivative in the coordinate space will define the real force of the system. Real and spring forces are decomposed into two components, parallel and perpendicular to the reaction path. Only the perpendicular component of the real force of the system, $\nabla E(\mathbf{I}_i)|_{\perp}$, and the parallel component of the spring force, $\mathbf{F}_i^S|_{\parallel}$, are used for minimization. Based on the elastic interaction model, the spring force is only needed to control the distance among the images along the path.

A calculation using N+1 images will form a set of \mathbf{I} images, [$\mathbf{I}_0, \mathbf{I}_1, \mathbf{I}_2, \dots, \mathbf{I}_N$], where the initial and final points, \mathbf{I}_0 and \mathbf{I}_N , are kept fixed, giving the energy values of the initial and final states. In NEB scheme, the total force, \mathbf{F}_i , acting under an image i , is the sum between the spring force, $\mathbf{F}_i^S|_{\parallel}$, parallel to the tangent, $\hat{\boldsymbol{\tau}}_i$, and the real force, $-\nabla E(\mathbf{I}_i)|_{\perp}$, perpendicular to $\hat{\boldsymbol{\tau}}_i$. In Eq. (2.33) is shown the definition for \mathbf{F}_i .

$$\mathbf{F}_i = \mathbf{F}_i^S|_{\parallel} - \nabla E(\mathbf{I}_i)|_{\perp} \quad (2.33)$$

The real force is given by:

$$\nabla E(\mathbf{I}_i)|_{\perp} = \nabla E(\mathbf{I}_i) - \nabla E(\mathbf{I}_i) \cdot \hat{\boldsymbol{\tau}}_i, \quad (2.34)$$

where E is the total energy of the system as a function of all the atomic coordinates of \mathbf{I}_i . $\hat{\boldsymbol{\tau}}_i$ must be a normalized vector, to ensure that vector subtraction on the right side of Eq. (2.34) is the perpendicular component of the total force. The spring force is given by Eq. (2.35), where k is the spring constant.

$$\mathbf{F}_i^S|_{\parallel} = k(|\mathbf{I}_{i+1} - \mathbf{I}_i| - |\mathbf{I}_i - \mathbf{I}_{i-1}|) \cdot \hat{\boldsymbol{\tau}}_i, \quad (2.35)$$

Typically in a NEB calculation, none of the images move to near the saddle point, the saddle point is defined by interpolation between the two images with the highest energy value. This means that the resolution of the value found near the TS is poor, and the estimation of the value for the TS is subjective and inexact. One way to avoid numerical

issues is to use the CI-NEB (Climbing Image - Nudged Elastic Band) method. The CI-NEB establishes a small modification of the NEB. All the information about the MEP is retained, but a strict convergence for the TS is obtained. Also, the change does not add any computational cost to the calculation. After some interactions with the NEB method, the image with the highest energy, I_{max} , is identified. The force on this image will no longer be defined by Eq. (2.33), but instead will be described as:

$$\begin{aligned} \mathbf{F}_{i_{max}} &= -\nabla E(I_{i_{max}}) + 2\nabla E(I_{i_{max}})|_{\parallel} \\ &= -\nabla E(I_{i_{max}}) + 2\nabla E(I_{i_{max}}) \cdot \hat{\mathbf{t}}_{i_{max}} \hat{\mathbf{t}}_{i_{max}}, \end{aligned} \quad (2.36)$$

where $\mathbf{F}_{i_{max}}$ is the force along the path of the reaction. Qualitatively, $I_{i_{max}}$ will move upward along the reaction path and, at the same time, it will move downward on the energy curve perpendicular to that defined by the MEP. In CI-NEB the other images serve to define what degree of freedom the energy maximization will take place. In other words, they will not let $I_{i_{max}}$ move out of the MEP. As the CI-NEB converges, $I_{i_{max}}$ will converge to the TS location in MEP.

Final considerations

This Chapter aimed to present the methodological aspects required in this work. More details can be seen in the articles and book Chapters quoted along this Chapter. For a deeper understanding of DFT and its different functional and implementations, there are reviews[65, 67] and textbooks[66, 77, 112] dealing with the complete description of the method. All of these methods have been extensively tested and are considered reference for theoretical calculations. Concerning to the crystallographic aspects of solids we suggest the Ashcroft[72] and Kittel[71] books. On the plane waves method and the pseudopotential implementation we suggest the Payne *et al.*[93] paper. For the DFTB2 method, we recommend to read the papers of the developers and the reviews about the theory.[105, 106, 113-118] For CI-NEB understanding, we recommend the articles quoted in this Chapter.[107, 109-111]

Calculation procedures, and additional computational techniques and protocols will be presented in the next Chapters.

Chapter 3 – Pyrite/arsenopyrite interface formationⁱⁱⁱ

Preamble: The Pyrite/arsenopyrite interface was investigated by means of the DFT approach. To build the interface models we tested the commensurability of the pyrite (100) surface with the twelve arsenopyrite surfaces reported in the literature.[119] Among these interfaces, the three most stable surfaces were built, and its structure, stability and electronic properties were evaluated. The projected density of states (PDOS), electronic band structure and electron localization function (ELF) analysis of the interfaces were compared with the results reported in the literature for pyrite and arsenopyrite mineral phases. This comparison showed that the interface shares structural and electronic characteristics with the pyrite and arsenopyrite isolated mineral structure. Even with the strains caused by the interface formation, the As-S and S-S bonds still have covalent character (ELF=0.7). In contrast, the Fe-S and Fe-As bonds present an ionic behavior (ELF=0.3), as expected when compared with the same bonds in pyrite and arsenopyrite minerals. The electron band structures show that the interface formation changes the density of states close to the Fermi level, shifting the valence states upwards and decreasing the band gap of the interfaces. The microstructure of the interaction of pyrite and arsenopyrite was evidenced by means of the work of adhesion and the formation energy of the interfaces. It has been shown that the adhesion and miscibility of the two phases are not thermodynamically favourable. This instability agrees with the structural analysis, where is observed the formation of distorted octahedron sites in the interface normal plane.

Introduction

Interface is the commonest microstructures in solids, and it has a pivotal role in various physical and chemical properties, such as in mechanics, electrics, carrier transports, corrosion and catalysis reaction.[120-160] Many important properties of

ⁱⁱⁱ The results presented in this chapter were published at Dos Santos, E.C., et al., J. Phys. Chem. C, 121, 8042-8051 (2017). DOI: 10.1021/acs.jpcc.7b02642.

materials are affected by the presence of interfaces. In addition, the physical properties and chemical reactivity of such material may be modified significantly in the interface. Interface imposes more difficulty to investigate if compared with other macroscopic aspects of the materials. However, the combination of experiments with computer techniques has permitted to analyse in details the interface. Actually, atomistic simulations are, in some cases, the only choice for exploring some aspects of the solid interfaces behaviour at a molecular level and indispensable for interpreting unambiguously the experiments.[161] In view of the characteristics of the solid-solid interface, the common tools for theoretical investigations are the electronic calculations based on density functional theory.

Galvanic interaction is a well-known phenomenon, however, the mechanisms of this process at an atomic level are not thoroughly understood for the sulfides. In this Chapter, the vicinities of the pyrite/arsenopyrite interface were investigated using the DFT approach aiming to provide better understanding of its structure, stability, electronic and mechanical properties at a molecular level. We believe that this is the first step to understand the influence of the inlaid arsenopyrite in the pyrite oxidation mechanism.

Computational details

It was studied the stability and electronic properties of the interfaces formed between pyrite and arsenopyrite minerals. To our knowledge, this is the first attempt to investigate the pyrite/arsenopyrite interface properties. All calculations were evaluated with QUANTUM-Espresso software.[162] All DFT calculations were performed using the Perdew-Burke-Ernzerhof (PBE) GGA functional[163] with spin polarization approach. The results reported in this work correspond to the most stable spin state of each structure. Geometry optimization were carried out by Damped dynamics^{iv} method[164] using Parrinello-Rahman extended Lagrangian,[165] and the forces on ions were converged to within 10^{-3} Ry.Bohr⁻¹. For all calculations, Kohn-Sham electronic orbitals were expanded in a plane-wave basis set up to a kinetic energy cutoff of 50 Ry (or 680 eV). A Gaussian smearing of 0.02 eV for the Fermi-Dirac distribution function was used

^{iv} Damped dynamics method was used in order to avoid bond-breaking along structural optimizations.

for all systems. Norm-conserving pseudopotential with: Fe ($3s^23p^64s^23d^64p^0$), S ($3s^23p^43d^0$), and As ($4s^24p^34d^0$) valence electron configuration were used. Following the Monkhorst-Pack scheme, different K-points meshes were used in order to obtain a good description of the electronic structure of the systems. For bulk calculations, we used a $4 \times 4 \times 4$ grid in optimizations and from the optimized structure, a single point calculation was made in the mesh of $10 \times 10 \times 10$ to get a better description of the wave function. We also tested the cutoff and K-points meshes convergence for pyrite and arsenopyrite bulk (see Figure A1, Figure A2, Figure A3, and Figure A4), and for both systems the total energy converged in 1 mRy.atom^{-1} . As the size of the systems reflects inversely in the periodic integration along Brillouin zone, for the interface models we used the $4 \times 4 \times 2$ K-points meshes in the optimizations and $10 \times 10 \times 6$ for post-processes. From the obtained wave function, the projected density of states calculations (PDOS), electronic band structure, and electron localization function (ELF) analysis were evaluated.

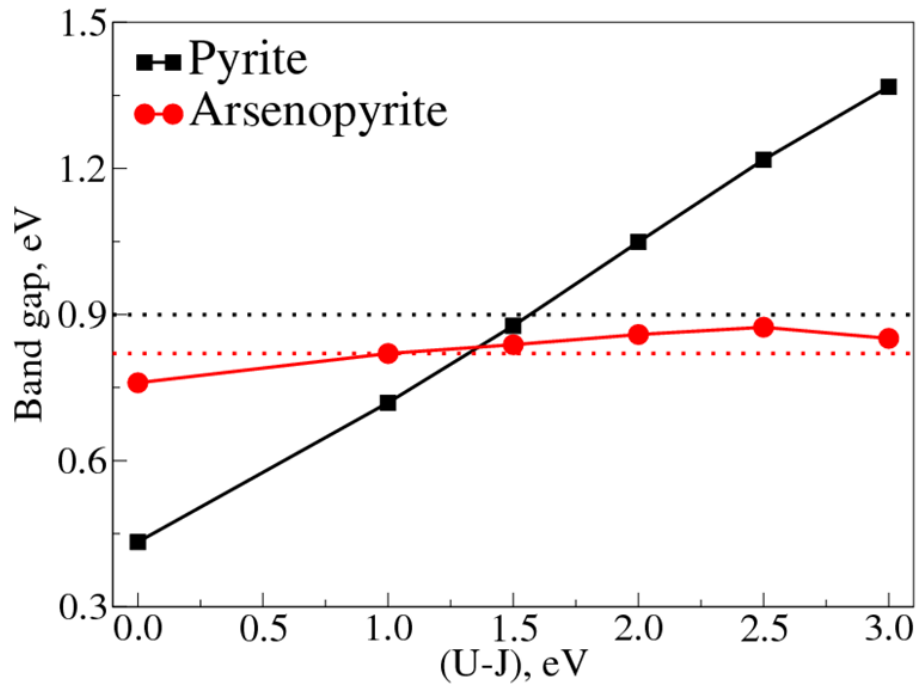


Figure 8- Pyrite and arsenopyrite calculated band gaps as function of the Hubbard (U-J) parameter. Black and red dashed lines represent the experimental band gap for pyrite[166, 167] (0.90 eV) and arsenopyrite[119, 168] (0.82 eV), respectively.

The Hubbard parameter (U-J) has been shown to be crucial to study sulfide minerals[169, 170] and particularly for interfaces.[120, 126, 141, 143, 145] For bulk and interface structures, the iron electronic states dominate both the valence and the

conduction band, so we tested the influence of the (U-J) parameter in all iron atoms. As we are interested in the minimal energy structures, stability, bond formation and electronic properties of the interface, we evaluated the Hubbard parameters to describe the band gap (BG), formation energy and structural parameters of both isolated phases. J was set to be equal to 0.0 eV and the U value was varied as $U = [1.0, 1.5, 2.0, 2.5 \text{ and } 3.0 \text{ eV}]$. As one can see in Figure 8, Hubbard value of 1.5 eV can describe the band gap of pyrite and arsenopyrite with a difference of approximately 0.2 eV for both systems. For this reason, in PDOS, band structure and ELF investigations a (U-J) value equals to 1.5 eV was set. As shown in Table 2, to use the (U-J) parameter for the systems do not improve the results for the formation energy (calculated by the Eq. (3.3)), thus for total energy calculations the Hubbard parameter were not used.

Table 2: Formation energy, E_f , for pyrite and arsenopyrite phases. $|\Delta|$ represents the percentage error between the calculated value and the experimental value.

Bulk System	(U-J), eV	E_f , eV.(formula unit) ⁻¹	$ \Delta $
Pyrite	0.0	-1.512	13
	1.5	-1.432	17
	Exp.[171]	-1.735	---
Arsenopyrite	0.0	-1.309	11
	1.5	-1.135	23
	Exp.[172]	-1.468	---

The unit cell used to start the pyrite bulk calculations was obtained by Brostigen and Kjekshus from crystallographic refinement data.[173] At Room Temperature, pyrite crystallizes in a face-centered cubic system (Pa3 space group) and presents four FeS₂ units in the primitive unit cell. The lattice parameter was determined experimentally to be 5.418 Å, and the Fe-S and S-S chemical bonds lengths 2.262 and 2.177 Å, respectively. Arsenopyrite exhibits a monoclinic cell and has a P2₁/c space group with four FeAsS units per unit cell. Its cell parameters were recently determined by Bindi *et al.*, [174] being: a= 5.761 Å, b= 5.684 Å, c= 5.767 Å, $\beta = 111.72^\circ$, and $\alpha = \gamma = 90.00^\circ$. At our theoretical level, the percent error found for the lattice parameters and bond lengths are around 2%. It shows how the DFT/PBE/plane wave methodology applied in this work can describe the bulk atomic structure of pyrite and arsenopyrite. Consequently the interfaces structure will

also be well described. Therefore, the results presented do not take into account the (U-J) parameter.

From the optimized bulk, it was built the pyrite and arsenopyrite surfaces, and from these surfaces we built the interfaces. For each surface, it was built a supercell in the stacking direction and the atomic-layer thickness were chosen in a way that the two interface distances were greater than 11 Å, which allowed non-physical interactions between the interface regions and to preserve bulk properties in the inner layer. All the structures presented in this Chapter share the feature that all of them are stoichiometric structures, and no defects were simulated.

Pyrite/arsenopyrite coherent interface construction

The construction of the interface models followed the same protocol presented in several papers in literature,[120-160] where two different approaches have been used in order to decrease the mismatch of the interacting phases. The first one is the coherent model, where a (1x1) bulk base unit cell is used and the lattice parameters are built and optimized to find the best match that increases the overlap area, $S_{A/B}$, between the surfaces A and B in contact. Then, the A(1x1)/B(1x1) interface is formed, see Figure 9. This model is widely used for *ab initio* calculations of interface model, and can be used for stacked surfaces with a relatively small mismatch.[120, 122, 124-126, 129-131, 133, 135-137, 140, 141, 143-154, 156, 158, 159] The second approach is the incoherent (also known as semi-coherent) model, and it is generally used to minimize the interfacial stress where it is not possible to achieve by a coherent model.[128, 151] This approach consist in minimizing the size difference of the **a** and **b** lattice parameters of the phases building two A(nxn) and B(mxm) supercells that presents a large number for $S_{A/B}$, forming the A(nxn)/B(mxm) interface. Therefore, in the last model, the stress energy needed for the construction of the interface is minimized and the interface built from two phases with larger difference in their lattice parameters can be investigated. Nevertheless, such interface models are huge with large number of atoms, hence it may not be suitable to run first principles calculations. Both approaches have been evaluated and compared,[151] and, despite the coherent model be less realistic than the semi-coherent model, this is

usually used to describe the adhesion and electronic properties of the interfaces. Accordingly, we chose the coherent model to build the pyrite/arsenopyrite interfaces.

Generally, the lattice parameters of two heterogeneous phases cannot be perfectly matched, thus it is necessary to evaluate the commensurability of the phases. Only in some cases, it is conceivable to build interfaces with the same crystalline phase and surface area via a unit-cell transformation,[143] nevertheless it is not the case of pyrite/arsenopyrite interfaces. So, since a new lattice parameter is necessary in the calculations for coherent solid-solid interface models, stress regions are naturally formed along the atomic structure.

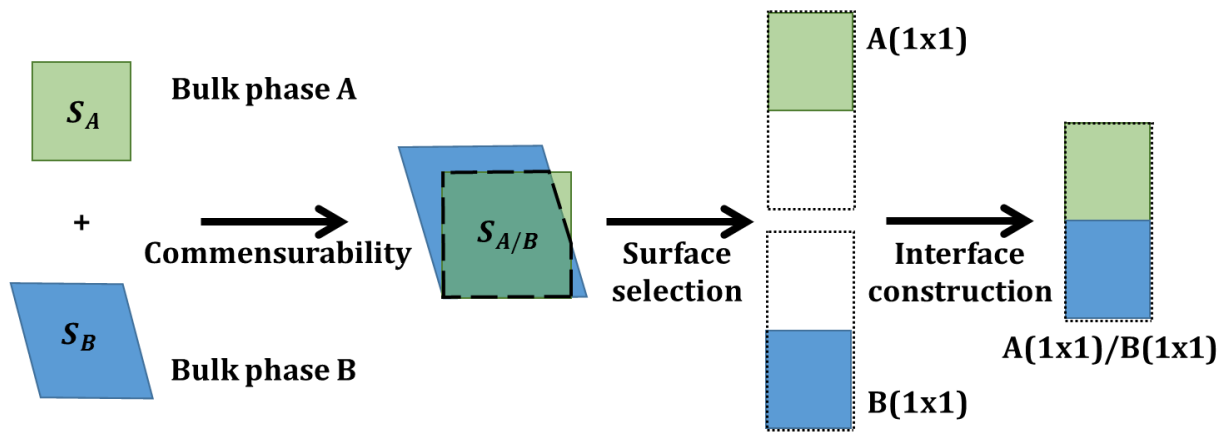


Figure 9- Scheme showing how to construct a coherent interface model that increases the overlapping area, $S_{A/B}$, between phase A and B.

To build a relevant and realistic interface model it is necessary to evaluate the mismatch, ξ , between A and B, which is in this case the pyrite (A) and arsenopyrite (B) phases. For ξ reads:

$$\xi = 1 - \frac{2S_{A/B}}{S_A + S_B}, \quad (3.1)$$

where S_A and S_B are the surface areas and $S_{A/B}$ is the overlapping surface area shown in Figure 9.

The pyrite (100) cleavage plane was used due to its highest occurrence in nature, in all pyritic soils, sediments, and substrates. Also, it has been largely investigated by experimental and theoretical techniques.[175] The choice of the arsenopyrite mineral

cleavage planes is, however, not straightforward.[119, 176] Recently, Silva *et al.* [119] reported a detailed investigation of arsenopyrite cleavage planes by means of GGA/DFT calculations. They investigated twelve possible cleavage surfaces and their surface energy estimates were very close in energy and reproduced in Table 3. The differences are no larger than 0.73 J/m². Furthermore, no preferential cleavage planes are observed in nature and X-ray diffractogram data identify different cleavage planes depending on the sample.

Table 3: Pyrite and arsenopyrite mismatch parameter, ξ , calculation. All the ξ values were calculated considering the (100) surface of pyrite. In brackets are the surface energy values for the surfaces related to the most stable interfaces estimated by our theoretical level.

Arsenopyrite Surfaces	Surface energy,* J.m ⁻²	ξ , %
(001)	1.05 [0.96]	5.5
(100)-As	1.07 [1.04]	5.5
(100)-S	1.09 [1.00]	5.5
(010)-triclinic	1.06	6.2
(010)-orthorhombic	---	41.2
(011)	1.30	22.8
(101)	1.47	29.8
(110)-S	1.52	21.1
(110)-As	1.57	21.1
(111)	1.51	38.2
(210)-1	1.44	42.9
(210)-2	1.78	42.9

* Values obtained from Ref. [119]. The surface energy for the pyrite (100) surface is 1.06 J.m⁻², Ref. [177]. The pyrite (100) surface energy estimated by our calculation is 1.03 J.m⁻².

The interface plane between the phases was chosen to determine the stacking direction by the evaluation of the mismatch parameter, ξ . Experimentally is shown that a low value for ξ is related to a stable interface formation. As one can see in Table 3, the mismatch with pyrite (100) surface and the arsenopyrite surfaces varies a lot for the twelve arsenopyrite surfaces considered in this work. The surfaces (011), (101), (110)-S, (110)-As, (111), (210)-1, and (210)-2 present large number for ξ (from 21.1 to 42.9%), it clearly shows that these surfaces do not mismatch with the pyrite to form a stable interface. The (010) surface could interact with the pyrite surface, but it is a triclinic cell, and as pyrite surface presents an orthorhombic cell, so it is necessary to evaluate a crystallographic transformation from the arsenopyrite(010) triclinic surface to an equivalent orthorhombic cell. This transformation, see Figure A5 for illustration, occurs

maintaining the size of the **a**-lattice parameter, instead the **b**-lattice parameter increases in size. This difference is sizeable and makes the ξ parameter change to 41.2%, which is very large to form a coherent interface. Finally, the surfaces (001) and (100) presented a relatively small mismatch, 5.5%, and these surfaces were used to prepare the three most stable interfaces formed from pyrite and arsenopyrite surfaces: FeS₂(100)/FeAsS(001), FeS₂(100)/FeAsS(100)-As, and FeS₂(100)/FeAsS(100)-S.

Structure and electronic properties

It was evaluated the structural, electronic, and local bonding properties of the most stable interfaces. From the Figure 10, it is possible to see that the interfaces are formed by a sequence of atomic layers composed of iron, sulfur, and arsenic, totalling 24 atomic layers for each structure in z-direction. Along the pyrite side (also labelled in this work as “pyrite region” or “pyrite phase”), the interface is formed by consecutive sulfur and iron layers, and the sequence of sulfur-iron-sulfur owns the same FeS₂ stoichiometry of the pyrite bulk structure. In the arsenopyrite side (also called in this work as “arsenopyrite region” or “arsenopyrite phase”), a sequence of sulfur-iron-arsenic-arsenic-iron-sulfur forms two FeAsS stoichiometry units of arsenopyrite. Each structure is formed by four FeS₂-layers in the pyrite region and four FeAsS-layers in the arsenopyrite side, and the average of the total eight interlayer distances was predicted by our calculations to be: 2.688 Å for FeS₂(100)/FeAsS(001), 2.693 Å for FeS₂(100)/FeAsS(100)-As, and 2.684 Å for FeS₂(100)/FeAsS(100)-S. All the values are in a small range of 2.688 to 2.697 Å. This range is comparable with the layer distances in the pyrite and arsenopyrite in the same crystalline direction. One-to-one, the bulk interlayer distances in FeS₂(100), FeAsS(001) and FeAsS(100) plane directions are 2.690, 2.656 and 2.625 Å.

As discussed by Wang and Smith,[151] optimize the interfacial unit cell is a good strategy to reduce the mismatch strain at the interface point, then a full optimization procedure was done in the calculations. To find the best cell parameter for the interfaces we optimized the systems in two steps. First, all the interfaces were optimized, maintaining the proportion of the structural lattice parameters, and keeping the angles fixed. In other words, we first optimize the systems changing the cell volume and

maintaining the cell shape. From the obtained structures, we also evaluate a full optimization procedure, and then we evaluated the structural parameters of the cell. Even after the complete optimization, all structures had angles close to 90°, and the angles difference error do not exceed 1% for each solid-solid interface models. The structural lattice parameters along the interface were found to be close to the average values of the pyrite and arsenopyrite crystalline phases [$\mathbf{a}_{\text{average}} = (\mathbf{a}_{\text{pyrite}} + \mathbf{a}_{\text{arsenopyrite}})/2 = 5.548 \text{ \AA}$ and $\mathbf{b}_{\text{average}} = (\mathbf{b}_{\text{pyrite}} + \mathbf{b}_{\text{arsenopyrite}})/2 = 5.515 \text{ \AA}$], and the structural parameters calculated were: ($\mathbf{a} = 5.557 \text{ \AA}$; $\mathbf{b} = 5.525 \text{ \AA}$) for FeS₂(100)/FeAsS(001), ($\mathbf{a} = 5.560 \text{ \AA}$; $\mathbf{b} = 5.523 \text{ \AA}$) for FeS₂(100)/FeAsS(100)-As, and ($\mathbf{a} = 5.560 \text{ \AA}$; $\mathbf{b} = 5.524 \text{ \AA}$) for FeS₂(100)/FeAsS(100)-S. It was also observed that all the values are comparable, and the structural cell parameters do not change significantly among the interfaces.

Since the hard phase in a mixture presents more resistance under stretching than the soft phase, the resultant cell parameters along the interface plane are typically found to be closer to the harder phase when an interface is formed. Comparing pyrite and arsenopyrite, pyrite (6.5 on Mohs scale) is, however, only slightly harder than arsenopyrite (around 5.5-6.0 on Mohs scale) and thus the difference between the initial bulk and interface cell parameters is insignificant, as expected since they are close to $\mathbf{a}_{\text{average}}$ and $\mathbf{b}_{\text{average}}$.

We also calculated the bulk modulus (BM) for the FeS₂ and FeAsS minerals and compared with the experimental results obtained by X-ray diffraction data for different pressures.[178, 179] At our theoretical level the BM was estimated to be 150 GPa (experimental value is 143 GPa) for pyrite and 147 GPa (experimental value of 137 GPa) for arsenopyrite in reasonable agreement with the experimental data. Comparing the values for the two solid phases, we find only a minor difference between the pyrite and arsenopyrite BM. Fan *et al.*[178] compared the BM values for the two minerals taking into account the crystalline phase present in the two structures. The authors suggested that the difference in the ionic radius of the As⁻¹ (1.59 Å) and S⁻¹ (1.44 Å) species in arsenopyrite distorts the crystal structure, changing its elastic behaviour.

Numerous works in the literature measured the interfacial distances trying to achieve how adhered is the interface phases, and an interfacial bond distance with the same magnitude of the bulk distances measure how strongly the phases are bonded.[149,

161, 180] Since new chemical bonds are formed along the interfacial periodic plane, it locally affects the symmetry of the surfaces, and the bulk region play a central role in bond formation of the interface. As exposed in Figure 10, we classified the structure of the interfaces in three types, I1 for an interface containing both Fe-Fe short and Fe-Fe long distances, I2 for the interface containing only Fe-Fe long, and I3 for the interface containing only Fe-Fe short bond distances. To understand this classification, it is interesting to compare the atomic structure in the interface region with the arsenopyrite and pyrite bulk Fe-Fe distances.[181-183] As discussed in detail by Nickel *et al.*,[183] in pyrite the neighbouring octahedrons in the structure share common corners, while in arsenopyrite they share edges. Consequently, in arsenopyrite two distinct Fe-Fe bond distances are presented in the structure, which are not present in the pyrite structure (where all the Fe-Fe bonds distances are equal, see Figure 10). Thus, for arsenopyrite minerals there are two different Fe-Fe bond distances, the short (estimated by our calculation in 2.732 Å) and the long (estimated in 3.741 Å). The FeS₂(100)/FeAsS(001) was classified as a I1 interface, and the interfacial iron-iron bond distances were estimated in 2.738 Å and 3.463 Å, respectively, and at the interface it is observed alternating long and short Fe-Fe bonds in the proportion of 1:1. The FeS₂(100)/FeAsS(100)-As system is a I2 interface, and it is composed by Fe-Fe long bonds with 4.090 Å size. The third interface, FeS₂(100)/FeAsS(100)-S, is formed by Fe-Fe short bonds, with 2.822 Å of size.

It will be called as equatorial (eq) the Fe-X (where X= As or S) chemical bonds that pointing in the interface direction, and axial (ax) distances when it crosses the interfacial normal plane, directed along the z-axis. Through the interface plane direction, the Fe-X_{eq} (Fe-As_{eq} and Fe-S_{eq}) and X-S (As-S and S-S) bond distances were measured. For Fe-X_{eq}, the percentage errors are around 0.5% in the pyrite region and 1.9% in the arsenopyrite size, being the greatest value 2.8% of error. For the interface coherent models, where the structures are generated with a stress interfacial region, these errors may be considered negligible, and some lattice distortion does not involve strong modifications on the electronic properties of the bulk. To prove this, we evaluated the stress influence in the electronic structure by the calculation of the density of the states for pyrite and arsenopyrite minerals with strained bulk [with the average size of the interfaces: a= 5.524 Å and b= 5.559 Å]. We observed that the shape and the intensity of the DOS features

remains the same, only minor changes were observed (see Figure 11). In addition, the deformation of the lattice parameters does not modify the position of the band gap. The last result suggest that the electronic structure of the interface will not be changed by the strained structure, and it is possible analyse the density of states to propose the electronic profile of interfaces.

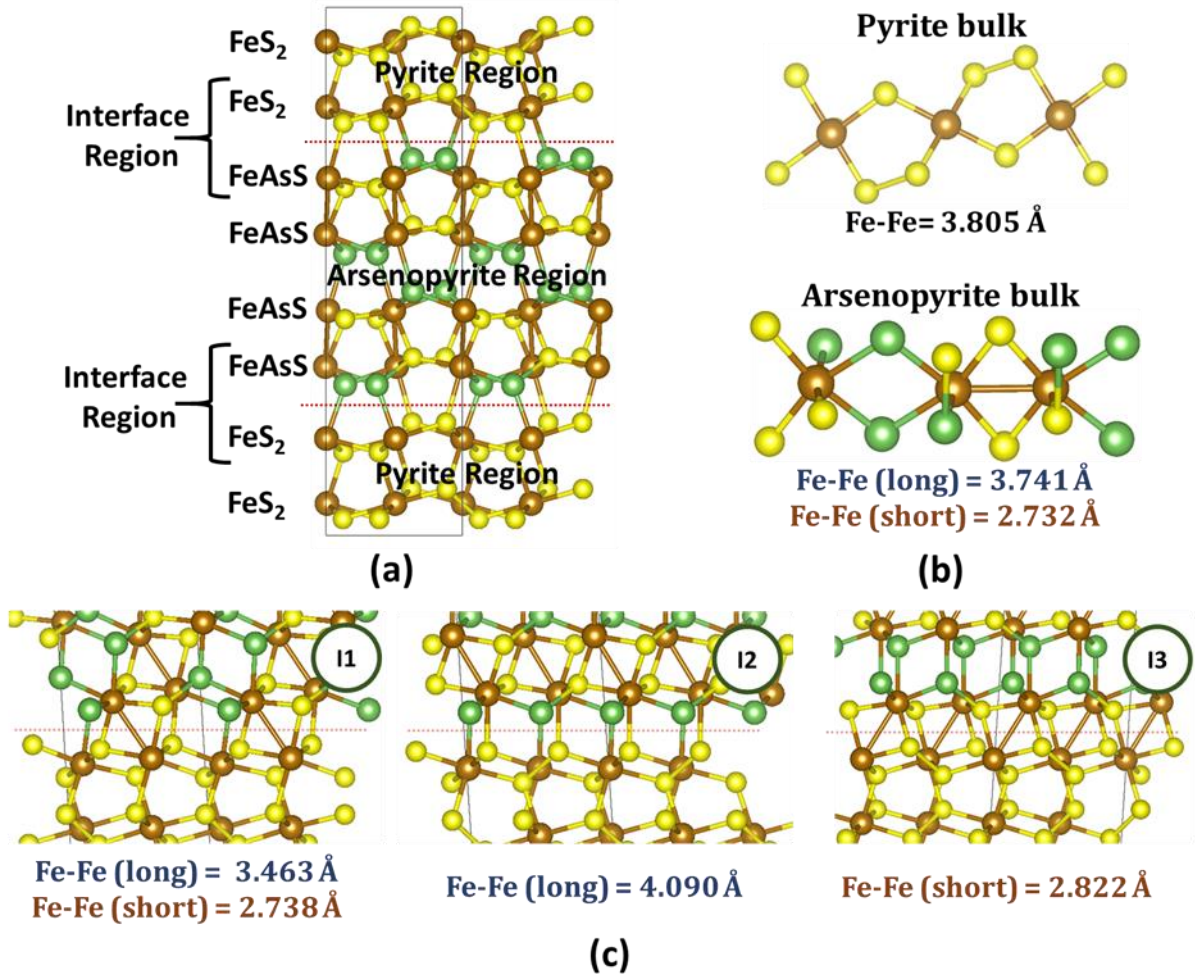


Figure 10- Interface structure. In (a) is shown the interface layered structure along the c-axis. In (b) are shown the pyrite and arsenopyrite bulk, where is highlighted the two Fe-Fe bond distances (short and long) in the structure of arsenopyrite. In (c) are shown the interfacial Fe-Fe bonds and the interface types. From left to right the interfaces in (c) are: $FeS_2(100)/FeAsS(001)$, $FeS_2(100)/FeAsS(100)-As$, and $FeS_2(100)/FeAsS(100)-S$. The red, yellow, and green spheres represent, respectively, the Fe, S, and As atoms. The red dotted lines represent the normal interfacial plane formed by the contact of the two phases.

Structural deviations were found for X-S bond distances placed in the equatorial position, Table A4. In the arsenopyrite side, the As-S bonds decrease in size by 2-3%. Otherwise, in the pyrite region, the forming interface bonds led to increase the sulfur-

sulfur distances. The last values increased from 3.1 to 3.8% for the three interfaces. It has been observed in the literature that for bulk and slab structures of pyrite[177, 184-193] and arsenopyrite,[119, 176, 194, 195] that the X-S bonds are stronger than the Fe-X, and X-S bonds have a covalent character. As the S-S distance from the pyrite region increased by more than 3%, an electron localization functions (ELF) calculation was evaluated in order to access the covalent character of the S-S bonds in the interface. For all the interfaces, the ELF values were found around 0.7, since a value close to 1 represents a perfect covalent bond environment, this clearly shows a strong S-S bond. The same behaviour was observed for the As-S bonds, where also a value about 0.7 was found in ELF analysis.

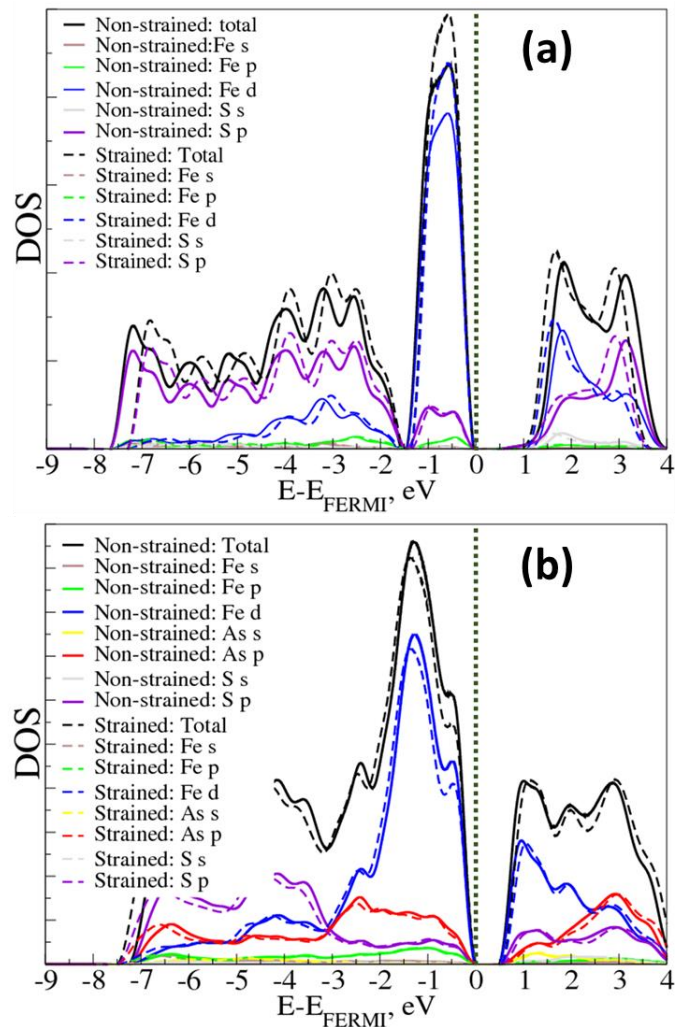


Figure 11- Strain influence in the electronic structure of pyrite (a) and arsenopyrite (b) minerals.

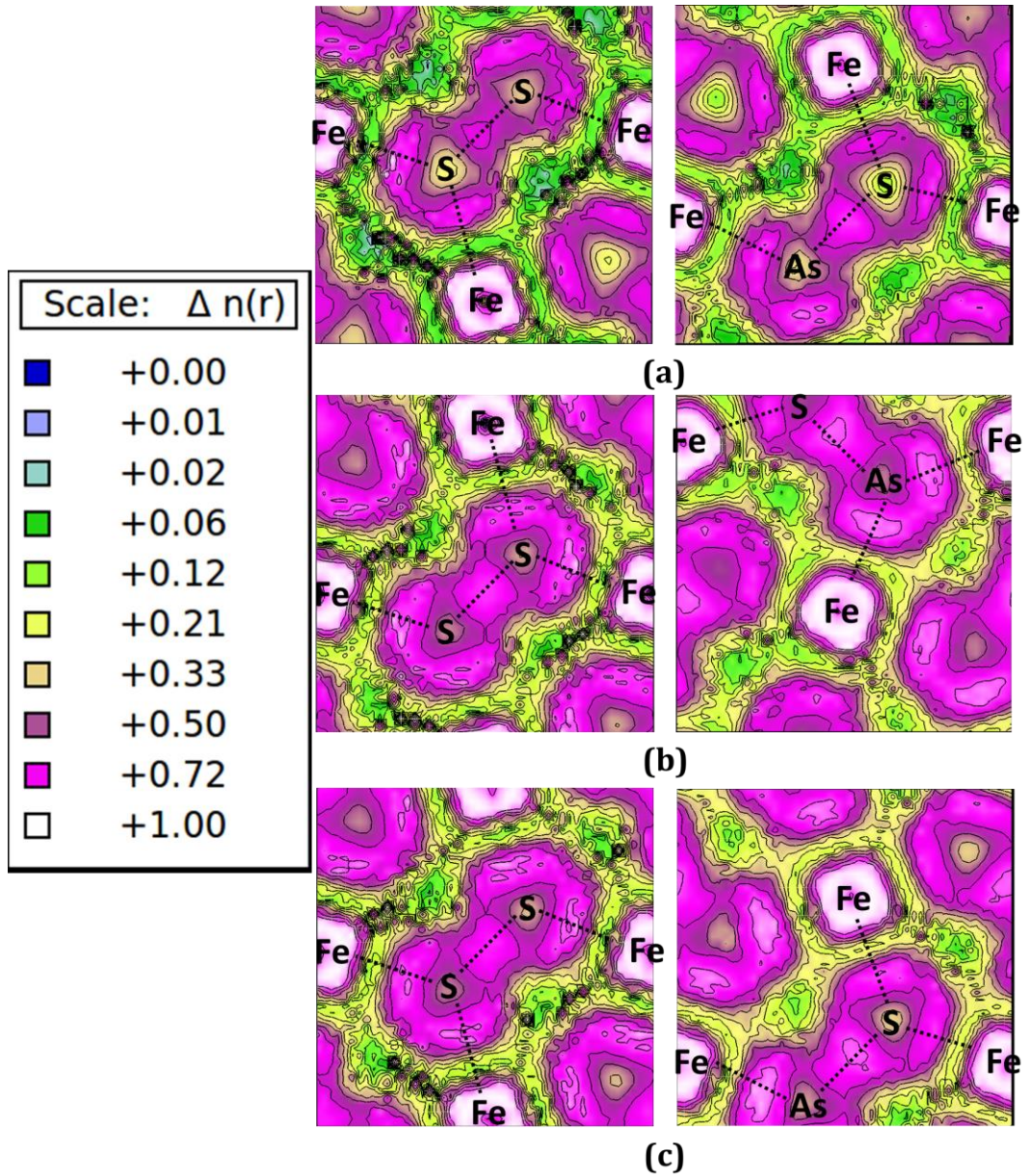


Figure 12- Electron localization function (ELF) for (a) $\text{FeS}_2(100)/\text{FeAsS}(001)$, (b) $\text{FeS}_2(100)/\text{FeAsS}(100)\text{-As}$, and (c) $\text{FeS}_2(100)/\text{FeAsS}(100)\text{-S}$ interface planes located in the pyrite region (left side) and arsenopyrite region (right side). The axial Fe-X bonds are shown in Figure A6.

By analysing of the projected DOS, ELF, and comparing the obtained results to what is well known for bulk isolated structures, it was possible to propose a chemical environment for the interfaces. Looking to the ELF contour plots depicted in Figure 12, all the Fe-X bonds showed an ionic character, and ELF values smaller than 0.3 are observed close to the bond midpoints. Otherwise, the ELF contour distribution along the S-S and As-S bonds clearly show high electrons pair localization around the bond region, suggesting that the S_2^{2-} and AsS^{2-} anionic dimers are present in pyrite/arsenopyrite

interfaces. Since the $(X-S)^{2-}$ dimers presents the oxidation number equivalent to -2, to ensure the neutrality of the FeS_2 and $FeAsS$ stoichiometric layers the iron ionic charge must be +2. We evaluated the spin polarization of the systems. To find it, we simulated different initial spin polarization guess for the three different atoms (Fe, As and S) located in interfacial region of the three interfaces. We tested: (i) the ferromagnetic, (ii) anti-ferromagnetic, and (iii) the electronic systems without any polarization localized in the individual atoms. These results are shown in Table A12, Table A13, and Table A14 and for all initial polarization guess, the results shows no spin density accumulation for any individual atoms. It suggests that Fe(II) ion are present in the interface instead of Fe(III) ion, because in the case of Fe(III) ions, the number of electrons in the iron valence would be 5, and spin polarization must be found.

In pyrite, the S_2^{2-} dimer is formed by two sulfur atoms with filled p -orbital states, which is consistent with the spin compensation observed for pyrite bulk[63, 185, 186, 191] and for the interfaces. For arsenopyrite, the different valences of As and S may suggest the formation of the AsS^{3-} trivalent anion. However, XPS experiments performed by Nesbitt *et al.*[196] and by Jones and Nesbitt[197] on arsenopyrite bulk led to the assignment of iron as divalent because the main peak in the spectra was found very close in binding energy to that of iron in pyrite. According to these authors, it is not possible to distinguish the Fe(II)-(S-S) and Fe(II)-(As-S) bond environments by XPS. They also suggested that the As and S atoms are in the -1 oxidation state in the arsenopyrite structure, and that the formal charges in arsenopyrite are $Fe^{2+}As^-S^-$. Supporting these arguments, a Mössbauer analysis provided by Bind *et al.*[198] indicated the presence of Fe(II) sites in arsenopyrite, where the doublets present in the spectrum suggest a low-spin configuration for the iron sites.

The bonding in arsenopyrite has been discussed to explain how the AsS^{2-} with an odd number of electrons can lead to spin compensation in the arsenopyrite. Hulliger and Mooser first suggested a chemical bond located in the short Fe-Fe distances regions and this could lead to spin compensation.[181, 183] However, recently, Silva *et al.*[119] argued, based on a Bader analysis, that there is no bonding behind the short Fe-Fe distances since only a ring critical point was found. Thus, as in the AsS^{2-} dianion the number of valence electrons is odd, why in the calculation is it not observed any spin

polarization? In order to understand the chemical bonding in the arsenopyrite it is necessary to remember that arsenic and sulfur centers are tetrahedral leading to hybrid sp^3 orbitals. At the arsenic center, there is one hybrid orbital doubly occupied and the other three are singly occupied. In the valence band the contribution of the arsenic is larger than from the sulfur atoms, see Figure 11b, around -2.5 eV below the Fermi level. The bonding is rationalized as follows: the doubly occupied hybrid orbitals donate charge to the Fe center to form the Fe-As bond along the Z-direction. The As-Fe-As bonding shown in Figure 13 is a 4c-2e bond due to the Fe d-orbitals and the singly occupied hybrid orbitals of As. The last singly occupied hybrid orbital interacts with the singly occupied hybrid sulfur orbital to form the As-S orbital. This explains why the Fe-As-Fe distances (2.403 Å) are larger than the Fe-AsS (2.178 Å) bond distances.

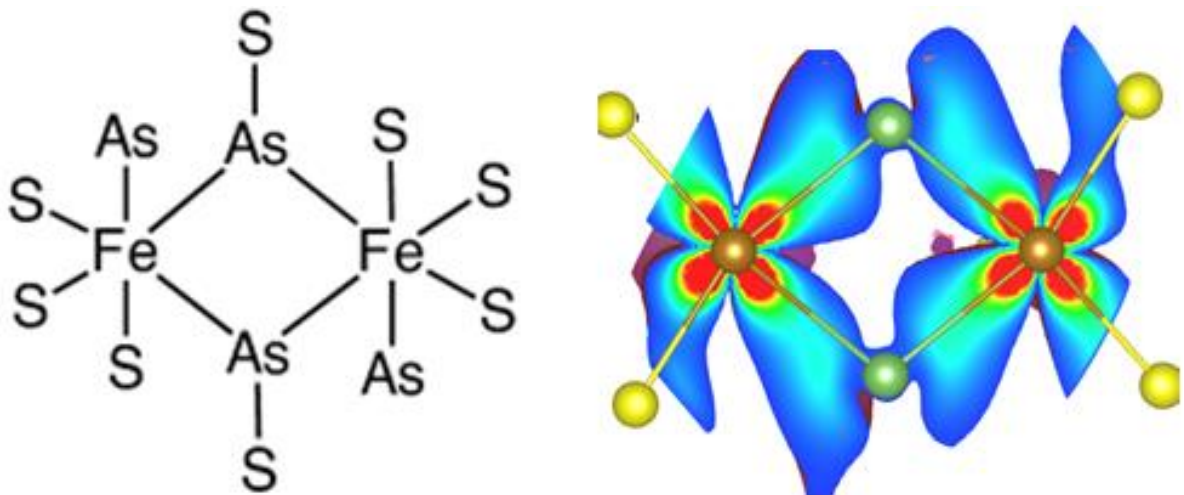


Figure 13- (Left) Illustration of the structure of arsenopyrite and (Right) isosurface and section of the 4c-2e electron state at -2.5 eV below Fermi level, calculated at the Γ point. The Isosurface factor of $0.01 e/\text{\AA}^3$ was set. Color code: yellow - Sulfur, green - Arsenic, brown -Iron.

For all interface systems, iron states dominate both the valence and conduction bands, see Figure 14. Only a small contribution to the valence band is observed from sulfur and arsenic p -orbitals. This is similar to the pyrite[199-206] and arsenopyrite[119, 181-183, 198, 207-209] bulk, where Fe $3d$ states dominate the valence states, with a small contribution from S and As. Many works have discussed the electronic structure of pyrite and arsenopyrite, and there is a consensus that in both minerals, the electronic structure can be described based on ligand-field theory. The similarities of the density of states projected on the interfaces, Figure 14, and the two individual phases, Figure 11, permit to

describe the Fe-X and X-S bonds as follows. The Fe d orbitals split to form the t_{2g} and e_g states in a pseudo-octahedral field, where the e_g orbitals are empty while the t_{2g} orbitals are filled with 6 electrons. The empty e_g states interact with the sp^3 hybrid orbitals of the AsS_2^- to form σ bonds, since the As (or S) atoms are bridging the two iron centers (see Figure 10). It agrees with the formal oxidation state of +2 for iron suggested by the absence of spin polarization in the Fe(II) sites and with the structural analysis for the interfacial bonds.

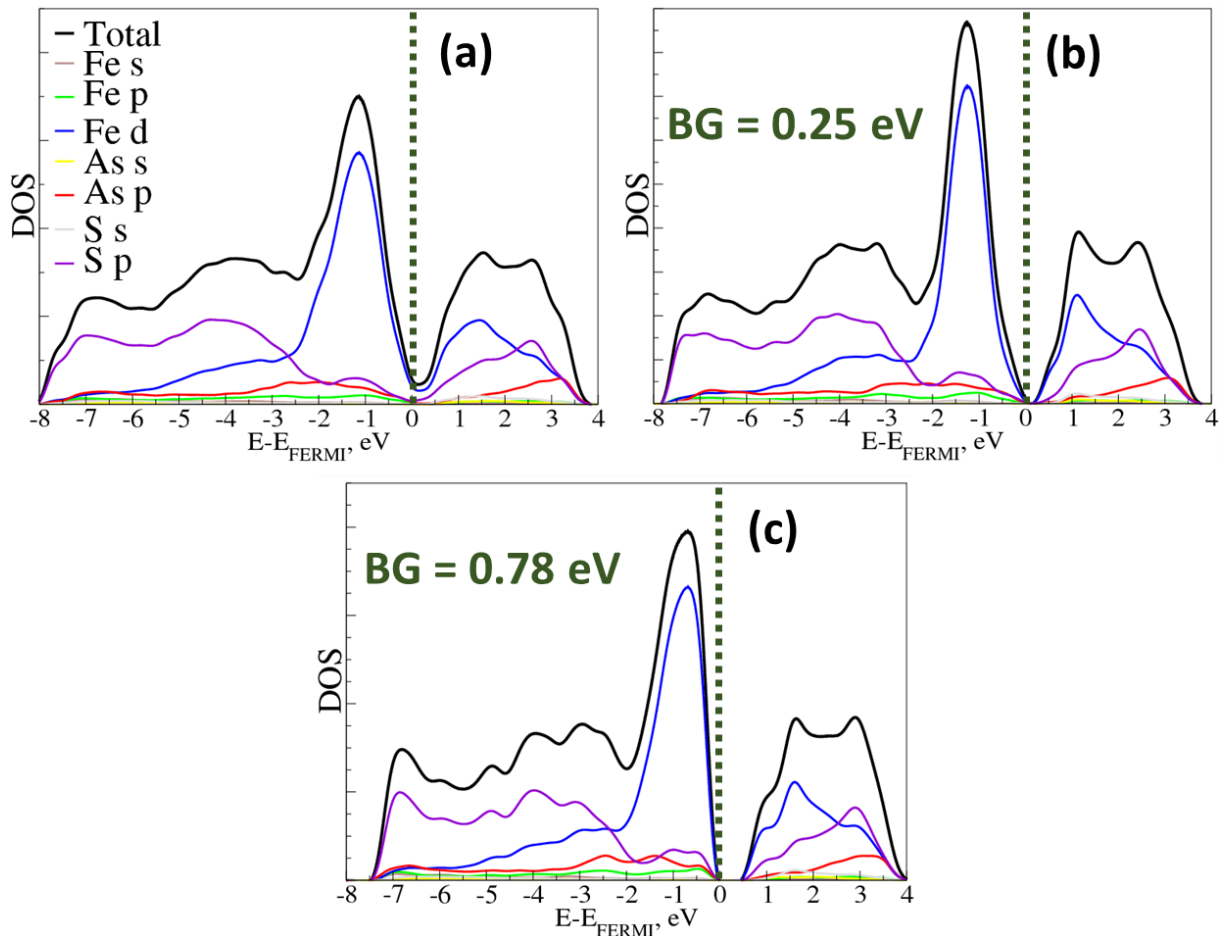


Figure 14- Density of states (DOS) projected for the interface atoms in the range of -8 to 4 eV: (a) is the $FeS_2(100)/FeAsS(001)$ system, (b) the $FeS_2(100)/FeAsS(100)-S$, and (c) the $FeS_2(100)/FeAsS(100)-As$ system. The band gap (BG) was calculated from the band structures shown in Figure A7.

Largest structural differences between the pure minerals and interfaces were found mainly for the Fe- X_{ax} bond distances, see Table A5. The formation of interfaces occurs through the interaction of the pyrite(100) surface with the arsenopyrite (001), (100)-As and (100)-S surfaces. For all of them, the exposed Fe(II) ions are five-fold-coordinated, which enables the surfaces to interact by forming new Fe-X bonds and thus

restoring the 6-fold octahedral structures of the bulk pure minerals. Due to the presence of the arsenic atom in the arsenopyrite structure, the Fe-S bond distances have different magnitudes in the two different interface regions. Moreover, the S-S in pyrite and the As-S bonds in arsenopyrite have different bond lengths and generate distorted octahedral sites, Figure 10, and the axial distances were thus found to be distinct from those of either the pyrite or arsenopyrite bulk.

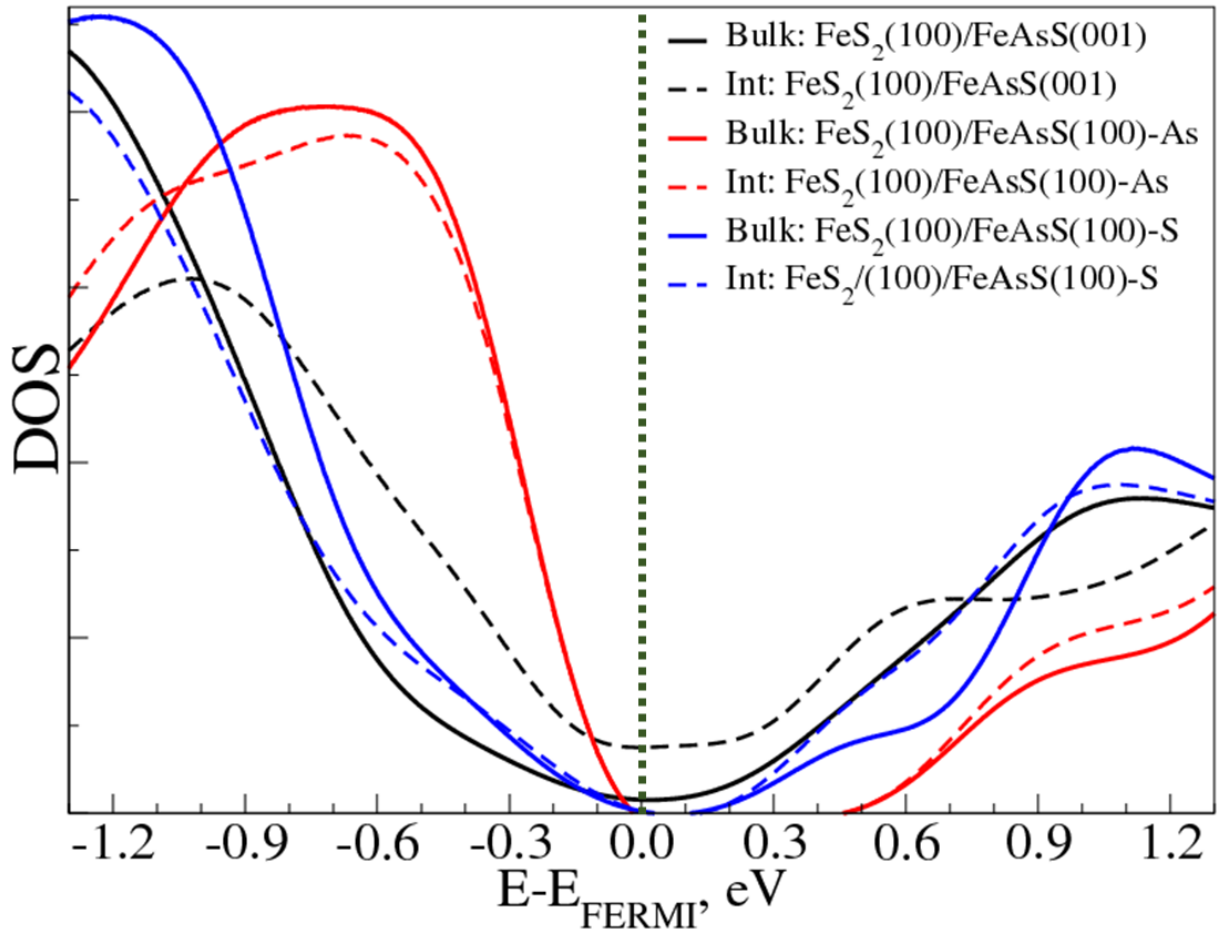


Figure 15- Projected density of states. “Bulk” and “Int” meanings the density of states from the bulk region and interface region, respectively.

Another important point is related to the composition of the arsenopyrite surfaces at the interface, where the atoms present in the first atomic layer vary according to the target surface. Consequently, octahedral sites with different atomic configurations are formed. In the case of the $\text{FeS}_2(100)/\text{FeAsS}(001)$ interface, sulfur and arsenic atoms are present in the first interfacial layer, and $\text{Fe}(\text{As})_3(\text{S})_3$, $\text{Fe}(\text{As})_2(\text{S})_4$, $\text{Fe}(\text{As})_1(\text{S})_5$ and $\text{Fe}(\text{S})_6$ sites are formed. In $\text{FeS}_2(100)/\text{FeAsS}(100)\text{-As}$ only arsenic atoms are exposed in the arsenopyrite region to form the interfacial bonds, hence, the $\text{Fe}(\text{As})_2(\text{S})_4$, $\text{Fe}(\text{As})_1(\text{S})_5$ and $\text{Fe}(\text{S})_6$ sites are formed. Finally, for $\text{FeS}_2(100)/\text{FeAsS}(100)\text{-S}$ only arsenopyrite sulfur

atoms are able to interact with pyrite Fe(II) sites, leading to formation of Fe(As)₂(S)₄, and Fe(S)₆ sites.

For the three interfaces the band gap corresponds mainly to a charge transfer excitation from the filled t_{2g} orbitals of Fe states to e_g^* antibonding states (formed by the hybridization of iron 3d and S and As p states). However, despite the interfaces having similar electronic structure, we find that the contact at the interface changes the density of states around the Fermi level. The interface FeS₂(100)/FeAsS(001) has a metallic behaviour while the other two interfaces are semiconducting with a band gap estimated as 0.25 and 0.78 eV, for the FeS₂(100)/FeAsS(100)-S and FeS₂(100)/FeAsS(100)-As interfaces, respectively (see Figure 14).

The projected density of states for the FeS₂ and FeAsS stoichiometric layers placed in the interface region (Int) and in the bulk region (Bulk) are shown in Figure 15. The PDOS for FeS₂(100)/FeAsS(001) shows that the states in the range of -1.2 to 1.2 eV are dominated by contributions from the interface atoms, and that the interface DOS is mainly responsible for modulating the band gap (BG) of the system. For the FeS₂(100)/FeAsS(100)-As and FeS₂(100)/FeAsS(100)-S interfaces, the density of states in the range of -0.3 to 0.3 eV is the same as in the bulk of the respective system. We would like to emphasize the limitations of DFT methodology for band gap calculations, which normally leads to underestimated BGs. The Hubbard correction used in the electronic structure calculations improves the estimates (Figure 1) in comparison with experiment for the bulk. Including this correction also for the interfaces we find smaller BG values than for the bulk pyrite and arsenopyrite minerals which can be expected to favour electron transport during the oxidation of arsenopyrite in the presence of pyrite.

Interface adhesion and stability

Usually, interface energies computed from theoretical methods are compared in the Young Dupré formalism to experimental measurements of wetting angle, which is the most widely used experimental probe of interface thermodynamics.[130, 131, 147, 149] These experiments consist of investigating the wetting behaviour of molten metal upon a refractory surface at high temperature. Our case differs from wetting thermodynamics by

two ways. First, the Young Dupré equation involves interfaces with a liquid or gas phase molecules that are not relevant to understand the formation of interfaces between sulfides mineral. Second, in wetting investigations, we are looking at the expansion of a liquid upon the surface of a solid substrate at constant matter quantity, whereas in our case, we are interested in the behaviour of the material when different solid phases are involved. In this scope, our strategy is to compare the ideal work adhesion, W_{ad} , between the pyrite and arsenopyrite phases, and the ideal work of self-adhesion of the two individual phases.

The ideal work of adhesion is the energy required to reversibly separate a material into two nonbonded surfaces.[121, 125, 130, 131, 135-137, 140, 141, 147, 149, 156] This property can be estimated by a DFT approach using the difference between the two surfaces (E_A^{DFT} and E_B^{DFT}) and the interface energies (E_{AB}^{DFT}). Ignoring dissipative plastic effects and defects in the structure, the work of adhesion is calculated using the Eq. (3.2), where the energy is calculated per unit area. Attractive interactions between two corresponds to $W_{ad} > 0$, otherwise the value is negative. Generally, the mechanical work needs to separate an interface is larger than the ideal work of adhesion calculated theoretically, thus the calculations presented in this work may be considered lower than any experiment. To the best of our knowledge, there is no work about the pyrite and arsenopyrite interfaces that measured this quantity, thereby in this work we will only discuss the relative values of W_{ad} .

The ideal work of self-adhesion, labelled W_{pyrite} for pyrite and $W_{arsenopyrite}$ for arsenopyrite, can be calculated as the opposite of the surface energy necessary to fracture the bulk along a plane direction to form two identical slabs. As for the work of adhesion, a greater self-adhesion work is related with a strong bonding of bulk along a plane direction.

$$W_{ad} = (E_A^{DFT} + E_B^{DFT} - E_{AB}^{DFT})/2S \quad (3.2)$$

Table 4 shows the work of adhesion and the work of self-adhesion for the three most stable interfaces. As discussed by Martin *et al.*, [141] three different situations might occurs in this analysis: (i) the self-adhesion of the two phases are lower than the work of adhesion, in this case the growth of one phase on top of the other is favoured, as a

consequence, the system will maximize the interfacial area, (ii) the work of self-adhesion of the phases are greater than W_{ad} , and the system will tend to minimize the size of the interface region instead of the surface or bulk grain regions, finally, (iii) the W_{ad} is a value between the surface energies, and the result of the interface growth is ambiguous, and cannot be predicted by only theoretical calculations. In our calculation for the three cases the work of adhesion is more than two times (x2) less than the work of self-adhesion (following the case (ii)). In this manner, we conclude by our calculation that the formation of the interfaces will not be favourable, and it will not maximize area to form a thermodynamic domain with bulk and surfaces.

Table 4: Work of adhesion, W_{ad} , and formation energy for the most stable interfaces. W_{pyrite} and $W_{arsenopyrite}$ meanings the work of self-adhesion for pyrite and arsenopyrite, respectively.

Interface	W_{pyrite} , J.m ⁻²	$W_{arsenopyrite}$, J.m ⁻²	W_{ad} , J.m ⁻²	E_{form} , eV.(formula unit) ⁻¹
FeS ₂ (100)/FeAsS(001)	4.12	3.84	1.63	-2.497
FeS ₂ (100)/FeAsS(100)-As	4.12	4.16	1.47	-2.533
FeS ₂ (100)/FeAsS(100)-S	4.12	4.00	1.70	-2.441

Another means of estimating the stability of the compounds is to calculate the energy of formation, E_{form} , of the compound from the standard state of the elements. E_{form} represents the energy required to form the material from its individual components and it is given by:

$$E_{form} = E_{bulk} - \sum_j x_j \mu_j^* \quad (3.3)$$

where E_{bulk} is the bulk energy per unit formula, x_j is the number of atoms, and μ_j^* is the chemical potential for the j species in standard state. To calculate μ_{Fe}^* it was used the iron BCC unit cell, for μ_{As}^* the grey arsenic rhombohedral cell, and for μ_S^* the S₈ orthorhombic cell (see optimized structures in Figure A8). The results are presented in Table 4, and the values were found to be in the range of -2.441 and -2.533 eV. Comparing the results shown in Table 4 for the interfaces and the results for pyrite and arsenopyrite bulk in Table 2 it is possible to compare the stability of the systems. By the sum of the formation of energy values for pyrite [-1.512 eV.(formula unit)⁻¹] and arsenopyrite [-1.309 eV.(formula unit)⁻¹] it was found the value of -2.821 eV.(formula unit)⁻¹. The last value is greater than the

values found for the interfaces. It means that the two phases are to be found forming two-phase mixture in the nature, and the interface contact formation is thermodynamically unfavourable.

The non-miscibility and adhesion properties of pyrite and arsenopyrite have been discussed in the literature. As a result of the structural differences between pyrite and arsenopyrite in As-rich ore soils and sediments it is generally found pyrite and arsenopyrite mixed forming two distinct phases.[25] In contrast, HRTEM and XAS data[210] for arsenian pyrites with lower arsenic concentrations suggest that the As atoms are in one-phase solid solution system. This result shows how the concentration of arsenic can modify the structure and the grains distribution present in the structure of pyrite and arsenopyrite. However, large arsenopyrite domains are only found in As-rich regions, as expected. Palenik et al.[61] documented a complex matrix for arsenian pyrite in auriferous soils. The heterogeneous nature of the matrix in these samples was described as a polycrystalline mixture of pyrite and arsenopyrite nanodomains of about 20 nm² in size. In addition, high resolution transmission electron microscopy (HRTEM) observations of As-rich arsenian pyrite from natural ore deposits by Fleet et al.[58] and Simon et al.[59, 211] suggested the presence of stacking faults separating alternating pyrite and arsenopyrite structure thin (10–12 Å) lamellae. These HRTEM observations suggest that high As-contents in arsenian pyrite might be related to the presence of nanoscale aggregates of sulfides, with As residing in arsenopyrite domains. As a conclusion, the compiled data showed clearly that pyrite and arsenopyrite surfaces do not present large adhesion, and as predicted by our calculations, this may not happen in a microscopic scale. Also, some works tried to synthesize pyrite and arsenopyrite, and the processes of nucleation follows a small rate, what is consistent with the adhesion estimated in our calculations.

Conclusion

The adhesion, bonding structure, and electronic properties of the pyrite/arsenopyrite interfaces were investigated by a DFT/PBE/plane wave method. It was evaluated the mismatch, ξ , between pyrite(100) surface and the arsenopyrite (001),

(100)-As, (100)-S, (010), (011), (101), (110)-S, (110)-As, (111), (210)-1, and (210)-2 surfaces. Only the arsenopyrite (001), (100)-As and (100)-S presented ξ values suitable to form stable interfaces with pyrite(100) surface. From the selected surface planes, the $\text{FeS}_2(100)/\text{FeAsS}(001)$, $\text{FeS}_2(100)/\text{FeAsS}(100)\text{-As}$, and $\text{FeS}_2(100)/\text{FeAsS}(100)\text{-S}$ were built and studied. The geometry optimization showed that the bond distances between the interfaces have large values in accordance with that observed for the two separate phases, and largest deviations were found in the interface region. As pyrite and arsenopyrite have different bond distances and lattice parameters, it is not possible to perfect match the phases, and distorted octahedron sites are formed in the interfacial region. This structural observation agrees with the work of adhesion and the formation energy analysis, where it was found that the contact phases at the molecular level are thermodynamically unfavourable. And, the formation of the interface in nature would be an unstable product, and possibly its formation would occur due to kinetic effects in the formation of two minerals when they are associated in nature. These results are consistent with the low miscibility between the two phases, which is observed experimentally.

The ELF and PDOS calculations for the interfaces compared with results reported previously for the pyrite and arsenopyrite bulk show that the electronic structure at the interfaces exhibits similarities to that of the pyrite and arsenopyrite bulk. However, even with the similarities, the band gaps ($t_{2g} \rightarrow e_g$ transition) of the pyrite/arsenopyrite interfaces are small (or metallic) and the atoms present in the interface region dominate the density of states at the Fermi level. The decrease in the band gap of the electron transference process is facilitated, which would facilitate the process of oxidation of these minerals in nature. Leading to increased release of pollutants in the environment.

Chapter 4 – Pyrite/arsenopyrite interface local reactivity

Preamble: From the interfaces studied in Chapter 3, it was evaluated the influence of the interface in the local reactivity of pyrite and arsenopyrite phases. Different surfaces were calculated along the perpendicular and parallel cleavage planes (details in Figure 17) of the three most stable interfaces: $\text{FeS}_2(100)/\text{FeAsS}(001)$, $\text{FeS}_2(100)/\text{FeAsS}(100)\text{-As}$ and $\text{FeS}_2(100)/\text{FeAsS}(100)\text{-S}$. All the cleavage energies calculated for the relaxed interfaces were found very close to the cleavage values obtained for pyrite and arsenopyrite pure phases. We also tested the chemical reactivity of the interfaces studying the adsorption of water in the different surfaces. For all systems, the values of adsorption energies were found to be the same of the obtained for pyrite and arsenopyrite exposed surfaces without solid-solid contact between the phases. The results for cleavage energy and water adsorption energy suggest that the local reactivity of the pyrite and arsenopyrite are not largely affected by the formation of the interface. This observation is in agreement with the electron charge difference calculations shown in this Chapter, where it was found that negligible electronic transference occurs at the interface point. Furthermore, the charge difference analysis also suggests that the charge transfer mechanism does not change the bulk characteristic in the vicinities of the interface region.

Introduction

The formation of the interface may affect the local properties of the materials. Mainly, two effects can change the chemical characteristics of a certain interface at molecular level. The first is the formation of new chemical bonds in the interface region. At the interface, the new bonds change the energy level profile of A/B solid-solid junction with respect to the pure A and B phases. Furthermore, the interfaces will invariably lead to the stress in the bonds and lattice parameters. This effect was studied in Chapter 3, where it is observed that the bonds present at the interface are at higher energy level (thus less stable) than the bulk chemical bonds. In addition, the work of adhesion found for the pyrite/arsenopyrite indicates that there is no additional stability generated by the interaction between the phases.

The second effect is that the greater is the structural and electronic difference between A and B phases, the greater is the change of the electronic density induced by the interface formation. This factor may even influence the electronics of the two phases by a charge transfer mechanism, where the electron-deficient phase receives electron density from the interface. This mechanism is very important to stabilize the interface.

This Chapter aims to study the changes of the electron density of the most stable pyrite/arsenopyrite interfaces with respect to the pure phases. It was evaluated the effect of this change to the local properties of these materials. Surface energy and water adsorption energy were used to evaluate the local chemical properties.

Methodology details and nomenclature of the systems

The electronic structure of the system was calculated using the DFT/plane waves methodology performed using the PBE XC functional. It has been shown that the PBE XC functional is capable to describe the structure and the electronic properties of sulfide minerals.[63, 104, 169, 170, 185] The cutoff radius energy was set to 50 Ry. K-points meshes were automatically generated by the Quantum-Espresso software, and[162] we used a Γ -centered 4x4x2 grid for all the systems. Except for the charge density difference calculations (see Figure 18 and Eq. (4.1)) we used a 10x10x6 k-point grid to obtain a better description of the electronic density of the system. A Fermi-Dirac Gaussian smearing of 0.02 eV was used for all systems. All the calculation parameters were tested and the results are shown in appendices A-D. Spin polarization were considered in all calculation, and the results reported in this work correspond to the most stable spin state of each structure. Spin trials were done, and the results are shown in the appendices G-I.

For the sake of clarity and avoid misunderstanding, a nomenclature was employed for the structures that we are studying and comparing in this Chapter (Chapter 4). This Chapter aims to compare the results obtained with the pyrite and arsenopyrite surfaces with the ones obtained with the interface (I-BULK) and after its cleavage (I-SLABs). The “surface” nomenclature will be used when it is directly obtained from the cleavage of pyrite or arsenopyrite, as can be seen in Figure 16. From the combination of these two surfaces as shown in Figure 9, the pyrite/arsenopyrite interface was built (see Chapter 3

for a better explanation). The pyrite/arsenopyrite interfaces will be called I-BULKs (interface bulks). From the cleavage along a specific crystallographic plan of the I-BULKs, it was generated the I-SLABs (interface slabs). The cleavage planes used to obtain the I-SLABs from the I-BULKs are show in Figure 17.

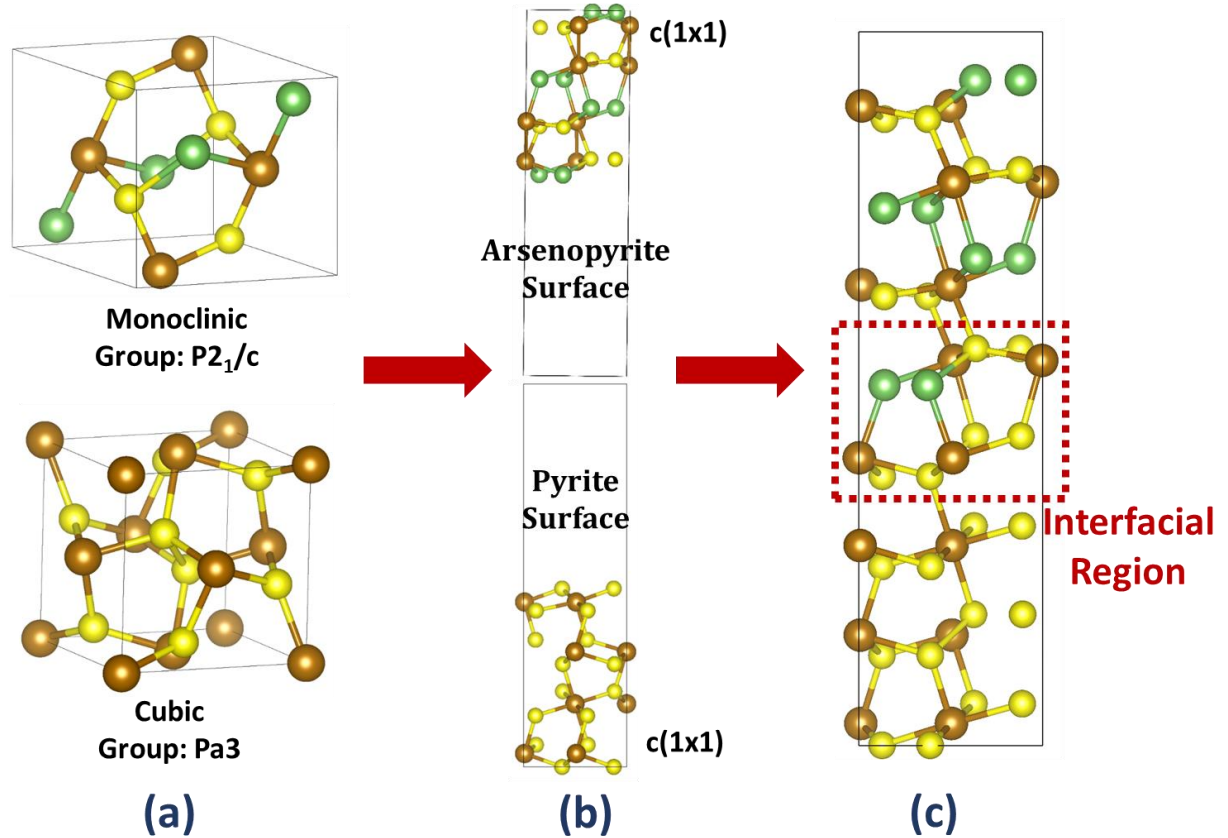


Figure 16- Nomenclature used in the present Chapter for (a) pyrite and arsenopyrite crystal bulk, (b) pyrite and arsenopyrite surface, (c) interface bulk (I-BULKs).

A special attention was given to the spin polarization of the systems to obtain better description for the total energy of the I-SLABs. Pyrite (100) surface is well-known to be a spin compensated system, however, to the best of our knowledge, there is no information reported in the literature for the arsenopyrite surfaces.[119, 176, 195] Therefore, we evaluated the spin test for the (001), (100)-As and (100)-S arsenopyrite surfaces (see Table A6, Table A7, and Table A8). It was considered the ferromagnetic, antiferromagnetic and spin compensated systems, and for all of the arsenopyrite slab surfaces the total magnetization of the system was found to be equal to zero. In contrast to the non-spin-polarized surface found for pyrite, our calculations indicate an antiferromagnetic spin configuration for the three arsenopyrite surfaces. Hence, we set

the spin states equals to zero for all atoms located in the pyrite phase, and we set an antiferromagnetic spin configuration for the atoms present in the arsenopyrite phase.

I-SLABs construction starting from the I-BULKs

It was calculated the fracture of the three interface structures considering the cleavage planes shown in the Figure 17. To define the best cleavage planes to be analyzed for the interfaces, we first identified the most stable cleavage planes in pyrite and arsenopyrite accordingly to the literature.[119, 177, 185, 188, 191, 194, 195, 212] Due to the structural similarities of pyrite/arsenopyrite interface with the arsenopyrite and pyrite pure phases, it is expected that pyrite/arsenopyrite surfaces present the same behaviour of the isolated surface. It is observed that both pyrite and arsenopyrite most stable cleavages occur by Fe-S and/or Fe-As bond breaking to form the surface. Hence, the S_2^{2-} and AsS_2^{2-} dimers remains intact on the surface. As discussed by Stirling *et al.*,[191], this cleavage process maintains the charge neutrality in the pyrite surfaces, minimizing the total energy of the system. Recently, the same characteristic was identified for arsenopyrite surfaces.[119]

For the interface atomistic calculations, it was used the same structures depicted in Figure 10. The three most stable interface-bulk systems [$FeS_2(100)/FeAsS(001)$, $FeS_2(100)/FeAsS(100)-As$ and $FeS_2(100)/FeAsS(100)-S$] are composed by four FeS_2 layers in the pyrite region and four $FeAsS$ layers in the arsenopyrite region, forming two equivalent interface regions in the same model. From the optimized interface bulk systems, we built the surface models (which will be called in this Chapter as I-SLABs, see Figure 17). In the I-SLABS, all atomic layers were placed in the xy-plane with periodic boundary conditions, and a vacuum space of 12 Å was used along z-axis to avoid the interaction between the slab and its periodic images along z-directions. All the simulated I-SLABS were built keeping the symmetric arrange of the atoms present in pyrite and arsenopyrite pure phases, thus no resultant dipole or charge accumulation regions are present in the structure.

No defects were simulated in this work, thus all the results here presented have to be considered for an ideal terminated surface. There is no experimental or theoretical

report in the literature about the fracture point occurring on the pyrite/arsenopyrite solid-solid junctions in nature. Then, all might be useful to give insights about this issue, providing a chemical picture of the pyrite/arsenopyrite interface local reactivity at molecular level. The same procedure has been used for pyrite and arsenopyrite studies,[119, 177, 185, 188, 191, 194, 195, 212] where stoichiometric surfaces have been used to understand more about pyrite and arsenopyrite pure minerals.

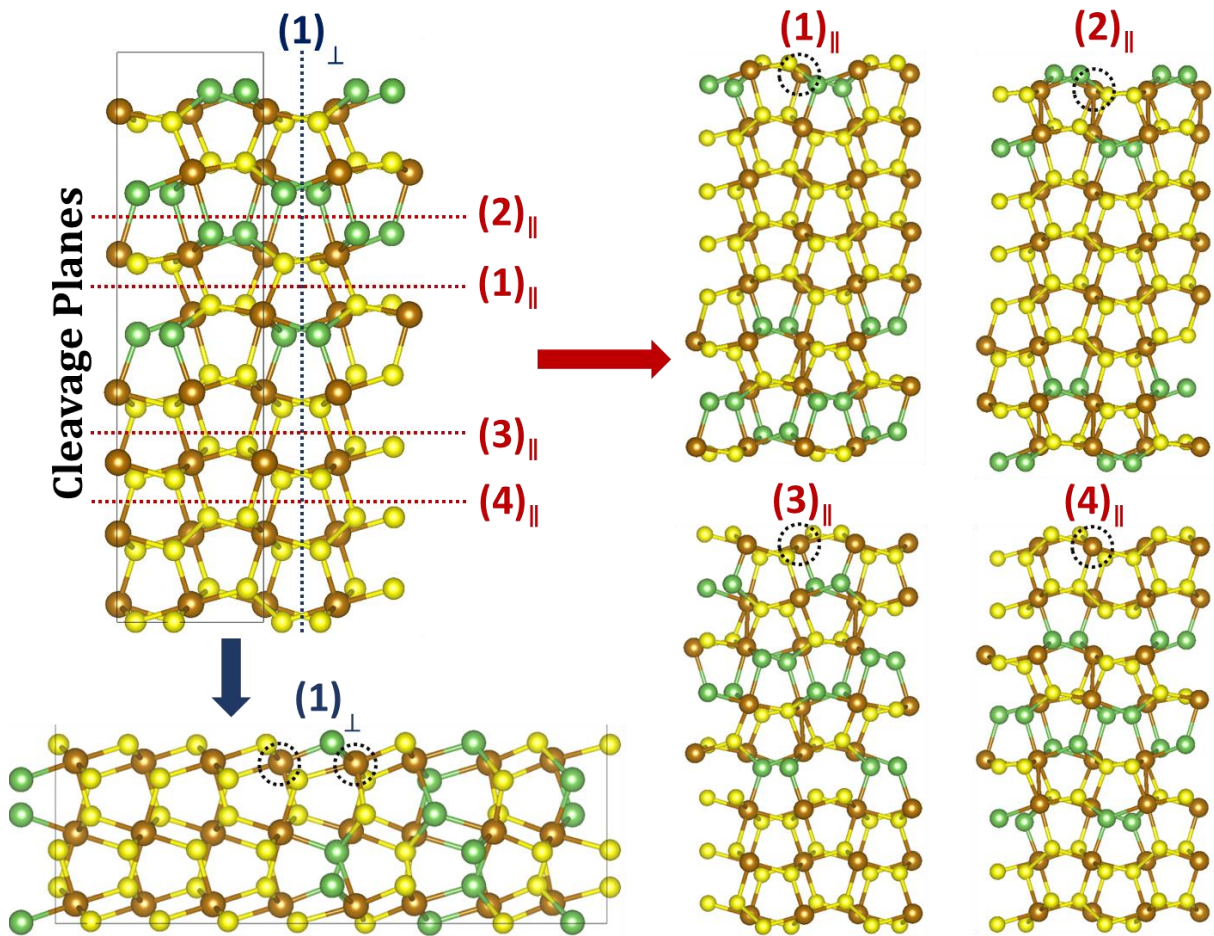


Figure 17- I-SLABs obtained from the I-BULKs. The blue dot lines represent the cleavage plane perpendicular $[(1)_{\perp}]$ to the interface, and the red dot lines the four parallel cleavage planes close to the interface region $[(1)_{\parallel}, (2)_{\parallel}, (3)_{\parallel}, \text{ and } (4)_{\parallel}]$. The red, yellow and green spheres represent the iron, sulfur and arsenic atoms in the structures above. The dotted circles show the iron sites that were used to adsorb water molecules.

The orientation of the structures and the number of layers must be considered to build the perpendicular structure of the I-SLABs. First, looking only to pyrite region in the three interfaces, the xz and yz-planes in the structures corresponding to the (100) and (010) cleavages in the pure pyrite bulk. Since the (100), (010) and (001) pyrite cleavage

planes are by symmetry equivalent, we may consider that in the interface both cleavages are equivalent. However, the (100), (010) and (010) arsenopyrite planes are not equivalent and, as a consequence, in the interface these cleavage directions are also not equivalent. For $\text{FeS}_2(100)/\text{FeAsS}(100)\text{-As}$ and $\text{FeS}_2(100)/\text{FeAsS}(100)\text{-S}$, the interfacial plane direction is the (100) from the arsenopyrite side, and so the other directions must be (010) and (001). We observed that in the (010) direction, for the three interface systems no cleavage plane occurs maintaining the As-S and S-S bonds, see Figure A9 in the appendix of this thesis.

The perpendicular cleavage planes were built using nine atomic layers, see Figure 17. It has been shown for pyrite[177, 185, 188, 191, 192] and arsenopyrite[119, 176] that a slab with small number of layers is capable to describe the structure and chemical reaction of the surfaces. These results showed clearly that the cleavage in pyrite and arsenopyrite only occurs very close to the interface, and we already think that an I-SLAB with just a few atomic layers (9 layers) might be proposed and will describe the cleavage energy value.

Particularly for pyrite, by photoelectron spectroscopy, Eggleston *et al.*[213] measure the pyrite surface thickness, and it was found to be a few atomic layers around the pyrite surface plane. Theoretically, Santos *et al.*[185] described the pyrite (100) surface chemical properties using a slab with 6 layer thickness, and the authors reproduced in good agreement with the results evaluated by Sit *et al.*[63] using a 12-layered surface.

Pyrite/arsenopyrite I-Bulks electronic reconstruction

When an interface is formed between two phases, charge transfer from bulk regions to the interface may occur.[161] This electronic mechanism is very important to stabilize the interface region. However, the magnitude of the charge transfer may cause charge deficiency in the bulk region near the interface weakening the bond strength. This charge transference process is very important to understand how the failure process occurs around an interface formation. As discussed by Liu *et al.*[180] and by Qi *et al.*,[214] there are three ways of the structure failure for a heterogeneous interface system. If the

interface is not well adhered, the failure point will be at the interface region. For an over-adhered interface, the failure point is at a few Ångstrom distance from the interface and happens in the softer phase. If the phases are perfectly adhered, the failure point will occur inside the softer phase, in the bulk region far away from the interface. In the case of a homogeneous interface, the cleavage point should be at the interface region, consequently, in homogeneous situations the formation of the interface is not favoured, if compared with the formation of a surface region. On this sense, the analysis of the fracture is essential for a comprehensive evaluation of the stability and cohesion of an interface system.

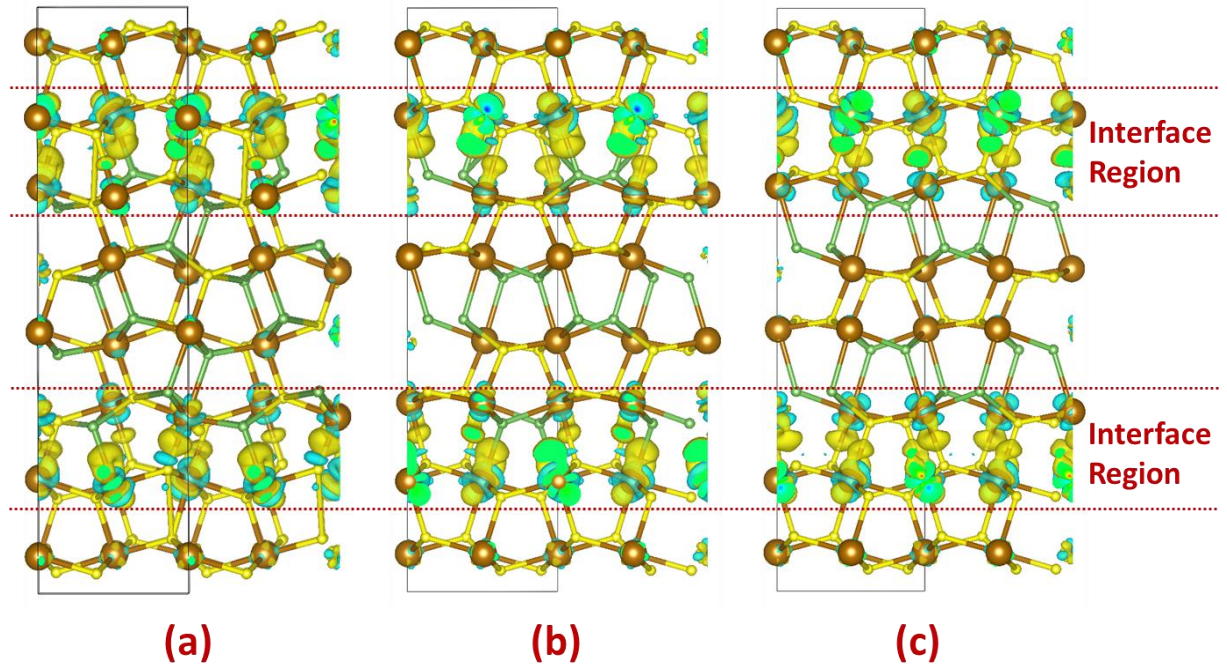


Figure 18- Structure and Charge density difference, $\Delta\rho$, for the interfaces. (a) is the $\text{FeS}_2(100)/\text{FeAsS}(001)$ interface, (b) the $\text{FeS}_2(100)/\text{FeAsS}(100)\text{-As}$ interface, and (c) the $\text{FeS}_2(100)/\text{FeAsS}(100)\text{-S}$ interface. Isosurfaces are shown for $0.01 \text{ e}/\text{\AA}^3$. Red, yellow, and green spheres represent, respectively, the Fe, S, and As atoms.

The electronic reconstruction over the interfaces were evaluated by the charge difference analyses, $\Delta\rho$, which is given by the Eq. (4.1), where $\rho_{\text{FeS}_2/\text{FeAsS}}$ is the density of the interface, and ρ_{FeS_2} and ρ_{FeAsS} are, respectively, the density of the pyrite and arsenopyrite phases.

$$\Delta\rho = \rho_{\text{FeS}_2/\text{FeAsS}} - \rho_{\text{FeS}_2} - \rho_{\text{FeAsS}} \quad (4.1)$$

The three interface systems share common features. As shown in Figure 18, the electron redistribution is rather localized in the interface region, it reveals only an electron density accumulation at the interface. The electronic influence on the electronic structure of FeS₂ and FeAsS is confined within the first three atomic layers of both phases (which is equivalent to a FeS₂-layer and FeAsS-layer in the pyrite and arsenopyrite side region). The charge density difference in the bulk region of the interface model shows no evidence of charge redistribution or a reconstruction occurs at the interface. In all the systems, the charge difference is concentrated in the directions of the Fe-S and Fe-As new bonds formed in the interface region.

Pyrite/arsenopyrite I-SLABs cleavage plane energies

The surface energy, γ , for the different cleavage planes and atomic terminations were calculated by the Eq. (4.2), where $E^{I-SLAB}(n)$ is the I-SLAB energy as function of the n layers, and E^{I-BULK} is the bulk energy per layer. Since in a cleavage process, the energy depends on the dimensions of the material, the area, S , should be considered in the calculation. In the calculations, we relaxed the two surfaces, then a $\frac{1}{2}$ was considered in the calculations. Considering that the interface free energy might be approximated by the value of the total energy, E , which is in the most cases a good approximation. The γ parameters measures the thermodynamic stability of the interface relative to the starting bulk (in this case the I-BULK), and a positive value indicates a stable surface. As a cleavage process involves always bond breaking, it is not expected negative values for γ .

$$\gamma = \frac{1}{2S} [E^{I-SLAB}(n) - nE^{I-BULK}] \quad (4.2)$$

The cleavage energies are summarized in Table 5. After full optimization of the I-SLABs, the cleavage values calculated were found around 0.94 and 1.01 J.m⁻². The obtained values are comparable with the cleavage energies for the pyrite and arsenopyrite cleavage energies (1.03 J.m⁻² for FeS₂(100); 0.96 J.m⁻² for FeAsS(001); 1.04 J.m⁻² for FeAsS(100)-As; and 1.00 J.m⁻² for FeAsS(100)-S).

Table 5- Surface energy calculated for the different cleavage planes shown in Figure 17.

I-SLAB	Cleavage Planes	γ , J.m ⁻²	ΔE_{ads} , kcal.mol ⁻¹ (eV)
FeS ₂ (100)/FeAsS(001)	(1) _⊥	0.99	FeS ₂ site: -14.5 (-0.63) FeAsS site: -14.9 (-0.65)
	(1) _∥	0.85	-12.1 (-0.52)
	(2) _∥	0.92	-13.9 (-0.60)
	(3) _∥	0.75	-12.8 (-0.55)
	(4) _∥	0.94	-13.3 (-0.58)
FeS ₂ (100)/FeAsS(100)-As	(1) _⊥	1.01	FeS ₂ site= -14.6 (-0.63) FeAsS site= -15.6 (-0.68)
	(1) _∥	0.84	-13.9 (-0.60)
	(2) _∥	1.03	-13.2 (-0.57)
	(3) _∥	0.80	-13.0 (-0.56)
	(4) _∥	0.92	-13.2 (-0.57)
FeS ₂ (100)/FeAsS(100)-S	(1) _⊥	0.94	FeS ₂ site: -14.4 (-0.62) FeAsS site: -16.2 (-0.70)
	(1) _∥	0.99	-13.1 (-0.57)
	(2) _∥	0.92	-13.3 (-0.58)
	(3) _∥	0.93	-12.9 (-0.56)
	(4) _∥	0.95	-13.0 (-0.56)

Pyrite/arsenopyrite I-SLABS chemical reactivity in the presence of water

It was evaluated the chemical reactivity of the I-SLABs by the water adsorption on the Fe(II) adsorption site present on the I-SLABs surfaces. All the results are shown in Table 5 and the optimized structures are illustrated in Figure 19. The adsorption energy, ΔE_{ads} , was calculated by the following equation:

$$\Delta E_{ads} = E_{I-SLAB+water} - E_{surf} - E_{water}, \quad (4.3)$$

where $E_{I-SLAB+water}$ is the total energy of the surface with one water molecularly adsorbed, E_{surf} the total energy of the bare surface, and E_{water} the water energy using the same theoretical level.

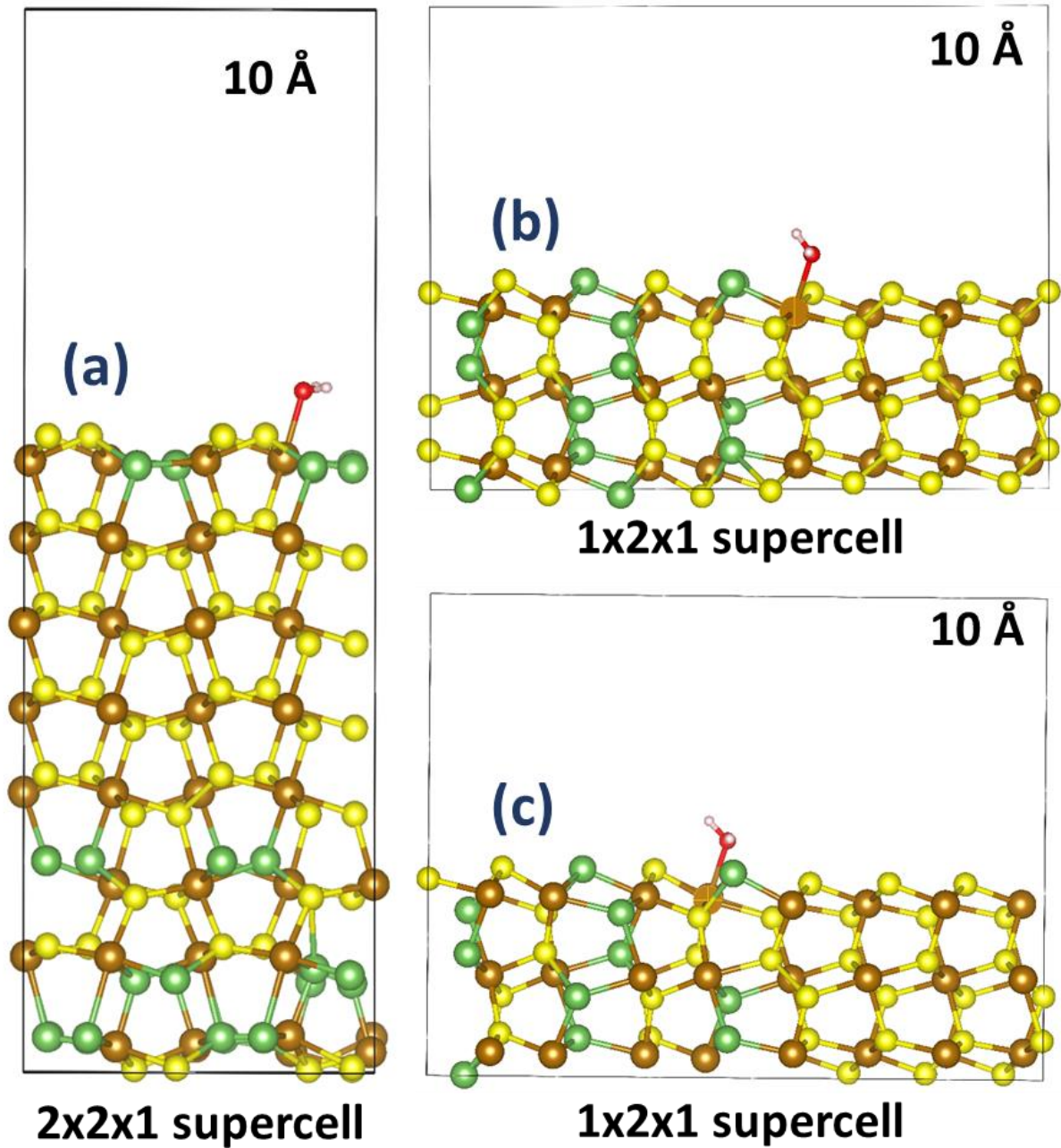


Figure 19- Water adsorption on the “FeS₂(100)/FeAsS(100)-As” I-SLABs. (a) adsorption on the parallel I-SLAB model, (b) adsorption on the perpendicular I-SLAB with the water located in the pyrite side, and (c) water adsorption on the perpendicular I-SLAB with the water located in the pyrite side.

Comparing the adsorption values for all I-SLAB models evaluated in this Chapter, there is no large variation among the adsorption energies values. As can be seen in Table 5, the values were found in the range of -12.1 to -16.2 kcal.mol⁻¹. The major differences were found when comparing the adsorptions for the (||)I-SLABs and (⊥)I-SLABs, and difference for ΔE_{ads} were found around 3.1 kcal.mol⁻¹. However, as discussed by Sit *et*

al.[63] and Stirling *et al.*,[191] such a difference can be considered within the expected errors of DFT calculations. As a consequence, it is not possible to differentiate the systems by their ΔE_{ads} values.

We also compare the obtained values in Table 5 with the ΔE_{ads} values found in the literature for pyrite and arsenopyrite surfaces. For pyrite (100) surface, DFT calculation with different XC functional found the adsorption energies between -12 and -16 kcal.mol⁻¹. [63, 64, 184, 191] Temperature-programmed experiments, on other hand, provided an estimate values of the water adsorption energy of -10 kcal.mol⁻¹. [13] For arsenopyrite, the DFT estimated water adsorption energy is equal to -10.8 kcal.mol⁻¹. [64] The ΔE_{ads} values indicate that the interface formation do not affects the local reactivity of both phases.

Final observations

The local properties of the I-SLABs were studied considering the surface energy, γ , and water adsorption energy, ΔE_{ads} . Some cleavage models for the I-SLABs were constructed from the three most stable I-BULKs: FeS₂(100)/FeAsS(001), FeS₂(100)/FeAsS(100)-As and FeS₂(100)/FeAsS(100)-S. In the I-SLABs construction the (\parallel) [sited parallel to the xy-plane] and (\perp) [sited perpendicular to the xy-plane] was taken into account. Among all the evaluated systems the γ energy values were found between the γ values of the pyrite (100) surface of the arsenopyrite (001), (100)-As and (100)-S surfaces. Thus, the direct contact between the two phases does not destabilize the system due to a directional charge transfer process. This result collaborates with the calculations of electronic charge difference, $\Delta\rho$, where it was found that the electronic reconstruction occurred more significantly near the interfacial region (mostly concentrated in the first FeS₂-layer of the pyrite phase and the first FeAsS-layer of the arsenopyrite phase).

Local reactivity of the I-SLABs was also evaluated from the adsorption of water at the Fe(II) sites present on the surface of these systems. As shown by comparing the values collected for the I-SLABs and the values obtained for the pyrite and arsenopyrite surfaces, the values found are within the errors estimated for DFT calculations. This suggests that all sites of all I-SLABs are equivalent when compared to water adsorption. This result

collaborates with the structural and electron localization analyses made in Chapter 3. After the total optimization of the I-BULKs, it was observed that their structural values did not exceed a maximum of 4% when compared to the pyrite and arsenopyrite pure phases.

Chapter 5 – Pyrite/Arsenopyrite interface band offset

Preamble: The electronic behaviour of the FeS₂/FeAsS interfaces was studied by means of DFT/PBE method. The FeS₂(100), FeAsS(001), FeAsS(100)-As and FeAsS(100)-S surfaces were used to construct the FeS₂(100)/FeAsS (001), FeS₂(100)/FeAsS (100)-As, and FeS₂(100)/FeAsS(100)-S interfaces. From these interfaces, the band offset values were calculated. In this calculation, it is possible to predict which of the two phases (pyrite or arsenopyrite) holds more for the valence band and which of these contributes to the conduction band. The valence band is composed by pyrite electronic states, and the conduction band by arsenopyrite electronic states. Our results suggest that pyrite/arsenopyrite form a p-n heterojunction and the electron transfer occurs in the “arsenopyrite → pyrite” direction. In addition, it was observed that the interface formation decreases the band gap value of the system, which facilitates the electron transfer.

FeS₂/FeAsS interface construction

To build the interface models it was used the interface coherent models, which has been previously successfully used to describe the electronic properties of different interface materials.[121, 123, 129, 143, 146, 152, 156] Considering the case of pyrite/arsenopyrite solid phases in contact, four steps were performed in order to build the interface coherent atomistic model. The First step is to define the interface plane between pyrite and arsenopyrite to determine the stacking direction (in this work the stacking direction was set along the z-axis direction). In the second step, the commensurability of the phases was evaluated in order to build a 2D periodic interface model. The third step consist in cleavage both pyrite and arsenopyrite surfaces that in contact will form the target interface. During this step, the last atomic layer on the structure depend on the chemical composition of the system, and it is possible to have more than one interface for the same considered contact plane direction. For example, there are two different cleavage for arsenopyrite along its (100) crystallographic plane, exposing the As atoms, (100)-As, and the S atoms, (100)-S, in the outlayer. In the fourth

and last step, the interface was built by bringing together the two pyrite and arsenopyrite phase, as can be seen in Figure 20.

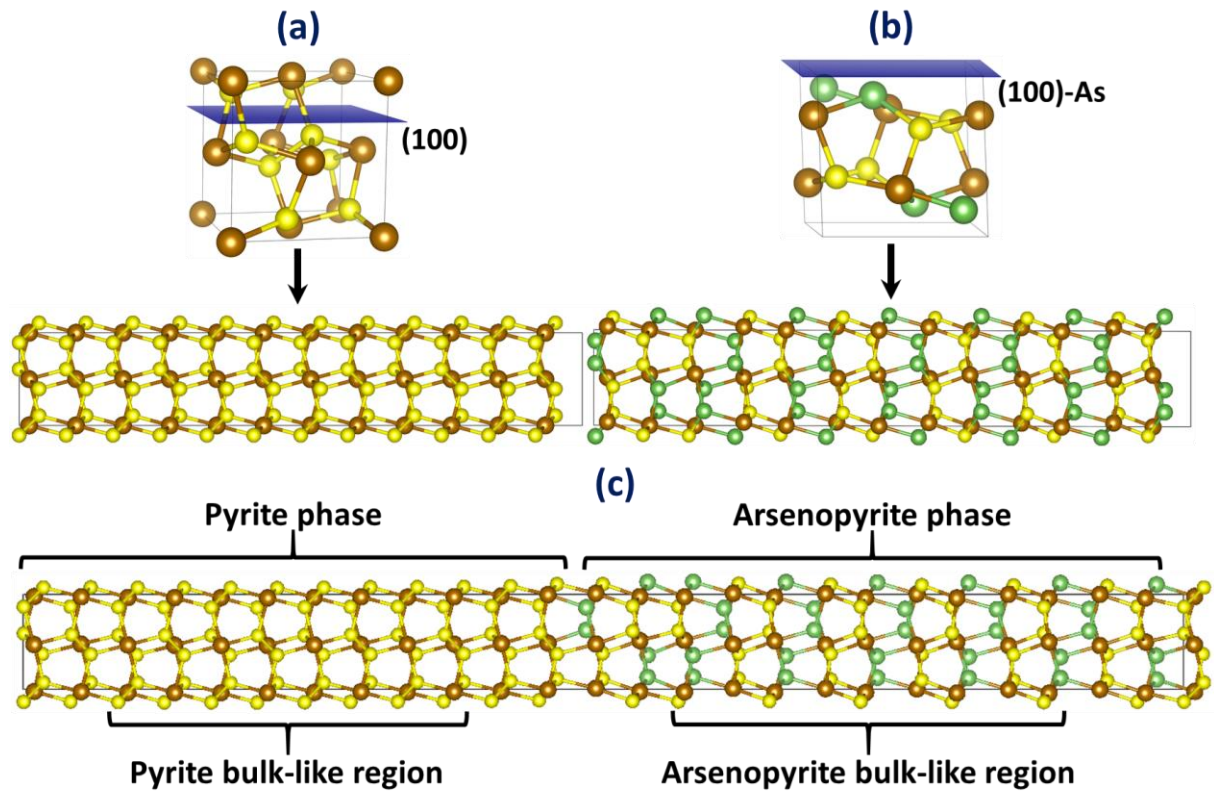


Figure 20- Interface model construction. (a) is the $\text{FeS}_2(100)$ pyrite bulk, (b) the $\text{FeAsS}(100)\text{-As}$ arsenopyrite bulk, and (c) the $\text{FeS}_2(100)/\text{FeAsS}(100)\text{-As}$ interface. The $\text{FeS}_2(100)/\text{FeAsS}(001)$ and $\text{FeS}_2(100)/\text{FeAsS}(100)\text{-As}$ constructions are shown in Figure A12 and Figure 16, respectively.

The commensurability of the phases

To build realistic models it was considered the most expressive surfaces of pyrite and arsenopyrite. Pyrite is the ubiquitous sulfide minerals in Earth, and its (100) cleavage are the surface with major occurrence in nature.[13] Thus, this surface was chosen to form interface with the arsenopyrite phase. Regarding to arsenopyrite surface, in nature it does not present a preferential cleavage, and at least twelve cleavage planes can be formed in its cleavage process.[119, 176, 195] Silva et al.[119] studied in detail all the possible surfaces involved in arsenopyrite cleavage. Among all of them, the (001), (100)-As, (100)-S, (010), (011), (101), (110)-As, (110)-S, (111), (210)-1 and (210)-2 exhibits

lower surface free energies, and can be suggested as a potential occurring surface in nature. Furthermore, Silva et al.[119] observed that all surfaces are very close in energy, been the energies no larger than 0.73 J/m² Considering all of those surfaces, in our previous paper[62] (Chapter 3) it was evaluated the commensurability of the pyrite and arsenopyrite surfaces along different crystallographic directions of pyrite and arsenopyrite. From all the evaluated structures, it was found that only the FeS₂(100)/FeAsS(001), FeS₂(100)/FeAsS(100)-As, and FeS₂(100)/FeAsS(100)-S are capable to match and form interfaces.

Interface model

The interfaces were built by the direct contact of pyrite and arsenopyrite bulk phases. In this work, all the surfaces are symmetric, thus, two identical interfaces appear in each model, see Figure 20c. The FeS₂/FeAsS interface models contain several layers of each pyrite and arsenopyrite phases. In the FeS₂(100) phase-side, 12 FeS₂ bulk-like stoichiometric layer were chosen. For arsenopyrite, different phases sizes were chosen accordingly to the three most stable interfaces studied in this work. The number of FeAsS-layers used for FeAsS(001), FeAsS(100)-As, FeAsS(100)-S were, respectively, 16, 13 and 13. Consequently, FeS₂(100)/FeAsS(001), FeS₂(100)/FeAsS(100)-As, and FeS₂(100)/FeAsS(100)-S totally have 28, 25 and 25 stoichiometric layers. The distance between two interfaces regions was greater than 34 Å. In order to avoid non-physical interactions between the interfaces and to preserve bulk properties in the inner layers. All the models were constructed maintaining the symmetry of the pyrite and arsenopyrite phases regarding to its unit-cell center. As discussed by Martin *et al.*[141] it is essential to avoid long-range dipole-dipole interactions.

All interfaces were built starting from pyrite and arsenopyrite bulk phases as shown in Figure 20a and b. The unit cell used to start the pyrite bulk calculations was obtained by Brostigen and Kjekshus crystallographic refinement data.[173] At room temperature, pyrite crystalizes in a face-centered cubic system (space group Pa3). The lattice parameter was determined experimentally to be 5.418 Å, and the Fe-S and S-S chemical bond lengths 2.262 and 2.177 Å, respectively. Arsenopyrite exhibits a

monoclinic cell with $P2_1/c$ space group. Its cell parameters were determined by Bindi *et al.*, [174] being: $a = 5.761 \text{ \AA}$, $b = 5.684 \text{ \AA}$, $c = 5.767 \text{ \AA}$, $\beta = 111.72^\circ$, and $\alpha = \gamma = 90.00^\circ$.

Computational details

Total energy calculations were performed by means of the Density Functional Theory (DFT), and the generalized gradient approximation (GGA) developed by Perdew-Burke-Ernzerhof (PBE) was employed. For all calculations, it was used a plane wave basis set up to kinetic energy of 40 Ry (or 544 eV). The DFT/PBE/plane waves method has been extensively tested in previously publications, and it is capable to describe electronic and structural properties of sulfide minerals [63, 104, 119, 185, 191] and interfaces. [121, 123, 129, 131, 133, 141, 143, 159] Brillouin zone integration was performed using the method of Monkhorst and Pack, and the energies were converged with respect to the k -point density of $3 \times 3 \times 2$ generated automatically in Quantum-Espresso package. [162] A 0.05 eV Fermi-Dirac smearing of the occupations number around the Fermi level was used to improve convergence in the self-consistent procedure. Spin-polarization was taken into account for all calculations. Norm-conserving pseudopotential with: Fe ($3s^2 3p^6 4s^2 3d^6 4p^0$), S ($3s^2 3p^4 3d^0$), and As ($4s^2 4p^3 4d^0$) valence electron configuration were used. To account for the energy of localized “d” orbitals properly, it was used the DFT+U approach with the invariant Hubbard correction (U-J) proposed by Dudarev *et al.* [96] For all interfaces it was used (U-J) equals to 1.5 eV. Test calculations were performed (see Appendix N) and the results showed that the theoretical level employed in this work is capable to describe the electronic structure of pyrite and arsenopyrite isolated bulk phases.

As discussed by Wang and Smith, [151] to obtain good results on the properties induced by the formation of a solid-solid interface, it is crucial to optimize the atomic geometry of the system. This procedure minimizes the mismatch strain over the interface region. Based on this, geometry optimization was performed for all the interfaces. Geometry optimizations were carried out using the Damped dynamics method [164] in the Parrinello-Rahman extended Lagrangian formulation, [165] and the forces on the ions were converged to within 10^{-3} Ry/Bohr. Finally, from the full optimized structures a single

point calculation was made in the \mathbf{k} -points mesh density of 6x6x4 to obtain the band structure of all interface compounds. From the obtained band structures, the valence band maximum (VBM), conduction band minimum (CBM), and band gap (BG= CBM - VMB) values were estimated.

The band offset calculation approach

One of the most important quantities that characterize a semiconductor-semiconductor interface is the band offset, which is the relative position of the energy levels on both sides of the interface. From the structures shown in Figure 20, it was possible to calculate the natural band offset (BO) for the three interfaces. The BO value is given by:

$$\Delta E_v(\text{FeS}_2/\text{FeAsS}) = \Delta E_{v,\phi'}(\text{FeS}_2) - \Delta E_{v,\phi}(\text{FeAsS}) + \Delta E_{\phi,\phi'}(\text{FeS}_2/\text{FeAsS}) \quad (5.1)$$

where $\Delta E_{v,\phi'}(\text{FeS}_2)$ and $\Delta E_{v,\phi}(\text{FeAsS})$ are the differences between the valence-band maximum energy and the electrostatic potential average for, one-to-one, the pyrite and arsenopyrite isolated phases (e.g. Figure 20a and Figure 20b). The third term, $\Delta E_{\phi,\phi'}(\text{FeS}_2/\text{FeAsS})$, is the difference average take in the bulk-like region obtained from the interface supercell (e.g. Figure 20c). The electrostatic potentials, $u(x, y, z)$, were calculated along the crystal direction perpendicular to the interface plane. The average of the electrostatic potential, $\phi(z)$, was calculated taking secant planes along z-direction as defined in the following equation:

$$\phi(z) = \frac{1}{ab} \int_0^a \int_0^b u(x, y, z) dx dy. \quad (5.2)$$

Putting together the results for the pyrite and arsenopyrite bulk and the FeS₂/FeAsS interfaces heterostructure the graphic shown in Figure 21 was constructed. From the obtained results, it is possible to evaluate the influence of the interface in the electrostatic potential.

The third term in the Eq. (5.1) comprises the determination of the BO due to the hydrostatic pressure generated in the matched phases. As can be seen in Figure 21 (see also Figure A10 and Figure A11), the pyrite/arsenopyrite interface formation do not change significantly the value of $\phi(z)$ along the coordinate. Small modifications were found mainly around the interface region, and the intensity and shape of the graph remained practically the same. That is in agreement with small values of $\Delta E_{\phi, \phi'}(FeS_2/FeAsS)$ found for the three interfaces: 0.07 eV for $FeS_2(100)/FeAsS(001)$, 0.09 eV for $FeS_2(100)/FeAsS(100)$ -As, and 0.09 eV for $FeS_2(100)/FeAsS(100)$ -S.

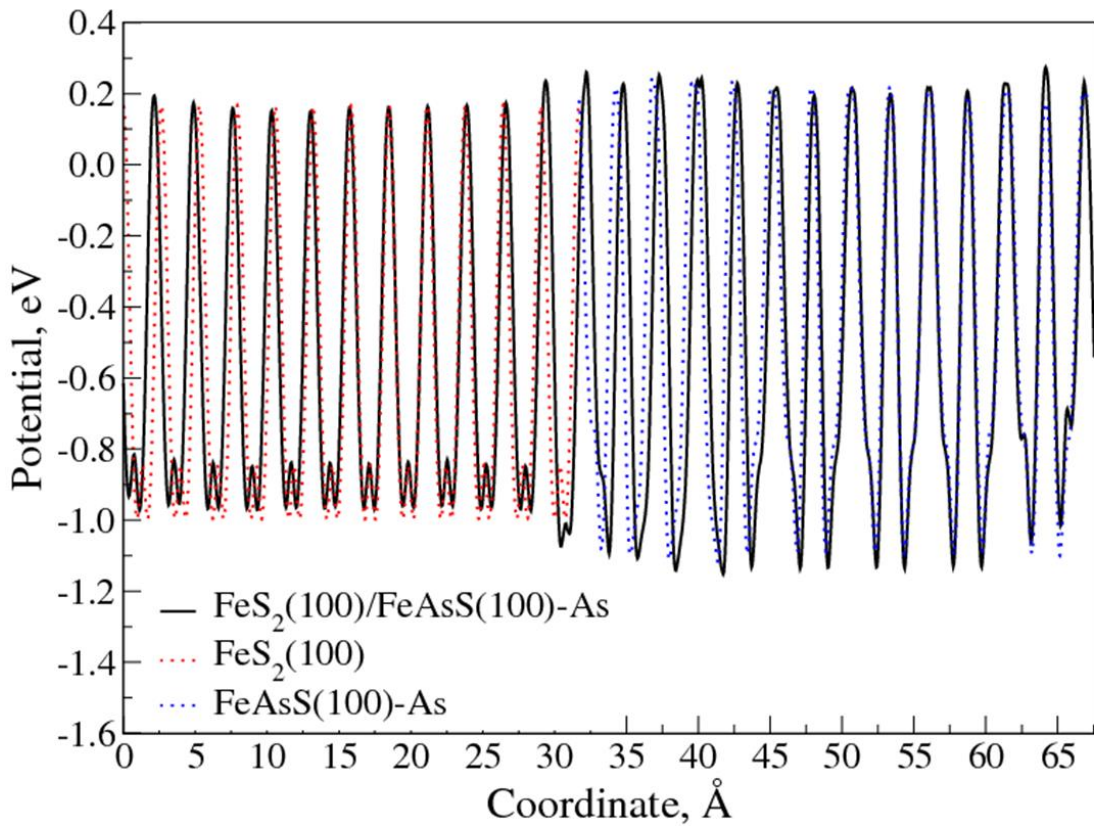


Figure 21- Displacement calculation for the $FeS_2(100)/FeAsS(100)$ -As interface model. The results found for the $FeS_2(100)/FeAsS(001)$ and $FeS_2(100)/FeAsS(100)$ -S interfaces are shown, respectively, in Figure A10 and Figure A11.

Pyrite and arsenopyrite calculation

The Hubbard parameter was tested for pyrite and arsenopyrite in order to improve the electronic properties of this mineral. It is shown in the literature that parameter (U-J) is able to modify structural, electronic and mechanical properties

parameter (U-J) it is possible to obtain structural modifications of about 5% for pyrite and arsenopyrite (the same behaviour was observed by our calculations and the results are present in Appendix N). However, the same authors have shown that the electronic properties of pyrite and arsenopyrite modify considerably more than the other properties approached. The DFT / PBE approach used in this work estimated the BG of pyrite at 0.41 eV, obtaining a deviation of 54% when compared to the experimental value of 0.90 eV. The BG of arsenopyrite was calculated as 0.71 eV, denoting in 13% of the experimental value of 0.82 eV. Therefore, it was evaluated the best (U-J) parameter that describe the electronic energy level values for VBM and CBM of the isolated bulk phases.

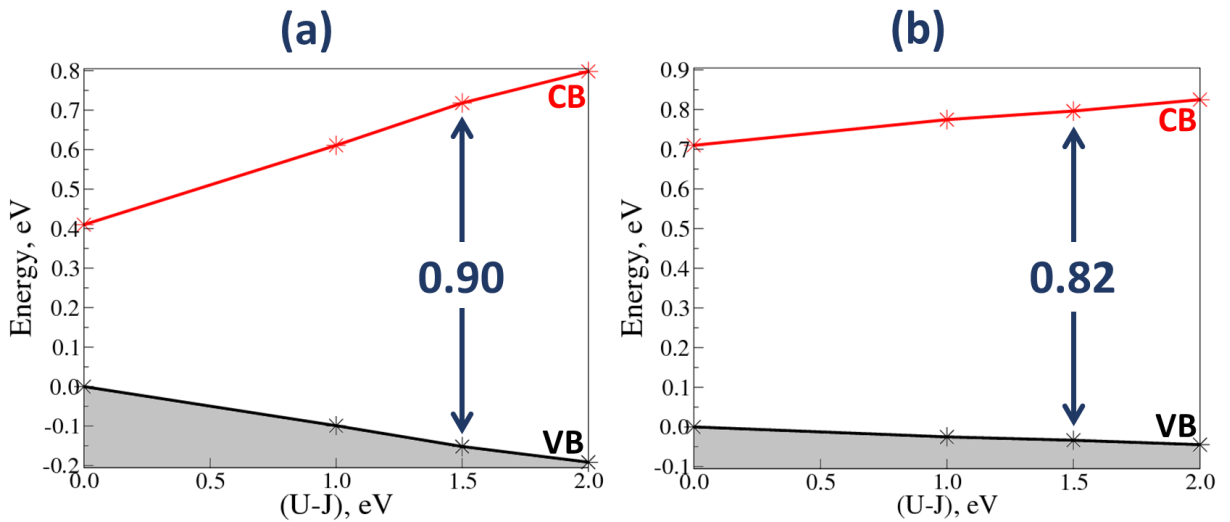


Figure 22- Valence band maximum (VBM) and Conduction band minimum (CBM) vs (U-J) Hubbard parameter for (a) pyrite and (b) arsenopyrite bulk minerals. Vertical lines represents the band gaps obtained for (U-J)= 1.5 eV. Grey shaded regions mean the occupied states level.

To achieve this, the Hubbard exchange correlation value (J) were set as 0.0 eV, and different values for the on-site Coulomb parameter was varied as $U = [0.0, 1.0, 1.5, \text{ and } 2.0 \text{ eV}]$. In Figure 22, it is shown the evolution of the conduction and valence band edges of the pyrite and arsenopyrite bulk compounds as a function of (U-J). Since the band gap values increase linearly with (U-J), the value of (U-J) was chosen to reproduce the experimental band gap ($BG = CBM - VMB$) of pyrite and arsenopyrite. As can be seen in Figure 22, the best description of BG was found for (U-J)= 1.5 eV for both compounds. The former value is capable to describe both pyrite (0.90 eV, [166, 167]) and arsenopyrite (0.82 eV, [119, 168]) band gaps with minor errors of 0.03 eV.

Pyrite/arsenopyrite interface band offset

The influence of the Hubbard correction in the band offset calculation was also evaluated, see Appendix N. The band offset calculation does not present large variation for the different (U-J) parameter tested, being the largest difference 0.05 eV when compared to the most different scenarios. Comparing Figure 22 and Table A18, it is observed that the BO values did not change as much as the values of BG. We believe that this is due to the linear behaviour of the values observed in Figure 22, thus, even if the BG values increase as the value of (U-J) increases, this change is systematically modified for the different systems addressed in this work. Also, it is being shown that for some systems that the (U-J) influence on the BO value is insignificant.[143] In this work, it was chosen the Hubbard parameter that describes well both values of BG and BO.

The projected density of states (PDOS) were calculated and the results were shifted accordingly to the energy given by the BO calculation. The results for the most stable interfaces are shown in Figure 24. The three interfaces share the same features, and for all the systems the valence-band maximum energy is located on the FeS₂ and the conduction-band minimum on the FeAsS phase. It is characteristic of a p-n junction.

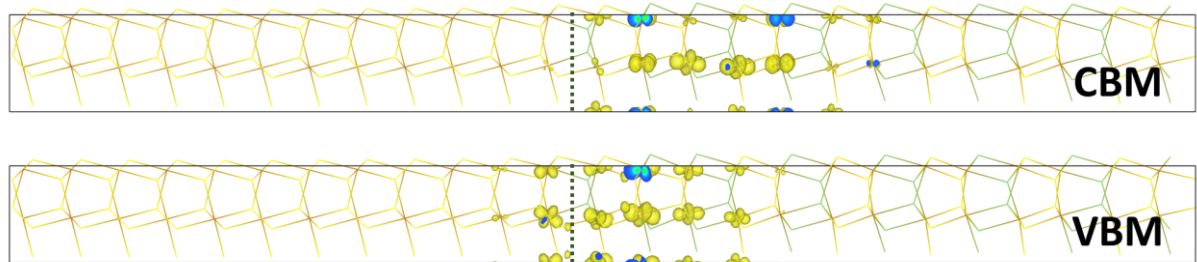


Figure 23- Interface frontier's orbitals for the FeS₂(100)/FeAsS(100)-As interface. The results found for the FeS₂(100)/FeAsS(001) and FeS₂(100)/FeAsS(100)-S interfaces are shown, one-to-one, in Figure A13 and Figure A15.

The evidence of the VBM and CBM were taken from the projected charge density over the frontier's orbital states. The projections were performed considering the last occupied and the first unoccupied bands at Γ -point calculation. The results are depicted in Figure 23. For all the systems, both VBM and CBM are located close to the interface plane. The VMB are located in FeS₂ phase and FeAsS, and the CBM are located only in the FeAsS phase. This result with the PDOS suggest that the transition occurs from the pyrite states to the arsenopyrite states.

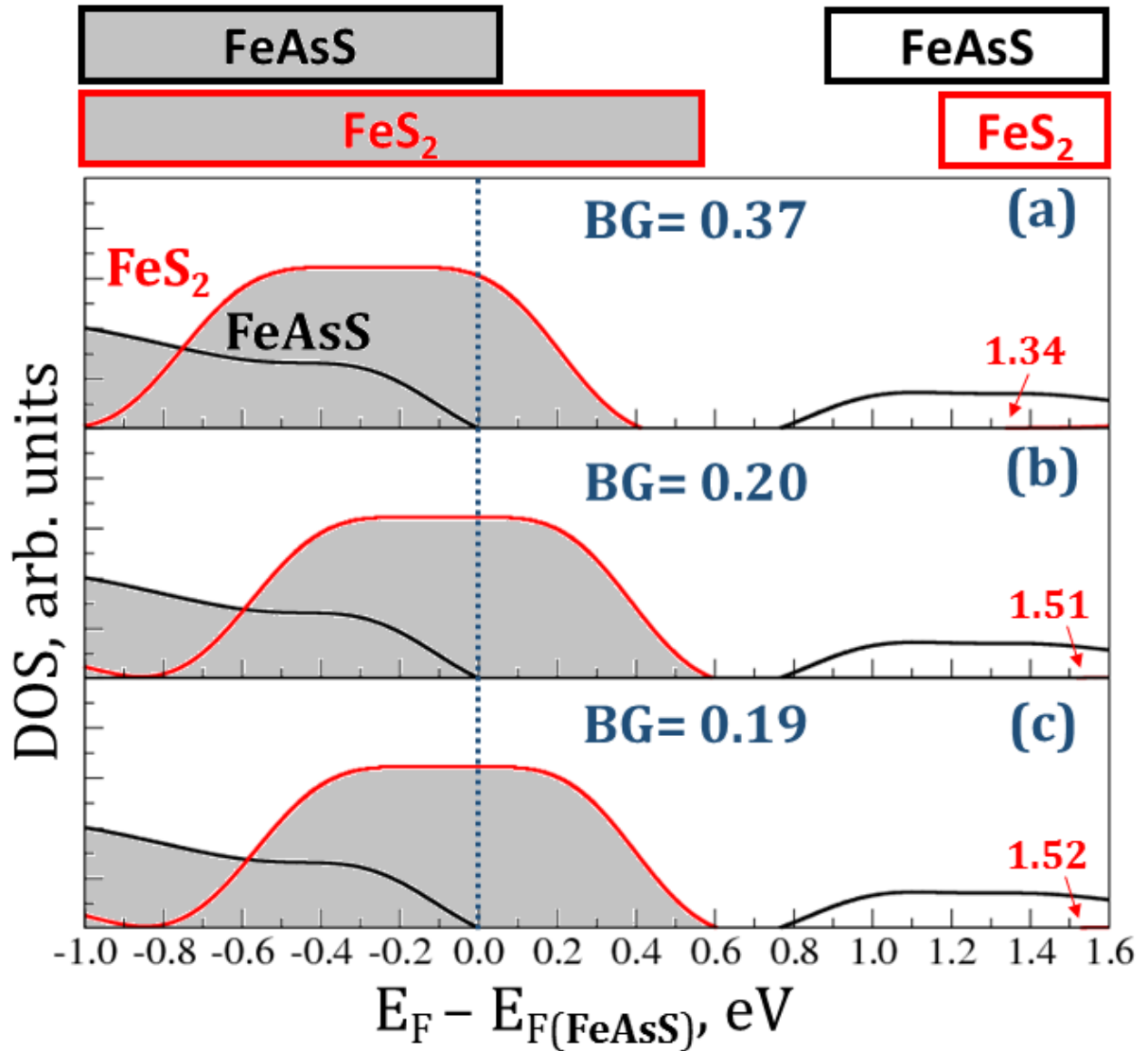


Figure 24- Interface band offset for (a) $\text{FeS}_2(100)/\text{FeAsS}(001)$, (b) $\text{FeS}_2(100)/\text{FeAsS}(100)\text{-As}$, and (c) $\text{FeS}_2(100)/\text{FeAsS}(100)\text{-As}$ interfaces. Grey shaded areas mean the occupied states level. The upper panel shows qualitatively the band alignment obtained for the three $\text{FeS}_2/\text{FeAsS}$ interfaces.

Environmental implications and conclusion

Putting together our BO calculations presented in this work and previous experimental data for pyrite/arsenopyrite,[48-55] pyrite/chalcopyrite,[40-47] and pyrite/metal[20-24] interfaces, it is possible to provide insight about how the oxidation process of arsenopyrite in the presence of pyrite occurs. Initially it is important to mention that in several reports about the oxidation of sulfide minerals, it has still been

discussed whether the reaction occurs via chemical mechanism or via electrochemical mechanism.^v It is been suggested in the literature that possibly the beginning of the oxidative process occurs most probably by chemical mechanism.[185] This hypothesis is very reasonable because at the beginning of dissolution process, the concentration of the ions in the medium is very small, and thus the redox potential in the medium will be almost zero. However, as the dissolution process occurs, the ion concentration increase modifying the electrochemical potential of the medium. For both pyrite and arsenopyrite, the chemical potential is regulated by the Fe²⁺/Fe³⁺ ionic pair. It has been shown in the literature[10] that longer exposure time of the minerals leads to ion concentration increase and the pH decrease. At this stage of the oxidation process, it will be expected that the dominant oxidation mechanism is the electrochemical. Also, it has been shown in the literature that galvanic interaction induces electrochemical dissolution of sulfides.[45] For this work, we will focus on electrochemical interpretation. Even though the beginning of the process is chemical, the mine tailings are exposed for the most part by long periods of leaching, where the oxidation process is advanced.

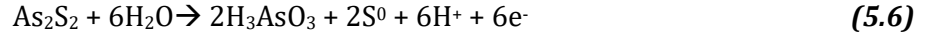
From Figure 24 it is possible to observe that the valence states are concentrated in the pyrite phase, this indicates that the reduction reactions will occur predominantly on the pyrite phase. As discussed above in this Chapter, in the presence of an electric potential (and in this case in the presence of corrosion potential of the medium controlled by the pair Fe²⁺/Fe³⁺ concentration), the electrons are transferred in the “arsenopyrite → pyrite” direction. This would make the pyrite to have always electrons available, thus being able to participate in the cathodic reactions below.



Eqs. (5.3) and (5.4) are not destructive, and consequently the structure of the pyrite would be maintained, not occurring the degradation of the material.

Different from pyrite, arsenopyrite would act as the anode of the reaction, thus being dissolved along the process according to the half-reactions below.

^v For the sake of simplification, it will be used in this thesis the terms "electrochemical" and "chemical" for reactions in which electron transfer occurs or not, respectively.



During the dissolution of arsenopyrite the degradation of this material would occur, releasing As[III] and As[V] in the medium. It is also experimentally predicted that arsenopyrite may form elemental sulfur on its surface, so Eq. (5.6) has been included among the above reactions.

Our results permitted to interpret the experimental data to provide the mechanism of the process at atomic level. Moreover, the results can be observed by interpreting the rest potential of the two materials. According to the experimental data, the resting potential of pyrite is estimated to be approximately 0.66 V,[25, 33] while the resting potential of arsenopyrite is estimated to be 0.43 V.[55, 215, 216] The value of BO (~ 0.25 eV) found for all three interfaces is well close to the difference between the resting potentials of the two materials (0.23 V). This shows that our results are consistent with the experimental values.

Another important factor is related to the stability of these materials. Recently we reported the evaluation of the affinity of the phases, and it was observed that a long interface domain will not form in nature.[62] This is in agreement with some works, where it is shown that the interactions between pyrite and arsenopyrite occurs in nanometric domain. This could suggest that there is no electron transfer between the two phases. However, it was found that interstitial arsenopyrite grains are surrounded by amorphous pyrite. Even though it does not have the formation of an interface perfectly formed at the atomic level, electron transfer can occur. Another aspect was mentioned by Ke *et al.*,[217] where it is argued that electron transfer between the two phases occurs via quantum tunnelling. In such cases the electron can be transferred from one material to another with a distance of up to 11 Å. Thus, electrons can be transferred even if there is no chemical bonding between the interfaces.

Chapter 6 – DFTB2 parametrization for Pyrite/Water interface

Preamble: In collaboration with Prof. Maicon P. Lourenço, the DFTB2 repulsion parameters based on the Material Science set (matsci) were redesigned to study the structure and dynamic properties of bulk water aiming to study the water and its interface with materials. In particular, the DFTB2 water parameters were developed and applied in the study of pyrite/water interface. The Reverse Monte Carlo method (RMC) approach was applied by simultaneously correcting the O-H and O-O DFTB2 repulsion energy to describe structural and dynamic properties of liquid water at 298 and 254 K. Our present parameters also describe the properties of pyrite bulk [e.g. structure, energy of formation and band gap] and pyrite (100) surface [cleavage energy]. Also, pyrite/water interaction was evaluated and compared with DFT calculations and experimental measurements. This Chapter represents the first attempt to describe the chemical reactivity of sulfides using DFTB2 theoretical calculations.

Liquid water: a contemporary challenge for simulations

Water plays an important role in chemistry and its interaction with the matter is complex and crucial in many phenomena that occur in life sciences, environment, geochemistry and chemistry. The complexity of the water/solid interfaces has required a joint effort between experiment and theory to tackle such endeavour [218-221]. In order to study water at atomic level, it is mandatory to have a good description of the static and dynamic properties of liquid water. It is important to keep in mind that a full description of liquid involves breaking/forming of new O-H bonds and/or a complex hydrogen-bonding network, therefore the approach using quantum mechanical methods becomes essential. DFT is known for not describing long-range interaction, thus much efforts have been put to develop XC functionals including dispersion corrections for water.[222-224] However, DFT simulations for water are limited by a small number of water molecules, which makes it impossible to simulate large water-box cells. Alternatively, the self-consistent-charge density-functional tight-binding (SCC-DFTB, or also called DFTB2) method is capable to perform electronic structure calculations of larger and complex systems, including liquid water.

Several approaches have been employed in order to improve the description of water using DFTB2 method. A *posteriori* Lennard-Jones dispersion corrections was proposed by Zhechkov *et al.*[118] aiming to correct the long-range water-water interactions. The authors developed a method specially developed for DFTB methods, however, it was proved to be not sufficiently to describe liquid neutral water.[225] Most of the efforts comes from the third order extension of the DFTB method, the so called DFTB3 method.[226] Again, it still not enough to describe water, and empirical correction are necessary to fully describe water. Finally, a Reverse Monte Carlo (RMC) correction has been done to improve the parametrization of the repulsive potential for bulk water.[227] Water-water long-range interaction is included in the total DFTB2 energies by modifying the repulsive potential using RMC correction.

Water parametrization

The DFTB2 parameters were corrected for long range interactions for DFTB2 potential energy. We modified the repulsive potential of the DFTB based on Eq. (6.1). It is called reverse Mont Carlo (RMC) scheme (also called as Boltzmann Inversion).[226, 228] As DFTB2 is a pairwise method, it is feasible to modify the potential energy according to the relevant pairs for the description of a certain electronic systems based on existent set of parameters. In the present work, the initial parameters for O-O, H-H and O-H were obtained from the matsci set[114] in order to simulate water systems. The DFTB2 repulsion energy curve (E_{rep}) for O-O and O-H was obtained to start the Reverse Monte Carlo approach as the following equation indicates:

$$E_{rep}^{i+1}(R) = E_{rep}^i(R) - k_B T \ln \left(\frac{g_{OX}^i(R)}{g_{OX}^{exp}(R)} \right), \quad (6.1)$$

where $g_{OX}^i(R)$ and $g_{OX}^{exp}(R)$ are the Radial Distribution Function of the O-X (X = O, H) from DFTB2 molecular dynamics calculation and experiment, respectively. $E_{rep}^i(R)$ is the i -th DFTB2 repulsion energy, k_B the Boltzmann constant and T is the temperature. The Radial distribution functions for the a - b atomic pair was calculated by:

$$g_{OX}^{System}(R) = \frac{\Omega}{4\pi r^2} P_{OX}^{System}(R), \quad (6.2)$$

where Ω represents the volume of the water box cell, and $P_{OX}^{System}(R)$ is the density probability of finding a particle type “X” at a certain distance (R) of particle “O”.

By substituting Eq. (6.2) in Eq. (6.1), DFTB2 repulsion is corrected and updated to the new iteration $E_{rep}^{i+1}(R)$. O-O and O-H RDF present a minimum and maximum for $g_{ab}^{System}(R)$ values in different R distance positions (see Figure 25), hence, it is necessary to define different numerical intervals for $E_{rep}^{i+1}(R)$. The RMC was employed in the range of 2.9–6.0 Å for O-O and 1.6-4.3 Å for O-H atomic pairs.

Two types of parameterization were done: (i) using the regular DFTB2 parameter (named as water-matsci) and (ii) using a *posteriori* dispersion correction[118] (name as water-matsci-UFF). For the first parameterization, we employed three RMC iterations by changing both O-H and O-O repulsions simultaneously. After that, we fixed the O-H parameter set and changed just the O-O in the fourth iteration. Four MD iterations were employed in order to get the repulsion DFTB2 parameters which describes, as better as, the experimental gO-O and gO-H. For the second parameters, we employed four RMC iterations by changing both O-H and O-O repulsions simultaneously. After that, we fixed the O-H parameter set and changed just the O-O for two more iterations. Then, a total of six iterations were employed in order to get the parameters that describes the experimental gO-O and gO-H RDF. We note that the different numbers of interactions required for water-matsci and water-matsci-UFF parametrization is related to the fact that dispersion correction modify the total energy potential of the system.

The molecular dynamic simulations were performed by using the DFTB+ program.[113] To simulate liquid water, a cubic cell of 12.42 Å size containing 64 water molecules was used. Along the simulations, box cell was not allowed to change volume and water density was kept constant ($\sim 0.99 \text{ g.cm}^{-3}$). The DFTB2 molecular dynamics was performed in a long NVT trajectory of 100 ps at 298 K. The temperature was thermalized by Berendsen thermostat. To propagate the trajectory, the Velocity-Verlet algorithm was used with a time step of 0.5 fs. The SCC tolerance was set to 10^{-6} . The description of the First Brillouin zone was described by the 1x1x1 (gamma point) Monkhorst-Pack scheme.

All the calculations shown in this work were done using NVT dynamics simulation. However, we also performed NVE simulation aiming to compare the RMC for both approaches. For NVE simulation, the initial velocities were obtained from the previous NVT simulation described above. After 100 ps dynamics, both NVT and NVE reached the same result (see Figure A18 and Figure A19 in Appendix O). For this reason, only the NVT results are presented and discussed in this Chapter, the remaining data from the NVT+NVE molecular dynamics can be seen in Appendix O.

Pyrite “Fe-X” pair parametrization

The DFTB2 parameterization of the Fe-X (X = Fe, S, O, H) in pyrite surface was carry out in two steps. First, the electronic contribution was evaluated by using the RLCAO^{vi} (Relativistic Linear Combination of Atomic Orbitals) program.[229] Second, the repulsive contribution was estimated by the FASP (Framework for Automatization of SLAKO Parameterization) program[115] developed by Lourenço *et al.*[115]. The DFTB2 parameters for Fe/S/O/H were calculated by Prof. Maicon P. Lourenço. We contributed to define the chemical models (Table A19) for the repulsive potentials and we performed all calculations presented in this Chapter.

Results: Bulk water properties

The DFTB2 parameterization based on the original DFTB2/matsci database and corrected by the Reverse Monte Carlo (RMC) was mainly designed to describe structural and dynamical properties of liquid water. O-O Experimental[230, 231] and DFTB2 radial distribution function is shown in Figure 25a. The first coordination-shell occurs around 2.8 Å for both water-matsci and water-matsci-UFF evaluation. However, a minimum difference in the maximum of probability was observed for water-matsci-UFF. Nevertheless, our parameters are able to describe water structure. By using the pure water-matsci repulsion for the RMC iterations, the first shell presents a good fit with the

^{vi} **We are indebted with the group of Prof. Seifert for providing us the copy of the program.**

RDF obtained from experimental X-ray diffraction measurements (e.g. Benchmark, Ref. [232]). Benchmark RDF was also used in the design of the recent force field water model, MB-Pol.[233, 234]

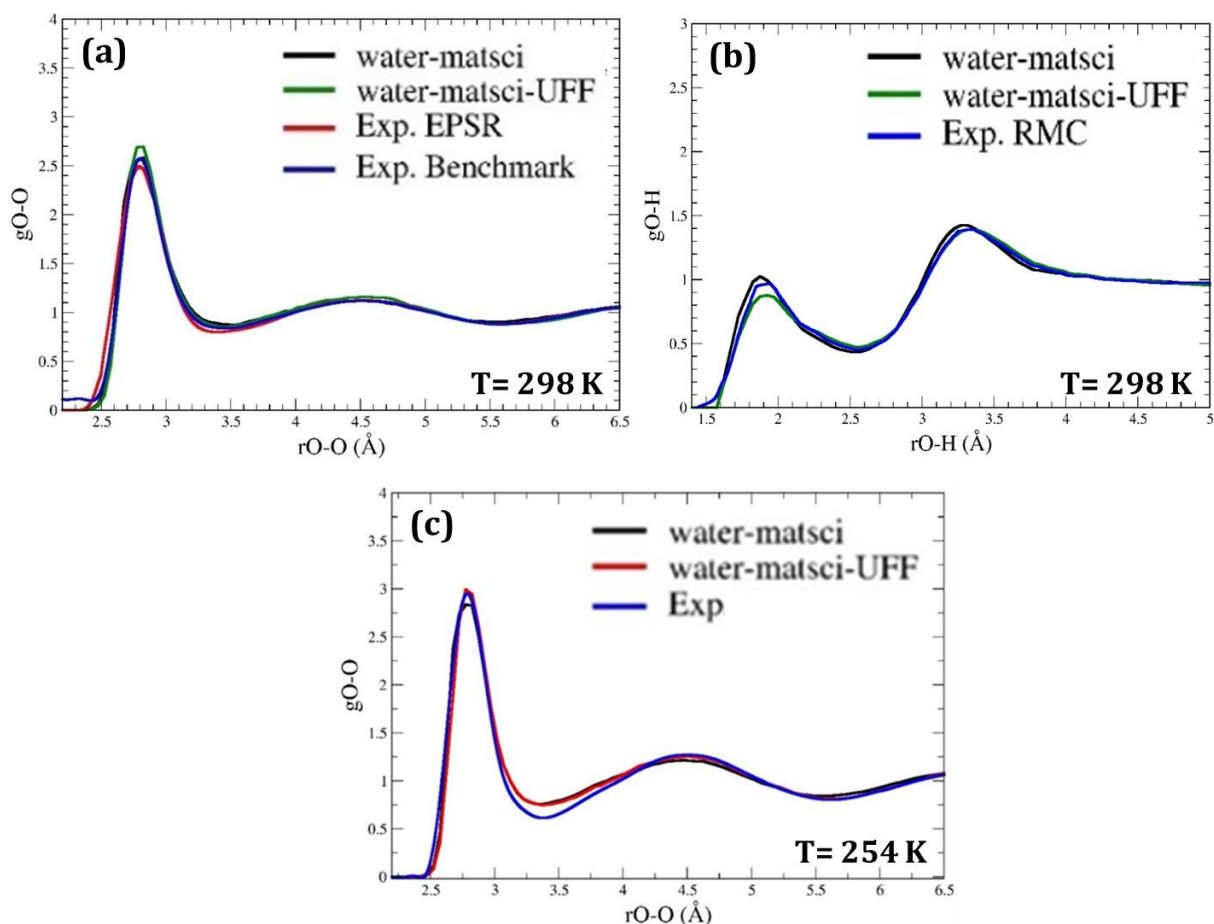


Figure 25- O-O and O-H radial distribution function obtained at different temperatures for neutral water. Experimental values quoted from Refs. [235-237].

Different from other corrections applied for DFTB2 calculation,[225, 226, 238] our parameters are capable to describe the second water coordination-shell, Figure 25a. The second coordination-shell (~ 4.5 Å) is related to the tetrahedrality of the liquid water.[236] As it can be seen, the water-matsci presented a good description of this region compared to the experimental one. Minor differences were observed when evaluated the effect on dispersion on the second coordination-shell. Gillan et al.[222] have studied the performance of several DFT XC functionals in the description of the bulk water at 298 K and most of them without dispersion corrections have serious problems in describing the second shell, which makes the water too rigid in the simulations. It also has been shown by Gilland et al. [222] and Møgelhøj et al. [224] the role of the dispersion in describing the

tetrahedrality of the liquid water at room temperature. The RMC modifies the potential energy and, iteratively, it converges to the reference RDF (in this case the experimental RDF).

The performance of the water-matsci and water-matsci-UFF parameters for the O-H and RDF is addressed in Figure 25b. The experimental gO-H used in the parameterization of the DFTB2 sets came from the FREE RMC method applied in X-ray and neutron diffraction data[239]. Both DFTB2 parameters set described the gO-H experimental curve. As observed by Doemer *et al.*,[228] correcting simultaneously both O-O and O-H atomic pairs is a good strategy. The RMC increases the accuracy of our parametrization, since it is closer to a realistic water behave. Several DFTB2 corrections have presented the same behaviour in describing experimental gO-O data, however, most of them fail to represent gO-H.[225, 238]

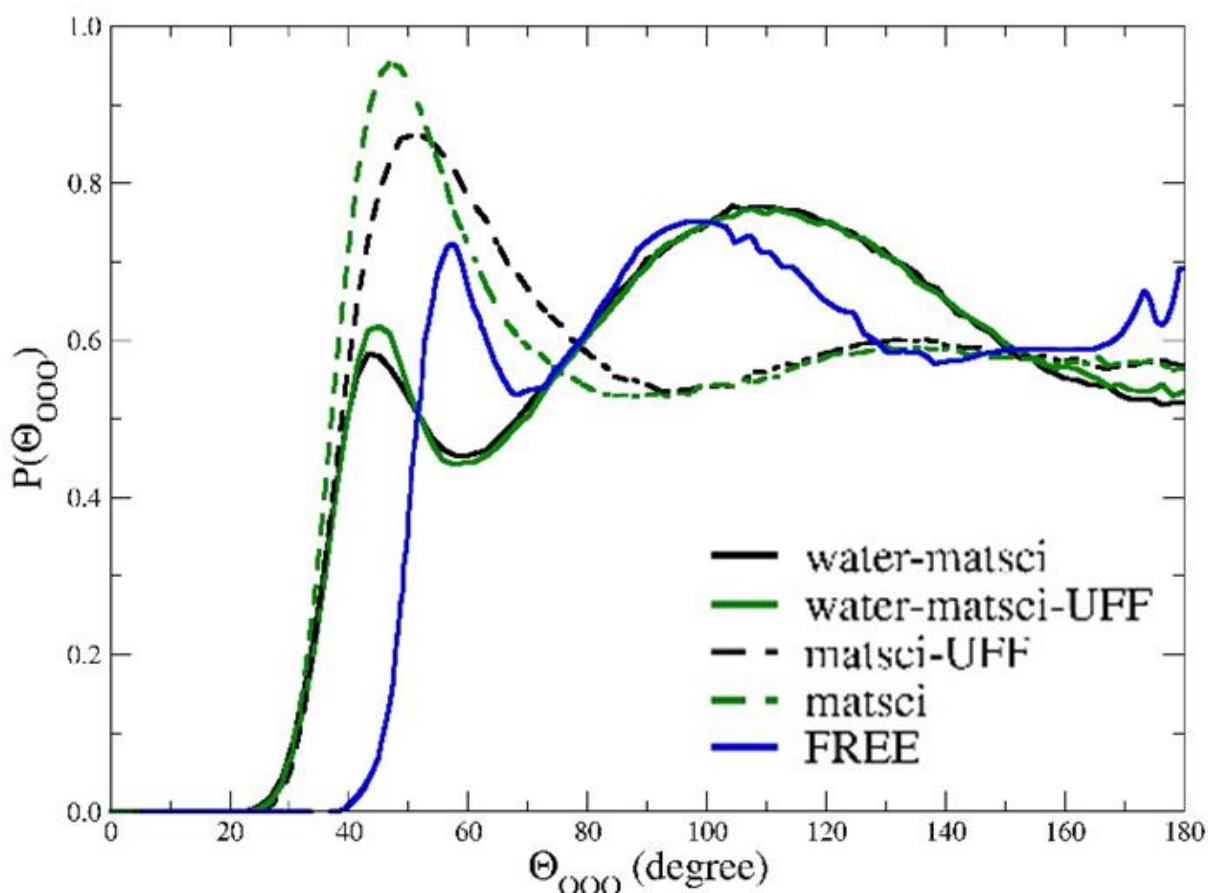


Figure 26- Water-matsci, water-matsci-UFF, matsci and the experimental (FREE, Ref. [236]) distribution of the angles O_1-Oc-O_1 . All calculations were done for liquid water at 298 K.

To guarantee a good water description, it is necessary to evaluate many parameters and compare to the experimental data. The RDF is an important parameter to evaluate the accuracy of our parametrization. Furthermore, it is also convenient to analyse the distribution of O₁-O_c-O₁ angles, which provides an accurate measurement of three-body correlations for a certain O₁ oxygen close to the central water oxygen (O_c). Assuming, for example, four nearest neighbours, a distribution peaking strongly around 109° would then indicate a tetrahedral distribution of oxygen positions. Figure 26 shows the O₁-O_c-O₁ distribution angles for the first-coordination shell of water. All triplets were calculated within a radius of 3.5 Å around each oxygen. This radius considers the first minimum in the O-O RDF for the currently DFTB2 parameters (see Figure 25a). By the analysis of Figure 26 it is clear that the parameters corrected by the RMC method show significant improvement when compared to the parameters without RMC correction. Significant improvement is observed in the region of 70° to 100°, where the parameters have a good agreement with the reference O₁-O_c-O₁ distribution (FREE).

Several approaches have been proposed to describe the tetrahedrality in a system. A useful and straightforward quantity is the $\langle q \rangle$ parameter[235, 236, 240] defined according to the equation (10).

$$\langle q \rangle = 1 - \left\langle \left(\cos(\theta_{000}) + \frac{1}{3} \right)^2 \right\rangle \quad (6.4)$$

$\langle q \rangle$ is the average of all O₁-O_c-O₁ angles (θ_{000}) inside a certain radius. We used 3.5 Å which includes the water molecules around O_c in the first water coordination-shell. By analysing Eq. (10), for $\theta_{000} = 109^\circ$, $\langle q \rangle$ is expected to be equal 1. This is the case of ice, and it indicates the maximum of tetrahedrality. The $\langle q \rangle$ values for all discussed DFTB2 parameters are presented in Table 6. The original *matsci* parameter naturally present a smaller $\langle q \rangle$ value (0.425) and 0.450 with UFF correction. These values are outside the range (0.488-0.603) derived from the RMC fits of different models to the experimental diffraction data[236] while the *water-matsci* (0.492) and *water-matsci-UFF* (0.495) parameters are well within this range and very close to the FREE value (0.499) of the least constrained RMC fit[236]. The former observation shows that the new DFTB2 parameters describes the water structure in liquid phase.

Table 6- Values of $\langle q \rangle$ parameter in the distribution of θ_{000} angles for different DFTB2 parameter sets compared to values from RMC fits to scattering data of Ref. [236].

Model	$\langle q \rangle$
water-matsci	0.495
water-matsci-UFF	0.492
matsci	0.425
matsci-UFF	0.450
SD	0.592
DD	0.603
SYM	0.552
ASYM	0.488
MIX	0.489
FREE	0.499

In order to evaluate dynamical structure of water along the time (t), it was evaluated the coefficient of self-diffusion of water (D) defined as:

$$\langle |R(t) - R(t_0)|^2 \rangle = 6tD, \quad (6.5)$$

where $R(t_0)$ represents the position of the oxygen atom at time origin (t_0), and $R(t)$ represents the position of the same oxygen atom along the NVT trajectory. The current DFTB2 water parameters were used to obtain the self-diffusion coefficients (D) of water, and the results are shown in Table 7. As one can see, for liquid water at room temperature, matsci and matsci-UFF parameter presents a good agreement with experimental measurements. Likewise, our water-matsci and water-matsci-UFF presented similar values for D , which indicates that the RMC corrections do not affect artificially the dynamic properties of the systems. We note that our results are comparable to the experimental number, what indicates that our cell box is large enough to describe liquid water. As a consequence, no finite size effects are evident in our calculations.

Transferability of the currently tight-binding parameters was evaluated by the calculation of RDF and self-diffusion for water at 254 K. The former temperature represents water in the supercooled regime holding the density of 0.994 g.cm⁻³. [241] Considering that at low temperatures the first water coordination-shell are more intense

and the second are significant, we believe that lower temperature dynamics indicates if our DFTB2 parameters would be overparametrized or artificially affecting the evaluated properties. As discussed in the literature, the RMC method should be applied to improve the intended properties, however it should not affect in the other properties. In the next section, it will be discussed about the adsorption of water on pyrite surface. In this case, it will be necessary to modify O-H and O-O pair repulsion keeping the O-H bonds intact. As discussed before in this Chapter, RMC was used only to correct long-range interactions. Even setting a minimum limit for RMC correction, we run new calculations to make sure that our parametrization is in agreement with water liquid behaviour.

Table 7- Neutral water self-diffusion coefficient ($\text{\AA}^2/\text{ps}$) of the oxygen atom at different temperatures. Quoted references in parenthesis.

Water	Self-diffusion coefficient	
	298 K	254 K
Exp.	0.19 ([242])	0.03 ([243])
water-matsci	0.08	0.05
water-matsci-UFF	0.08	0.06
matsci	0.10	0.09
matsci-UFF	0.11	0.09

In Figure 25c DFTB2 RDF's was compared to the experimental data obtained by Skinner *et al.*[237] Both parameters presented good agreement with the experimental value, and are capable to describe the two first coordination-shell of water at 254 K with minor differences. DFTB2 first coordination-shell (2.5-3.5 \AA) have a maximum value slight lower (~ 0.2) to reference value, differently the minimum value is 0.4 higher than the experimental value. The second coordination-shell overlay the experimental value on Figure 25c curve. It indicates that our parameters are capable to describe the structure of supercooled water. We note that we are looking for parameters that describe surface/water reactivity, and a parameter that describe rigorously water properties is beyond the scope of this work. We believe that there are other methods more suitable for that.[236] Finally, water self-diffusion were found to be 0.05 $\text{\AA}^2/\text{ps}$ for water-matsci parameter and 0.06 $\text{\AA}^2/\text{ps}$ water-matsci-UFF. These values are comparable to the

experimental value of $0.03 \text{ \AA}^2/\text{ps}$, see Table 7. Again, our parameters with the RMC correction present better results than the initial matsci parameter.

Results: Pyrite bulk and surface properties

The DFTB2 calculations were performed using the implementation of the DFTB+ software.[113] We calculated pyrite bulk cell in the cubic face centered system (space group Pa3) containing 12 atoms per unit cell (corresponding to the Fe_4S_8 chemical formula). Total energy was obtained for a $2 \times 2 \times 2$ supercell using Γ point. All atoms and cell vectors were allowed to move freely on the conjugated-gradient optimization. After full relaxation of the systems, the present parameters (water-matsci and water-matsci-UFF) found the same cell parameter of 5.64 \AA , which is 0.23 (5%) lower than the experimental value of 5.42 \AA found for Brostiger and Kjekshus.[173] DFT calculations also show significant differences when compared to the expected experimental values, and differences of 3% have been found in the calculations. Considering that DFTB is an approximation of DFT method, it is expected differences with respect to experiment greater or equal for DFTB compared to DFT. Therefore, the difference of 3% or 5% is considered negligible in this work. It has been shown elsewhere differences that extend to more than 8% when comparing DFTB2 with experimental observable.[106, 114]

The parameterization of the DFTB2 methods as implemented in the FASP program aims to modify the total energy of the system, in this sense it is important to evaluate a parameter that depends directly on the total energy value of the system. For this, the pyrite formation energy was calculated by Eq. (3.3) in Chapter 3. To calculate μ_{Fe}^* the iron BCC unit cell was used, and for μ_{S}^* the S_8 orthorhombic cell. Our DFTB2 parameters found a value of -1.53 and $-1.61 \text{ eV}/(\text{formula unit})$ for water-matsci and water-matsci-UFF parameters, respectively. Both numbers are in the same order of magnitude of the experimental measurements [$-1.74 \text{ eV}/(\text{formula unit})$] and DFT/PBE estimations [$-1.51 \text{ eV}/(\text{formula unit})$].[62, 171]

DFTB2 Pyrite density of states (Figure 27) is in agreement with experimental measurements[187, 193, 244, 245] and DFT calculations.[62, 185, 192] Both the highest occupied and the lowest unoccupied states are essentially localized on the surface iron

ions. The currently parameters found a band gap of 0.69 eV, which is in good agreement with PBE (0.50 eV) and experimental (0.90 eV) evaluations. We note that pyrite electronic properties are generally improved by using Hubbard corrections[62] or by using many-body perturbation theory,[246] but, in our parametrization only DFT XC potentials were used with no Hubbard corrections.

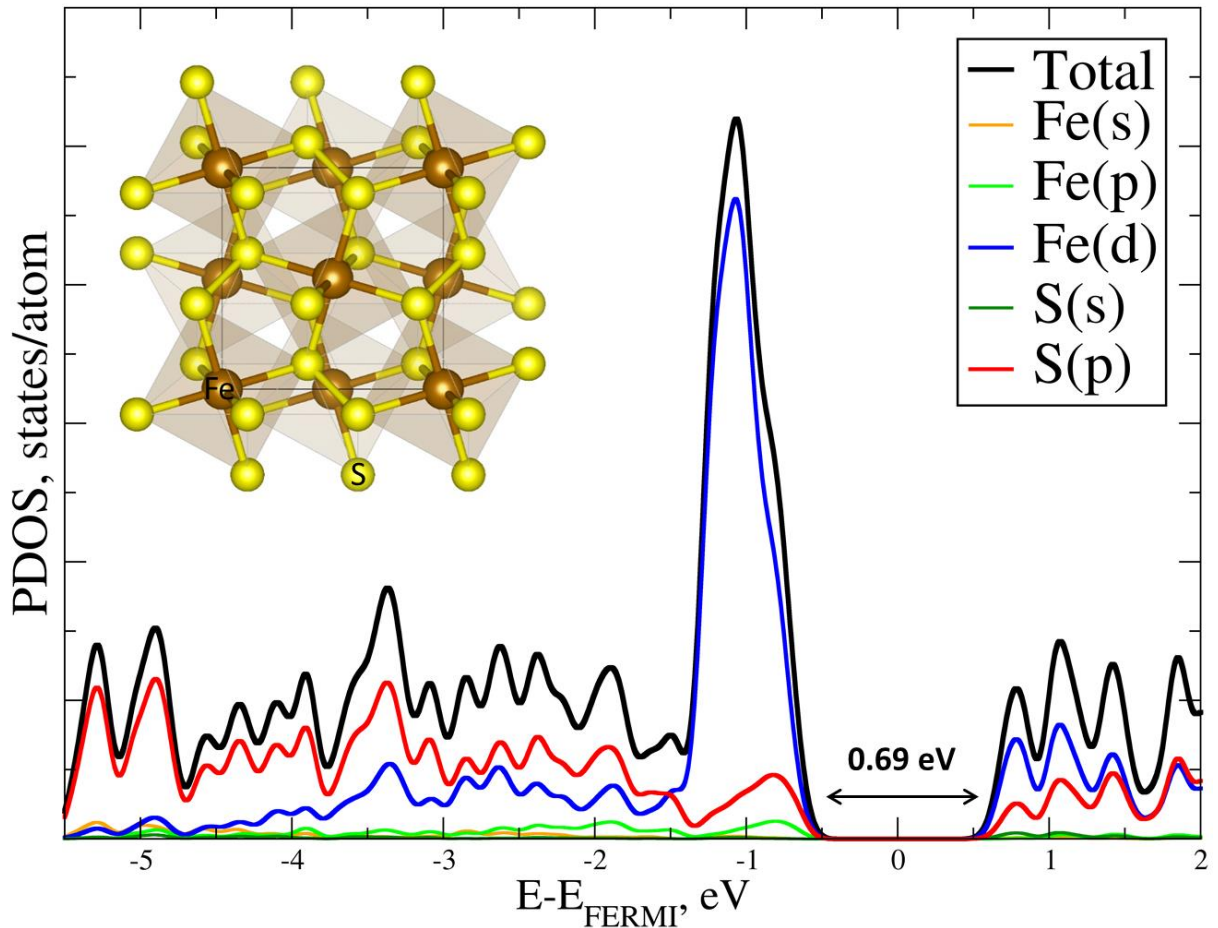


Figure 27- Pyrite projected density of states in the vicinity of Fermi level. Inset figure represents pyrite unit cell.

Bare pyrite (100) surface was simulated to represent pyrite on nature. It is well-known that pyrite preferential cleavage is more likely to occur over (100) surface directions. Similarly, many works aiming to understand pyrite chemical reactivity use (100) facets as a good model to represent pyrite in ambient conditions or under experimental control. In this sense, $\text{FeS}_2(100)$ surface was built according to the findings in the literature.[62, 63, 185, 191] Our surface contains totally 9 atomic layers and was constructed by the S-Fe-S sequence, maintaining the pyrite bulk stoichiometry of the system. Recently, it was suggested in the literature that non-stoichiometric pyrite

surfaces are expected to form, though in low concentration. We chose to work with the system maintaining the stoichiometry of the evaluated material. A two-dimensional c(2x2) surface and a vacuum space of 10 Å was considered.

Pyrite cleavage energy (γ) was evaluated by the following relation:

$$\gamma = \frac{1}{2S} [E^{SLAB}(n) - nE^{BULK}]. \quad (6.6)$$

γ provides the stability of the slab surface relative to bulk phase, and commonly is computed by the subtraction of slab ($E^{SLAB}(n)$) and bulk (E^{BULK}) energies normalized by the slab area (S). As FeS₂(100) surface forms a symmetrical slab (upper and bottom parts are equivalents), it is necessary to include in the calculations the division by two (1/2). Our current DFTB2 parameters found the value of 1.03 J/m². The former result is relatively close to the value obtained using PW91[247] (1.06 J/m²) and PBE[185] (1.14 J/m²) XC functional. de Leeuw *et al.*[184] estimated pyrite cleavage energy using empirical potential to be 1.23 J/m².

Results: Water adsorption on pyrite (100) surface

Over the decades, the reactivity of pyrite has been investigated in order to evaluate at the molecular level for a variety of molecules. Particularly, by the study of pyrite (100) and water interaction it was possible to understand the first step of pyrite oxidation. Guevremont *et al.*[248] have analysed the adsorption of water by a programmed thermal sorption analysis. They obtained that the most probable value for adsorption of water on the pyrite surface is about -10.0 kcal/mol.

Table 8- Water adsorption energy (calculated by Eq. (4.3)) and Fe-OH₂ distance. DFT values quoted from Ref. [185].

Structures	ΔE_{ads} , kcal/mol			Fe-OH ₂ distance, Å		
	DFT	DFTB2	DFTB2-LJ	DFT	DFTB2	DFTB2-LJ
FeS ₂ (100)/OH ₂	-14.5	-19.3	-16.4	2.152	2.059	2.048
FeS ₂ (100)/8.OH ₂	---	-16.2	-16.5	---	2.082	2.054

It was evaluated the water adsorption on the pyrite surface by adding one or eight water molecules on top of $\text{FeS}_2(100)$ surface. Water molecules were placed on the surface aiming to find the best structure that optimize acid-basic interaction of the oxygen atoms from water and iron sites on the surface. Optimized structures and adsorption energies are shown in Figure 28 and Table 8, respectively. As can be observed, our calculations describe the adsorption energy with a good agreement with the experimental value. The difference is less than 9 kcal/mol (i.e. what is considered very accurate considering that DFTB2 is a method containing many fundamental and numerical approximations). This difference becomes less pronounced when compared to DFT values published in the literature. It is estimated by PBE functional that water adsorption is around -14 kcal/mol, which the difference with our calculations do not exceed 5 kcal/mol.

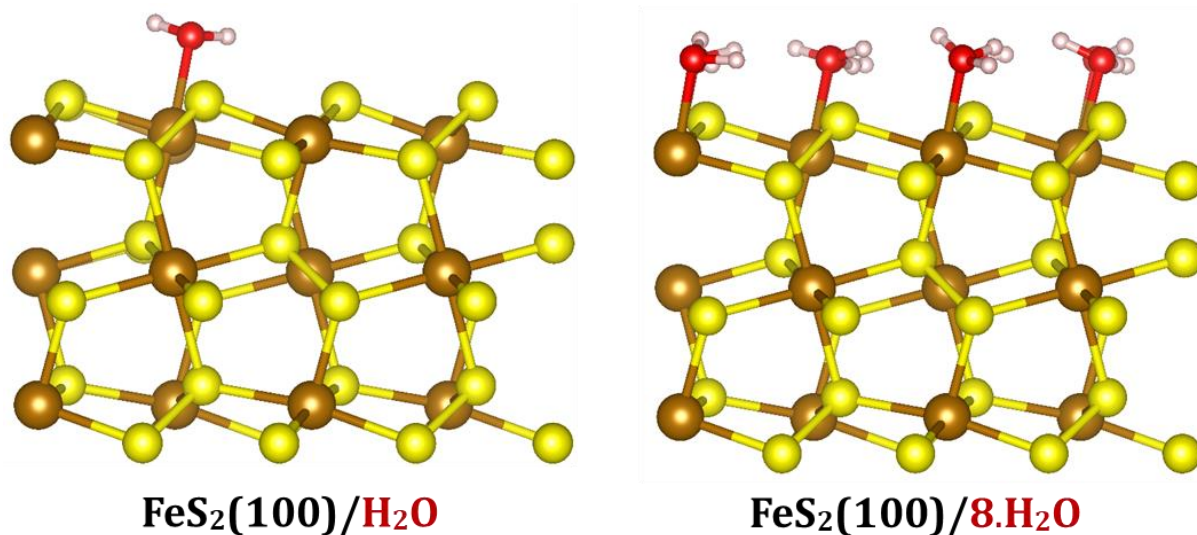


Figure 28- Water adsorption on pyrite (100) surface. Color code: yellow, sulfur; brown, iron; red, oxygen; and white, hydrogen.

Conclusion

The Slater-Koster files for describing bulk water in the framework of the DFTB2 method have been developed. These parameters lead to a description of bulk water that is in very good agreement with the state-of-the-art experimental data. The new *water-matsci* parameters can be used together with the other *matsci* parameters available to investigate materials and phenomena of increasing complexity involving water as solvent

or reactant. The strategy of using the RMC approach to improve the *E_{rep}* based on the gO-O and gO-H experimental RDFs leads to general improvement of the *matsci* parameters. Water simulated at room temperature and in the supercooled regime (at 254 K) lead to gO-O and gO-H RDF's in good agreement with the experimental data. The self-diffusion coefficients and the tetrahedrality parameters have also been estimated demonstrating that the new *water-matsci* parameters are able to describe both structural and dynamic properties of bulk water.

As observed for water liquid-phase, pyrite/water interface was also described for the new DFTB2 parameters developed in this Chapter. Properties such as: formation energy and density of states compared to published DFT calculation shows that our developed DFTB2 parameters are capable to describe bulk properties of pyrite. The water adsorption energy estimates indicate that: (a) the water parameters set with RMC correction do not affect water interaction with a solid phase; and (b) water- and pyrite *matsci* DFTB2 parameters are adequate to advance investigating the reactivity of the water/pyrite interfaces.

Chapter 7 – SO₃ and SO₄ formation on pyrite (100) surface

Preamble: Much efforts have been made to unveil the oxidation mechanism of sulfide minerals such as pyrite, arsenopyrite, covelite and chalcopyrite. Our research group made important progress using Density Functional calculations to investigate the main intermediates and energy barriers of the initial steps of the intricate mechanism. The effect of the water/pyrite interface is still a challenge for theoreticians and experimentalists. During my master studies, we have investigated in detail the oxidation mechanism of pyrite,[185] since this is the most studied sulfide mineral with large amounts of experimental data. However, recently it has been argued[249] that a new route should also be important mainly in the presence of abundant oxygen promoting directly the oxidation of the sulfides. This new route could explain the formation of the sulfur-containing species, such as SO₂, SO₃ and SO₄ on the surface. This new reaction route clarifies new aspects of the mechanism obtained by experimental analysis.

Introduction

As mentioned in the introduction of this thesis, pyrite is the commonest form of sulfide minerals, usually found associated with other sulfides or oxides in quartz veins, igneous rocks, and sedimentary beds.[13, 200-206] For most of ores and concentrates containing pyrite, the pyrite itself is rarely of economic importance. Actually, it is often viewed as an impurity in coal and other minerals, particularly, in the recovery of valuable metals such as gold, copper, and zinc.[10] Meanwhile, pyritic soils are the primary source of toxic metalloids and metals (e.g. As, Hg and Pb).[10] The main reason is that both transition metals and metalloids with similar properties to Fe and S tend to be incorporated into the crystal structure of pyrite.[250-252] It is also important to mention that pyrite dissolution is important for the geological cycle of iron, however mining produce tons of toxic materials that represent human hazard.

Pyrite oxidation has been extensively studied for many decades and it is still an open question. In the literature, there are many reports about the pyrite oxidation in aqueous systems.[63, 185, 250-258] The research on pyrite mainly focused on: (i) the formation mechanism of intermediate products; (ii) oxidation kinetics and its influencing

factors.[11] Actually, the pyrite oxidation can be seen as the break of the S-S and S-Fe bonds to form new bonds. It is considered that the S-S bond in pyrite is weaker than the Fe-S bond.[63, 185, 255] According to Taylor et al.[258] aqueous Fe²⁺ is released in the solution during the pyrite oxidation process. XPS analysis[11, 249] has detected the presence of the SO₄²⁻, SO₃²⁻, and S₂O₃²⁻ species along the reaction.

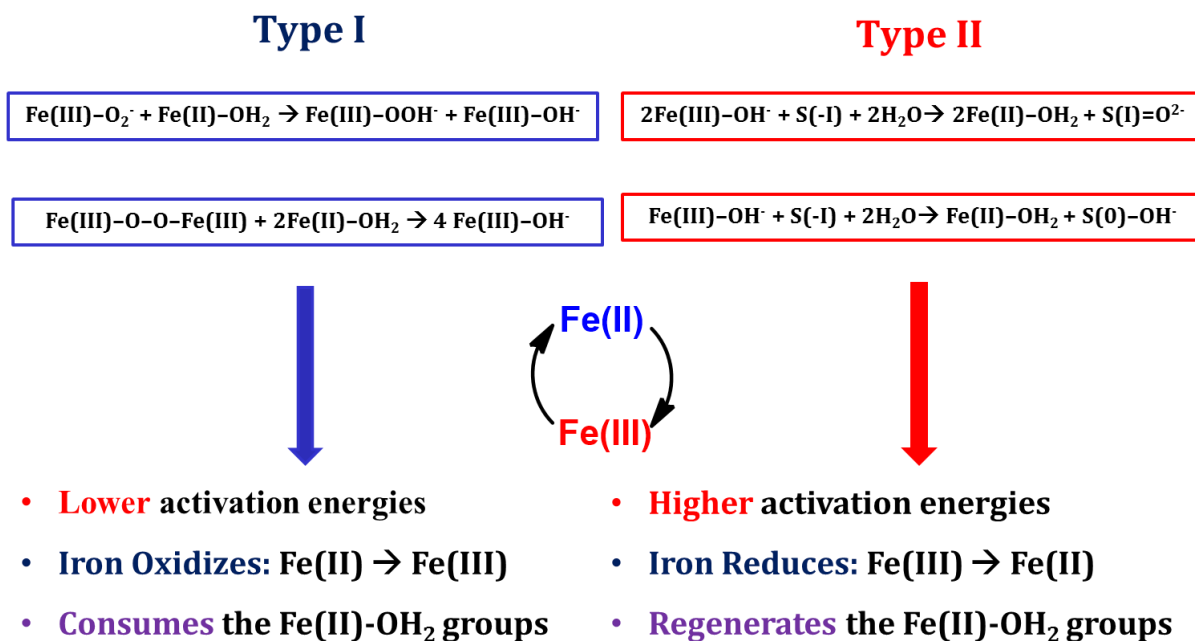


Figure 29- Pyrite oxidation mechanism in aqueous medium explained by Type I and Type II reactions. Figure quoted from Ref. [185].

DFT calculations[6, 62-64, 104, 119, 184, 185, 191, 192] have shown that the formation of sulfate on pyrite surfaces happens by two types of reactions (Type I and Type II).[63, 185, 191] Type I reactions, involve proton transference on the pyrite surface leading to the formation OH groups chemisorbed on the exposed iron sites. This reaction occurs with low activation energy and dominates the initial stage of pyrite oxidation. The OH acts oxidizing the Fe(II) sites on pyrite to Fe(III). In the second reaction set (Type II) oxygen atoms from bulk water are incorporated on the surfaces and O-H bonds are broken. The former reactions regenerate the Fe(II) on the surface, and has been used to explain why only Fe(II) is released in the oxidation process. The activation energy of Type II reactions are two times higher than Type I reactions and are more likely to determine the reaction rate of pyrite oxidation. Figure 29 shows the scheme of the two reactions and the estimated values for the reaction free energies and barriers.

Very recently[249] it was suggested experimentally that oxygen molecules possible play an important role on pyrite oxidation process. This process is called by the authors as Type III reaction, and to the best of our knowledge, it has not been evaluated by theoretical calculations. In this Chapter, Type III reactions were investigated and a new reaction path for the oxidative dissolution of pyrite was evaluated leading to the formation of sulfate and bisulfate. We advance that this new path is favourable with low energy barriers.

Theoretical framework

Our calculations were carried out using the same theory level of our published paper.[185] The generalized gradient approximation (GGA) of the density functional theory was used employing the exchange-correlation functional proposed by Perdew, Burke, and Ernzerhof[163] (PBE) as implemented in Quantum-Espresso[162] package. The ionic cores were described by norm-conserving pseudopotentials, whereas the valence electrons were treated by a plane-wave basis set with 50 Ry (or 680 eV) cut-off. This cutoff was used to ensure convergence of the total energy within 10^{-5} eV. Monkhost-Pack scheme, Brillouin zone integration was carried out at $1 \times 1 \times 1$ special k-grids along the 2D Brillouin zone for all slabs. Fermi-Dirac smearing of the occupations number around the Fermi level was employed.

The (100) Pyrite surface was simulated on a stoichiometric (2x2) slab with 9 layers in the z-direction at the optimized lattice constant of 5.418 Å (see Figure 30). All atomic layers in the slabs were placed on the xy plane with periodic boundary conditions. Along the xy-plane, a c(2x2) supercell was used concerning to bulk termination in the same direction. A vacuum space of 15 Å was used to avoid spurious interactions between the periodic images along the z-direction. Upon constructing the surface adsorption models, structural relaxations were first conducted with the criteria for energy and atom force convergence set to 10^{-5} eV and 0.01 eV \AA^{-1} , respectively. The six topmost atomic-layers of FeS₂(100) were free to relax while the three bottom layers were constrained at their bulk-like positions. Gas-phase molecules (H₂O and O₂) were calculated in a 10 \AA^3 cubic cell and using the same computational level as for pyrite surfaces. Spin-polarized calculations

were carried out, and the most stable spin state for all systems was reported in this Chapter. The oxygen molecule was calculated in its triplet ground state.

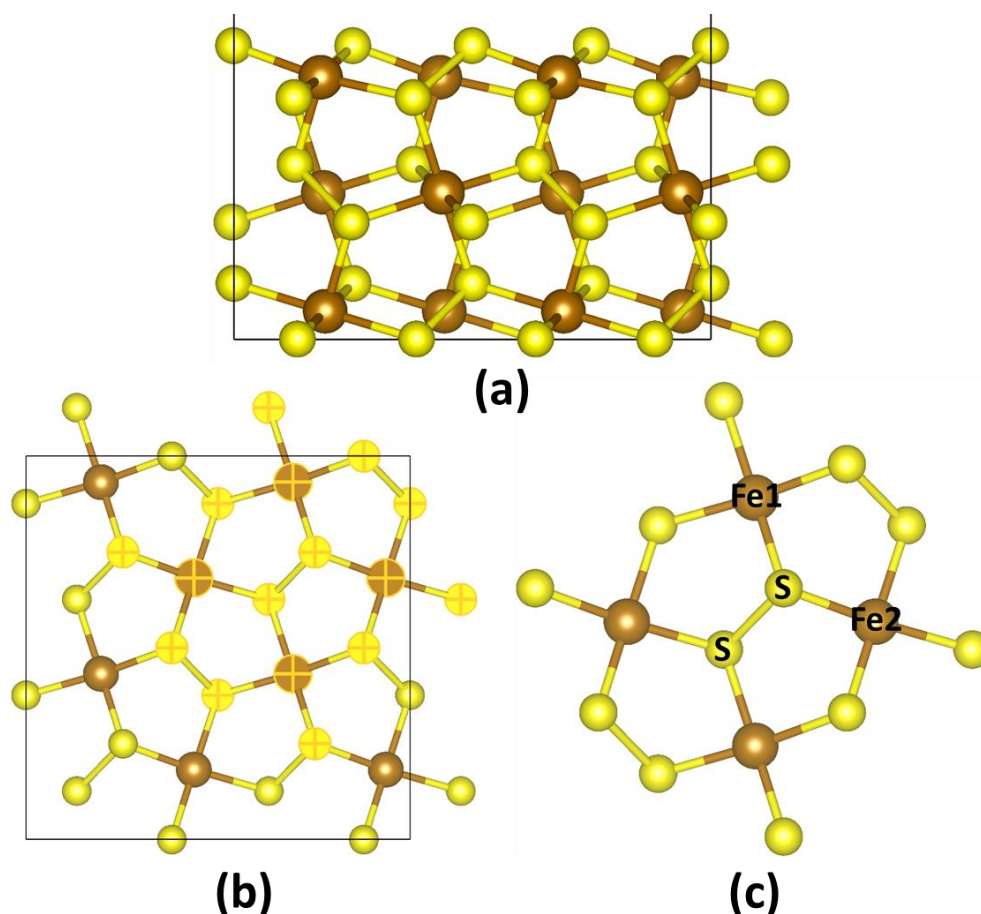


Figure 30- Side (a) and top (b) view of pyrite slab used in all calculations. Fragment of pyrite (c) used to show the reactions. Colour code: yellow - Sulfur, brown - Iron.

Transition states were calculated by the CI-NEB (climbing image - nudged elastic band) method,[108] also implemented in the Quantum-ESPRESSO package.[162] The activation energies (E_a) were calculated by the following equation

$$E_a = E_{TS} - E_{IS} \quad (7.1)$$

where E_{TS} is the transition state energy and E_{IS} is the energy of the initial state. Sixteen images were used in all calculations, and in the CI-NEB optimization process, each image converged to the minimum energy pathway using the convergence accuracy of $0.05 \text{ eV } \text{\AA}^{-1}$. The Velocity Verlet algorithm was used in all CI-NEB optimizations. More details about CI-NEB method and theory on Chapter 2.

Results and discussion

The initial steps of pyrite oxidation (Figure 31) were simulated as previously published in the literature.[63, 185] Pyrite is known to initially react with both water and oxygen molecules (H_2O+O_2) to form adsorbed Fe(III)-OH species on the surface. Sit *et al.*[63] have simulated a surface phase-diagram containing Fe(IV)=O, Fe(III)-O₂, Fe(III)-OH, molecular water and dissociated water on the surface. It was found that Fe(III)-OH is the most stable species on the surface, what suggest that the adsorbed OH⁻ should be an intermediate in the initial states of pyrite mechanism. This is in agreement with XPS analysis,[196] that shows, along the initial stage of pyrite oxidation, adsorbed water and oxygen are converted to Fe(III)-OH on the surface. The former reaction follows concerted mechanism, where the oxygen molecule dissociates at the same time that adsorbed water transfer its hydrogen promoting oxidation of the Fe(II)-OH₂ sites. These are called Type I reactions, and represent the initial oxidation step on pyrite surface. Consequently, occurring very fast in the surface due to low energy barriers of about 0.18 eV. Considering that Type I reactions are not the determinant step of the pyrite dissolution, we will not recalculate these reactions.

The reaction called Type II were evaluated as indicated in Figure 31. These reactions present higher activation energies than Type I reactions, and regulate the reaction rate of oxygen insertion on pyrite surface. As can be seen in Figure 31, the insertion of the first and the second oxygen on the surface where estimated in 0.62 and 0.80 eV, respectively.

SO formation weakens the S-S bond of the (S_2^{2-}) on pyrite surface. It was found that the S-O bond formation makes the neighbouring S-S bond 7% longer than the same S-S bond before Type II reaction (Figure 31). Considering this, it was also calculated the energy necessary to dissociate the surface SO group as indicated in Figure A21. The energy necessary is about 1.14 eV, almost two times greater than the energy for the formation of SO₂ from Type II reactions (Figure 31). We attribute this high energy by the fact that the pyrite S-atom stil have strong bond with two adjacent Fe-S bonds, and the transition state involves two Fe-S bond-breaking.

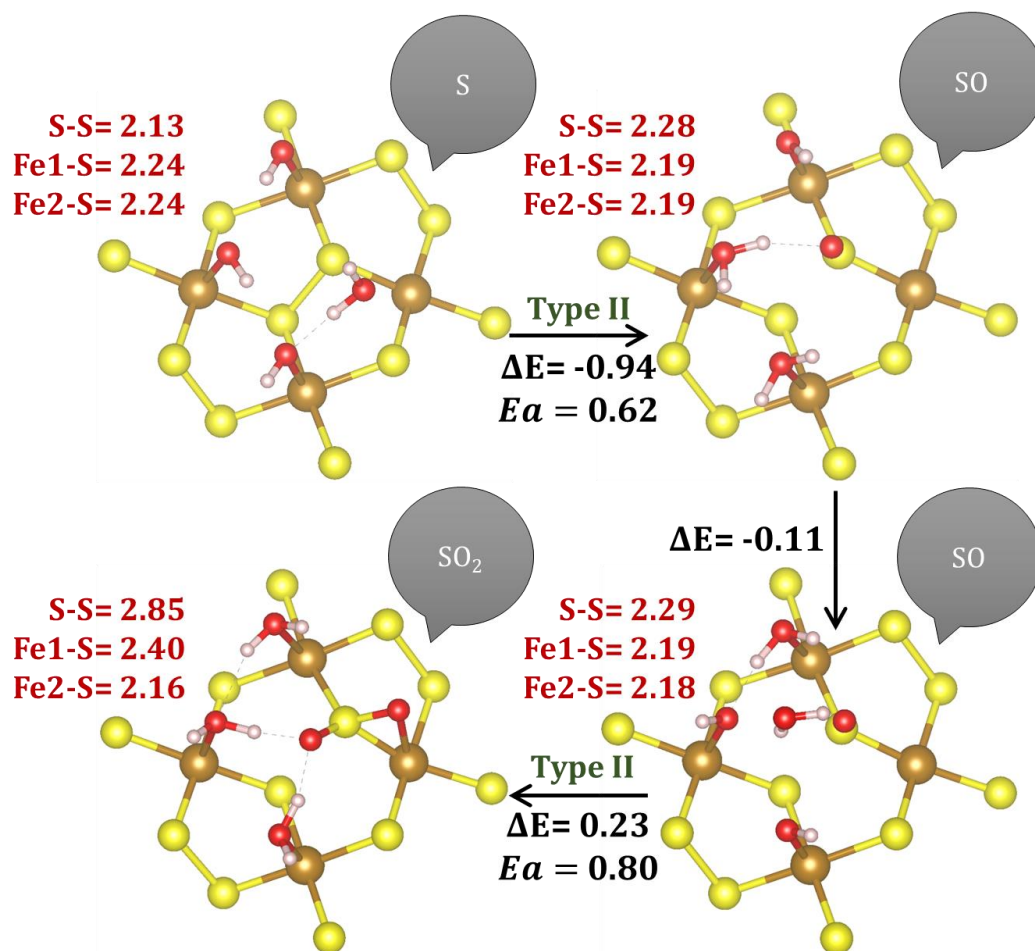


Figure 31- Fragment of pyrite (100) surface depicting the initial steps of pyrite oxidation. Energies in electronvolt and bond distances in Angstrom. Colour code: yellow - Sulfur, red - oxygen, white - hydrogen, brown - Iron.

We have also evaluated the rearrangement energy of SO₂ in the site where it was formed (Figure 31) Figure 32 shows this dissociation based on two different reaction mechanisms. The first mechanism involves two steps: (i) SO₂ dissociation forming the (SO₂)_{d,1} group on the surface (ΔE= 0.16 eV and E_a= 0.33 eV), and (ii) forming (SO₂)_{d,2} group on the surface (ΔE= -0.08 eV and E_a= 0.44 eV). The activation energy for this process was estimated in 0.44 eV and a positive energy variation of 0.08 eV for the global reaction. The activation energies for the formation of (SO₂)_{d,2} is about two times lower than the activation energy for the formation of SO₂ formation on the surface (0.80 eV). The second mechanism involves the formation of the (SO₂)_{d,2} group from SO₂ in one step. This activation energy (E_a= 0.72 eV) is expected to be 0.28 eV higher than the first mechanism evaluated in Figure 32.

Afterwards, a series of reactions was studied in order to evaluate the formation of $(\text{SO}_x)_d$ $X = [2, 3, 4]$, on the surface. As can be seen in Figure 33, starting from $(\text{SO}_2)_{d,2}$, the Type II reactions are favourable, and the activation energies were found to be of 0.13 and 0.11 eV for $(\text{SO}_3)_d$ and $(\text{SO}_4)_d$ formation, respectively. It shows that $(\text{SO}_2)_d$ is a reactive species and after its formation (see Figure 32), the activation energy decreases along the process. It is interesting to note that, the adsorbed $(\text{SO}_2)_{d,2}$ formation is not favourable to form on the surface. However, after its formation, all the activation energies decrease considerably and the reactions are exothermic. Also, the activation energy for the formation of $(\text{SO}_2)_{d,2}$ group is lower in 0.18 eV than the formation of SO and SO_2 on the surface. This reveals that, not just one route for S-containing aqueous species would be observed, and many reaction mechanisms would lead to the formation of $(\text{SO}_x)_d$.

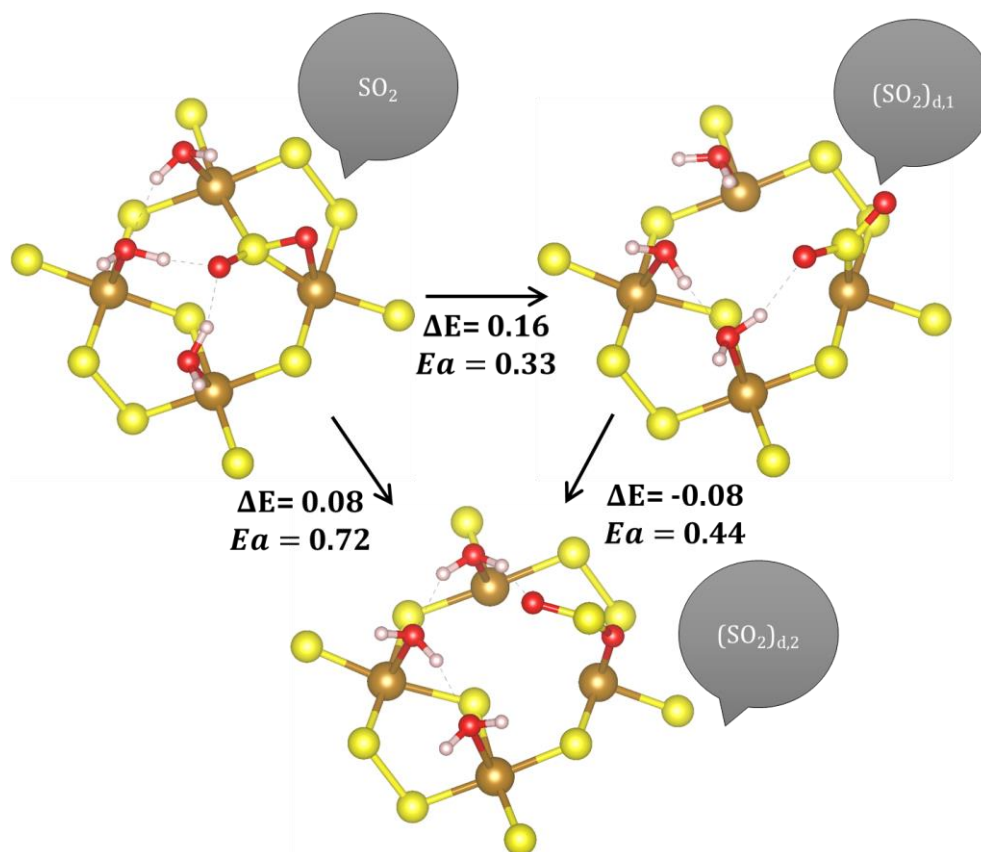


Figure 32- SO_2 dissociation on pyrite surface to form $(\text{SO}_2)_d$.

There is a debate on the literature about which species would be released on the oxidative process. It is not sure whether the sulfate or the bisulfate would be the main product in the chemical reaction.[11] Based on this assumption, proton transference to $(\text{SO}_x)_d$ species were evaluated on the surface. These phenomena occur by Type I reactions

and lead to the formation of $(\text{HSO}_x)_d$ hydrated species. It was observed that the energy barrier to transfer a proton from an adsorbed water on the surface are 0.13 and 0.16 eV for $(\text{HSO}_3)_d$ and $(\text{HSO}_4)_d$, respectively. Both reaction energies were found to be exothermic (see Figure 33), suggesting that hydrated intermediaries are also candidates to be released from the surface.

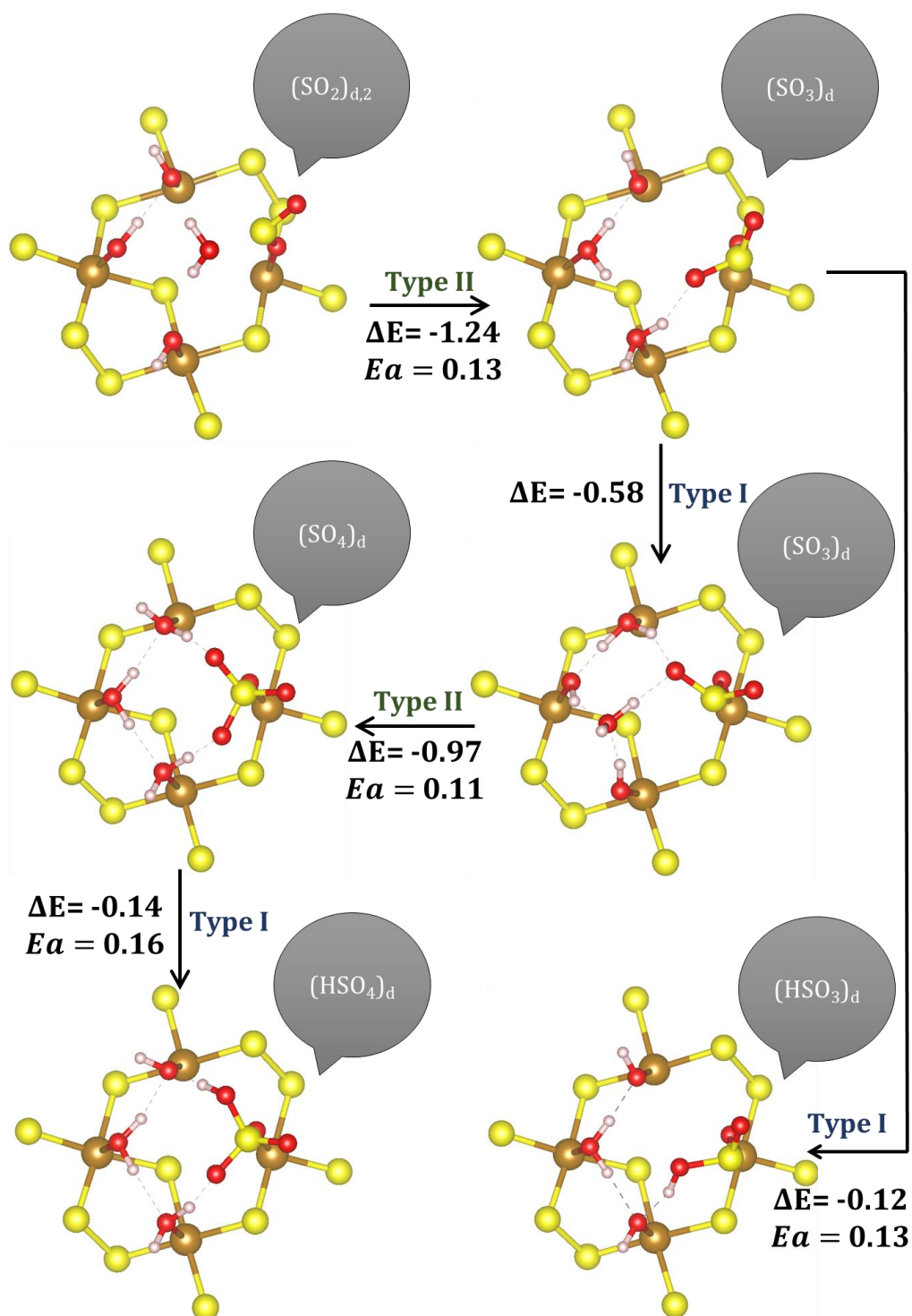


Figure 33- $(\text{SO}_3)_d$, $(\text{HSO}_3)_d$, $(\text{HSO}_4)_d$ and $(\text{SO}_4)_d$ formation on pyrite surface by Type II reactions.

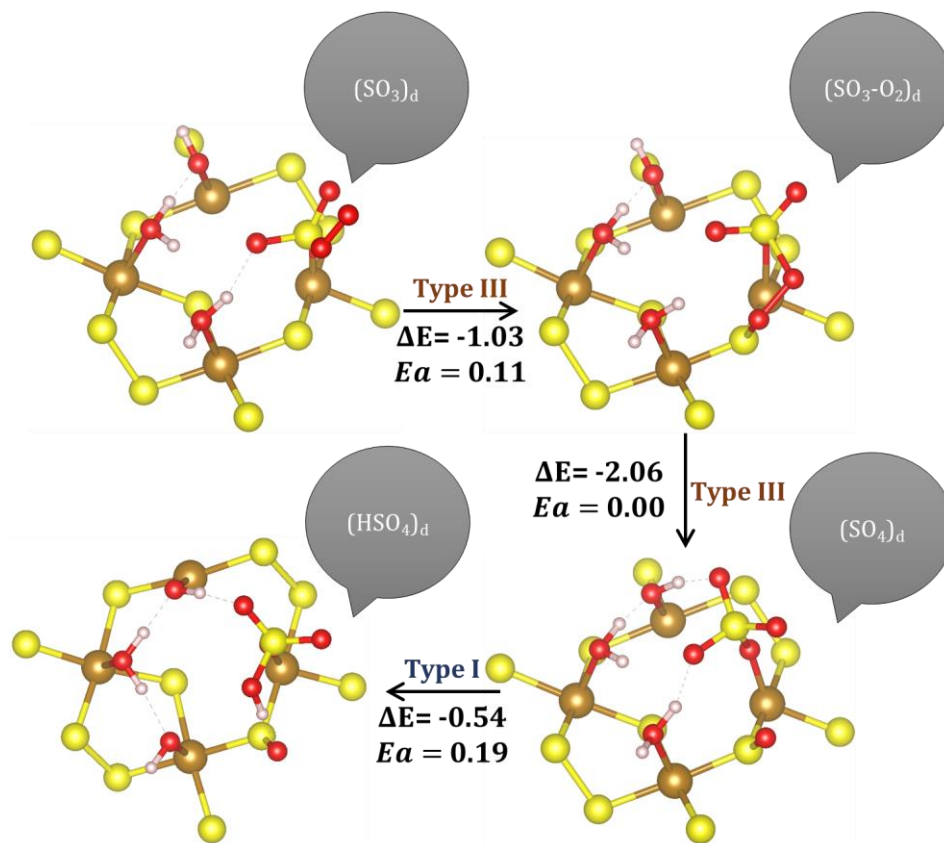


Figure 34- $(\text{SO}_4)_d$ and $(\text{HSO}_4)_d$ and formation on pyrite surface by Type III reactions.

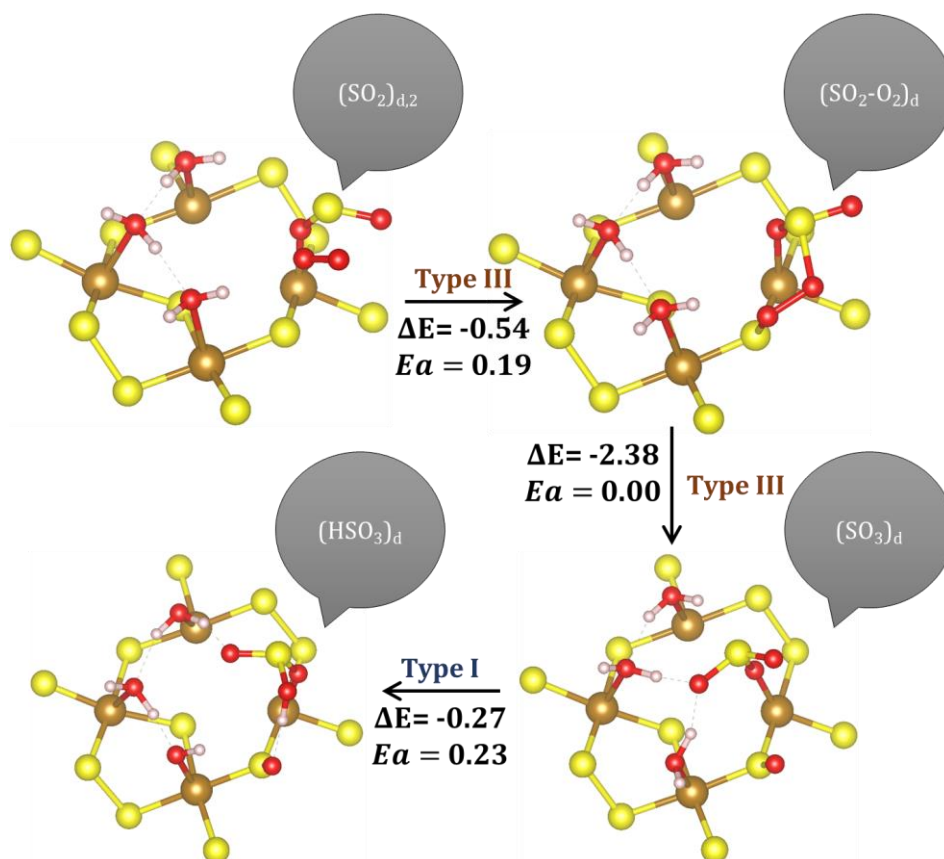


Figure 35- $(\text{SO}_3)_d$ and $(\text{HSO}_3)_d$ and formation on pyrite surface by Type III reactions.

Type III reactions were also evaluated to form $(\text{SO}_x)_d$ sulfoxides. We considered the oxygen molecule in the vicinities of $(\text{SO}_2)_d$ (i.e. about 6 Å from the surface in z-direction). Afterwards, it was evaluated the oxygen adsorption energy as shown in Figure 35 and Figure 34. The most stable structure contains the S-O-O-S bond. In pyrite surfaces, there are many sulfur sites close to surface iron sites. After full optimization, the oxygen molecules formed two bond S-O: one with the sulfur in $(\text{SO}_2)_d$ group and a second with an adjacent S-site on pyrite surface. The optimized oxygen molecule bond is (1.48 Å), which is very close to the O-O bond distance of hydrogen peroxide at the same theoretical level (1.46 Å), indicating that an oxidation process occurred with the reduction of O_2 to O_2^{2-} . The adsorption of the oxygen molecule was estimated to be -0.54 eV and the activation energy is 0.19 eV. Dissociation of O-O from S-O-O-S group was evaluated on the surface to form $(\text{SO}_3)_d$ and $(\text{SO}_4)_d$ on the surface. It was found an exothermic reaction energy (-2.38 eV → Figure 35; and -2.06 eV → Figure 34) with negligible activation energy. This adsorption/dissociation energy is lower than the values found for the adsorption of oxygen on the pyrite Fe-sites[63, 185] (i.e. -0.61 eV for end-on adsorption; -0.72 eV for side-on adsorption; and -1.86 eV for dissociative adsorption). This suggested that the oxygen molecule coming from aqueous medium would prefer to react with the $(\text{SO}_2)_d$ rather than the available iron sites on the surface. Considering the exothermicity of O-O dissociation and the activation energy, we suggest that this reaction would rapidly occur, and the S-O-O-S intermediary will not be observed in the surface. The formation of $(\text{SO}_4)_d$ and $(\text{HSO}_4)_d$ were evaluated from Type III reactions. The results are similar to what is observed to the formation of $(\text{HSO}_3)_d$ and $(\text{SO}_3)_d$ from type II reactions.

Final remarks

One key question is to regard the origin of the oxygen atoms incorporated in the pyrite dissolution products. There is a debate on the literature in order to fully understand the role of the oxygen molecule in the main mechanism. An interesting experiment with isotopically labelled water (H_2^{18}O) was reported. Bailey and Peters[259] were the first to perform such analysis, and Taylor *et al.*[260] confirmed their results in a broad range of temperature using mass spectrometry. Later, Usher *et al.*[261, 262] performed an *in situ* horizontal attenuated total reflectance infrared (HATR-IR) isotope study leading to the

same conclusions. All the authors found that water is the primary source of oxygen atoms present in the sulfates observed in the medium. In agreement with these data, two other results contribute to this hypothesis. The first was developed by Kendelewicz *et al.*[263] which showed that the formation of sulfates occurs very slowly when the surface (100) of pyrite is exposed to only oxygen gas. Furthermore, previously reported DFT calculations[63, 185, 191] show that the formation of the S-O bond of pyrite from the dissociation of the oxygen molecule has activation energy about 2 eV greater than the activation energy of the same reaction in the presence of water.

The mechanism presented in this Chapter provides an explanation for that data. The formation of the $(\text{SO}_2)_d$ group on the surface (Figure 32) enables an oxygen molecule to act on the surface and dissociate to form $(\text{SO}_3)_d$ and/or $(\text{SO}_4)_d$ on the surface (Figure 35 and Figure 34). We named these reactions as Type III reactions, because the oxygen molecule is reacting directly with the surface to form the species $(\text{SO}_x)_d$. The activation energies found are less than 0.19 eV.

It is important to remember that $(\text{SO}_2)_d$ groups can also react with water molecules to form the $(\text{SO}_x)_d$ species by Type II reactions. The activation energies of Type II reactions were found to be around 0.11 and 0.13 eV. The last values are in the same order of magnitude as the same values found for Type III reactions. This result can be used to understand why most water molecules are the source of oxygen atoms for the formation of pyrite dissolution products. One possible explanation would be associated with the abundance of available water molecules to react. Since the reactions have similar activation energies and there are more water molecules available to react than oxygen molecules, it is expected that Type II reactions will prevail over Type III reactions. Only a small portion of the oxygen molecules would react directly with the sulfur atoms to form $(\text{SO}_x)_d$. Another factor that may decrease the amount of available oxygen is Type I reactions that lead to the formation of Fe(III)-OH on the surface. These have low activation energies, and act by consuming the oxygen molecules. In this sense, there will be a competition for the oxygen molecules in both Type I and Type III reactions.

According to our results, a small scheme was developed showing the formation of the $(\text{SO}_x)_d$ species on the (100) pyrite surface. Initially the reaction proceeds from the Type I reactions, where the formation of the Fe(III)-OH species occurs on the surface.

These reactions present the initial stages of the pyrite oxidation reaction. The reason for separating these reactions is that they have activation energies twice smaller than the Type II reactions that lead to the formation of SO₂ on the surface. Type II reactions have the highest activation energies (0.62 and 0.80 eV) and will be the limiting steps of the overall process. In the last stage (stage 3), (SO_x)_d species are formed by the dissociation of SO₂ on the surface. The activation energy for the (SO₂)_d formation is 0.44 eV. The last value is about two times lower than the activation energy estimate for the SO₂ formation on the surface (0.80 eV).

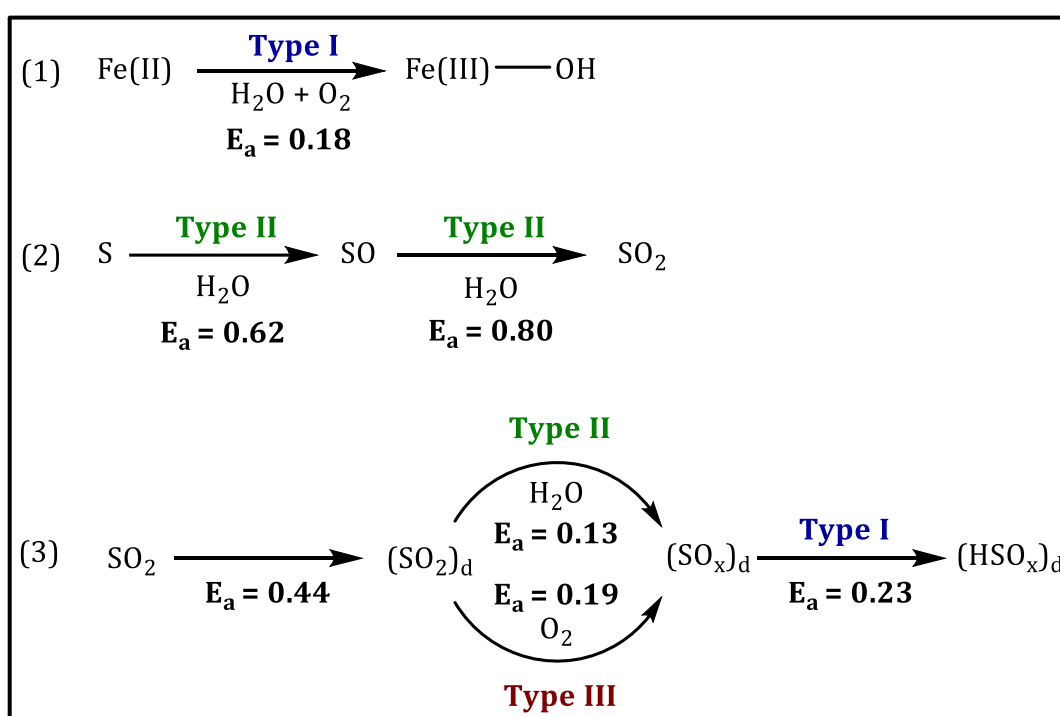
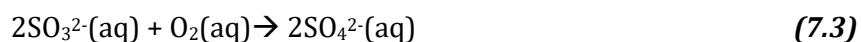


Figure 36- Scheme showing the oxidation mechanism of pyrite (100) surface in three different stages [(1), (2) and (3)]. Activation energies (E_a) for stage (1) quoted from literature.[185] All " E_a " calculations are in the same theoretical level. Values in electronvolt [eV].

The (SO₂)_d species is very reactive and leads to formation of (SO₃)_d and (SO₄)_d on the surface. It can occur via Type II and III reactions. Considering that the difference in activation energies is less than 0.06 eV for the two reactions, it can be concluded that both reaction paths can occur in the process. As previously suggested in the literature,[249] another important fact to note is the desorption of (SO₂)_d and (SO₃)_d to aqueous medium (i.e. forming H₂SO_{3,(aq)} and H₂SO_{4,(aq)}). In this case, the redox reactions shown in Eqs. (7.2) and (7.3) will occur catalysed by the pyrite. However, the results presented in this Chapter

(Figure 35 and Figure 34) indicate that pyrite can catalyse the formation reactions of the species (SO_x). In addition, Type III reactions have the lowest activation energies.



Another aspect considered was the hydrolysis reactions of $(\text{SO}_2)_d$ and $(\text{SO}_3)_d$ on the surface of pyrite to form $(\text{HSO}_x)_d$ species. As shown in Figures 33, 34 and 35, the proton transfer of the waters adsorbed on the surface occurs with activation energies between 0.16 and 0.23 eV. Thus, it is possible to conclude that both $(\text{SO}_x)_d$ and $(\text{HSO}_x)_d$ can desorb to aqueous medium. It is reasonable to argue that this will be driven by the pH of the medium and ionic strength.

Chapter 8 – Final considerations and perspectives

The understanding of the galvanic interactions of mineral sulfides was the major target of the present thesis. To the best of our knowledge there are no attempts to investigate interfaces formed in nature using the first-principles calculations in spite of its evident importance. In this sense, we investigated the FeS₂/FeAsS galvanic-pair at atomic level. Pyrite is known to cleave along the (100) crystalline planes, but the arsenopyrite is polydisperse in nature. Because of that, it was necessary to determine the most probable cleavage planes that would lead to interfaces that minimizes the total energy of the system. The mismatch parameter was evaluated to estimate the commensurability of both phases. This parameter is not based on thermodynamics, but on experimental evidences that phases with distinct crystalline structures do not present favourable values of matching. Thus, three surfaces were selected: “FeS₂(100)/FeAsS(001)”, “FeS₂(100)/FeAsS (100)-As”, and “FeS₂(100)/FeAsS(100)-S”. From the selected structures the structural properties of the surfaces were elaborated. All structures were found to form distorted octahedron sites in the interface region (Figure 10), and, therefore, stability results did not show favourable results. Both the work of adhesion and the energy of formation evaluation have shown that long interface domains are not likely to form in natural environment. These results are consistent with the low miscibility between the two phases.

We note that solid solutions are formed in nature, forming arsenic-containing pyrites. However, this work did not focus on the study of these materials. As mentioned in Chapter 3, Reich *et al.*[60] published a paper taking into account the arsenic incorporation into pyrite bulk, nevertheless no work has yet studied the effect of arsenic atoms on the surface of pyrite. This work may be promising because, as shown by Silva *et al.*,[64, 119] on the arsenopyrite (001) surface the arsenic atoms have greater affinity between the oxygen molecule than the sulfur atoms. The reason is the formation of the stable Fe-O-As intermediary on the surface. Questions about the reaction mechanism can be answered by simple simulation schemes (like the calculations shown in Chapter 7 for pyrite oxidation).

Although the pyrite/arsenopyrite interface are simplified model that do not account for defects present in the natural system, the chemical and electrochemical

properties of the three most stable interfaces were estimated and are described in Chapters 4 and 5. To evaluate if the presence of the interface modifies the local reactivity of the surfaces, the water adsorption (ΔE_{ads}) was used as a parameter. For all FeS₂/FeAsS cleavage structure shown in Figure 17, all ΔE_{ads} values (Table 5) showed a small numerical variations, what indicates that the Lewis acid-basic properties of the surfaces have not changed on the interface region. Even the adsorption energies located on the interface region presented values of ΔE_{ads} close to the value expected on pyrite and arsenopyrite surface.

In this point of the work, we raise the question of how the atomic microstructures of the interface systems can affect the electrochemical behaviour when a galvanic pair is formed. To evaluate the electrochemical effect of the reactions, the Band Offset analysis was performed in Chapter 5. The results of the energy levels showed the electron transfer from arsenopyrite to pyrite would occur (more details in Figure 24). These data suggest that the pyrite would act as the cathode in the reaction while the arsenopyrite would act as the anode of the reaction, undergoing the process of oxidative dissolution. These results showed that the galvanic effect is a purely electronic phenomenon, and that the reaction in the presence of a galvanic pair would occur via electrochemical mechanism. These results are in agreement with experimental observation,[48-55, 215, 216] and, as far as we know, our work was the first attempt to obtain the effects of the interfaces focusing on oxidation of minerals.

The intricate reaction pathway of the sulfide mineral oxidation is a challenge for chemists. Information is being gathered about the surface structure, bonding, electronic structure, spectroscopic properties, and reaction mechanisms. Theoretical calculations provide information at a molecular level testing hypothesis, helping to design and interpret experiments. However, the computer modelling of such complex system is challenging mostly when realistic models involving the interface water/solid is desired.

Chapters 6 represent an attempt to propose a theoretical model that represents what is expected in the real environment. Putting our investigation in perspective the central question is how our computational results connect to the conditions of the real world. It is well known that DFT (and also DFTB) has its limits, but both are also known for their remarkable success in explaining and predicting chemical properties. The

predominant concern is whether or not our model is adequate. In this regard there are a number of factors that could be addressed. The most relevant, from our point of view, are listed below.

1. **Solvation** – Will the inclusion of water bulk molecules shift the relative energetics for the different reaction steps, and will it open up new more favourable reaction routes?
2. **pH and corrosion potential** – Are these sufficiently addressed?
3. **Leaching ions** – How much the dissolved ions (e.g., Fe^{2+} , Fe^{3+} , AsO_3^{3-} , Cl^- , SO_4^{2-} and K^+) impact in the reactions?
4. **Surface and interface models** – Are there other relevant ways to design surfaces and interfaces?

Although computationally demanding chemical models accounting for all of the above may be essential in order to properly model realistic conditions. It is important to note that the assumptions made here in this thesis have been made by an active choice. Future testing will tell if the neglected factors are important or not. The only answer we have is that more simulations should be done in order to answer these questions. By systematically improving the models it is possible to comprehend which factors affect the reactions and which can be safely disregarded. Based on this, DFTB calculations arises as a possibility to include new effects in our chemical model. It is a DFT approximated method, and when properly parametrized can be used as an important tool in order to achieve these goals. But, why is it so relevant?

When it comes to the solvation effects (point 1), it is computationally expensive but very much possible to properly include these effects using modern computational methods. We intend to investigate this further by adding a number of explicit water molecules in the models. Nevertheless, it is expected that the first solvent layer (i.e. water molecules closest to the surface) will have the largest effect on the results. The dynamics of the reaction could be followed by the transition path sampling methods, based on the metadynamics framework as employed elsewhere.[264] In metadynamics thermal effects related to water diffusion on the surface can be included in our calculation. At the moment, our ambitions lies more in applying our new DFTB parameters developed in Chapter 6 (water-matsci) to understand the new mechanism of pyrite studied in Chapter 7. It is a

consensus in the literature that an accurate account of the solvation effect improves the estimation of reaction barriers. The same effect is not fully achieved by static CI-NEB calculations when complex hydrogen bonds are formed over the target surface.

Concerning point 2, the pH and corrosion potential are two factors that have been completely omitted in this thesis. Both pH and corrosion potential are important factors that could alter the reaction mechanisms and energetics significantly. An interesting angle is, furthermore, the possibility that species dissolved in water could interfere in the main reactions. As mentioned in the introduction of this thesis, the concentration of iron ion in the medium defines the leaching potential. In this case, the presence of $\text{Fe}^{2+}/\text{Fe}^{3+}$ pair in aqueous medium defines the reduction potential. In this case, we have a correlation of point 2 and point 3. One such possibility is that anions such as Cl^- , AsO_3^{3-} or SO_4^{2-} adsorb and inhibit the reactions by blocking the active sites. Another possibility is that cations such as K^+ , Fe^{2+} or Fe^{3+} could act catalytically on the reactions by serving, for example, as acceptors of the anions formed during the reactions. Our simulations do not take into account all these possibilities, and more calculations should be done in order to understand and evaluate if these questions are relevant or not. Again, we are putting our efforts on DFTB method for this purpose. DFTB computations allowed to design complex and large systems. Our estimation is that a pyrite (or arsenopyrite) cell with more than 2000 atoms would be necessary to put in the same unit cell water molecules and leaching agents. Then, a realistic simulation will account for more natural effects.

It is appropriate to analyse the choice of surface models (point 4). For pyrite it has been chosen the (100) surface to evaluate reaction energetics for oxidative dissolution of mineral sulfides. Pyrite holds a preferential cleavage plane on the (100) direction, however, it is observed different facets of the mineral in the nature. Therefore, it cannot be excluded that there are other FeS_2 surfaces worth considering besides those included in this work. A second factor that can largely affect the reaction is the impurities in pyrite sample. We start studying it in this thesis, and we know that galvanic effects are likely to happen. In this sense, different galvanic pair should be evaluated to completely understand the real situation of the mineral. The final factor that we will comment is the defects. This is well-known effect and has been evaluated by DFT method.[265] Since

mineral sulfides is prone to defect formation, future investigations should address this topic. Specially a work considering the oxidation of pyrite to $(\text{SO}_x)_d$ species.

As a perspective, it is of interest to use DFTB parameters to understand mainly the oxidation process of pyrite and arsenopyrite in the presence/absence of the galvanic pairs. In a near future, we believe that pyrite and arsenopyrite isolated phases has to be the atomic model for DFTB parameter validation. It would be important to analyse the oxidation of both phases in the presence of leaching ions. Finally, all the effects mentioned above will be evaluated considering the formation of the galvanic pair. Figure 37 shows schematically the complexity of the systems. In order to achieve this goal, the interface models have to be in contact to each other and, at the same time, in contact with the water molecules containing the leaching ions. Furthermore, metadynamics could be used to probe minimum energy reaction-path.

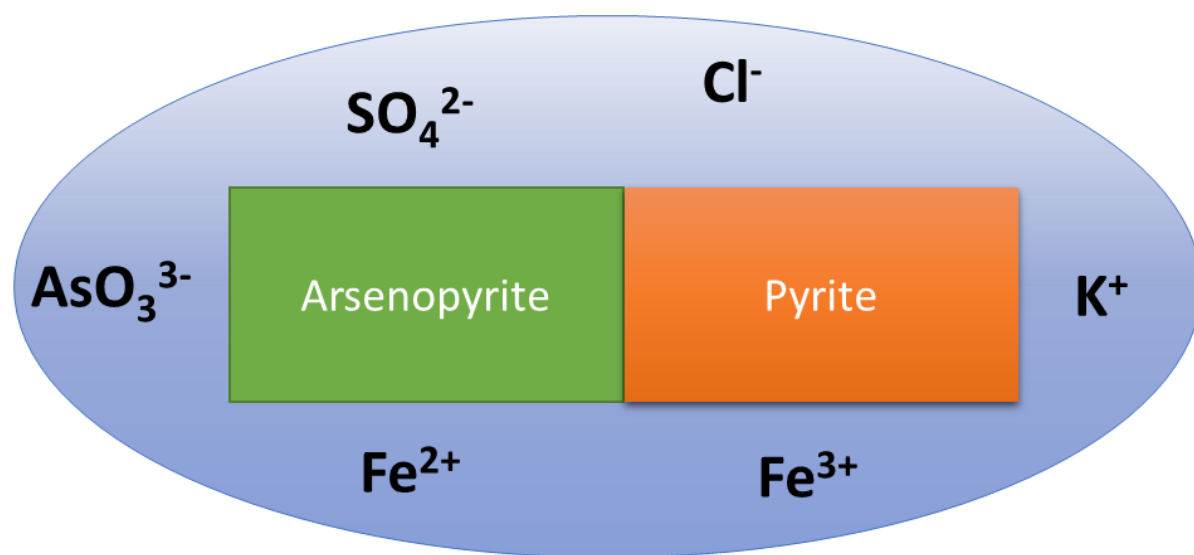


Figure 37- Scheme showing how complex is the oxidation of pyrite/arsenopyrite interface in ambient conditions.

To date, such a realistic model is beyond the state-of-the-art of computational chemistry, however it is important to highlight that this is not just a matter of computational capability. A realistic simulation would require large cell size and include the static and dynamics and different species which invariably would lead to convergence problems, numerical instability and propagation errors. Furthermore, the huge amount of data would need to be analysed in order to get useful conclusions. Therefore, we end this thesis citing P. A. M. Dirac:[266]

“The underlying physical laws necessary for the mathematical theory of a large part of physics and the whole of chemistry are thus completely known, and the difficulty is only that the exact application of these laws leads to equations much too complicated to be soluble.”

But then he completes saying:

“It therefore becomes desirable that approximate practical methods of applying quantum mechanics should be developed, which can lead to an explanation of the main features of complex atomic systems without too much computation.”

It seems that we have touched this paradigm of the computational chemistry.

Bibliography

1. Hanumantha Rao, K. and I. V. Chernyshova, *Challenges in Sulphide Mineral Processing*. The Open Mineral Processing Journal, 2010. **3**(1): p. 7-13.
2. Tossell J.A. and Vaughan D.J., *Theoretical Geochemistry: Application of Quantum Mechanics in the Earth and Mineral Sciences*. Vol. 1. 1992: Oxford University Press: New York.
3. Vaughan, D.J., U. Becker, and K. Wright, *Sulphide mineral surfaces : theory and experiment*. Int. J. Miner. Process., 1997. **51**: p. 1-14.
4. Raveau, B. and T. Sarkar, *Superconducting-like behaviour of the layered Chalcogenides CuS and CuSe below 40 K*. Solid State Sciences, 2011. **13**(10): p. 1874-1878.
5. Mazin, I.I., *Structural and electronic properties of the two-dimensional superconductor CuS with 113-valent copper*. Physical Review B, 2012. **85**(11).
6. de Lima, G.F., H. Avelino de Abreu, and H. Anderson Duarte, *Surface reactivity of the sulfide minerals*, in *Chemical Modelling: Volume 10*. 2014, The Royal Society of Chemistry. p. 153-182.
7. Blöchl, E., et al., *Reactions depending on iron sulfide and linking geochemistry with biochemistry*. Proc. Natl. Acad. Sci. USA, 1992. **89**: p. 8117-8120.
8. Huber, C., *Activated Acetic Acid by Carbon Fixation on (Fe,Ni)S Under Primordial Conditions*. Science, 1997. **276**(5310): p. 245-247.
9. Akcil, A. and S. Koldas, *Acid Mine Drainage (AMD): causes, treatment and case studies*. Journal of Cleaner production, 2006. **14**: p. 1139-1145.
10. Akcil, A. and S. Koldas, *Acid Mine Drainage (AMD): causes, treatment and case studies*. Journal of Cleaner Production, 2006. **14**(12-13): p. 1139-1145.
11. Chandra, A.P. and A.R. Gerson, *The mechanisms of pyrite oxidation and leaching: A fundamental perspective*. Surface Science Reports, 2010. **65**(9): p. 293-315.

12. Ma, S. and J.F. Banfield, *Micron-scale Fe²⁺/Fe³⁺, intermediate sulfur species and O₂ gradients across the biofilm–solution–sediment interface control biofilm organization*. *Geochimica et Cosmochimica Acta*, 2011. **75**(12): p. 3568-3580.
13. Murphy, R. and D. Strongin, *Surface reactivity of pyrite and related sulfides*. *Surface Science Reports*, 2009. **64**(1): p. 1-45.
14. Evangelou, V.P. and Y.L. Zhang, *A review: Pyrite oxidation mechanisms and acid mine drainage prevention*. *Critical Reviews in Environmental Science and Technology*, 1995. **25**(2): p. 141-199.
15. Moses, C.O. and J.S. Herman, *Pyrite oxidation at circumneutral pH*. *Geochimica et Cosmochimica Acta*, 1991. **55**(2): p. 471-482.
16. Moses, C.O., et al., *Aqueous pyrite oxidation by dissolved oxygen and by ferric iron*. *Geochimica et Cosmochimica Acta*, 1987. **51**(6): p. 1561-1571.
17. Hustwit, C.C., T.E. Ackman, and P.E. Erickson, *The role of oxygen transfer in acid mine drainage (AMD) treatment*. *Water Environment Research*, 1992. **64**(6): p. 817-823.
18. Parbhakar-Fox, A. and B.G. Lottermoser, *A critical review of acid rock drainage prediction methods and practices*. *Minerals Engineering*, 2015. **82**: p. 107-124.
19. Weber, P.A., et al., *Improved acid neutralisation capacity assessment of iron carbonates by titration and theoretical calculation*. *Applied Geochemistry*, 2004. **19**(5): p. 687-694.
20. Aghamirian, M.M. and W.T. Yen, *Mechanisms of galvanic interactions between gold and sulfide minerals in cyanide solution*. *Minerals Engineering*, 2005. **18**(4): p. 393-407.
21. Barriga Mateos, F., I. Palencia Pérez, and F. Carranza Mora, *The passivation of chalcopyrite subjected to ferric sulfate leaching and its reactivation with metal sulfides*. *Hydrometallurgy*, 1987. **19**(2): p. 159-167.

22. HISKEY, J.B. and M.E. WADSWORTH, *Galvanic Conversion of Chalcopyrite*. METALLURGICAL TRANSACTIONS B, 1975. **6**(1): p. 183-190.
23. Lorenzen, L. and J.S.J. van Deventer, *Electrochemical interactions between gold and its associated minerals during cyanidation*. Hydrometallurgy, 1992. **30**(1-3): p. 177-193.
24. Madhuchhanda, M., et al., *Galvanic interaction between sulfide minerals and pyrolusite*. Journal of Solid State Electrochemistry, 2000. **4**(4): p. 189-198.
25. Abraitis, P.K., R.A.D. Patrick, and D.J. Vaughan, *Variations in the compositional, textural and electrical properties of natural pyrite: a review*. International Journal of Mineral Processing, 2004. **74**(1-4): p. 41-59.
26. Ahlberg, E. and J. Ásbjörnsson, *Carbon paste electrodes in mineral processing: an electrochemical study of galena*. Hydrometallurgy, 1993. **34**(2): p. 171-185.
27. Broadbent, S.R. and J.M. Hammersley, *Percolation processes*. Mathematical Proceedings of the Cambridge Philosophical Society, 2008. **53**(03): p. 629.
28. Chmielewski, T. and J. Lekki, *The effect of contact of copper sulphide grains on the initial rate of leaching in oxygenated sulphuric acid solution*. Hydrometallurgy, 1985. **15**(2): p. 203-208.
29. Cruz, R., et al., *An experimental strategy to determine galvanic interactions affecting the reactivity of sulfide mineral concentrates*. Hydrometallurgy, 2005. **78**(3-4): p. 198-208.
30. Doyle, F.M. and A.H. Mirza, *Electrochemical oxidation of pyrite samples with known composition and electrical properties*. Electrochemical Proceedings, 1996. **96**(6): p. 203-214.
31. Hammersley, J.M., *Percolation processes*. Mathematical Proceedings of the Cambridge Philosophical Society, 2008. **53**(03): p. 642.

32. Holmes, P.R. and F.K. Grundwell, *Kinetic aspects of galvanic interactions between minerals during dissolution*. Hydrometallurgy, 1995. **39**(1-3): p. 353-375.
33. Majima, H., *How oxidation affects selective flotation of complex sulphide ores*. Canadian Metallurgical Quarterly, 1969. **8**(3): p. 269-273.
34. Nowak, P., E. Krauss, and A. Pomianowski, *The electrochemical characteristics of the galvanic corrosion of sulphide minerals in short-circuited model galvanic cells*. Hydrometallurgy, 1984. **12**(1): p. 95-110.
35. Paramguru, R.K., *Galvanic Interaction Between Manganese Dioxide and Pyrite*. Journal of The Electrochemical Society, 1996. **143**(12): p. 3987.
36. Shao-Horn, Y. and Q.C. Horn, *Chemical, structural and electrochemical comparison of natural and synthetic FeS₂ pyrite in lithium cells*. Electrochimica Acta, 2001. **46**(17): p. 2613-2621.
37. Urbano, G., et al., *Galvanic interactions between galena-sphalerite and their reactivity*. International Journal of Mineral Processing, 2007. **82**(3): p. 148-155.
38. Vasil'yeva, E.G., et al., *The electrode potential of pyrite*. Geochemistry International, 1990. **27**: p. 32-45.
39. Wang, J. and B.A. Freiha, *Evaluation of differential pulse voltammetry at carbon electrodes*. Talanta, 1983. **30**(5): p. 317-322.
40. Abraitis, P.K., et al., *Acid leaching and dissolution of major sulphide ore minerals: processes and galvanic effects in complex systems*. Mineralogical Magazine, 2004. **68**(2): p. 343-351.
41. Berry, V.K., L.E. Murr, and J.B. Hiskey, *Galvanic interaction between chalcopyrite and pyrite during bacterial leaching of low-grade waste*. Hydrometallurgy, 1978. **3**(4): p. 309-326.

42. Dixon, D.G., D.D. Mayne, and K.G. Baxter, *Galvanox™ – a Novel Galvanically-Assisted Atmospheric Leaching Technology for Copper Concentrates*. Canadian Metallurgical Quarterly, 2008. **47**(3): p. 327-336.
43. Dutrizac, J.E., *Elemental sulphur formation during the ferric chloride leaching of chalcopyrite*. Hydrometallurgy, 1990. **23**(2-3): p. 153-176.
44. Liu, Q.Y., H.P. Li, and L. Zhou, *Galvanic interactions between metal sulfide minerals in a flowing system: Implications for mines environmental restoration*. Applied Geochemistry, 2008. **23**(8): p. 2316-2323.
45. Majuste, D., et al., *Quantitative assessment of the effect of pyrite inclusions on chalcopyrite electrochemistry under oxidizing conditions*. Hydrometallurgy, 2012. **113**: p. 167-176.
46. Mehta, A.P. and L.E. Murr, *Fundamental studies of the contribution of galvanic interaction to acid-bacterial leaching of mixed metal sulfides*. Hydrometallurgy, 1983. **9**(3): p. 235-256.
47. Qing You, L., L. Heping, and Z. Li, *Study of galvanic interactions between pyrite and chalcopyrite in a flowing system: implications for the environment*. Environmental Geology, 2006. **52**(1): p. 11-18.
48. Beattie, M.J.V. and G.W. Poling, *A study of the surface oxidation of arsenopyrite using cyclic voltammetry*. International Journal of Mineral Processing, 1987. **20**(1-2): p. 87-108.
49. Costa, M.C., A.M. Botelho do Rego, and L.M. Abrantes, *Characterization of a natural and an electro-oxidized arsenopyrite: a study on electrochemical and X-ray photoelectron spectroscopy*. International Journal of Mineral Processing, 2002. **65**(2): p. 83-108.
50. Cruz, R., et al., *Surface characterization of arsenopyrite in acidic medium by triangular scan voltammetry on carbon paste electrodes*. Hydrometallurgy, 1997. **46**(3): p. 303-319.

51. Huang, G. and S. Grano, *Galvanic interaction between grinding media and arsenopyrite and its effect on flotation*. International Journal of Mineral Processing, 2006. **78**(3): p. 182-197.
52. Huang, G., S. Grano, and W. Skinner, *Galvanic interaction between grinding media and arsenopyrite and its effect on flotation: Part II. Effect of grinding on flotation*. International Journal of Mineral Processing, 2006. **78**(3): p. 198-213.
53. Lázaro, I., et al., *Electrochemical oxidation of arsenopyrite in acidic media*. International Journal of Mineral Processing, 1997. **50**(1-2): p. 63-75.
54. McGuire, M.M., J.F. Banfield, and R.J. Hamers, *Quantitative determination of elemental sulfur at the arsenopyrite surface after oxidation by ferric iron: mechanistic implications*. Geochemical Transactions, 2001. **2**(4): p. 25.
55. Urbano, G., et al., *Pyrite–Arsenopyrite Galvanic Interaction and Electrochemical Reactivity*. The Journal of Physical Chemistry C, 2008. **112**(28): p. 10453-10461.
56. Shuey, R.T., *Semiconducting Ore Minerals. Developments in Economic Geology Series. Vol. 4*. 1975: Elsevier, Amsterdam.
57. Majima, H. and E. Peters, *Electrochemistry of sulphide dissolution in hydrometallurgical systems*. Proc. Int. Min. Proc. Cong., 1968: p. 13pp.
58. Fleet, M.E. and A.H. Mumin, *Gold-bearing arsenian pyrite and marcasite and arsenopyrite from Carlin Trend gold deposits and laboratory synthesis*. American Mineralogist,, 1997. **82**: p. 182-193.
59. G., S., et al., *Oxidation state of gold and arsenic in gold-bearing arsenian pyrite*. American Mineralogist,, 1999. **84**: p. 1071–1079.
60. Reich, M. and U. Becker, *First-principles calculations of the thermodynamic mixing properties of arsenic incorporation into pyrite and marcasite*. Chemical Geology, 2006. **225**(3-4): p. 278-290.

61. Palenik, C.S., et al., "Invisible" gold revealed: Direct imaging of gold nanoparticles in a Carlin-type deposit. *American Mineralogist*, 2004. **89**(10): p. 1359-1366.
62. Dos Santos, E.C., et al., *Stability, Structure, and Electronic Properties of the Pyrite/Arsenopyrite Solid-Solid Interface—A DFT Study*. *The Journal of Physical Chemistry C*, 2017. **121**(14): p. 8042-8051.
63. Sit, P.H.-L., M.H. Cohen, and A. Selloni, *Interaction of Oxygen and Water with the (100) Surface of Pyrite: Mechanism of Sulfur Oxidation*. *The Journal of Physical Chemistry Letters*, 2012. **3**: p. 2409-2414.
64. Silva, J.C.M., *PROPRIEDADES QUÍMICAS DA ARSENOPIRITA, ADSORÇÃO DE AGENTES LIXIVIANTE E SEU MECANISMO DE OXIDAÇÃO A PARTIR DE CÁLCULOS DFT in Chemistry Department*. 2016, UFMG. p. 148.
65. Duarte, H.A., *Índices de Reatividade química a partir da Teoria do Funcional de Densidade: Formalismos e Perspectivas*. *Quim. Nova*, 2001. **24**: p. 501-508.
66. Koch, W. and M.C. Holthausen, *A Chemist's Guide to Density Functional Theory*. Second Edition ed. 2001.
67. Morgon, N.H., *Computação em química teórica: informações e técnicas*. *Quim. Nova*, 2001. **24**: p. 676-682.
68. Morgon, N.H. and K. Coutinho, *Métodos de Química Teórica e Modelagem Molecular*. First Edition ed. 2007: Livraria da Física. 539.
69. Drude, P., *Zur Elektronentheorie der Metalle*. *Annalen der Physik*, 1900. **306**(3): p. 566-613.
70. Hauer, F.v., *Die elektrische Leitfähigkeit von Metallen*. *Annalen der Physik*, 1916. **356**(18): p. 189-219.
71. Kittel, C., *Introdução à Física do Estado Sólido* 2006: LTC.
72. Ashcroft, N.W. and N.D. Mermin, *Física do Estado Sólido* 2011: CENGAGE Learning. 870.

73. Hohenberg, P. and W. Kohn, *Inhomogeneous Electron Gas*. Physical Review, 1964. **136**(3B): p. B864-B871.
74. Kohn, W. and L.J. Sham, *Self-Consistent Equations Including Exchange and Correlation Effects*. Physical Review, 1965. **140**(4A): p. A1133-A1138.
75. Levy, M., *Universal variational functionals of electron densities, first-order density matrices, and natural spin-orbitals and solution of the v -representability problem*. Proceedings of the National Academy of Sciences, 1979. **76**(12): p. 6062-6065.
76. Parr, R.G. and W. Yang, *Density-functional theory of the electronic structure of molecules*. Annu Rev Phys Chem, 1995. **46**: p. 701-28.
77. Parr, R.G., *Density Functional Theory*. Annu Rev Phys Chem, 1983. **34**(1): p. 631-656.
78. Perdew, J.P. and K. Burke, *Comparison shopping for a gradient-corrected density functional*. International Journal of Quantum Chemistry, 1996. **57**(3): p. 309-319.
79. Vosko, S.H., L. Wilk, and M. Nusair, *Accurate spin-dependent electron liquid correlation energies for local spin density calculations: a critical analysis*. Canadian Journal of Physics, 1980. **58**(8): p. 1200-1211.
80. Slater, J.C., *A Simplification of the Hartree-Fock Method*. Physical Review, 1951. **81**(3): p. 385-390.
81. Becke, A.D., *Density-functional thermochemistry. I. The effect of the exchange-only gradient correction*. The Journal of chemical physics, 1992. **96**(3): p. 2155.
82. Perdew, J.P., *Accurate density functional for the energy: Real-space cutoff of the gradient expansion for the exchange hole*. Phys Rev Lett, 1985. **55**(16): p. 1665-1668.
83. Perdew, J.P. and W. Yue, *Accurate and simple density functional for the electronic exchange energy: Generalized gradient approximation*. Physical Review B, 1986. **33**(12): p. 8800-8802.

84. Perdew, J.P. and W. Yue, *Accurate and simple density functional for the electronic exchange energy: Generalized gradient approximation*. Phys Rev B Condens Matter, 1986. **33**(12): p. 8800-8802.
85. Becke, A.D., *Density-functional exchange-energy approximation with correct asymptotic behavior*. Physical Review A, 1988. **38**(6): p. 3098-3100.
86. Lee, C., W. Yang, and R.G. Parr, *Development of the Colle-Salvetti correlation-energy formula into a functional of the electron density*. Physical Review B, 1988. **37**(2): p. 785-789.
87. Becke, A.D., *A new mixing of Hartree-Fock and local density-functional theories*. The Journal of chemical physics, 1993. **98**(2): p. 1372.
88. Kim, K. and K.D. Jordan, *Comparison of Density Functional and MP2 Calculations on the Water Monomer and Dimer*. The Journal of Physical Chemistry, 1994. **98**(40): p. 10089-10094.
89. Stephens, P.J., et al., *Ab Initio Calculation of Vibrational Absorption and Circular Dichroism Spectra Using Density Functional Force Fields*. The Journal of Physical Chemistry, 1994. **98**(45): p. 11623-11627.
90. Perdew, J.P., M. Ernzerhof, and K. Burke, *Rationale for mixing exact exchange with density functional approximations*. The Journal of chemical physics, 1996. **105**(22): p. 9982.
91. Adamo, C. and V. Barone, *Toward reliable density functional methods without adjustable parameters: The PBE0 model*. The Journal of chemical physics, 1999. **110**(13): p. 6158.
92. Heyd, J., G.E. Scuseria, and M. Ernzerhof, *Hybrid functionals based on a screened Coulomb potential*. The Journal of chemical physics, 2003. **118**(18): p. 8207.
93. Payne, M.C., et al., *Iterative minimization techniques for ab initio total-energy calculations: molecular dynamics and conjugate gradients*. Reviews of Modern Physics, 1992. **64**(4): p. 1045-1097.

94. Phillips, J.C. and L. Kleinman, *New Method for Calculating Wave Functions in Crystals and Molecules*. Physical Review, 1959. **116**(2): p. 287-294.
95. Kaxiras, E., *Atomic Electronic Structure of Solids*. 2003: Cambridge University Press.
96. Dudarev, S.L., et al., *Electron-energy-loss spectra and the structural stability of nickel oxide: An LSDA+U study*. Physical Review B, 1998. **57**(3): p. 1505-1509.
97. Liechtenstein, A.I., V.I. Anisimov, and J. Zaanen, *Density-functional theory and strong interactions: Orbital ordering in Mott-Hubbard insulators*. Physical Review B, 1995. **52**(8): p. R5467-R5470.
98. Himmetoglu, B., et al., *Hubbard-corrected DFT energy functionals: The LDA+U description of correlated systems*. International Journal of Quantum Chemistry, 2014. **114**(1): p. 14-49.
99. Becke, A.D. and K.E. Edgecombe, *A simple measure of electron localization in atomic and molecular systems*. The Journal of chemical physics, 1990. **92**(9): p. 5397.
100. de Oliveira, C., et al., *Native Defects in α -Mo₂C: Insights from First-Principles Calculations*. The Journal of Physical Chemistry C, 2014. **118**(44): p. 25517-25524.
101. De Santis, L. and R. Resta, *Surface reconstructions and bonding via the electron localization function: the case of Si(001)*. Solid State Communications, 1999. **111**(10): p. 583-588.
102. Savin, A., et al., *Electron Localization in Solid-State Structures of the Elements: the Diamond Structure*. Angewandte Chemie International Edition in English, 1992. **31**(2): p. 187-188.
103. Silvi, B. and A. Savin, *Classification of chemical bonds based on topological analysis of electron localization functions*. Nature, 1994. **371**(6499): p. 683-686.
104. Soares, A.L., et al., *The Stability and Structural, Electronic and Topological Properties of Covellite (001) Surfaces*. ChemistrySelect, 2016. **1**(11): p. 2730-2741.

105. Frauenheim, T., et al., *A self-consistent charge density-functional based tight-binding method for predictive materials simulations in physics, chemistry and biology*. . Physica Status Solidi B-Basic Solid State Physics,, 2000. **217(1)**: p. 41-62.
106. Elstner, M., et al., *Self-consistent-charge density-functional tight-binding method for simulations of complex materials properties*. Physical Review B, 1998. **58(11)**: p. 7260-7268.
107. Sheppard, D., R. Terrell, and G. Henkelman, *Optimization methods for finding minimum energy paths*. J Chem Phys, 2008. **128(13)**: p. 134106.
108. Dewar, M.J.S., E.F. Healy, and J.J.P. Stewart, *Location of transition states in reaction mechanisms*. Journal of the Chemical Society, Faraday Transactions 2, 1984. **80(3)**.
109. Henkelman, G., B.P. Uberuaga, and H. Jónsson, *A climbing image nudged elastic band method for finding saddle points and minimum energy paths*. The Journal of Chemical Physics, 2000. **113(22)**: p. 9901-9904.
110. Klimes, J., D.R. Bowler, and A. Michaelides, *A critical assessment of theoretical methods for finding reaction pathways and transition states of surface processes*. J Phys Condens Matter, 2010. **22(7)**: p. 074203.
111. Qian, G.-R., et al., *Variable cell nudged elastic band method for studying solid–solid structural phase transitions*. Computer Physics Communications, 2013. **184(9)**: p. 2111-2118.
112. Szabo, A. and N.S. Ostlund, *Modern Quantum Chemistry: Introduction to Advanced Electronic Structure Theory*. . 1996: Dover Publications, INC, Mineola,. 480.
113. Aradi, B., B. Hourahine, and T. Frauenheim, *DFTB+, a sparse matrix-based implementation of the DFTB method*. J Phys Chem A, 2007. **111(26)**: p. 5678-84.
114. Guimaraes, L., et al., *Imogolite nanotubes: stability, electronic, and mechanical properties*. ACS Nano, 2007. **1(4)**: p. 362-8.

115. Lourenço, M.P., et al., *FASP: a framework for automation of Slater–Koster file parameterization*. Theoretical Chemistry Accounts, 2016. **135**(11).
116. Oliveira, A.F., et al., *Density-Functional Based Tight-Binding: an Approximate DFT Method*. J. Braz. Chem. Soc., 2009. **20**(7): p. 1193-1205.
117. Slater, J.C. and G.F. Koster, *Simplified LCAO Method for the Periodic Potential Problem*. Physical Review, 1954. **94**(6): p. 1498-1524.
118. Zhechkov, L., et al., *An Efficient a Posteriori Treatment for Dispersion Interaction in Density-Functional-Based Tight Binding*. J Chem Theory Comput, 2005. **1**(5): p. 841-7.
119. Silva, J.C.M., H.a. De Abreu, and H.a. Duarte, *Electronic and structural properties of bulk arsenopyrite and its cleavage surfaces – a DFT study*. RSC Adv., 2014. **5**: p. 2013-2023.
120. Aliano, A., G. Cicero, and A. Catellani, *Origin of the accumulation layer at the InN/a-In2O3 interface*. ACS Appl Mater Interfaces, 2015. **7**(9): p. 5415-9.
121. Arya, A. and E.A. Carter, *Structure, bonding, and adhesion at the ZrC(100)/Fe(110) interface from first principles*, in *Surface Science*. 2004. p. 103-120.
122. Asta, M., et al., *Solidification microstructures and solid-state parallels: Recent developments, future directions*. Acta Materialia, 2009. **57**(4): p. 941-971.
123. Batyrev, I., A. Alavi, and M. Finnis, *Equilibrium and adhesion of Nb/sapphire: The effect of oxygen partial pressure*. Physical Review B, 2000. **62**(7): p. 4698-4706.
124. Biswas, D. and K. Maiti, *Surface-interface anomalies and topological order in Bi2Se3*. Epl, 2015. **110**(1): p. 17001.
125. Dai, H.S., et al., *First-principle study of the AlP/Si interfacial adhesion*. Physica B-Condensed Matter, 2010. **405**(2): p. 573-578.

126. Dalverny, A.L., J.S. Filhol, and M.L. Doublet, *Interface electrochemistry in conversion materials for Li-ion batteries*. Journal of Materials Chemistry, 2011. **21**(27): p. 10134-10142.
127. Dmitriev, S.V., et al., *Atomistic structure of the Cu(111)/ α -Al₂O₃(0001) interface in terms of interatomic potentials fitted to ab initio results*. Acta Materialia, 2004. **52**(7): p. 1959-1970.
128. Ehlers, F.J.H. and R. Holmestad, *Ab initio based interface modeling for fully coherent precipitates of arbitrary size in Al alloys*. Computational Materials Science, 2013. **72**: p. 146-157.
129. Frolov, T. and Y. Mishin, *Thermodynamics of coherent interfaces under mechanical stresses. I. Theory*. Physical Review B, 2012. **85**(22).
130. Hashibon, A. and C. Elsasser, *Approaches to atomistic triple-line properties from first-principles*. Scripta Materialia, 2010. **62**(12): p. 939-944.
131. Hashibon, A., et al., *First-principles study of thermodynamical and mechanical stabilities of thin copper film on tantalum*. Physical Review B, 2007. **76**(24).
132. Heifets, E., et al., *Electronic structure and thermodynamic stability of double-layered SrTiO₃(001) surfaces: Ab initio simulations*. Physical Review B, 2007. **75**(11).
133. Ibagon, I., M. Bier, and S. Dietrich, *Three-phase contact line and line tension of electrolyte solutions in contact with charged substrates*. J Phys Condens Matter, 2016. **28**(24): p. 244015.
134. Jiang, D. and E. Carter, *Prediction of strong adhesion at the MoSi/Fe interface*. Acta Materialia, 2005. **53**(17): p. 4489-4496.
135. Liu, L.M., S.Q. Wang, and H.Q. Ye, *First-principles study of metal/nitride polar interfaces: Ti/TiN*. Surface and Interface Analysis, 2003. **35**(10): p. 835-841.

136. Liu, L.M., S.Q. Wang, and H.Q. Ye, *Adhesion of metal-carbide/nitride interfaces: Al/TiC and Al/TiN*. Journal of Physics-Condensed Matter, 2003. **15**(47): p. 8103-8114.
137. Liu, L.M., S.Q. Wang, and H.Q. Ye, *Atomic and electronic structures of the lattice mismatched metal-ceramic interface*. Journal of Physics-Condensed Matter, 2004. **16**(32): p. 5781-5790.
138. Liu, L.M., S.Q. Wang, and H.Q. Ye, *First-principles study of polar Al/TiN(111) interfaces*. Acta Materialia, 2004. **52**(12): p. 3681-3688.
139. Liu, L.M., S.Q. Wang, and H.Q. Ye, *Adhesion and bonding of the Al/TiC interface*. Surface Science, 2004. **550**(1-3): p. 46-56.
140. Malyi, O.I., et al., *Effect of sulfur impurity on the stability of cubic zirconia and its interfaces with metals*. Journal of Materials Chemistry, 2011. **21**(33): p. 12363-12368.
141. Martin, L., et al., *First principles calculations of solid-solid interfaces: an application to conversion materials for lithium-ion batteries*. Journal of Materials Chemistry, 2012. **22**(41): p. 22063-22071.
142. Nokbin, S., J. Limtrakul, and K. Hermansson, *DFT plane-wave calculations of the Rh/MgO(001) interface*. Surface Science, 2004. **566-568**: p. 977-982.
143. Padilha, A.C.M., A.R. Rocha, and G.M. Dalpian, *DFT+USimulation of theTi407-TiO2Interface*. Physical Review Applied, 2015. **3**(2).
144. Piskunov, S. and R.I. Eglitis, *First principles hybrid DFT calculations of BaTiO3/SrTiO3(001) interface*. Solid State Ionics, 2015. **274**: p. 29-33.
145. Pu, L., et al., *Structural properties of Ge on SrTiO3 (001) surface and Ge/SrTiO3 interface*. Journal of Applied Physics, 2015. **117**(10): p. 105307.
146. Radican, K., et al., *Epitaxial molybdenum oxide grown onMo(110): LEED, STM, and density functional theory calculations*. Physical Review B, 2007. **75**(15).

147. Saiz, E., R.M. Cannon, and A.P. Tomsia, *High-temperature wetting and the work of adhesion in metal/oxide systems*. Annual Review of Materials Research, 2008. **38**(1): p. 197-226.
148. Shu, G.G., Q. Xu, and P. Wu, *Study of wetting on chemically softened interfaces by using combined solution thermodynamics and DFT calculations: forecasting effective softening elements*. ACS Appl Mater Interfaces, 2015. **7**(14): p. 7576-83.
149. Sinnott, S.B. and E.C. Dickey, *Ceramic/metal interface structures and their relationship to atomic- and meso-scale properties*. Materials Science & Engineering R-Reports, 2003. **43**(1-2): p. 1-59.
150. Stroppa, A. and M. Peressi, *Structural properties and stability of defected ZnSe/GaAs(001) interfaces*. Computational Materials Science, 2005. **33**(1-3): p. 256-262.
151. Wang, X.G. and J.R. Smith, *Si/Cu interface structure and adhesion*. Phys Rev Lett, 2005. **95**(15): p. 156102.
152. Wei, W., et al., *Density Functional Characterization of the Electronic Structures and Band Bending of Rutile RuO₂/TiO₂(110) Heterostructures*. Journal of Physical Chemistry C, 2015. **119**(22): p. 12394-12399.
153. Wood, G.J. and L.A. Bursill, *The Formation Energy of Crystallographic Shear Planes in TiO₂n-1*. Proceedings of the Royal Society of London Series a-Mathematical Physical and Engineering Sciences, 1981. **375**(1760): p. 105-125.
154. Yadav, S.K., et al., *First-principles study of Cu/TiN and Al/TiN interfaces: weak versus strong interfaces*. Modelling and Simulation in Materials Science and Engineering, 2014. **22**(3): p. 035020.
155. Zaoui, A., *Energetic stabilities and the bonding mechanism of ZnO{0001}/Pd(111) interfaces*. Physical Review B, 2004. **69**(11).
156. Zhang, Q., et al., *Adhesion and nonwetting-wetting transition in the Al/ α -Al₂O₃ interface*. Physical Review B, 2004. **69**(4).

157. Zhang, W. and J.R. Smith, *Nonstoichiometric interfaces and Al₂O₃ adhesion with Al and Ag*. Phys Rev Lett, 2000. **85**(15): p. 3225-8.
158. Zhang, W., J.R. Smith, and A.G. Evans, *The connection between ab initio calculations and interface adhesion measurements on metal/oxide systems: Ni/Al₂O₃ and Cu/Al₂O₃*. Acta Materialia, 2002. **50**(15): p. 3803-3816.
159. Zhao, G.L., et al., *First-principles study of the alpha-Al₂O₃(0001)/Cu(111) interface*. Interface Science, 1996. **3**(4): p. 289-302.
160. Zhukovskii, Y.F., et al., *First principles slab calculations of the regular Cu/MgO(001) interface*. Surface Science, 2004. **566-568**: p. 122-129.
161. Wang, S. and H. Ye, *Theoretical studies of solid–solid interfaces*. Current Opinion in Solid State and Materials Science, 2006. **10**(1): p. 26-32.
162. Giannozzi, P., et al., *Quantum Espresso: a modular and open-source software project for quantum simulations of materials*. Journal of physics. Condensed matter, 2009. **21**: p. 395502.
163. Perdew, J.P., K. Burke, and M. Ernzerhof, *Generalized Gradient Approximation Made Simple*. Phys Rev Lett, 1996. **77**(18): p. 3865-3868.
164. Beeman, D., *Some multistep methods for use in molecular dynamics calculations*. Journal of Computational Physics, 1976. **20**(2): p. 130-139.
165. Parrinello, M. and R. A., *Polymorphic transitions in single crystals: A new molecular dynamics method*. Journal of Applied Physics, 1981. **52**(12): p. 7182.
166. Ferrer, I.J., et al., *About the band gap nature of FeS₂ as determined from optical and photoelectrochemical measurements*. Solid State Communications, 1990. **74**(9): p. 913-916.
167. Ennaoui, A., et al., *Iron disulfide for solar energy conversion*. Solar Energy Materials and Solar Cells, 1993. **29**(4): p. 289-370.

168. Almeida, C.M.V.B. and B.F. Giannetti, *Electrochemical study of arsenopyrite weathering*. Physical Chemistry Chemical Physics, 2003. **5**(3): p. 604-610.
169. Krishnamoorthy, A., et al., *Electronic states of intrinsic surface and bulk vacancies in FeS₂*. J Phys Condens Matter, 2013. **25**(4): p. 045004.
170. Morales-Garcia, A., et al., *First-principles calculations and electron density topological analysis of covellite (CuS)*. J Phys Chem A, 2014. **118**(31): p. 5823-31.
171. Chase, M.W., Jr., *NIST-JANAF Thermochemical Tables*. 1998: J. Phys. Chem. Ref. Data. p. 1-1951.
172. Pokrovski, G.S., S. Kara, and J. Roux, *Stability and solubility of arsenopyrite, FeAsS, in crustal fluids*. Geochimica et Cosmochimica Acta, 2002. **66**(13): p. 2361-2378.
173. Brostigen, G. and A. Kjekshus, *Redetermined Crystal Structure of FeS₂ (Pyrite)*. Acta Chemica Scandinavica, 1969. **23**(6): p. 2186-&.
174. Bindi, L., et al., *STOICHIOMETRIC ARSENOPYRITE, FeAsS, FROM LA ROCHE-BALUE QUARRY, LOIRE-ATLANTIQUE, FRANCE: CRYSTAL STRUCTURE AND MOSSBAUER STUDY*. Canadian Mineralogist, 2012. **50**(2): p. 471-479.
175. Andersson, K.J., et al., *Preparation, Structure, and Orientation of Pyrite FeS₂{100} Surfaces: Anisotropy, Sulfur Monomers, Dimer Vacancies, and a Possible FeS Surface Phase*. The Journal of Physical Chemistry C, 2014. **118**(38): p. 21896-21903.
176. Corkhill, C., M. Warren, and D. Vaughan, *Investigation of the electronic and geometric structures of the (110) surfaces of arsenopyrite (FeAsS) and enargite (Cu₃AsS₄)*. MINERALOGICAL MAGAZINE, 2011. **75**(1): p. 45-63.
177. Hung, A., et al., *Density-functional theory studies of pyrite FeS₂(100) and (110) surfaces*. Surface Science, 2002. **513**(3): p. 511-524.
178. Fan, D.W., et al., *X-ray diffraction study of arsenopyrite at high pressure*. Physics and Chemistry of Minerals, 2010. **38**(2): p. 95-99.

179. Merkel, S., et al., *Equation of state, elasticity, and shear strength of pyrite under high pressure*. *Physics and Chemistry of Minerals*, 2002. **29**(1): p. 1-9.
180. Liu, L.M., S.Q. Wang, and H.Q. Ye, *First-principles study of the effect of hydrogen on the metal-ceramic interface*. *Journal of Physics-Condensed Matter*, 2005. **17**(35): p. 5335-5348.
181. Hulliger, F. and E. Mooser, *Semiconductivity in pyrite, marcasite and arsenopyrite phases*. *Journal of Physics and Chemistry of Solids*, 1965. **26**(2): p. 429-433.
182. Pearson, W.B., *Compounds with the marcasite structure*. *Zeitschrift für Kristallographie - Crystalline Materials*, 1965. **121**(1-6).
183. Nickel, E.H., *Structural stability of minerals with the pyrite, marcasite, arsenopyrite and lollingite structures*. *Can. Mineral.*, 1968. **9**(3): p. 311-321.
184. de Leeuw, N.H., et al., *Modeling the Surface Structure and Reactivity of Pyrite: Introducing a Potential Model for FeS₂*. *The Journal of Physical Chemistry B*, 2000. **104**: p. 7969-7976.
185. Dos Santos, E.C., J.C. de Mendonça Silva, and H.A. Duarte, *Pyrite Oxidation Mechanism by Oxygen in Aqueous Medium*. *The Journal of Physical Chemistry C*, 2016. **120**(5): p. 2760-2768.
186. Eyert, V., et al., *Electronic structure of FeS₂: The crucial role of electron-lattice interaction*. *Physical Review B*, 1998. **57**(11): p. 6350-6359.
187. Gudelli, V.K., et al., *Phase Stability and Thermoelectric Properties of the Mineral FeS₂: An Ab Initio Study*. *The Journal of Physical Chemistry C*, 2013. **117**(41): p. 21120-21131.
188. Hung, A., et al., *Density-functional theory studies of pyrite FeS₂ (111) and (210) surfaces*. *Surface Science*, 2002. **520**(1-2): p. 111-119.
189. Opahle, I., K. Koepernik, and H. Eschrig, *Full-potential band-structure calculation of iron pyrite*. *Physical Review B*, 1999. **60**(20): p. 14035-14041.

190. Rosso, K.E., U. Becker, and M.F. Hochella, *The interaction of pyrite {100} surfaces with O₂ and H₂O: Fundamental oxidation mechanisms*. American Mineralogist, 1999. **84**: p. 1549-1561.
191. Stirling, A., M. Bernasconi, and M. Parrinello, *Ab initio simulation of water interaction with the (100) surface of pyrite*. The Journal of chemical physics, 2003. **118**: p. 8917-8926.
192. Stirling, A., M. Bernasconi, and M. Parrinello, *Defective pyrite (100) surface: An ab initio study*. Physical Review B, 2007. **75**(16): p. 165406.
193. Bither, T.A., et al., *Transition metal pyrite dichalcogenides. High-pressure synthesis and correlation of properties*. Inorganic Chemistry, 1968. **7**(11): p. 2208-2220.
194. Corkhill, C.L., et al., *The oxidative dissolution of arsenopyrite (FeAsS) and enargite (Cu₃AsS₄) by Leptospirillum ferrooxidans*. Geochimica et Cosmochimica Acta, 2008. **72**(23): p. 5616-5633.
195. Ford, M. and C.C. Ferguson, *Cleavage Strain in the Variscan Fold Belt, County Cork, Ireland, Estimated from Stretched Arsenopyrite Rosettes*. Journal of Structural Geology, 1985. **7**(2): p. 217-223.
196. Nesbitt, H.W., I.J. Muir, and A.R. Prarr, *Oxidation of arsenopyrite by air and air-saturated, distilled water, and implications for mechanism of oxidation*. Geochimica et Cosmochimica Acta, 1995. **59**(9): p. 1773-1786.
197. Jones, R.A. and H.W. Nesbitt, *XPS evidence for Fe and As oxidation states and electronic states in loellingite (FeAs₂)*. American Mineralogist, 2002. **87**(11-12): p. 1692-1698.
198. Bindi, L., et al., *STOICHIOMETRIC ARSENOPYRITE, FeAsS, FROM LA ROCHE-BALUE QUARRY, LOIRE-ATLANTIQUE, FRANCE: CRYSTAL STRUCTURE AND MOSSBAUER STUDY*. The Canadian Mineralogist, 2012. **50**(2): p. 471-479.
199. Murphy, R. and D.R. Strongin, *Surface reactivity of pyrite and related sulfides*. Surface Science Reports, 2009. **64**(1): p. 1-45.

200. Li, E.K., et al., *Localized and Bandlike Valence-Electron States in FeS₂ and NiS₂*. *Phys Rev Lett*, 1974. **32**(9): p. 470-472.
201. van der Heide, H., et al., *X-ray photoelectron spectra of 3d transition metal pyrites*. *Journal of Solid State Chemistry*, 1980. **33**(1): p. 17-25.
202. Folmer, J.C.W., F. Jellinek, and G.H.M. Calis, *The electronic structure of pyrites, particularly CuS₂ and Fe_{1-x}Cu_xSe₂: An XPS and Mössbauer study*. *Journal of Solid State Chemistry*, 1988. **72**(1): p. 137-144.
203. Nesbitt, H.W., et al., *Identification of pyrite valence band contributions using synchrotron-excited X-ray photoelectron spectroscopy*. *American Mineralogist*, 2004. **89**(2-3): p. 382-389.
204. Bocquet, A.E., et al., *Electronic structure of 3d transition metal pyrites (M = Fe, Co or Ni) by analysis of the M 2p core-level photoemission spectra*. *J. Phys.: Condens. Matter*, 1996. **8**: p. 2389-2400.
205. Nesbitt, H.W., et al., *Resonant XPS study of the pyrite valence band with implications for molecular orbital contributions*. *American Mineralogist*, 2004. **88**(8-9): p. 1279-1286.
206. Charnock, J.M., et al., *3d transition metal L-edge X-ray absorption studies of the dichalcogenides of Fe, Co and Ni*. *Physics and Chemistry of Minerals*, 1996. **23**(7).
207. Fuess, H., et al., *Crystal structure refinement and electron microscopy of arsenopyrite*. *Zeitschrift für Kristallographie*, 1987. **179**(1-4): p. 335-346.
208. Goodenough, J.B., *Energy bands in TX₂ compounds with pyrite, marcasite, and arsenopyrite structures*. *Journal of Solid State Chemistry*, 1972. **5**(1): p. 144-152.
209. Tossell, J.A., D.J. Vaughan, and J.K. Burdett, *Pyrite, marcasite, and arsenopyrite type minerals: Crystal chemical and structural principles*. *Physics and Chemistry of Minerals*, 1981. **7**(4): p. 177-184.

210. Savage, K.S., et al., *Arsenic speciation in pyrite and secondary weathering phases, Mother Lode Gold District, Tuolumne County, California*. Applied Geochemistry, 2000. **15**(8): p. 1219-1244.
211. Simon, G., S.E. Kesler, and S. Chryssoulis, *Geochemistry and textures of gold-bearing arsenian pyrite, Twin Creeks, Nevada; implications for deposition of gold in carlin-type deposits*. Economic Geology, 1999. **94**(3): p. 405-421.
212. Corkhill, C.L., M.C. Warren, and D.J. Vaughan, *Investigation of the electronic and geometric structures of the (110) surfaces of arsenopyrite (FeAsS) and enargite (Cu₃AsS₄)*. Mineralogical Magazine, 2011. **75**(1): p. 45-63.
213. Eggleston, C.M., J.-J. Ehrhardt, and W. Stumm, *Surface structural controls on pyrite oxidation kinetics; an XPS-UPS, STM, and modeling study*. American Mineralogist, 1996. **81**(9-10): p. 1036-1056.
214. Qi, Y. and L.G. Hector, *Adhesion and adhesive transfer at aluminum/diamond interfaces: A first-principles study*. Physical Review B, 2004. **69**(23).
215. Gu, G.-h., et al., *Galvanic coupling and its effect on origin potential flotation system of sulfide minerals*. Journal of Central South University of Technology, 2004. **11**(3): p. 275-279.
216. Deng, S., et al., *Catalytic effect of pyrite on the leaching of arsenopyrite in sulfuric acid and acid culture medium*. Electrochimica Acta, 2018. **263**: p. 8-16.
217. Ke, B., et al., *DFT study on the galvanic interaction between pyrite (100) and galena (100) surfaces*. Applied Surface Science, 2016. **367**: p. 270-276.
218. Pettersson, L.G.M., R.H. Henchman, and A. Nilsson, *Water—The Most Anomalous Liquid*. Chemical Reviews, 2016. **116**(13): p. 7459-7462.
219. Nilsson, A. and L.G.M. Pettersson, *The structural origin of anomalous properties of liquid water*. Nature Communications, 2015. **6**: p. 8998.

220. Nilsson, A. and L.G.M. Pettersson, *Perspective on the structure of liquid water*. Chemical Physics, 2011. **389**(1): p. 1-34.
221. Björneholm, O., et al., *Water at Interfaces*. Chemical Reviews, 2016. **116**(13): p. 7698-7726.
222. Gillan, M.J., D. Alfè, and A. Michaelides, *Perspective: How good is DFT for water?* The Journal of Chemical Physics, 2016. **144**(13): p. 130901.
223. Wang, J., et al., *Density, structure, and dynamics of water: The effect of van der Waals interactions*. The Journal of Chemical Physics, 2011. **134**(2): p. 024516.
224. Møgelhøj, A., et al., *Ab Initio van der Waals Interactions in Simulations of Water Alter Structure from Mainly Tetrahedral to High-Density-Like*. The Journal of Physical Chemistry B, 2011. **115**(48): p. 14149-14160.
225. Maupin, C.M., B. Aradi, and G.A. Voth, *The self-consistent charge density functional tight binding method applied to liquid water and the hydrated excess proton: benchmark simulations*. J Phys Chem B, 2010. **114**(20): p. 6922-31.
226. Goyal, P., et al., *Molecular simulation of water and hydration effects in different environments: challenges and developments for DFTB based models*. J Phys Chem B, 2014. **118**(38): p. 11007-27.
227. Goyal, P., et al., *Molecular Simulation of Water and Hydration Effects in Different Environments: Challenges and Developments for DFTB Based Models*. The Journal of Physical Chemistry B, 2014. **118**(38): p. 11007-11027.
228. Doemer, M., et al., *In situ parameterisation of SCC-DFTB repulsive potentials by iterative Boltzmann inversion*. Molecular Physics, 2013. **111**(22-23): p. 3595-3607.
229. Gaus, M., et al., *Automatized parametrization of SCC-DFTB repulsive potentials: application to hydrocarbons*. J Phys Chem A, 2009. **113**(43): p. 11866-81.

230. Soper, A.K., *The Radial Distribution Functions of Water as Derived from Radiation Total Scattering Experiments: Is There Anything We Can Say for Sure?* ISRN Physical Chemistry, 2013, 2013: p. 67.
231. Skinner, L.B., et al., *Benchmark oxygen-oxygen pair-distribution function of ambient water from x-ray diffraction measurements with a wide Q-range.* J Chem Phys, 2013. **138**(7): p. 074506.
232. Skinner, L.B., et al., *Benchmark oxygen-oxygen pair-distribution function of ambient water from x-ray diffraction measurements with a wide Q-range.* The Journal of Chemical Physics, 2013. **138**(7): p. 074506.
233. Babin, V., C. Leforestier, and F. Paesani, *Development of a "First Principles" Water Potential with Flexible Monomers: Dimer Potential Energy Surface, VRT Spectrum, and Second Virial Coefficient.* Journal of Chemical Theory and Computation, 2013. **9**(12): p. 5395-5403.
234. Medders, G.R., V. Babin, and F. Paesani, *Development of a "First-Principles" Water Potential with Flexible Monomers. III. Liquid Phase Properties.* Journal of Chemical Theory and Computation, 2014. **10**(8): p. 2906-2910.
235. Soper, A.K. and C.J. Benmore, *Quantum Differences between Heavy and Light Water.* Phys Rev Lett, 2008. **101**(6): p. 065502.
236. Wikfeldt, K.T., et al., *On the range of water structure models compatible with X-ray and neutron diffraction data.* J Phys Chem B, 2009. **113**(18): p. 6246-55.
237. Skinner, L.B., et al., *The structure of water around the compressibility minimum.* J Chem Phys, 2014. **141**(21): p. 214507.
238. Goyal, P., M. Elstner, and Q. Cui, *Application of the SCC-DFTB method to neutral and protonated water clusters and bulk water.* J Phys Chem B, 2011. **115**(20): p. 6790-805.

239. Wikfeldt, K.T., et al., *On the Range of Water Structure Models Compatible with X-ray and Neutron Diffraction Data*. The Journal of Physical Chemistry B, 2009. **113**(18): p. 6246-6255.
240. Chau, P.-L. and A.J. Hardwick, *A new order parameter for tetrahedral configurations*. J. Mol. Phys. , 1998. **93** p. 511.
241. Hare, D.E. and C.M. Sorensen, *The density of supercooled water. II. Bulk samples cooled to the homogeneous nucleation limit*. The Journal of Chemical Physics, 1987. **87**(8): p. 4840-4845.
242. Mills, R., *Self-Diffusion in Normal and Heavy Water in the Range 1-45°*. J. Phys. Chem. B, 1973. **77**(5): p. 685-688.
243. S., P.W., et al., *Temperature Dependence of the Self-Diffusion of Supercooled Heavy Water to 244 K*. J. Phys. Chem. B 2000. **104**: p. 5874-5876.
244. Eyert, V., et al., *Electronic structure of FeS₂: The crucial role of electron-lattice interaction*. Physical Review B, 1998. **57**(11): p. 6350-6359.
245. Opahle, I., K. Koepf, and H. Eschrig, *Full potential band structure calculation of iron pyrite*. Computational Materials Science, 2000. **17**(2-4): p. 206-210.
246. Schena, T., G. Bihlmayer, and S. Blügel, *First-principles studies of FeS₂ using many-body perturbation theory in the G₀W₀ approximation*. Physical Review B, 2013. **88**(23).
247. Hung, A., et al., *Density-functional theory studies of pyrite FeS₂(0) and (100) surfaces*. Surface Science, 2002. **513**(3): p. 511-524.
248. Guevremont, J.M., D.R. Strongin, and M.A.A. Schoonen, *Effects of surface imperfections on the binding of CH₃OH and H₂O on FeS₂(100): using adsorbed Xe as a probe of mineral surface structure*. Surface Science, 1997. **391**(1-3): p. 109-124.

249. Zhu, J., et al., *Surface structure-dependent pyrite oxidation in relatively dry and moist air: Implications for the reaction mechanism and sulfur evolution*. *Geochimica et Cosmochimica Acta*, 2018. **228**: p. 259-274.
250. Nakano, A., et al., *Geochemical assessment of arsenic contamination in well water and sediments from several communities in the Nawalparasi District of Nepal*. *Environmental Earth Sciences*, 2014. **72**(9): p. 3269-3280.
251. Tabelin, C.B., T. Igarashi, and R. Takahashi, *Mobilization and speciation of arsenic from hydrothermally altered rock in laboratory column experiments under ambient conditions*. *Applied Geochemistry*, 2012. **27**(1): p. 326-342.
252. Tabelin, C.B., T. Igarashi, and T. Yoneda, *Mobilization and speciation of arsenic from hydrothermally altered rock containing calcite and pyrite under anoxic conditions*. *Applied Geochemistry*, 2012. **27**(12): p. 2300-2314.
253. Feng, J., et al., *Pyrite oxidation mechanism in aqueous medium*. *Journal of the Chinese Chemical Society*, 2019.
254. Ma, B., et al., *Kinetics of FeSe₂ oxidation by ferric iron and its reactivity compared with FeS₂*. *Science China Chemistry*, 2014. **57**(9): p. 1300-1309.
255. Nesbitt, H.W., et al., *Sulfur and iron surface states on fractured pyrite surfaces*. *American Mineralogist*, 1998. **83**(9-10): p. 1067-1076.
256. Reedy, B.J., J.K. Beattie, and R.T. Lowson, *A vibrational spectroscopic 18O tracer study of pyrite oxidation*. *Geochimica et Cosmochimica Acta*, 1991. **55**(6): p. 1609-1614.
257. Tauson, V.L., et al., *Surface typochemistry of hydrothermal pyrite: Electron spectroscopic and scanning probe microscopic data. II. Natural pyrite*. *Geochemistry International*, 2009. **47**(3): p. 231-243.
258. Taylor, B.E., M.C. Wheeler, and D.K. Nordstrom, *Isotope composition of sulphate in acid mine drainage as measure of bacterial oxidation*. *Nature*, 1984. **308**(5959): p. 538-541.

259. Bailey, L.K. and E. Peters, *Decomposition of pyrite in acids by pressure leaching and anodization: the case for an electrochemical mechanism*. Canadian Metallurgical Quarterly, 1976. **15**(4): p. 333-344.
260. Taylor, B.E., M.C. Wheeler, and D.K. Nordstrom, *Stable isotope geochemistry of acid mine drainage: Experimental oxidation of pyrite*. Geochimica et Cosmochimica Acta, 1984. **48**(12): p. 2669-2678.
261. Usher, C.R., et al., *Origin of Oxygen in Sulfate during Pyrite Oxidation with Water and Dissolved Oxygen: An In Situ Horizontal Attenuated Total Reflectance Infrared Spectroscopy Isotope Study*. Environmental Science & Technology, 2004. **38**(21): p. 5604-5606.
262. Usher, C.R., et al., *Mechanistic Aspects of Pyrite Oxidation in an Oxidizing Gaseous Environment: An in Situ HATR-IR Isotope Study*. Environmental Science & Technology, 2005. **39**(19): p. 7576-7584.
263. Kendelewicz, T., et al., *Initial oxidation of fractured surfaces of FeS₂() by molecular oxygen, water vapor, and air*. Surface Science, 2004. **558**(1-3): p. 80-88.
264. Cheng, T., H. Xiao, and W.A. Goddard, 3rd, *Full atomistic reaction mechanism with kinetics for CO reduction on Cu(100) from ab initio molecular dynamics free-energy calculations at 298 K*. Proc Natl Acad Sci U S A, 2017. **114**(8): p. 1795-1800.
265. Rozgonyi, T. and A. Stirling, *DFT Study of Oxidation States on Pyrite Surface Sites*. The Journal of Physical Chemistry C, 2015. **119**(14): p. 7704-7710.
266. Dirac, P.A.M., *Quantum Mechanics of Many-Electron Systems*. Proceedings of the Royal Society A: Mathematical, Physical and Engineering Sciences, 1929. **123**(792): p. 714-733.
267. Oliveira, A.F., et al., *Density-Functional Based Tight-Binding: an Approximate DFT Method*. Journal of the Brazilian Chemical Society, 2009. **20**(7): p. 1193-1205.
268. Koskinen, P. and V. Makinen, *Density-functional tight-binding for beginners*. Computational Materials Science, 2009. **47**(1): p. 237-253.

Appendix

Appendix A: Pyrite K-points and cutoff testes.

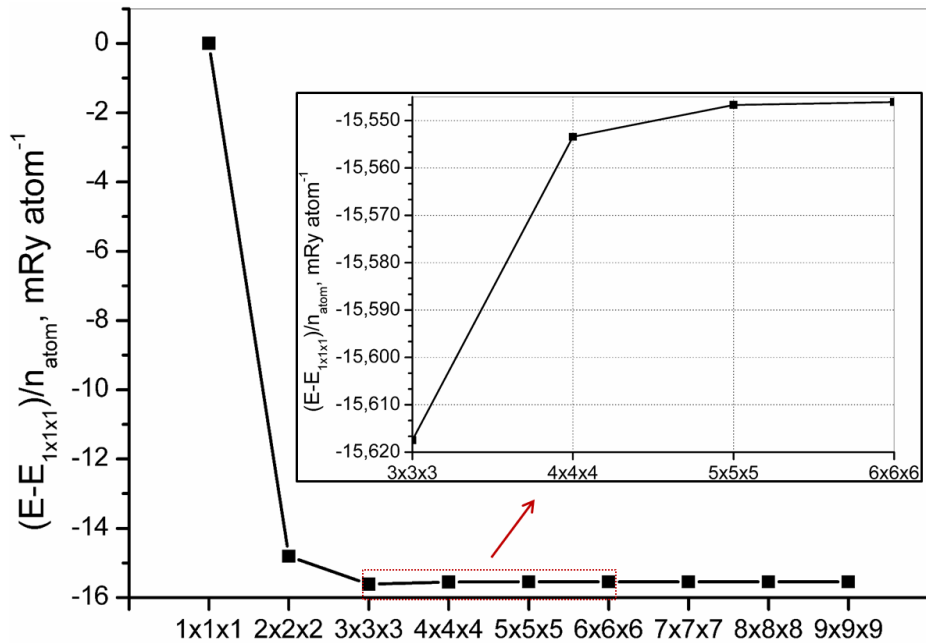


Figure A1- Convergence test for the total energy as a function of the K-points meshes. In the graph E_{1x1x1} represents the total energy for the calculation at the Γ point and n_{atom} is the total number of atoms in the pyrite unit cell. In all calculations, the cutoff of 80 Ry was used.

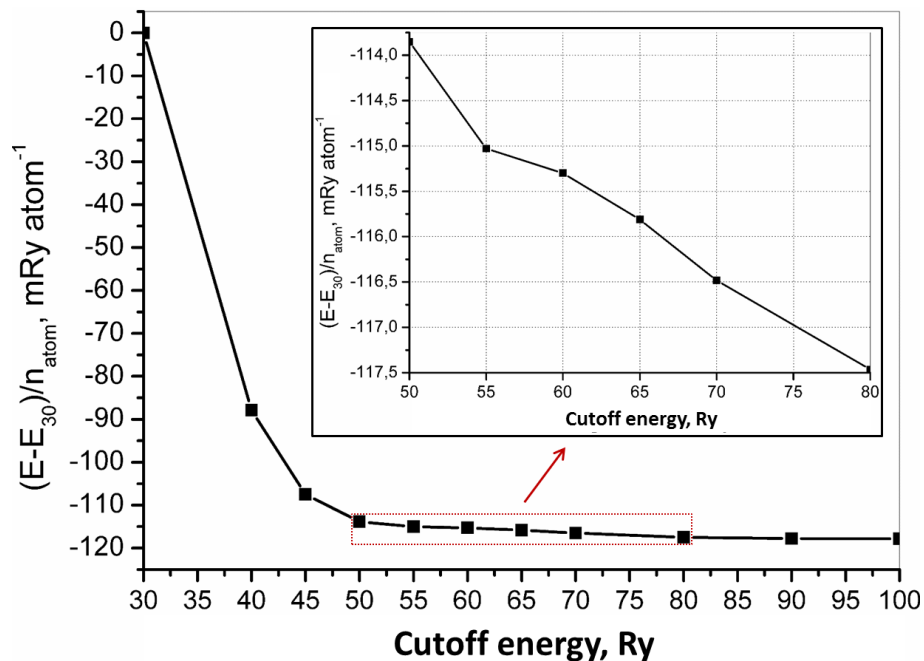


Figure A2- Convergence test for the total energy as a function of the cutoff. In the graph E_{30} represents the total energy for the calculation with 30 Ry cutoff and n_{atom} is the total number of atoms in the pyrite unit cell. In all calculations, the 6x6x6 K-points meshes was used.

Appendix B: arsenopyrite K-points and cutoff testes.

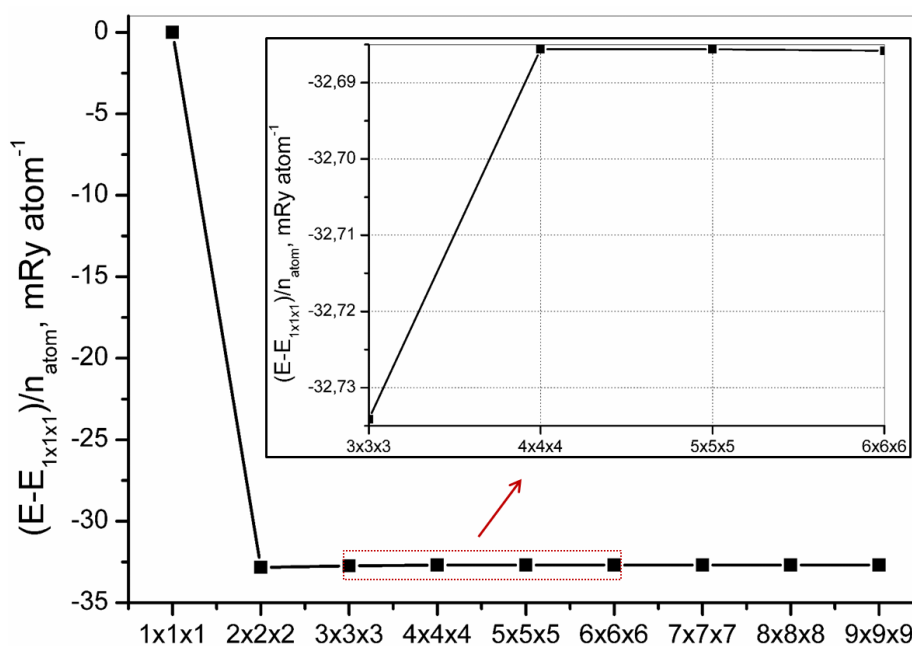


Figure A3- Convergence test for the total energy as a function of the K-points meshes. In the graph $E_{1 \times 1 \times 1}$ represents the total energy for the calculation at the Γ point and n_{atom} is the total number of atoms in the pyrite unit cell. In all calculations, the cutoff of 80 Ry was used.

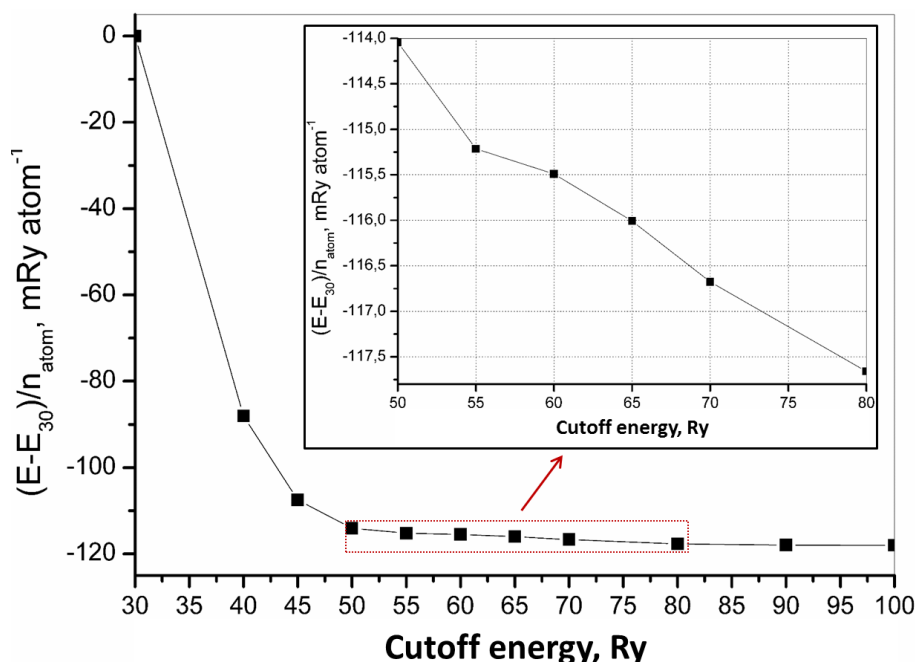


Figure A4- Convergence test for the total energy as a function of the cutoff. In the graph E_{30} represents the total energy for the calculation with 30 Ry cutoff and n_{atom} is the total number of atoms in the pyrite unit cell. In all calculations, the 6x6x6 K-points meshes was used.

Appendix C: Pyrite Hubbard parameter test.

Table A1: Pyrite Hubbard (GGA+U) parameter test. The cutoff of 50 Ry and the K-point of 4x4x4 were used in all the calculation. BG meanings the band gap of the system for the tested GGA+U parameters.

GGA+U	a/ Å	b/ Å	c/ Å	Fe-S/ Å	S-S/ Å	BG/ eV
0.0	5.381	5.381	5.381	2.245	2.179	0.43
1.0	5.383	5.383	5.383	2.248	2.162	0.72
1.5	5.386	5.386	5.386	2.250	2.154	0.88
2.0	5.390	5.390	5.390	2.253	2.145	1.05
2.5	5.395	5.395	5.395	2.256	2.139	1.22
3.0	5.402	5.402	5.402	2.260	2.131	1.37
Exp.[173]	5.407	5.407	5.407	2.262	2.135	0.90

Appendix D: Arsenopyrite Hubbard parameter test.

Table A2: Arsenopyrite Hubbard (GGA+U) parameter test for arsenopyrite structure. The cutoff of 50 Ry and the K-point of 4x4x4 were used in all the calculation.

GGA+U	a/ Å	b/ Å	c/ Å	$\beta/^\circ$
0.0	5.714	5.648	5.737	112.1
1.0	5.706	5.646	5.730	112.1
1.5	5.700	5.647	5.724	112.0
2.0	5.699	5.646	5.723	112.1
2.5	5.696	5.647	5.720	112.1
Exp.[174]	5.744	5.675	5.785	112.3

Table A3: Arsenopyrite Hubbard (GGA+U) parameter test for arsenopyrite structure and band gap (BG). The cutoff of 50 Ry and the K-point of 4x4x4 were used in all the calculations.

GGA+U	Fe-S/ Å	Fe-As/ Å	As-S/ Å	Fe-Fe(long)/ Å	Fe-Fe(short)/ Å	BG/ eV
0.0	2.182 2.192 2.204	2.405 2.404 2.374	2.398	3.751	2.655	0.76
1.0	2.178 2.189 2.205	2.403 2.401 2.373	2.391	3.746	2.650	0.82
1.5	2.177 2.187 2.205	2.399 2.401 2.375	2.388	3.747	2.649	0.84
2.0	2.176 2.186 2.208	2.402 2.397 2.373	2.385	3.742	2.645	0.86
2.5	2.174 2.185 2.210	2.401 2.396 2.373	2.381	3.740	2.642	0.87
3.0	2.173 2.184 2.212	2.400 2.395 2.374	2.378	3.738	2.639	0.85
Exp.[174]	2.239 2.250 2.257	2.336 2.371 2.357	2.346	3.627	2.922	0.82

Appendix E: Crystallographic transformation of the arsenopyrite (010) surface.

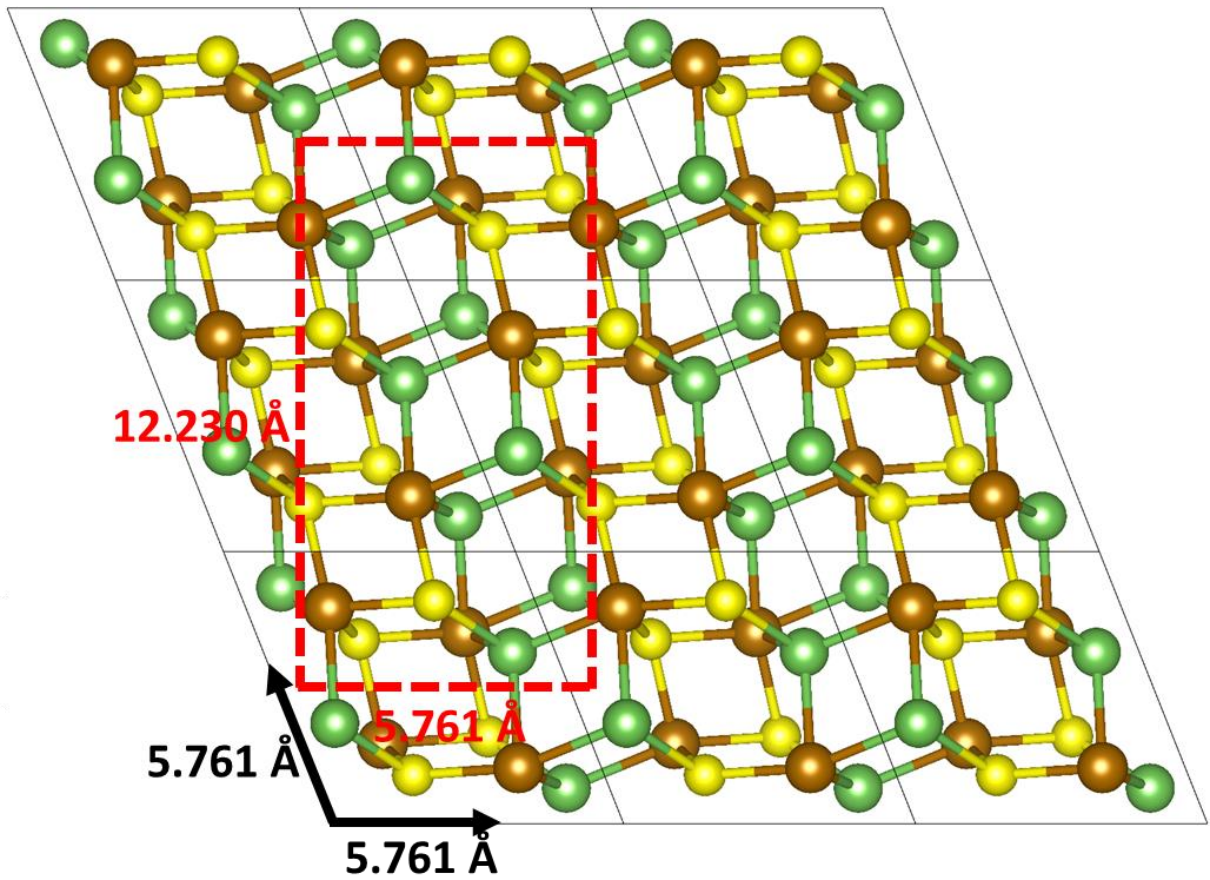


Figure A5- Crystallographic transformation of the arsenopyrite (010) surface from triclinic to an orthorhombic structure.

Appendix F: Structure of the interfaces.

Table A4: Fe- X_{eq} and X-S bond distances of the three interfaces.

Bond Distances, Å	FeS ₂ (100)/FeAsS(001)	FeS ₂ (100)/FeAsS(100)-As	FeS ₂ (100)/FeAsS(100)-S
Fe-S _{eq} (FeAsS)	2.169 (-1.7)	2.155 (-1.1)	2.198 (0.2)
Fe-As _{eq} (FeAsS)	2.327 (-1.5)	2.357 (-2.8)	2.331 (-2.6)
Fe-S _{eq} (FeS ₂)	2.304 (0.3)	2.300 (0.5)	2.288 (-0.2)
S-S	2.262 (3.8)	2.259 (3.6)	2.248 (3.1)
As-S	2.324 (-3.1)	2.337 (-2.5)	2.350 (-2.0)

Table A5- Fe- X_{ax} and interfacial contact distances, δ_0 , of the three interface systems. In the red parenthesis are the percentage difference** between the interfaces structure parameters and the arsenopyrite bulk structure. In the green brackets are the percentage difference** between the interfaces and the arsenopyrite bulk.

System	δ_0 , Å	Fe-As _{ax} , Å	Fe-S _{ax} , Å
FeS ₂	2.690	---	2.245
FeAsS	2.656	2.394	2.193
FeS ₂ (100)/FeAsS(001)	2.685 (-0.2)[1.1]	2.329 (---)[-2.7]	2.251 (0.3)[2.6]
FeS ₂ (100)/FeAsS(100)-As	2.890 (7.4)[8.7]	2.340 (---)[-2.3]	2.368 (5.5)[8.0]
FeS ₂ (100)/FeAsS(100)-S	2.669 (-0.8)[0.5]	---	2.224 (0.9)[1.4]

** Calculated by: $\%diff = \frac{|"Interface\ parameter" - "Pyrite\ or\ arsenopyrite\ parameter"|}{"Pyrite\ or\ arsenopyrite\ parameter"} 100\%$

Appendix G: Spin teste for the most stable arsenopyrite surfaces.

Table A6: Spin test for the arsenopyrite (001) surface. “TM” meanings the total magnetization of the system and “AM” the absolute magnetization of the system. The cutoff of 50 Ry and the K-point of 4x4x4 were used in all the calculations.

Fe1	Fe2	Fe3	As1	As2	As3	S1	S2	S3	Energy, Ry	TM	AM
0.0	0.0	0.0	0.0	0.0	0.0	0.0	0.0	0.0	-2363.50698	-1.05	3.51
0.0	0.0	0.0	0.0	0.0	0.0	0.0	0.3	-0.3	-2363.52688	0.00	5.90
0.0	0.0	0.0	0.0	0.3	-0.3	0.0	0.0	0.0	-2363.52688	0.00	5.90
0.0	0.3	-0.3	0.0	0.0	0.0	0.0	0.0	0.0	-2363.52688	0.00	5.90
0.0	0.3	-0.3	0.0	0.3	-0.3	0.0	0.3	-0.3	-2363.52688	0.00	5.90
0.0	0.3	0.3	0.0	0.0	0.0	0.0	0.0	0.0	-2363.52687	2.00	5.80
0.0	0.3	0.3	0.0	0.3	0.3	0.0	0.3	0.3	-2363.52687	2.00	5.80

Table A7: Spin test for the arsenopyrite (100)-As surface. “TM” meanings the total magnetization of the system and “AM” the absolute magnetization of the system. The cutoff of 50 Ry and the K-point of 4x4x4 were used in all the calculations.

Fe1	Fe2	Fe3	As1	As2	As3	S1	S2	S3	Energy, Ry	TM	AM
0.0	0.0	0.0	0.0	0.0	0.0	0.0	0.0	0.0	-2363.50329	0.00	0.01
0.0	0.0	0.0	0.0	0.0	0.0	0.0	0.3	-0.3	-2363.50329	0.00	0.01
0.0	0.0	0.0	0.0	0.3	-0.3	0.0	0.0	0.0	-2363.50329	0.00	0.00
0.0	0.3	-0.3	0.0	0.0	0.0	0.0	0.0	0.0	-2363.50352	0.00	2.33
0.0	0.3	-0.3	0.0	0.3	-0.3	0.0	0.3	-0.3	-2363.50352	0.00	2.33
0.0	0.3	0.3	0.0	0.0	0.0	0.0	0.0	0.0	-2363.49273	3.14	4.91
0.0	0.3	0.3	0.0	0.3	0.3	0.0	0.3	0.3	-2363.49273	3.14	4.91

Table A8: Spin test for the arsenopyrite (100)-S surface. “TM” meanings the total magnetization of the system and “AM” the absolute magnetization of the system. The cutoff of 50 Ry and the K-point of 4x4x4 were used in all the calculations.

Fe1	Fe2	Fe3	As1	As2	As3	S1	S2	S3	Energy, Ry	TM	AM
0.0	0.0	0.0	0.0	0.0	0.0	0.0	0.0	0.0	-2363.45194	0.12	0.23
0.0	0.0	0.0	0.0	0.0	0.0	0.0	0.3	-0.3	-2363.48051	0.00	6.56
0.0	0.0	0.0	0.0	0.3	-0.3	0.0	0.0	0.0	-2363.48051	0.00	6.56
0.0	0.3	-0.3	0.0	0.0	0.0	0.0	0.0	0.0	-2363.49051	0.00	6.55
0.0	0.3	-0.3	0.0	0.3	-0.3	0.0	0.3	-0.3	-2363.48051	0.00	6.56
0.0	0.3	0.3	0.0	0.0	0.0	0.0	0.0	0.0	-2363.49008	4.00	6.02
0.0	0.3	0.3	0.0	0.3	0.3	0.0	0.3	0.3	-2363.49008	4.00	6.02

Appendix H: Finding the most stable interfaces

Table A9: Py(100)/AsPy(001) total energy. The cutoff of 50 Ry and the K-point of 4x4x4 were used. In all the calculations the lattice parameters were fixed, and only the atom positions were allowed to move freely in the optimization process. Highlighted in red the structure with the lowest energy.

$\theta, ^\circ$	$\Delta x, \text{Å}$	$\Delta y, \text{Å}$	Energy, Ry
0	2.775	1.397	-4764.63652
0	2.775	2.794	-4764.63658
90	2.775	4.192	-4764.44021
180	0.000	0.000	-4764.63651
180	0.000	1.397	-4764.63652
180	0.000	2.794	-4764.63635

Table A10: FeS₂(100)/FeAsS(100)-As total energy. The cutoff of 50 Ry and the K-point of 4x4x4 were used. In all calculations the lattice parameters were fixed, and only the atom positions were allowed to move freely in the optimization process. Highlighted in red the structure with the lowest energy.

$\theta, ^\circ$	$\Delta x, \text{Å}$	$\Delta y, \text{Å}$	Energy, Ry
0	0.000	2.884	-4764.49039
0	0.000	4.326	-4764.28552
180	2.842	1.442	-4764.67917
180	2.842	2.884	-4764.50874

Table A11: FeS₂(100)/FeAsS(100)-S total energy. The cutoff of 50 Ry and the K-point of 4x4x4 were used. In all calculations the lattice parameters were fixed, and only the atom positions were allowed to move freely in the optimization process. Highlighted in red the structure with the lowest energy.

$\theta, ^\circ$	$\Delta x, \text{Å}$	$\Delta y, \text{Å}$	Energy, Ry
0	0.000	0.000	-4764.43690
0	0.000	2.884	-4764.45138
0	0.000	4.326	-4764.61572
180	2.842	0.000	-4764.43686
180	2.842	1.442	-4764.43554
180	2.842	4.326	-4764.61570
270	4.263	2.884	-4764.41468

Appendix I: Interface spin test.

Different initial spin guesses were tested to find the best spin state for the different interfaces: $\text{FeS}_2(100)/\text{FeAsS}(001)$, $\text{FeS}_2(100)/\text{FeAsS}(100)\text{-As}$ and $\text{FeS}_2(100)/\text{FeAsS}(100)\text{-S}$. The total magnetization (TM, $M_T = \int (\rho(r)^{up} - \rho(r)^{down})dr$) and the absolute magnetization (AM, $M_A = \int |\rho(r)^{up} - \rho(r)^{down}|dr$) converged to be the same value for all $\text{FeS}_2(100)/\text{FeAsS}(001)$ tests. That is the reason for the same energy values computed in Table A12. We performed the same test for pyrite and arsenopyrite pure minerals spin polarization, and at the end of the optimization process, all TM and AM values were found to be equal to zero. For the $\text{FeS}_2(100)/\text{FeAsS}(100)\text{-As}$ interface, all the energies and magnetization values were found to be the same, see Table A13. In contrast, different values for energy, TM and AM were found for the $\text{FeS}_2(100)/\text{FeAsS}(100)\text{-S}$ interface (Table A14). However, the ground energy state was found to be spin compensated (AM=TM=0).

Table A12: Spin teste for the $\text{FeS}_2(100)/\text{FeAsS}(001)$ interface. “ALT” meanings that alternated initial spin states were used, following the sequencie Up-Down-Up-Down for the iron, sulfur and arsenic sites in the interface region. “Up” meanings all spin states up and “O” that no spin polarization was used for the atoms in the DFT SCF calculations. “TM” is the total magnetization, and “AM” the absolute magnetization. The cutoff of 50 Ry and the K-point of 4x4x4 were used.

Fe	S	As	Energy, Ry	TM	AM
0	0	0	-4764.63788	0.00	0.00
ALT	0	0	-4764.63788	0.04	0.06
ALT	0	ALT	-4764.63788	0.04	0.06
ALT	ALT	ALT	-4764.63788	0.04	0.06
Up	Up	Up	-4764.63788	0.04	0.06
Up	0	0	-4764.63788	0.04	0.06

Table A13: Spin teste for the FeS₂(100)/FeAsS(100)-As interface. “ALT” meanings that alternated initial spin states were used, following the sequencie Up-Down-Up-Down for the iron, sulfur and arsenic sites in the interface region. “Up” meanings all spin states up and “0” that no spin polarization was used for the atoms in the DFT SCF calculations. “TM” is the total magnetization, and “AM” the absolute magnetization. The cutoff of 50 Ry and the K-point of 4x4x4 were used.

Fe	As	S	Energy, Ry	TM	AM
0	0	0	-4764.67928	0.00	0.00
ALT	0	0	-4764.67928	0.00	0.00
ALT	ALT	0	-4764.67928	0.00	0.00
ALT	ALT	ALT	-4764.67928	0.00	0.00
Up	Up	Up	-4764.67928	0.00	0.00
Up	0	0	-4764.67928	0.00	0.00

Table A14: Spin teste for the FeS₂(100)/FeAsS(100)-S interface. “ALT” meanings that alternated initial spin states were used, following the sequencie Up-Down-Up-Down for the iron, sulfur and arsenic sites in the interface region. “Up” meanings all spin states up and “0” that no spin polarization was used for the atoms in the DFT SCF calculations. “TM” is the total magnetization, and “AM” the absolute magnetization. The cutoff of 50 Ry and the K-point of 4x4x4 were used.

Fe	S	As	Energy, Ry	TM	AM
0	0	0	-4764.62825	0.02	0.04
ALT	0	0	-4764.62659	1.56	3.16
ALT	ALT	0	-4764.62659	1.56	3.16
ALT	ALT	ALT	-4764.62487	1.30	1.78
Up	Up	Up	-4764.62720	2.66	3.70
Up	0	0	-4764.62706	2.67	3.70

Appendix J: Electron localization function for the pyrite/arsenopyrite interfaces

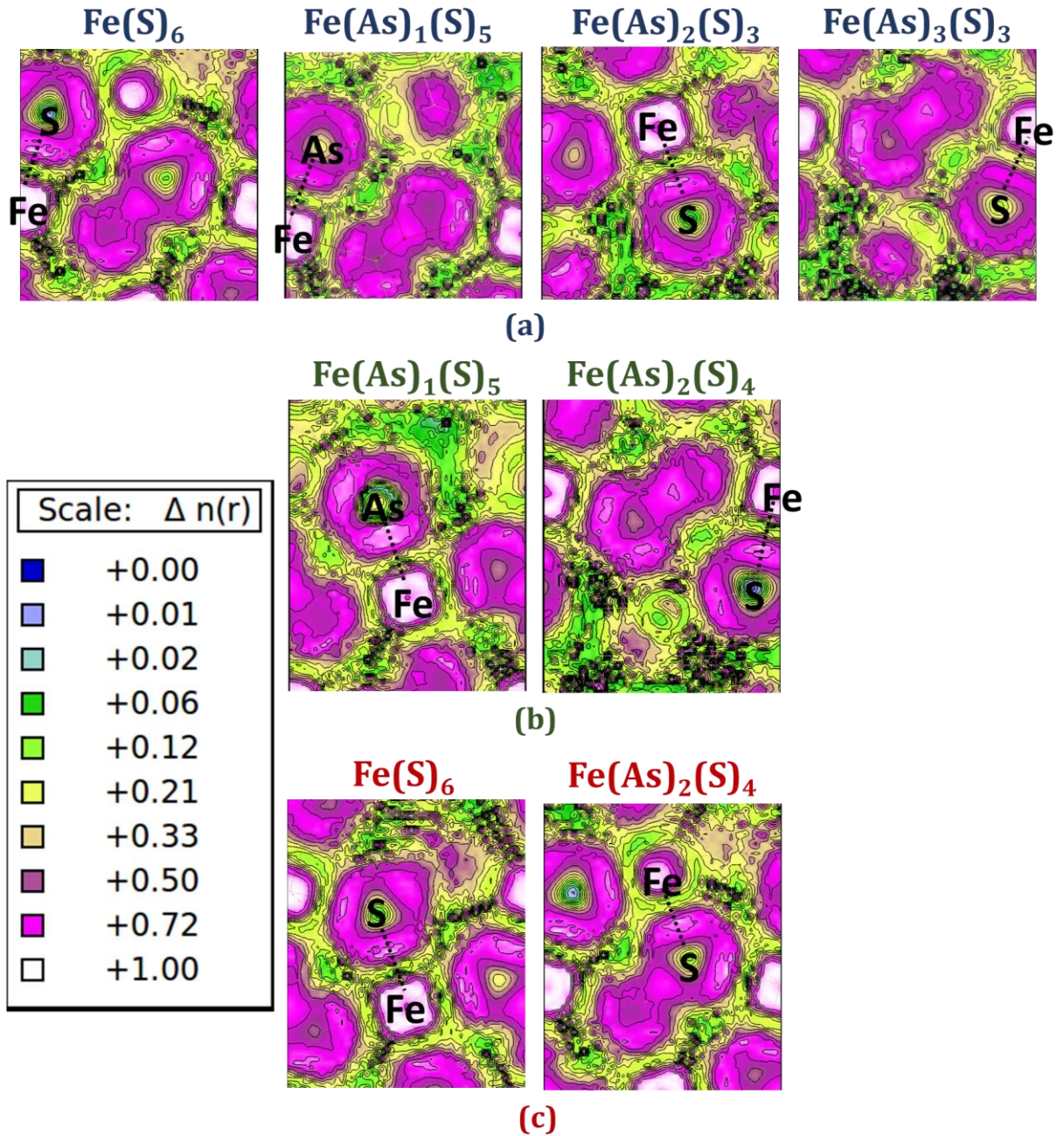


Figure A6- Electron localization function for (a) $FeS_2(100)/FeAsS(001)$, (b) $FeS_2(100)/FeAsS(100)$ -As, and (c) $FeS_2(100)/FeAsS(100)$ -S Fe- X_{ax} bonds.

Appendix K: The electronic structure of the pyrite/arsenopyrite interfaces

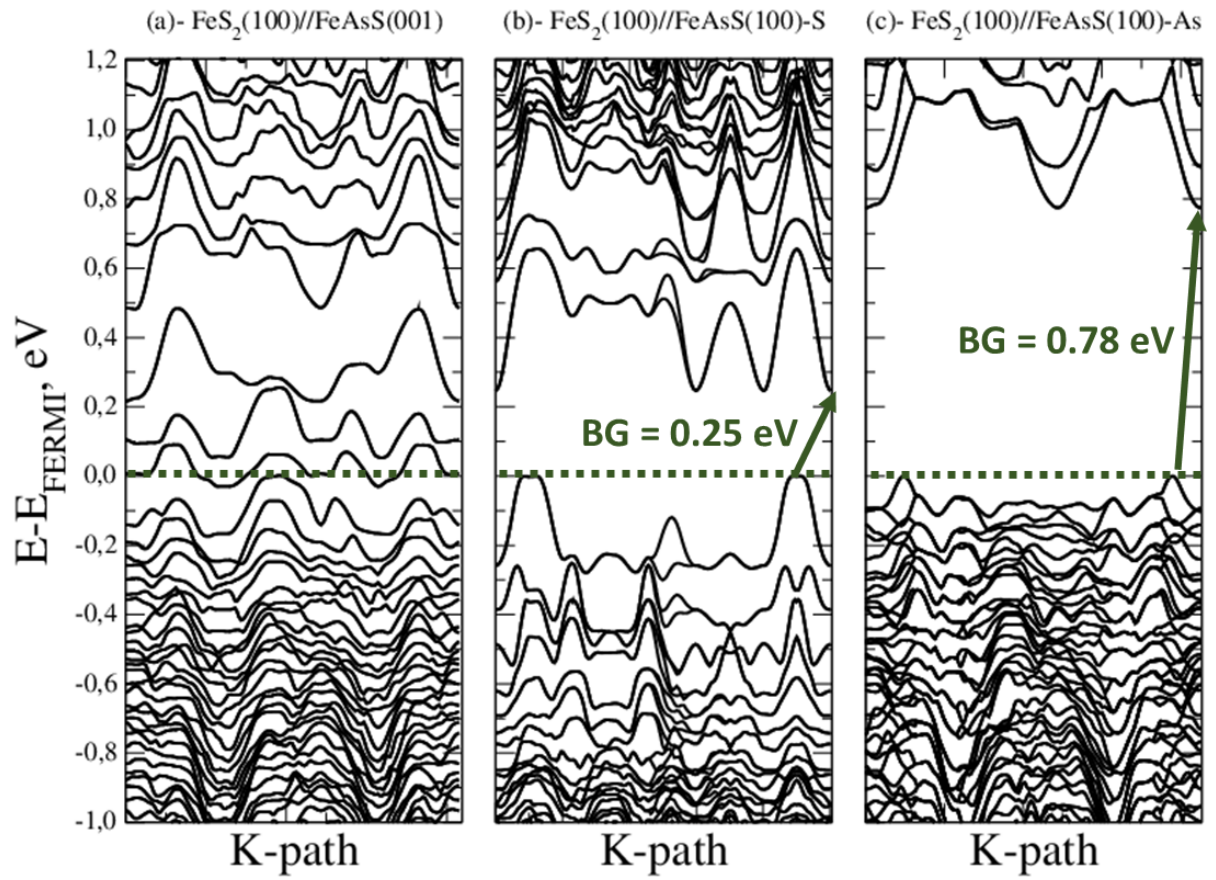


Figure A7- Band structure. BG meanings the band gap of the interfaces. K-Path G-Y-H-C-E-M1-A-Z-D-G-A-X-H1-G from the monoclinic lattice.

Appendix L: Structures used to calculate the formation energy by Eq. (3.6).

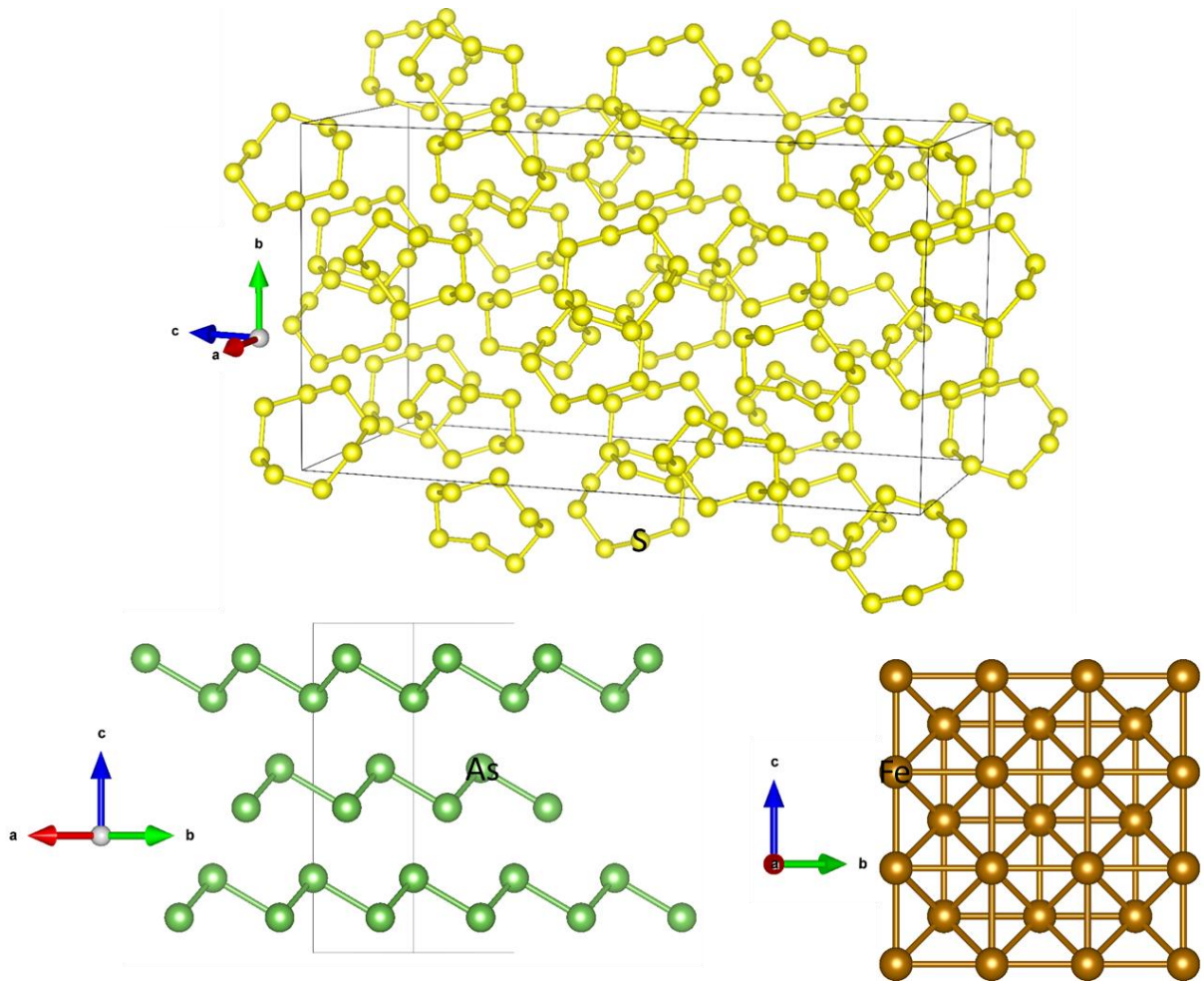


Figure A8- Structures used to calculate the formation energy of the interfaces and the pyrite and arsenopyrite bulk.

Table A15: Structural parameters obtained for the structures shown in Figure A8.

Systems	a, Å	b, Å	c, Å	α , °	β , °	γ , °	Bonds, Å
Arsenic (Hexagonal)	3.810	3.810	10.786	90.0	90.0	120.0	As-As= 2.551
Sulfur (orthorhombic)	12.269	14.533	26.445	90.0	90.0	90.0	S-S= 2.063
Iron (cubic BCC)	2.866	2.866	2.866	90.0	90.0	90.0	Fe-Fe= (2.482; 2.866)

Appendix M: I-SLABs cleavage plane.

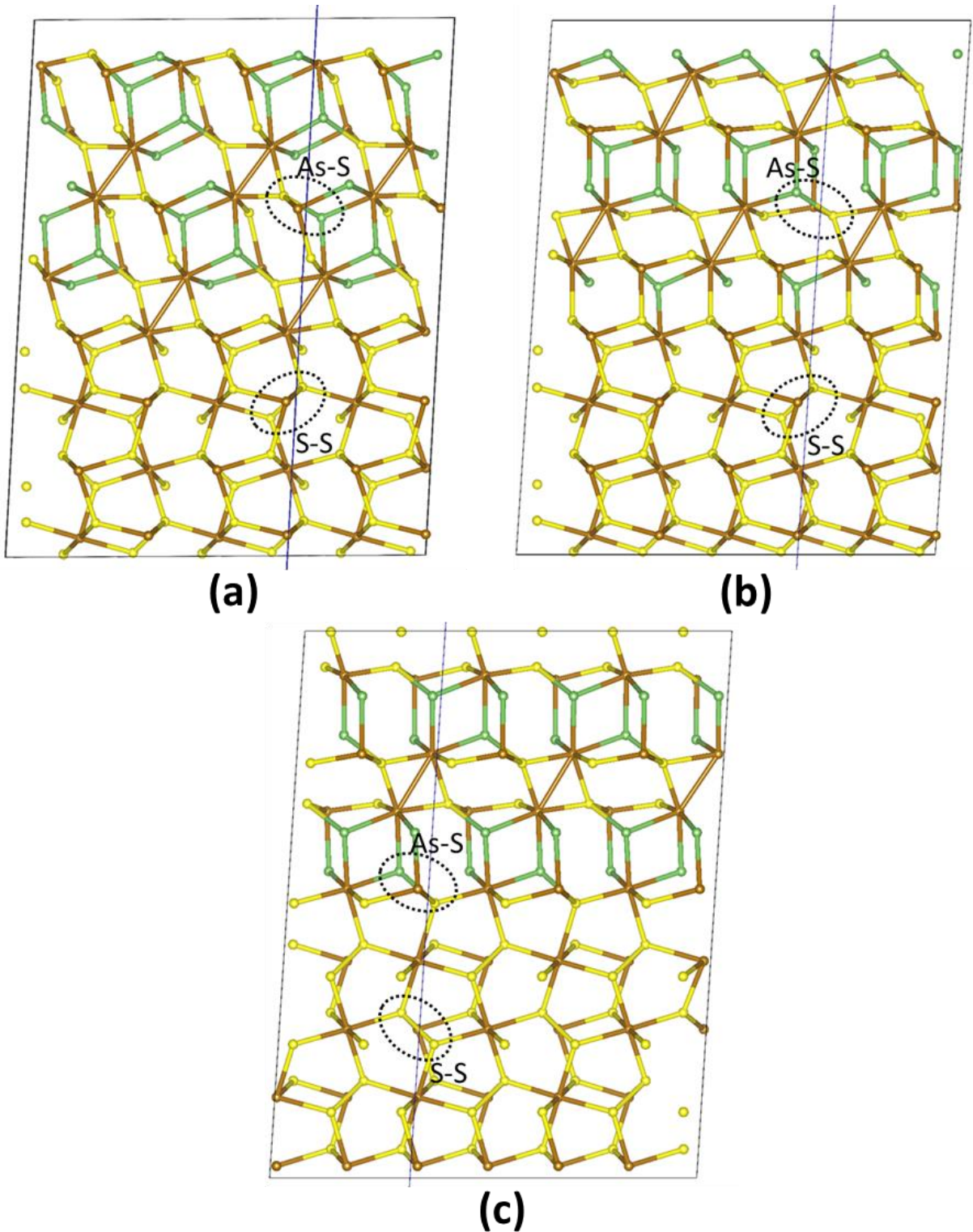


Figure A9- Interface cleavage planes along the (010) direction. (a), (b) and (c) represents, one-to-one, the interfaces: FeS₂(100)/FeAsS(001), FeS₂(100)/FeAsS(100)-As, and FeS₂(100)/FeAsS(100)-S. The blue line is the plane direction, and dashed ellipses indicate the cleaved As-S and S-S bonds.

Appendix N: K-point and cutoff tests evaluated in Chapter 5 and the band offset calculation values.

Table A16: Hubbard parameter (U-J) test for pyrite isolated mineral. A cutoff of 40 Ry and 6x6x4 k-point mesh were used in all the calculations. BG means the band gap of the system for the tested (U-J) parameters.

(U-J)	a/ Å	b/ Å	c/ Å	BG/ eV
0.0	5.243 (3.0%)	5.243 (3.0%)	5.242 (3.0%)	0.41 (54%)
1.0	5.245 (3.0%)	5.244 (3.0%)	5.245 (3.0%)	0.71 (21%)
1.5	5.247 (3.0%)	5.246 (3.0%)	5.247 (3.0%)	0.87 (3%)
2.0	5.249 (2.9%)	5.249 (2.9%)	5.248 (2.9%)	0.99 (10%)
Exp.	5.407[173]	5.407[173]	5.407[173]	0.90[166, 167]

**** Calculated by: %erro = $\frac{|"Calculated BG" - "Experimental BG"|}{"Experimental BG"} 100\%$**

Table A17- Hubbard parameter (U-J) test for arsenopyrite structure. A cutoff of 40 Ry and 6x6x4 k-point mesh were used in all the calculations. BG means the band gap of the system for the tested (U-J) parameters. (%erro **)

(U-J)	a/ Å	b/ Å	c/ Å	BG / eV
0.0	5.556 (3.3%)	5.515 (2.8%)	5.586 (3.4%)	0.71 (13%)
1.0	5.552 (3.4%)	5.513 (2.9%)	5.582 (3.5%)	0.80 (3%)
1.5	5.549 (3.4%)	5.512 (2.9%)	5.580 (3.6%)	0.83 (1%)
2.0	5.547 (3.4%)	5.512 (2.9%)	5.577 (3.6%)	0.87 (6%)
Exp.	5.744[174]	5.675[174]	5.785[174]	0.82[119, 168]

**** Calculated by: %erro = $\frac{|"Calculated BG" - "Experimental BG"|}{"Experimental BG"} 100\%$**

Table A18- (U-J) influencie in band offset calculation. All the calculation were done following the Eq. (1). For the total energy calculation it was used the 4x4x2 k-points grid and the cutoff of 40 Ry.

Systems	(U-J)				
	0.0	1.0	1.5	3.0	5.0
FeS ₂ (100)/FeAsS(001)	0.37	0.39	0.42	0.43	0.43
FeS ₂ (100)/FeAsS(100)-As	0.54	0.55	0.59	0.58	0.59
FeS ₂ (100)/FeAsS(100)-S	0.56	0.57	0.60	0.60	0.59

Appendix O: Band Offset calculation and frontier's orbitals.

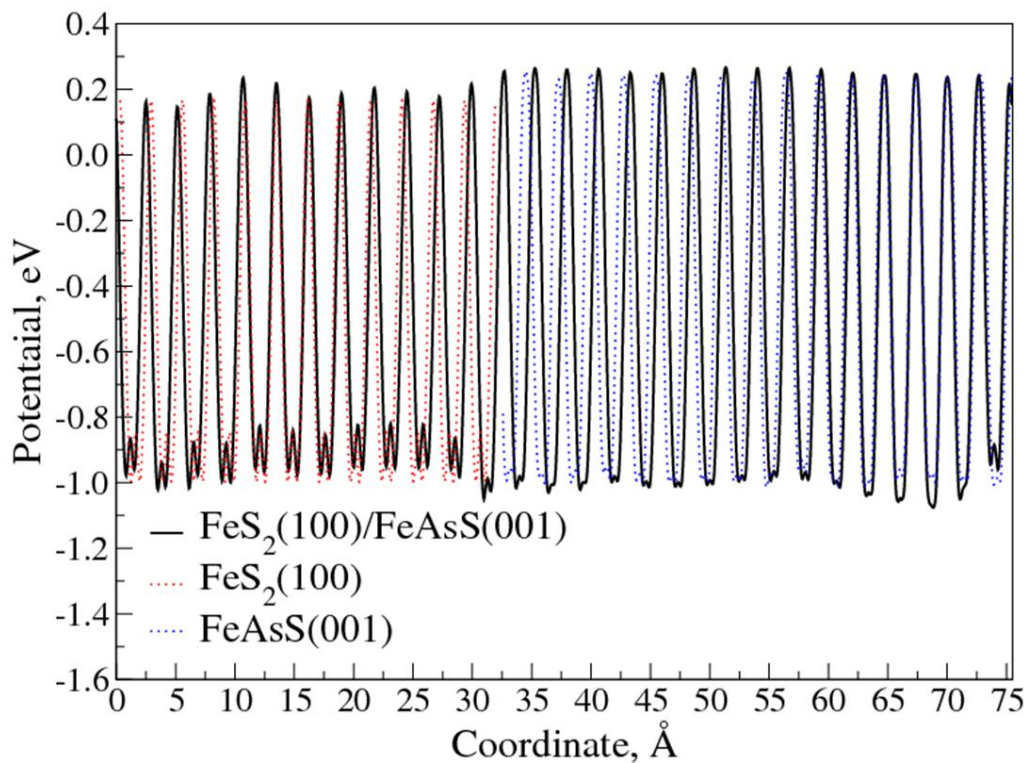


Figure A10- Displacement calculation for the $\text{FeS}_2(100)/\text{FeAsS}(001)$ interface model.

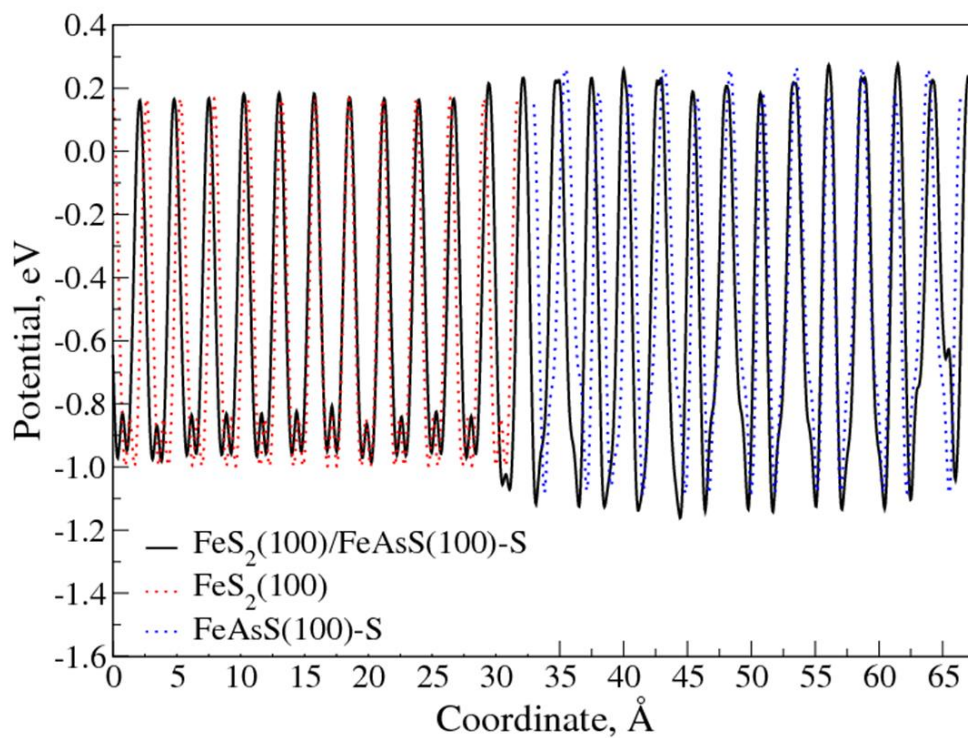


Figure A11- Displacement calculation for the $\text{FeS}_2(100)/\text{FeAsS}(100)\text{-S}$ interface model.

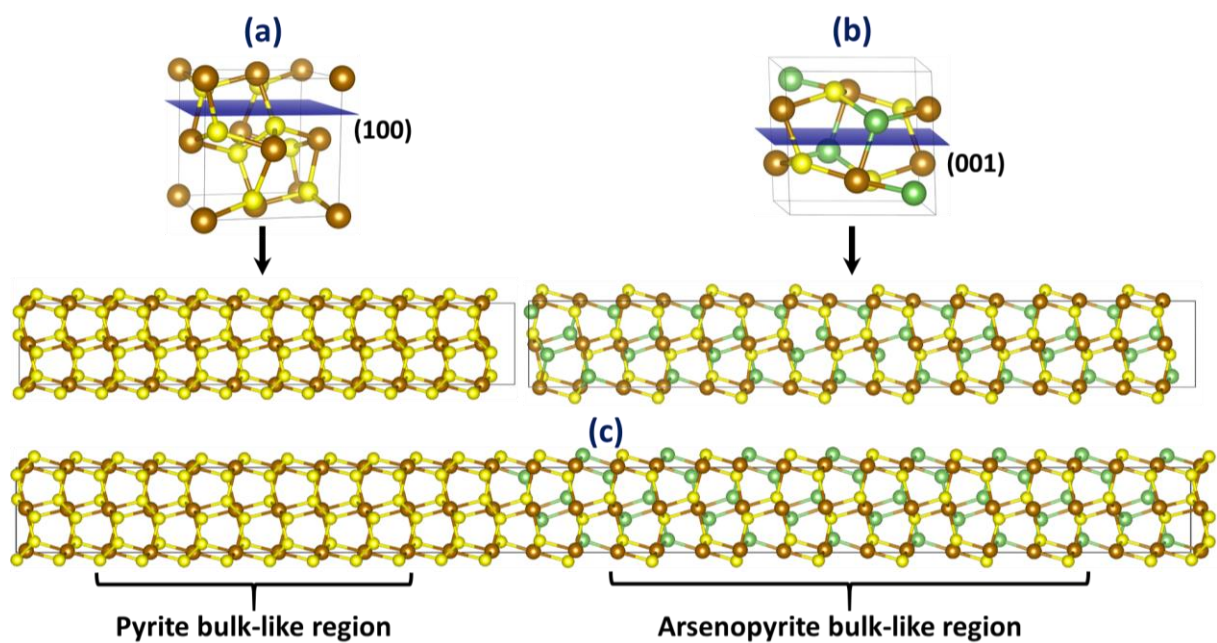


Figure A12- Illustration showing the $FeS_2(100)/FeAsS(001)$ interface model construction from pyrite and arsenopyrite isolated phases.

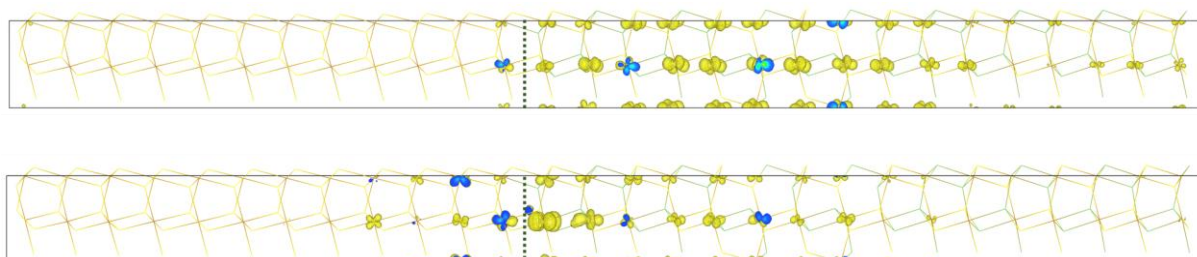


Figure A13- (left) VBM and (right) CBM states for the $FeS_2(100)/FeAsS(001)$ interface model.

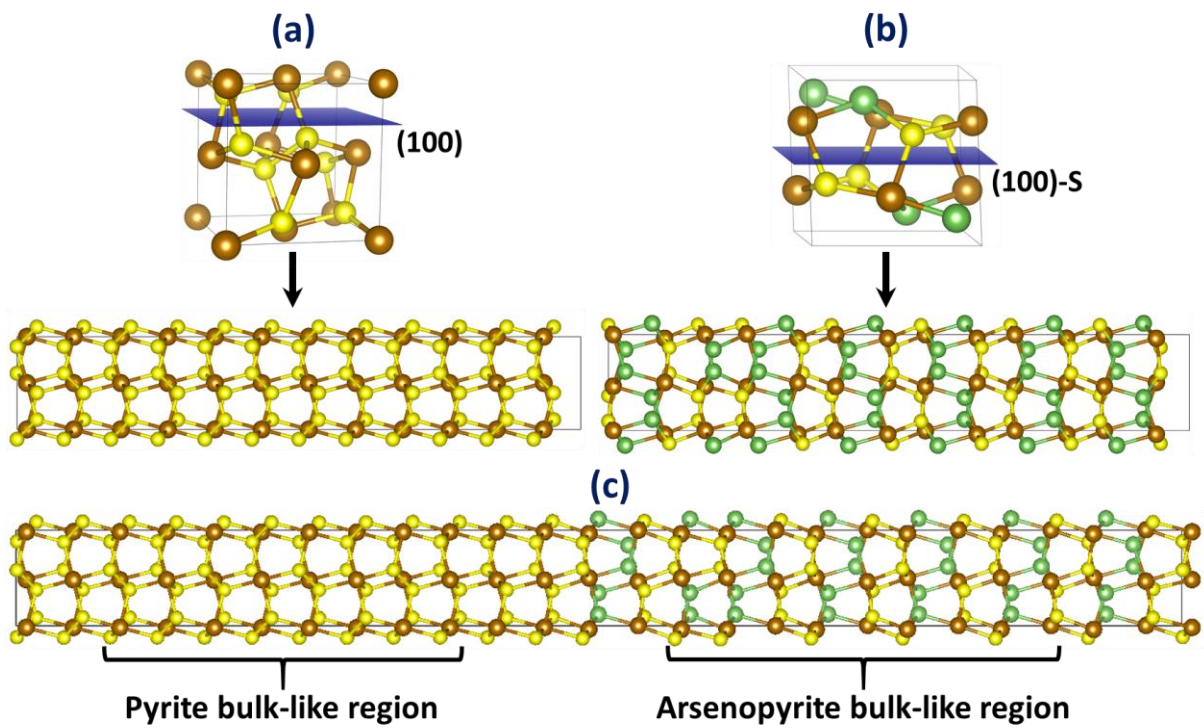


Figure A14- Illustration showing the $\text{FeS}_2(100)/\text{FeAsS}(100)\text{-S}$ interface model construction from pyrite and arsenopyrite isolated phases.

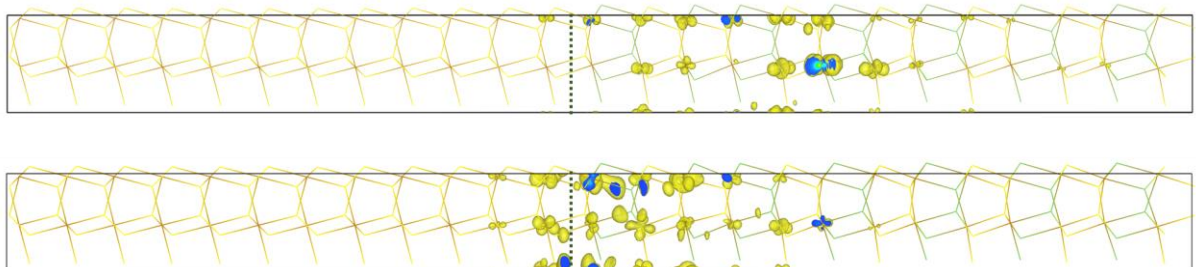


Figure A15- (left) VBM and (right) CBM states for the $\text{FeS}_2(100)/\text{FeAsS}(100)\text{-S}$ interface model.

Appendix O: DFTB2 radial distribution function for bulk water.

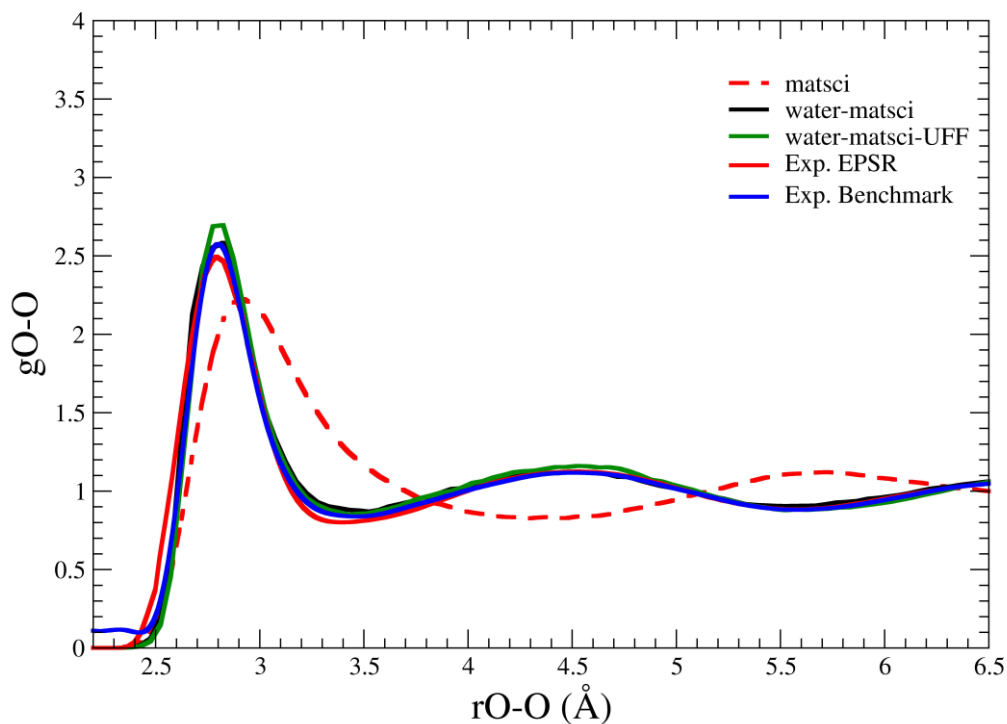


Figure A16- Radial distribution function for O-O obtained by RMC NVT molecular dynamics. It includes the original matsci RDF.

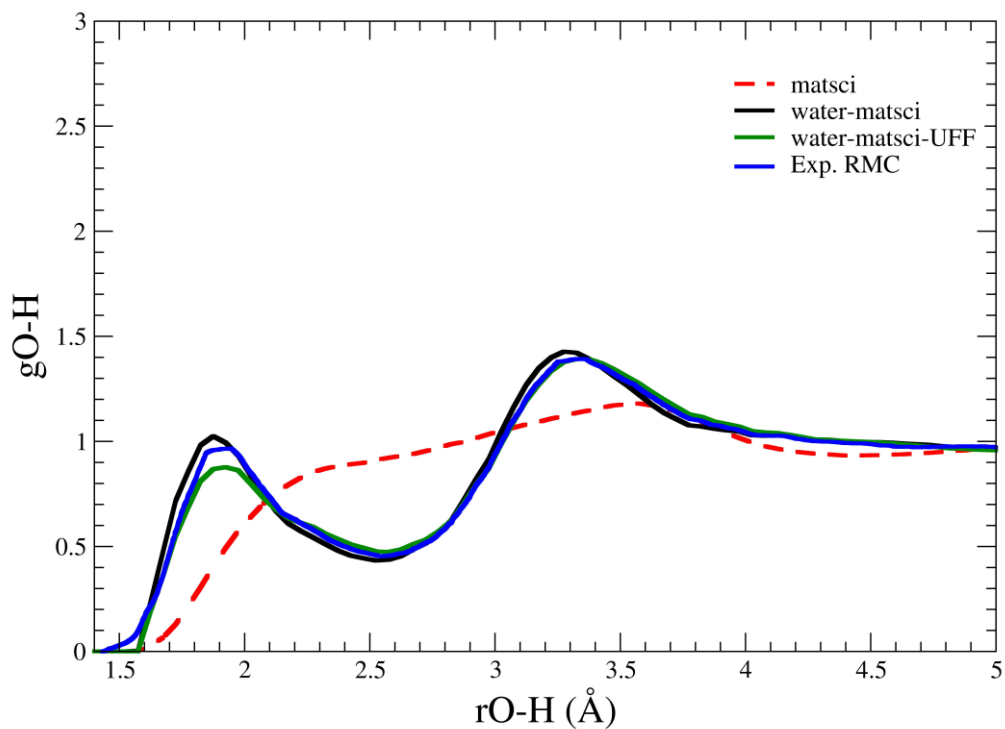


Figure A17- Radial distribution function for O-H obtained by RMC NVT molecular dynamics. It includes the original matsci RDF.

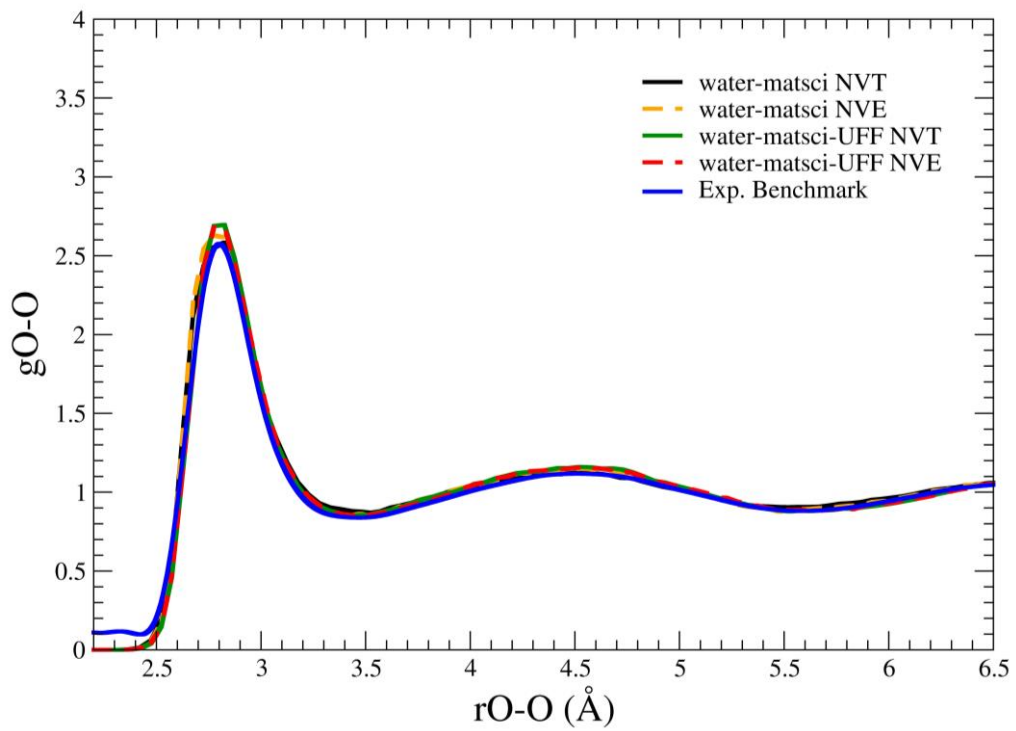


Figure A18- Radial distribution function for O-O obtained by RMC. NVT and NVE molecular dynamics.

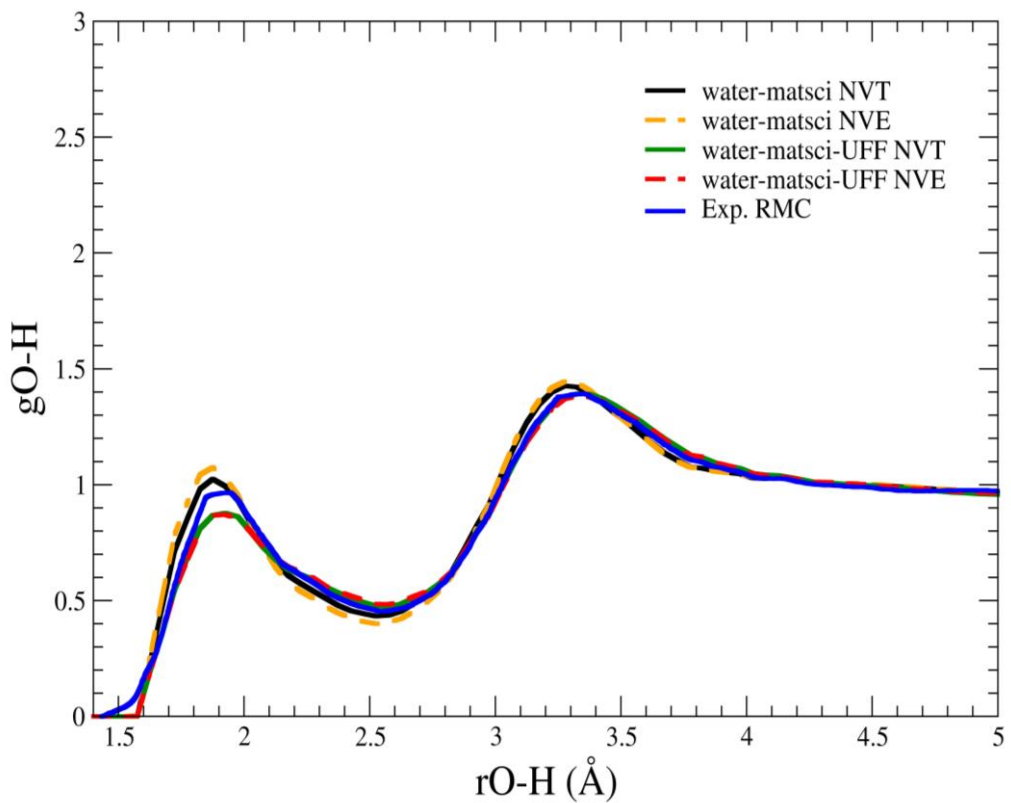


Figure A19- Radial distribution function for O-H obtained by RMC. NVT and NVE molecular dynamics.

Appendix P: Pyrite Fe-X parametrization

The RLCAO code was used to perform the calculations and generate the DFTB2 parameters. The confinement radius used to obtain the elements of the Hamiltonian matrix for Fe and S atoms was 3.70 and 3.90 bohr, respectively. The former are capable to describe the electronic properties of pyrite (our target systems) and metallic iron. The results of the optimum confinement radius are shown in Figure A20.

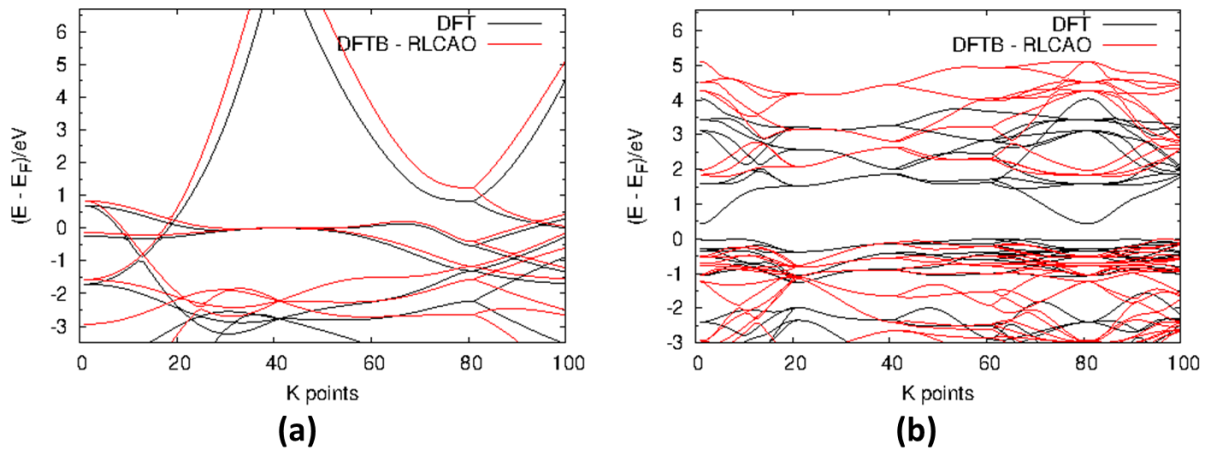


Figure A20- DFT and DFTB2 band structure of iron-FCC (a) and pyrite (b) bulk structures.

The FASP program was used to parameterize the repulsion energy (E_{rep}) for the Fe-X (X = Fe, S, O, H) atomic pairs. The FASP program automates the procedure of finding the best polynomial fit which describes the E_{rep} of atomic pairs for certain interception point of the band (E_{bnd}) and reference (E_{ref}) energy[267, 268]. The atomic pairs, the reference systems used to obtain the E_{rep} as well as their dependencies, and E_{bnd} and E_{ref} interception points together with the cut radius can be found on Table A19. The TZP-DFT calculations for the optimization of the small reference molecules as well as to build the Fe-X potential curve surfaces were evaluated by the ADF program. The DFTB computations for getting the potential E_{bnd} curves (without repulsion) for the Fe-X pairs were evaluated by the ADF-DFTB software.

For the solid systems (Fe-BCC and pyrite) the DFT computations were done by the Quantum-Espresso[162] package in order to optimize the structure and cell parameters and get the electronic properties, such as the Band Structure. The DFT structural properties of bulk and surface of pyrite, during the parameterization, were used as

reference to optimize the Fe-S DFTB2 repulsion parameters. The DFTB+ program was used to test, on-the-fly, by means of FASP interface, the DFTB2 Fe-X (X = Fe, S, O, H) repulsive parameters in several systems (molecules, clusters and solids), for instance, the ones described in Table A19. The structural properties were used as criteria to select the best DFTB2 parameters, as shown in Table A19.

Table A19- Repulsion energy parametrization. Atomic pairs, reference systems, dependencies for a-b pairs, E_{bnd} and E_{ref} interception point (IP), the cut radius (R_{cut}), and bond distances. Only singlet spin configuration was considered for all reference systems.

a-b Pairs	Reference systems	Dependencies	IP, bohr	R_{cut} , bohr	Bond Distances, Å	
					DFT	FASP
Fe-Fe	Fe ₂	No	4.24	4.29	-	-
S-S	S ₂	No	4.02	4.12	1.93	1.93
Fe-S	FeS	No	5.80	5.82	2.40	2.48
Fe-O	FeO	No	3.94	4.09	-	-
Fe-H	FeH ₂	H-H	2.82	2.92	1.50	1.48
S-O	SO ₂	O-O	3.14	3.23	1.46	1.47
S-H	H ₂ S	H-H	3.70	3.73	1.36	1.36

Appendix Q: SO dissociation on the surface

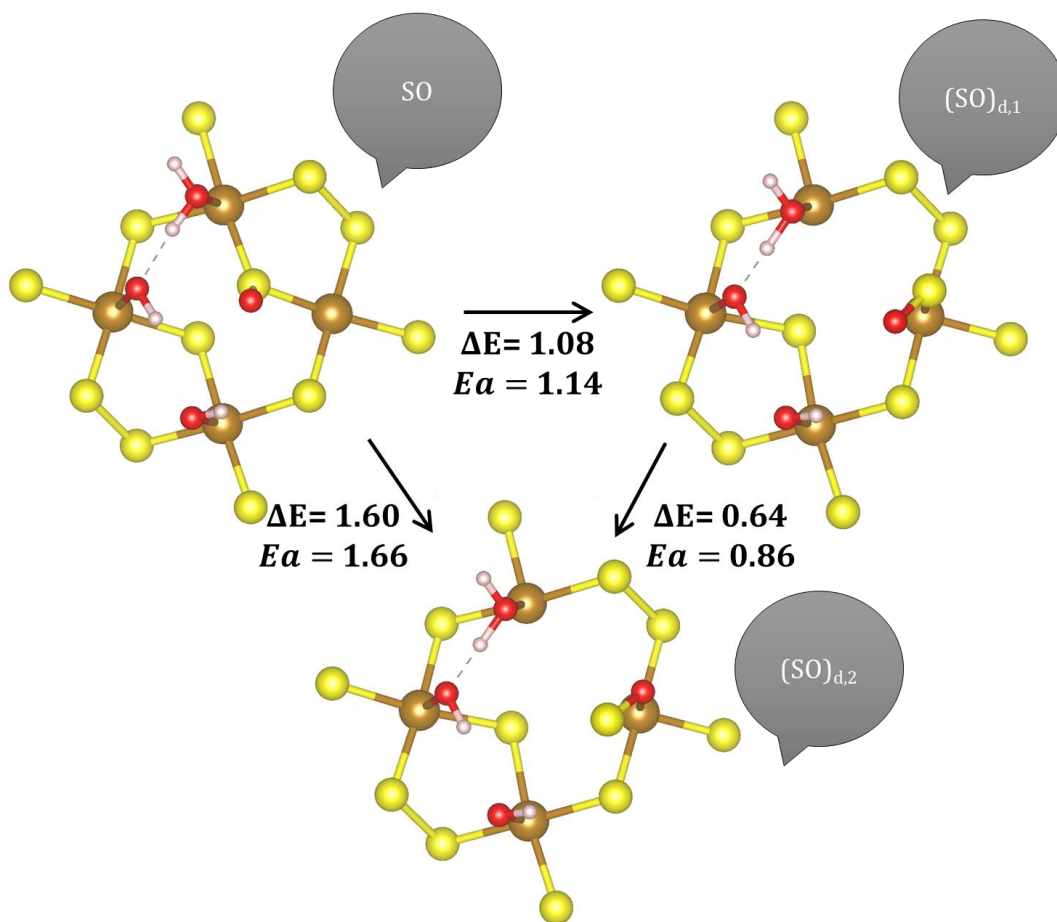


Figure A21- SO dissociation on pyrite surface. Color code: yellow - Sulfur, green - Arsenic, brown -Iron.

Appendix R: Curriculum Vitae.

Full name: Egon Campos dos Santos

Birth: 12/06/1989 – Belo Horizonte/MG - Brasil

Formal Education

2016-2019 Doctorate in Chemistry (CAPES 7)

Universidade Federal de Minas Gerais- UFMG, Belo Horizonte, Brasil *with one-year period in Stockholm University (Advisor: Lars G. M. Pettersson)*

Title: Simulação computacional da interface pirita/arsenopirita- efeitos galvânicos na reatividade química de minerais

Advisor: Hélio Anderson Duarte

Scholarship from: Coordenação de Aperfeiçoamento de Pessoal de Nível Superior

2014-2016 Master in Chemistry (CAPES 7)

Universidade Federal de Minas Gerais- UFMG, Belo Horizonte, Brasil

Title: Mecanismo de oxidação da pirita: Uma abordagem através de cálculos DFT

Advisor: Hélio Anderson Duarte

Scholarship from: Coordenação de Aperfeiçoamento de Pessoal de Nível Superior

2010-2014 Graduation in Chemistry

Universidade Federal de Minas Gerais- UFMG, Belo Horizonte, Brasil

Complete articles published in journals

1. STENLID, JOAKIM HALLDIN; **DOS SANTOS, EGON CAMPOS**; JOHANSSON, ADAM JOHANNES; PETTERSSON, LARS G. M. On the Nature of the Cathodic Reaction

- during Corrosion of Copper in Anoxic Sulfide Solutions. *Journal of the Electrochemical Society*, v. 166, p. C196-C208, 2019.
2. HEDSTRÖM, SVANTE; **DOS SANTOS, EGON CAMPOS**; LIU, CHANG; CHAN, KAREN; ABILD-PEDERSEN, FRANK; PETTERSSON, LARS G. M. Spin Uncoupling in Chemisorbed OCCO and CO₂: Two High-Energy Intermediates in Catalytic CO Reduction. *Journal of Physical Chemistry C.*, v.122, p. 12251-12258, 2018.
 3. SILVA, JULIANA C.M.; **DOS SANTOS, EGON C.**; DE OLIVEIRA, ALINE; HEINE, THOMAS; DE ABREU, HEITOR A.; DUARTE, HÉLIO A. Adsorption of water, sulfates and chloride on arsenopyrite surface. *Applied Surface Science*, v.434, p. 389-399, 2018.
 4. DUARTE, HÉLIO ANDERSON; **DOS SANTOS, EGON CAMPOS**; SILVA, JULIANA CECÍLIA DE MENDONÇA; DE LIMA, GUILHERME FERREIRA.; DE ABREU, HEITOR AVELINO. Modeling the oxidation mechanism of pyrite and arsenopyrite – connection to acid rock drainage. *Chemical Modelling*, 162–194, 2018.
 5. SILVA, JULIANA CECÍLIA DE MENDONÇA; **DOS SANTOS, EGON CAMPOS**; HEINE, THOMAS; DE ABREU, HEITOR AVELINO; DUARTE, HÉLIO ANDERSON Oxidation Mechanism of Arsenopyrite in the Presence of Water. *Journal of Physical Chemistry C.*, v.121, p. 26887-26894, 2017.
 6. SOARES JR, ANTONIO L; **DOS SANTOS, EGON C**; MORALES-GARCÍA, A; HEINE, THOMAS; DE ABREU, HEITOR A; DUARTE, HÉLIO A. Two-dimensional crystal CuS- electronic and structural properties. *2D Materials*, v. 4, p. 015041, 2017.
 7. **DOS SANTOS, EGON C.**; LOURENÇO, MAICON P.; PETTERSSON, LARS G. M.; DUARTE, HÉLIO A. Stability, Structure, and Electronic Properties of the Pyrite/Arsenopyrite Solid-Solid Interface-A DFT Study. *Journal of Physical Chemistry C*, v. 121, p. 8042-8051, 2017.
 8. **DOS SANTOS, EGON C.**; DE MENDONÇA SILVA, JULIANA CECÍLIA; DUARTE, HÉLIO ANDERSON. Pyrite Oxidation Mechanism by Oxygen in Aqueous Medium. *Journal of Physical Chemistry. C*, v. 120, p. 2760-2768, 2016.
 9. SOARES, ANTONIO L.; **DOS SANTOS, EGON C.**; MORALES-GARCÍA, A.; DUARTE, HÉLIO A.; DE ABREU, HEITOR A. The Stability and Structural, Electronic and Topological Properties of Covellite (001) Surfaces. *ChemistrySelect*, v. 1, p. 2730-2741, 2016.

10. DA SILVA, MAURÍCIO CHAGAS; **DOS SANTOS, EGON CAMPOS**; LOURENÇO, MAICON PIERRE; GOUVEA, MATEUS PEREIRA; DUARTE, HÉLIO ANDERSON. Structural, Electronic, and Mechanical Properties of Inner Surface Modified Imogolite Nanotubes. *Frontiers in Materials*, v. 2, p. 1-10, 2015.
11. MORALES-GARCÍA, A.; SOARES, ANTONIO LENITO; **DOS SANTOS, EGON C.**; DE ABREU, HEITOR A.; DUARTE, HÉLIO A. First-Principles Calculations and Electron Density Topological Analysis of Covellite (CuS). *The Journal of Physical Chemistry. A*, v. 118, p. 140211104640002, 2014.
12. SILVA, MAURÍCIO CHAGAS; **DOS SANTOS, EGON CAMPOS**; LOURENÇO, MAICON PIERRE; DUARTE, HÉLIO ANDERSON. Structural, mechanical and electronic properties of nano-fibriform silica and its organic functionalization by dimethyl silane: a SCC-DFTB approach. *Journal of Molecular Modeling*, v. 19, p. 1995-2005, 2013.

More details in

<http://buscatextual.cnpq.br/buscatextual/visualizacv.do?id=K4323644U0>

2D Materials



PAPER

Two-dimensional crystal CuS—electronic and structural properties

Antonio L Soares Jr^{1,2}, Egon C Dos Santos¹, A Morales-García³, Thomas Heine^{3,4}, Heitor A De Abreu¹ and Hélio A Duarte¹RECEIVED
7 September 2016REVISED
1 December 2016ACCEPTED FOR PUBLICATION
2 December 2016PUBLISHED
19 December 2016¹ GPQIT, Departamento de Química, ICEx, Universidade Federal de Minas Gerais, Belo Horizonte, 31.270-901, Minas Gerais, Brazil² Department of Physics & Earth Sciences, Jacobs University Bremen, Campus Ring 1, D-28759 Bremen, Germany³ Department of Physical and Macromolecular Chemistry, Faculty of Science, Charles University in Prague, Hlavova 2030, 128 43, Prague 2, Czech Republic⁴ Wilhelm-Oswald-Institut für Physikalische und Theoretische Chemie, Universität Leipzig, Linnéstr. 2, D-04103 Leipzig, Germany

E-mail: duarteh@ufmg.br

Keywords: covellite, layers, nanosheets, sulfide mineral, DFT

Supplementary material for this article is available online

Abstract

Covellite is a metallic layered mineral with rather strong interlayer interaction. Recently, synthesis of covellite nanosheets of 3.2 nm thickness was reported (Du *et al* 2012 *Nat. Commun.* 3 1177), which raises the question: ‘What is the thinnest possible covellite nanosheet?’ Based on density functional/plane waves calculations, we have shown that graphene-like structure CuS (1L-CuS) is unstable but can be stabilized on a support. Here, however, we demonstrate that the three layered CuS (3L-CuS) with thickness of 0.773 nm (including the atomic radius of the outer plans atoms) is predicted to be intrinsically stable, as confirmed by phonon analysis and Born–Oppenheimer molecular dynamics simulations, with 3L-CuS about 0.15 eV per CuS less stable than the bulk. Interestingly, the electronic band structure shows metallic character with four bands crossing the Fermi level. The nature of chemical bonding is confirmed by a detailed topological analysis of the electron density.

1. Introduction

Copper sulfides (Cu₂S) have received special attention because of their opto-electronic properties [1]. Cu₂S materials ($x > 1$) are p-type semiconductors (except for $x = 1$ which is metallic), and, depending of the value of x ($1 \leq x \leq 2$), one can tune their properties towards applications in different fields, such as solar cells [2–4], Li-ion rechargeable batteries [1, 5–7], catalysts [8], biosensors [9] and gas sensors [10, 11]. Covellite (CuS) is one of the most studied copper sulfides due to its absorption band gap in the near infrared region and its large ion diffusion permitting to envisage its application in solar energy and rechargeable batteries. Furthermore, it has been shown that covellite can be synthesized to form nanosheets [1, 12], nanoplates [13, 14], nanowires [15–17], nanoribbons [18], and nanospheres [19–21], broadening its potential technological applications.

Covellite (CuS) bulk structure has a rich and varied atomic environment formed by trigonal planar (1) and tetrahedral (2) units surrounding two distinct copper atom types, creating [Cu(2)S(2)₃S(1)] and [Cu(1)S(1)₃

motifs, respectively (figure 1(a)) [22]. The structure can be also described as a sequence of –212212212– lattice planes along the (001) direction, where the 21 and 22 units are connected by Cu–S and through S–S bonds, respectively. By means of theoretical predictions, we recently reported the plausible existence of a hexagonal flat monolayer, labeled as 1L-CuS [23] after the relaxation of the A–S(2) surface along (001) direction (figure 1(b)). However, free-standing 1L-CuS is unstable, but it can be stabilized by a support.

The two-dimensional (2D) materials field has received special attention since the isolation of single-layer graphene by Novoselov *et al* in 2004 [24]. 1L-CuS shows a structure analogous to the 2D honeycomb lattice of graphene, h-BN (hexagonal boron nitride), AlN, CdS, SiC, ZnO, ZnS and MgO [25–27]. 1L-CuS is formed and moves away from (001) covellite surface due to the breaking of the weakest bond, Cu(2)–S(1) [28, 29], mimicking the exfoliation process.

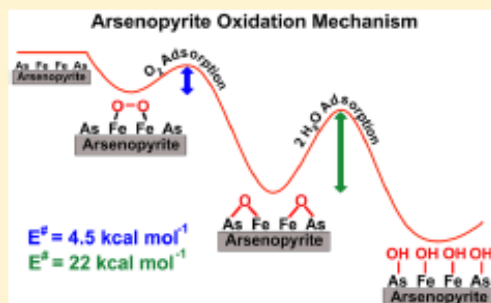
The formation of thin films of three-dimensional bulk systems is well-known. For example for wurtzite ZnO, Freeman *et al* [30] predicted that the bond

Oxidation Mechanism of Arsenopyrite in the Presence of Water

Juliana C. M. Silva,^{†,‡} Egon C. dos Santos,[†] Thomas Heine,^{‡,§} Heitor A. De Abreu,[†] and H elio A. Duarte^{*,†,§}[†]Grupo de Pesquisa em Qu mica Inorg nica Te rica–GPQIT–Departamento de Qu mica, ICEx, Universidade Federal de Minas Gerais (UFMG), Av. Ant nio Carlos, 6627, 31270-901 Belo Horizonte, MG, Brazil[‡]Department of Physics & Earth Sciences, Jacobs University Bremen, Campus Ring 1, 28759 Bremen, Germany[§]Wilhelm-Ostwald-Institute of Physical and Theoretical Chemistry, University of Leipzig, Linn str. 2, 04103 Leipzig, Germany

Supporting Information

ABSTRACT: Arsenopyrite is commonly present in mining tailings and, together with pyrite, is responsible for acid rock drainage (ARD) phenomenon. The mineral undergoes oxidation in contact with oxygen and water producing a solution containing acid and heavy metals and, hence, causing important environmental impacts. Density functional/plane wave calculations were carried out to investigate the oxidation of arsenopyrite aiming to understanding its intricate mechanism at a molecular level. Molecular oxygen is dissociatively adsorbed in the Fe–O–As adsorption sites leading to the oxidation of arsenic and iron sites in good agreement with the available experimental data. It avoids the many steps observed for the pyrite oxidation mechanism. The presence of water is extremely important for the next steps of the oxidation mechanism similarly to the oxidation mechanism of pyrite. The present work reinforces the fact that the removal of the humidity can inhibit the oxidation of the arseno(pyrites) in an aerobic condition.



1. INTRODUCTION

Arsenopyrite, FeAsS, is the most important arsenic containing mineral, normally associated with noble metals such as gold and copper. The mineral processing of arsenopyrite rich ores normally leads to mining tailings with high concentration of arsenic.^{1,2} Arsenopyrite is stable under reducing conditions, however, like other sulfide minerals, it is oxidized by weathering effects when exposed to the atmosphere in a process called acid rock drainage (ARD). This process occurs mainly during the industrial extraction of metals from ores, in which the sulfide mineral oxidizes in contact with water and oxygen, yielding sulfuric acid. This acid can solubilize the solid mineral constituents, producing a solution containing acid and dissolved metals, which can contaminate soils and natural waters.

The oxidation reaction of arsenopyrite has slow kinetics, yet it can be catalyzed by microorganisms present in the environment.¹ Specifically the ARD of arsenopyrite releases arsenite and arsenate species, which requires a special treatment during the oxidation process due to its toxicity.² Arsenic is a public health problem in many regions of the world and the main environmental concern with respect to the noble metal extraction, which is found associated with pyrites. Mitigation of the ARD problem and the development of countermeasures are facilitated by understanding its mechanism. For this reason, understanding the kinetics and mechanisms of dissolution of this mineral in different conditions is crucial for envisaging

efficient strategies of waste control with environmental, social and economic importance.

Many investigations have been performed with the purpose of identifying the products formed in arsenopyrite oxidation in different media^{1–6} and two studies have been made concerning the structure of arsenopyrite surface.^{9,10} However, since the solutions formed in this process are very complex, as well as the reactions involved, the results found for products and kinetics of arsenopyrite oxidation are not in agreement and a lack of consensus is observed.¹

Buckley and Walker,³ as well as Mikhlin et al.,⁷ suggested a depletion in Fe and As on arsenopyrite surface after acid treatment. Costa et al.¹¹ observed elemental sulfur formation when arsenopyrite was exposed to acid. However, Richardson and Vaughan¹² found the opposite: a surface enriched in Fe and As after reaction with H₂SO₄. Nesbitt and Muir⁵ reported the absence of sulfur on arsenopyrite surface reacted in acidic mine wastewater. Corkhill et al.⁸ observed the species Fe(III)–OH, As(III)–O, As(IV)–O, thiosulfate, and sulfate for arsenopyrite reacted in H₂SO₄ solution, and As is the most rapidly oxidized element in this condition. Nesbitt et al.² and Schaufuss et al.¹³ found a preferential enrichment of arsenic as As-oxides on the overlayer of oxidized arsenopyrite due to diffusion of this atom

Received: September 29, 2017

Revised: November 12, 2017

Published: November 13, 2017



Stability, Structure, and Electronic Properties of the Pyrite/Arsenopyrite Solid–Solid Interface—A DFT Study

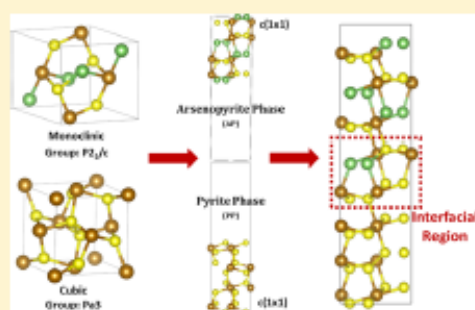
Egon C. Dos Santos,[†] Maicon P. Lourenço,[†] Lars G. M. Pettersson,[‡] and Hélio A. Duarte^{*†}

[†]GPOIT, Departamento de Química, ICEX, Universidade Federal de Minas Gerais, Belo Horizonte, 31.270-901 Minas Gerais, Brazil

[‡]Department of Physics, AlbaNova University Center, Stockholm University, S-10691 Stockholm, Sweden

Supporting Information

ABSTRACT: Pyrite is the most common sulfide in the Earth. In the presence of arsenopyrite its oxidation is delayed, and instead, the arsenopyrite increases its oxidation rate, releasing As(III) and As(V) species in the medium. DFT/plane waves calculations were performed on pyrite/arsenopyrite interface models to understand the stability, structure, and electronic properties of the interface. This is the first step to understand the influence of the inlaid arsenopyrite in the pyrite oxidation mechanism. The interface is slightly stressed with minor changes in the bond lengths and lattice parameters with respect to the pure phases. The work of adhesion and the formation energy indicate that the miscibility of the two phases is not favorable, explaining the presence of large domains of either pyrite or arsenopyrite forming bulk granular regions. The valence band of the pyrite/arsenopyrite interface has large contributions from the pyrite phase, while the conduction band has large contributions from the arsenopyrite. This is consistent with the pyrite as cathode and arsenopyrite as anode in a galvanic contact. Furthermore, the interface formation shifts the valence states upward and decreases the band gap, facilitating interfacial electron transfer.



1. INTRODUCTION

In nature, sulfide ores are complex solid mixtures, and consequently, their structural, mechanical, and electrochemical properties are difficult to assess. Hydrometallurgical routes rather than pyrometallurgical processes are always considered for treating low-grade ores. However, hydrometallurgical recovery of noble metals has to deal with the secondary reactions provoked by the galvanic interactions between associated minerals within the concentrates. In aqueous leaching or bioleaching processes the galvanic interaction substantially increases the oxidative dissolution of one or both of the minerals constituting the galvanic cell.^{1–5} The outcome will depend on the electrochemical characteristics of the minerals and on the occurrence of the distinct sulfides contained in the soils, sediments, substrates, and ore concentrates.

Pyrite (FeS₂) is the most abundant and widespread sulfide mineral and commonly found associated with other minerals that have economic interest, such as marcasite,¹ galena,⁶ sphalerite,⁷ covellite,⁷ chalcopyrite,⁸ and arsenopyrite.^{9–13} Furthermore, it is mostly responsible for acid rock drainage (ARD) due to its oxidation when exposed to air, releasing acid and heavy metals. ARD is hazardous for the environment and is a major concern in the mineral industry. Since sulfide minerals are semiconductor materials that can participate in redox reactions, the contact between the distinct minerals may lead to galvanic effects. One mineral will act as anode by promoting the

oxidation reaction and the other as cathode, in which the reduction reaction occurs.^{14,15} Abraitis et al.⁷ showed that, in the presence of pyrite, the dissolution of sulfide mixed-mineral systems can be dramatically affected by galvanic effects, and the rates can increase by a factor greater than 30 if compared with the isolated phases under the same experimental conditions. Therefore, it is important to consider how other sulfide minerals inlaid in pyrite affect its chemical reactivity toward oxidation.

Arsenopyrite (FeAsS) is also an important mineral because it is primarily associated with other sulfide minerals and valuable metals (e.g., copper, silver, and gold). In certain ores, extracting the arsenopyrite contribution has considerable economic significance since it carries the major portion of the gold in the ore. When mined and exposed to the environment, its oxidation also leads to ARD releasing arsenite [As(III)] and arsenate [As(V)] in addition to acid and heavy metals. Natural arsenopyrite samples are always associated with pyrite and are generally found with large domains of pyrite randomly inlaid in its structure.^{16–21} In several studies the galvanic effect between arsenopyrite and pyrite minerals has been found to lead to an increase in the dissolution oxidation process.^{9–13,22–24} More recently, Urbano et al.¹³ carried out a voltammetric study of arsenopyrite containing 11.84% of pyrite mineralogical impurity

Received: March 20, 2017

Published: March 22, 2017



Full Length Article

Adsorption of water, sulfates and chloride on arsenopyrite surface



Juliana C.M. Silva^{a,b}, Egon C. dos Santos^a, Aline de Oliveira^a, Thomas Heine^{b,c},
Heitor A. De Abreu^a, Hélio A. Duarte^{a,*}

^a Grupo de Pesquisa em Química Inorgânica Teórica – GPOIT, Departamento de Química, ICEX, Universidade Federal de Minas Gerais (UFMG), Av. Antônio Carlos, 6627, 31270-901 Belo Horizonte, MG, Brazil

^b Physics & Earth Sciences, Jacobs University Bremen, Campus Ring 1, 28759 Bremen, Germany

^c Wilhelm-Ostwald-Institute of Physical and Theoretical Chemistry, University of Leipzig, Linnestr. 2, 04103 Leipzig, Germany

ARTICLE INFO

Article history:

Received 29 March 2017

Received in revised form 18 October 2017

Accepted 24 October 2017

Keywords:

Arsenopyrite

Adsorption

Density functional theory

Plane waves

Sulfide minerals

Sulfates

ABSTRACT

Arsenopyrite is one of the sulfide minerals responsible for acid rock drainage (ARD) and is one of the most hazardous in regions affected by mining activities. This phenomenon involves complex reaction mechanism. Although it is intensely investigated, there is a lack of consensus concerning the reaction mechanisms and more information is still necessary. In this work, the adsorption of water, hydrochloric acid, and sulfuric acid on arsenopyrite (001) surface was investigated by means of Density Functional calculations and the results compared to other sulfides aiming to understand the mineral/water interface. The interaction of the chemical species with the (001) FeAsS surface is the first step to understand the intricate oxidation mechanism of arsenopyrite. Molecular water adsorption on (001) FeAsS is more favored than the adsorption of sulfate favoring the dissolution of sulfates and enhancing its oxidation. The estimated adsorption energies of water, sulfates and chloride on other sulfide minerals are compared with the estimated values for arsenopyrite and the chemical reactivity differences discussed in detail.

© 2017 Elsevier B.V. All rights reserved.

1. Introduction

Pyrites are an important class of minerals in the earth crust such as pyrite (cubic FeS₂), marcasite (orthorhombic FeS₂), arsenopyrite (FeAsS) and chalcopyrite (CuFeS₂). Noble metals such as gold, platinum, silver, copper and other metals of economic importance are normally found incrustated in pyrite and arsenopyrite. However, they also host many toxic metals, such as lead and cadmium [1]. In the process of extraction, great amounts of mineral are handled exposing it to the atmosphere and humidity. In the presence of oxygen and water, pyrites are oxidized releasing sulfuric acid in the very end of the process and, thus, enhancing the mobilization of heavy metals to the environment and aquifers. This phenomenon is called acid rock drainage (ARD) and is one of the most hazardous in the mining industry related to noble metal extraction. In spite of the anthropogenic causes, natural processes can also happen whenever the pyrites are exposed to the environment.

Efforts have been made to understand the structure and chemical reactivity of pyrite [2–6], arsenopyrite [7–11], covellite [12,13] and chalcopyrite [14–19] surfaces. The adsorption of water on

pyrite has received much attention [20–23] due to the importance of this mineral in flotation techniques to separate it from valuable metals and also to ARD. The interaction of HCl and H₂SO₄ on chalcopyrite surface [16] has been investigated aiming to understand the low kinetics of the leaching process for copper extraction.

Investigating solid/liquid interface is the first step to understand the reactivity of the mineral surface and, consequently, the first steps of its oxidation mechanism. It has been shown that the water has an important role in this process and the leaching agents such as hydrochloric acid and sulfuric acid can bring new insights about the surface/liquid interface at the molecular level [16]. In this context, first-principle calculations can provide insights about the arsenopyrite surface reactivity and a molecular view of the surface/solution interface.

In natural environments, and especially in mining tailings, arsenopyrite surface is in contact with water, and the role of this molecule in the oxidation mechanism has not yet been investigated. The behavior of this mineral in aqueous medium is a step that must be investigated before any attempt to understand the mineral oxidation can be taken.

Arsenopyrite is a diamagnetic semiconductor [24]. Its unit cell has space group P2₁/c [25] and contains 4 FeAsS formula units. The structure contains arsenic and sulfur dianions (As–S) coordinated to Fe atoms in a distorted octahedron. The Fe atoms are coordinated

* Corresponding author.

E-mail address: duarteh@ufmg.br (H.A. Duarte).



Spin Uncoupling in Chemisorbed OCCO and CO₂: Two High-Energy Intermediates in Catalytic CO₂ Reduction

Svante Hedström,[†] Egon Campos dos Santos,^{‡,†} Chang Liu,[†] Karen Chan,[§] Frank Abild-Pedersen,[§] and Lars G. M. Pettersson^{*†}

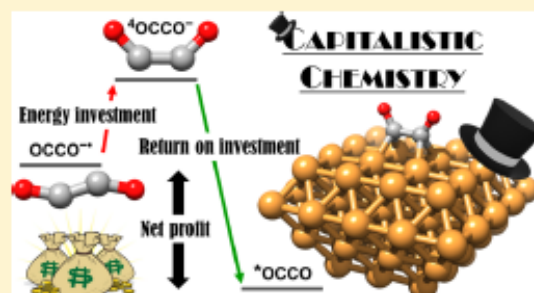
[†]Department of Physics, Albanova University Center, Stockholm University, 10691 Stockholm, Sweden

[‡]GPQIT, Departamento de Química, ICEx, Universidade Federal de Minas Gerais, Belo Horizonte 31270-901, Minas Gerais, Brazil

[§]SUNCAT Center for Interface Science and Catalysis, SLAC National Accelerator Laboratory, Menlo Park, California 94025, United States

Supporting Information

ABSTRACT: The production of useful compounds via the electrochemical carbon dioxide reduction reaction (CO₂RR) is a matter of intense research. Although the thermodynamics and kinetic barriers of CO₂RR are reported in previous computational studies, the electronic structure details are often overlooked. We study two important CO₂RR intermediates: ethylenedione (OCCO) and CO₂ covalently bound to cluster and slab models of the Cu(100) surface. Both molecules exhibit a near-unity negative charge as chemisorbed, but otherwise they behave quite differently, as explained by a spin-uncoupling perspective. OCCO adopts a high-spin, quartetlike geometry, allowing two covalent bonds to the surface with an average gross interaction energy of -1.82 eV/bond. The energy cost for electronically exciting OCCO⁻ to the quartet state is 1.5 eV which is readily repaid via the formation of its two surface bonds. CO₂, conversely, retains a low-spin, doubletlike structure upon chemisorption, and its single unpaired electron forms a single covalent surface bond of -2.07 eV. The 5.0 eV excitation energy to the CO₂⁻ quartet state is prohibitively costly and cannot be compensated for by an additional surface bond.



INTRODUCTION

The electrochemical CO₂ reduction reaction (CO₂RR) is projected as an important part of a sustainable, carbon-neutral energy economy.^{1–3} Many different products can be formed, depending on the element⁴ and structure of the metal catalyst,^{5,6} the applied potential, solvent pH,⁷ and other reaction conditions.^{8,9} Product molecules with more than one carbon atom are highly sought after because they have a higher energy density and industrial demand. Despite the rich chemical landscape of the catalytic CO₂RR, the pathways to many products share a limited number of important intermediates. Examples of such intermediates, in order of increasing degree of reduction, include chemisorbed *CO₂, *CO, and *OCCO,^{10–12} where * denotes a surface-adsorbed state.

In the gas phase, neutral singlet ethylenedione, or OCCO, is unstable with respect to dissociation into 2 CO^{13,14} and the triplet state is metastable but readily crosses to the dissociative singlet state under experimental conditions. However, the cationic, anionic, and dianionic redox states are stable and have been studied in significant detail by ab initio¹⁵ and experimental^{14,16–18} methods. On metal catalyst surfaces, *OCCO is produced by dimerization of *CO and has been

identified as a crucial, early intermediate toward multicarbon products in CO₂ reduction.^{10–12} Formation of a double C=C bond entails a high kinetic barrier, making *OCCO formation a potentially rate-limiting step in the route to CO₂RR products such as ethanol and ethylene. Another high-energy intermediate is chemisorbed *CO₂ because CO₂ in either the gas or aqueous phase is thermodynamically highly stable, and so its chemisorption and concomitant reduction have been suggested to be a rate-determining step in the CO₂RR under certain conditions,^{19–25} particularly on weakly binding metals such as Au.²⁶ Despite the importance of *CO₂ and *OCCO, their electronic structures under electrocatalysis-like conditions have so far not been reported in detail, with previous studies rather focusing on larger-scale energetics and kinetics.

We focus here on the electronic structure of *CO₂ and *OCCO on the Cu(100) facet because its geometry favors *OCCO adsorption and shows a higher activity for CO₂ reduction into multicarbon products^{27–29} and moreover has been suggested to be the eventual predominant facet for

Received: March 5, 2018

Revised: April 26, 2018

Published: May 8, 2018